# Structural and Property investigations into low-doped lithium nitridometallates

## $Li_{3-x-y}M_xN$, x = Co, Ni and Cu

By

Donald Kenneth Carmichael MSci


Submitted in fulfilment of the requirements for the Degree of Doctor of Philosophy

School of Chemistry

College of Science and Engineering

University of Glasgow

April 2011

# Abstract

Bulk samples of the lithium nitridometallates of the general form $Li_{3-x}M_xN$ and $Li_{3-x-y}M_xN$, where M = Co, Ni and Cu, $x \leq 0.1$ and y = vacancy, have been synthesised. The products of the syntheses have been characterised by Powder X-ray Diffraction (PND), Constant Wavelength Powder Neutron Diffraction (CW PND), Time of Flight Powder Neutron Diffraction (ToF PND), SEM and SQUID magnetometry. The transition metal entirely substituted for the Li(1) at the interplanar site and resulted in a retention of the $Li_3N$-type structure, P6/*mmm*. These materials displayed similar structural trends as seen in lithium nitridometallates with higher transition metal levels, and with vacancies, which were also dependent on reaction time and temperature at this low level. For longer reacted lithium nitridometallates a large concentration of vacancies was obtained despite a small quantity of dopant transition metal. The resultant charge was deemed too high to be solely balanced by the transition metal, as is usual in these materials. A charge compensation mechanism involving the nitrogen ion was assumed for the high-vacancy materials.

The materials displayed some interesting forms of magnetism such as spin-glass magnetic behaviour and also Pauli paramagnetism. $Li_{2.95}Ni_{0.05}N$ and $Li_{2.90}Co_{0.1}N$ displayed a high specific capacity upon electrochemical testing when applied as a potential anode material, and gave better charge capacities than that of the previous best lithium anode material and showed signs of improvement upon cycling.

Preliminary investigations into hydrogen adsorption of the materials had been attempted, with one particular material, $Li_{2.95}Ni_{0.05}N$, giving a hydrogen adsorption of 7.839 wt % over 90 hours with a hydrogen pressure of 20 bar and temperature of 250 $^oC$. A corresponding 3.5 wt % loss was achieved upon desorption at the same temperature.

Table of Contents

List of Tables

List of Figures

# Acknowledgements

I would firstly like to thank my supervisor Prof. Duncan H. Gregory, for all his support and guidance throughout the PhD, and for livening up our group nights out by giving me an opportunity to talk ‘footy’ for a while, however I would like to point out that his team has cost me a fortune in failed bets in the last few years.

I would most importantly like to thank my family, my sisters Cathy and Caroline, but especially my mum and dad Ann and Calum, for all their help, support, cash, blood, sweat and tears etc etc. Without them I would never be in the position I am in life, and also now hopefully you can get off my case dad and stop asking me how many pages I’ve written today, worst slave driver ever.

I’d like to thank my beautiful wife to be Michelle Rooney for putting up with me all throughout this time and being so understanding when I have been moody and not given her enough time, and at least there is definitely one good thing to have come of my time in the Department, and that is meeting her. I would like to thank my ‘second family’ also, ‘the Rooneys’, Ann, Mick and Joanne, you have been so kind to me since day one, thank you for that.

I would also like to thank all of the Gregory group at the Chemistry Department, especially Dr Robert Hughes for being my ‘phone a friend’ for every question and query I have had, Saleem Denholme for providing me with much amusement as my flatmate also (fairy liquid beef olives?! Yummy) and Lucia Carassiti for her words of wisdom at times. I would also like to thank some of the friends I made in the Department in my time there especially Neil Hamilton (pub, gym, party and mayhem partner), Craig Richmond (remember the green men and the Bucky balls), Andrew Kennedy (Bad Kavos), Stuart Blain (Caprice) and David Lockhart (The affrontery!).

Finally I would like to thank Dr Clemens Ritter (CW PND), Dr Ron I. Smith (ToF PND), Jim Gallagher and Saleem Denholme (SEM), Dr Rosa Palacin and Dr Frederic Gillot (Electrochemistry), Dr Marek Jura (SQUID), Dr Robert Hughes (PCT), The Department of Chemistry technicians (mostly Stuart Mackay) and The University of Glasgow for the funding.

"*It requires wisdom to understand wisdom: the music is nothing if the audience is deaf.*" – Walter Lippman

# 1. Introduction

## 1.1 Background to Physical Properties of $Li_3N$

In recent years functional materials have found an important role in newly emerging areas of technology and, as a consequence, research in the field of solid state chemistry has become fundamental to the growth of this industry. Materials that display useful or interesting properties such as superconductivity, ionic conductivity, hydrogen storage and magnetic properties have found application in systems such as Superconducting QUantum Interference Devices (SQUID) in the case of superconducting materials, to lithium rechargeable batteries for materials displaying high ionic conductivity. The properties that these materials display stem from their structural configurations and, in order for these properties to be fully understood, the structures must be well investigated. Once understood sufficiently, tailoring of the properties can be achieved through modifications to the structure, and therefore understanding of the structure-property relationships in these new materials is fundamental to their development.

### *1.1.1Electronic conductivity of solids*

For the purpose of envisaging bonding in solids, it is best to employ the linear combination of atomic orbitals (LCAO) approach. If this is assumed for a chain of atoms, i.e. hydrogen atoms, there will be a bonding orbital whereby all of the 1s orbitals combine in phase, σ, and a higher energy antibonding orbital, σ*, whereby the 1s orbitals combine out of phase[1] this can be seen in Figure 1.1.

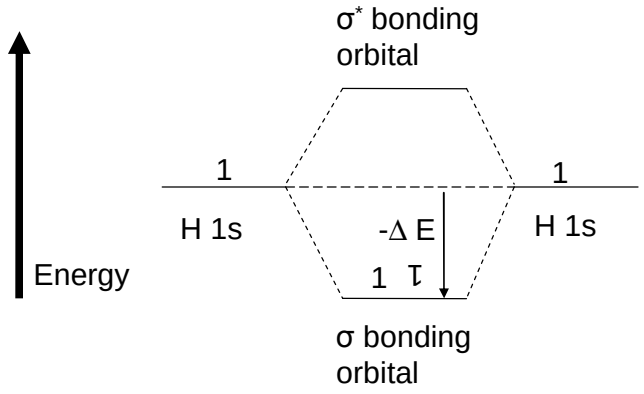


**Figure 1.1 LCAO diagram for the molecular bonding σ and antibonding σ* of two H atoms.**

When the number of atoms is increased, the number of energy levels also increases, but the separation between each of these does not increase so dramatically. So when considered for chains in a crystal, there is negligible separation between these levels, and the energy levels are then considered as an energy continuum or energy band. For solids, the better the overlap of the orbitals, then the greater the band width, and at 0 K the highest occupied energy level is called the Fermi level.

Due to the fact that electrons have momentum and direction, in the absence of an applied electric field, there is an even number of electrons moving in all different number of directions. However when an electric field is applied, those electrons that are travelling in the same direction as the field are accelerated and therefore their energy, and that of the energy level the electrons are located in will be reduced. The converse is true for the energy levels of electrons moving in the opposite direction and electrons from these energy levels will drop to lower energy levels. The conductivity is governed by the expression:

$$\sigma = nZe\mu \qquad \mathbf{1.1}$$

Where *n* is the number of charge carriers per unit of volume, *Ze* is the charge and $\mu$ is the mobility[1]. Only if there are empty levels of lower energy bands can electrons move from higher energy bands to these and therefore only metals which have partially-filled energy bands will make for good electronic conductors.

### *1.1.2 Ionic conductivity of solids*

As perfect crystals only exist at 0 K, crystalline materials almost always have imperfections within their structure, or defects as they are most commonly known. These can be either intrinsic or extrinsic defects, the latter being defects that are brought about through the introduction of an atom foreign to the material into the structure, and the former being defects which are inherent to the material itself. These intrinsic defects can be further subcategorised into either Schottky or Frenkel defects[1], the latter being when an ion migrates to an interstitial site within the structure and therefore creates a vacancy, the former being where there is an absence of both an anion and cation, for the purposes of maintaining charge neutrality.

As a result, these defects can then migrate through the structure and ionic mobility could occur either by the movement of a vacancy through the lattice of the material, or through the movement of an interstitial ion to an adjacent interstitial site. The same form of expression for electronic conductivity can be used for ionic conductivity. Due to there being an energy barrier to ion migration within the lattice, either in promoting an interstitial ion or vacancy promotion, there will therefore be a temperature dependence which can be defined by way of an Arrhenius equation:

$$\mu = \mu_0 \exp\left(-E_a \big/ kT\right) \qquad \textbf{1.2}$$

where $\mu_0$ is a pre-exponential factor, $E_a$ is the activation energy, k is the Boltzmann constant and T the temperature in degrees Kelvin. When equation 1.2 is then incorporated in 1.1, we get the expression:

$$\sigma = \left(\sigma_0 \big/ T\right) \exp\left(-E_a \big/ T\right) \qquad \textbf{1.3}$$

Mixed conductors are materials in which there is a significant contribution to the overall conductivity from both electronic and ionic conduction.

### *1.1.3 Magnetic behaviour*

Magnetic behaviour is observed as an effect of the electrons in a material. Diamagnetism is a type of magnetic behaviour exhibited when a material is placed in a magnetic field and it opposes the applied field. All materials display this to some extent as it is a feature of paired electrons.

The more interesting magnetic behaviour of materials arises from the effects of the unpaired electrons termed paramagnetism, and in the presence of an applied external field, these unpaired electrons tend to align with the field. There are several different types of paramagnetism that materials can display such as Curie-type, whereby the magnetisation of the material decreases with increasing temperature. Another type is Curie-Weiss paramagnetism, whereby there is a decrease again in the magnetisation with increasing temperature, however when the inverse magnetisation is plotted versus temperature, it does not intersect the origin, as a paramagnet would. Instead these materials cross the x-axis either when $x < 0$ for a material with a net antiferromagnetic effect, and $x > 0$ for a net ferromagnetic effect. Pauli paramagnetism is another paramagnetic effect that can be seen, and this is where the magnetisation of the material is temperature independent with a Curie-Weiss contribution. These types of magnetism are discussed here further and also in section 2.4.

A subset of paramagnetism is ferromagnetism, and this is whereby the electron moments have a tendency to align parallel to an applied field in the same way as for a paramagnetic material, but once the field is removed, unlike normal paramagnets, these materials have a tendency to show magnetic order. This is where the moments have a tendency to align parallel to one another to give a lower energy state. Ferromagnets all have a unique temperature, the Curie temperature $T_C$, which when the material is heated above this, they lose their magnetization and often there is a characteristic effect known as ‘hysteresis’ to their magnetisation. Hysteresis is where there is a history to the magnetisation when the field is removed. The elements nickel, iron, cobalt, gadolinium and alloys of these materials display ferromagnetic behaviour.

Two other types of magnetic behaviour are antiferromagnetism and ferrimagnetism. The former type occurs when an external field is applied, but

the domains within the material have a tendency to align anti-parallel to one another, rather than parallel to one another as in ferromagnetism. Anti-ferromagnets have no overall magnetisation as the number of spins in opposing directions to one another cancel out. In some materials we see evidence of spin frustration in antiferromagnetic materials, and this is where the spins of neighbouring electrons align anti-parallel to one-another but where two domains meet, they cannot align that way i.e. where the edge of two magnetic domains meet, the spins of the electrons across the domains would try to align anti-parallel to each other but this would affect their alignment with relation to the spins of the other electrons in the domain. The temperature at which a transition from paramagnetic or Curie-Weiss behaviour becomes antiferromagnetic is known as the Néel temperature, $T_N$.

Ferrimagnetism is similar to antiferromagnetic behaviour but, with this type of magnetic behaviour, rather than the number of opposing spins cancelling each other out to give no overall magnetisation, there is a stronger magnetisation of the spins in one direction than in the other, thus giving an overall magnetisation in the direction of those spins.

## 1.2 Lithium Nitride

### *1.2.1 Synthesis*

There are several ways in which lithium nitride can be synthesised. The easiest of these being the direct reaction of the lithium metal with nitrogen gas at elevated temperatures. This reaction can even begin to happen at ambient temperatures, but this method leads to a poorly crystalline product and typically containing impurities such as lithium oxide and hydroxide if the strictest of conditions to eliminate oxygen or moisture have not been adhered to. Crystallinity of the product is improved by the reaction of the nitrogen with molten lithium as opposed to solid lithium metal, or solid lithium dissolved in molten sodium[2]. The phase diagram for the reaction of lithium with nitrogen is very simple as can be seen in Figure 1.2.

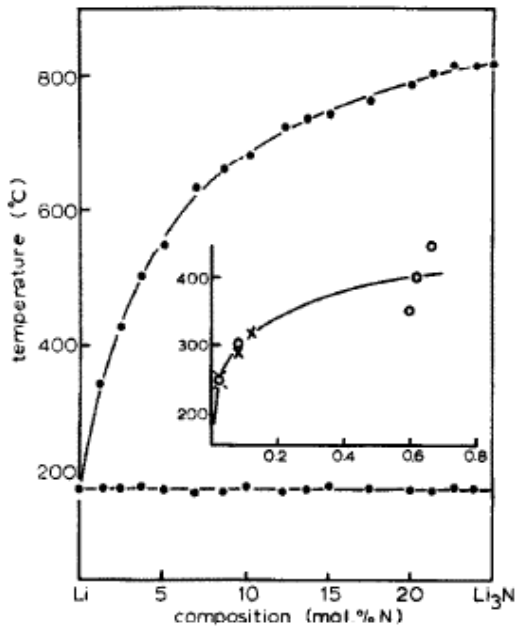


**Figure 1.2 Phase diagram for Li-$Li_3N$ system with Li rich end at the left and lithium nitride rich end at the right. The inset of the figure relates to results of dilute solutions of lithium in nitrogen. The axes of the inset are the same as for that of the main figure.**

As can be seen, there is a smooth liquidus existing from the melting point of lithium at 185° C all the way up to the melting point of $Li_3N$ at 815° C[3-4]. The area between the two lines corresponds to solid $Li_3N$, and therefore if the temperature is too low, below 185° C, even with a high concentration of nitrogen, solid $Li_3N$ will not be achieved. Similarly if the temperature is high, 815° C, but the concentration of nitrogen too low, $Li_3N$ will not be synthesised.

## *1.2.2 Structure*

Lithium nitride, $Li_3N$, is one of the most studied materials in the field of nitride chemistry gaining much interest from its early discovery[5]. Its structure was initially thought to be cubic, based on that of ammonia, but was eventually correctly characterised by Zintl and Brauer as being hexagonal from single crystal investigations[6-7]. This configuration that they proposed had a nitrogen atom co-ordinated to 8 lithium atoms in a hexagonal bipyramid. It wasn't until over 40 years later that this structure was confirmed by Rabenau and Schulz using modern techniques that had not been previously available, and they assigned the space group of *P6/mmm*[8].

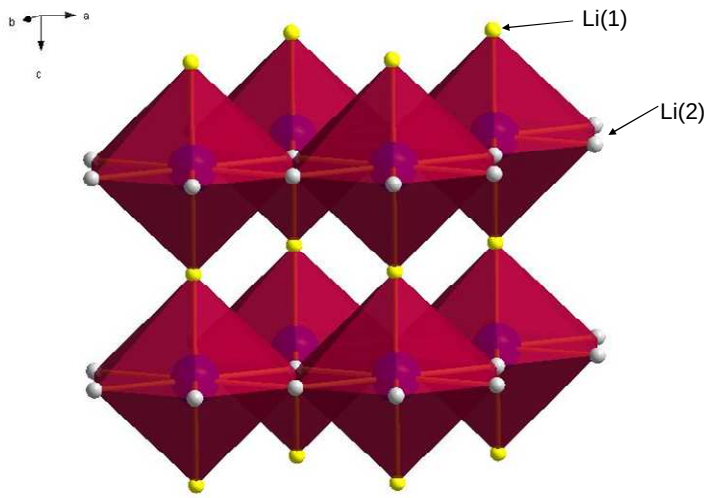


**Figure 1.3 A polyhedral representation of α-$Li_3N$. The ruby red polyhedra are centred by blue nitrogen atoms. Yellow spheres denote interplanar lithium and grey spheres intraplanar lithium atoms.**

As Zintl and Brauer had thought, each nitrogen atom is indeed coordinated to 8 lithium atoms. As can be seen in Figure 1.3 there are six lithium in a hexagonally coordinated plane to the nitrogen. This forms a [$Li_2N$] layer in the direction of the *ab* plane, which can be seen best when viewed from above in Figure 1.4.

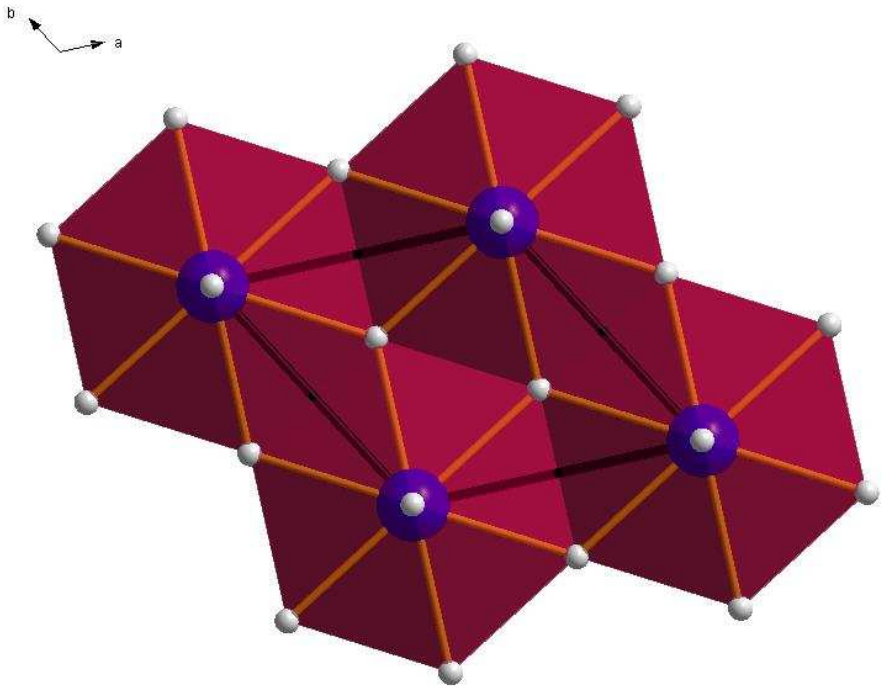


**Figure 1.4 Polyhedral representation of α-$Li_3N$ viewed down the *c*-axis. The ruby red polyhedra are centred by blue nitrogen atoms. Yellow spheres denote interplanar lithium and grey spheres intraplanar lithium atoms, and unit cell outlined in black.**

It can be seen that within the plane that there is a repeating unit of one quarter of four nitrogen atoms and two whole lithium atoms, in a trigonal planar geometry with nitrogen, contained within the unit[9]. This is where the [$Li_2N$] notation is derived from. There are then two lithium atoms linearly coordinated above and below each nitrogen, comprising a lithium layer which connects the [$Li_2N$] layers in the *c* axis direction[9]. Some of the properties of lithium nitride are unexpected, such as its colour, which can range from ruby red through to dark purple, when most ionic compounds of this type are typically white. It was these anomalous properties that first instigated the research into its bonding and structure.

Two other forms of lithium nitride were reported to exist at higher pressures, namely the beta (β) and gamma (γ) phases. The β-$Li_3N$ phase (P63/*mmc*) was first discovered in $^7$Li-NMR experiments that were carried out at elevated pressures on $Li_3N$ single crystals prepared by the Czochralski method[10]. Using He gas as the pressure inducing medium, the hexagonal phase of α-$Li_3N$ remains constant with increasing pressure at 297 K until 4.2 kbar when the intensity of

the $^{7}Li$ signals begin to increase[10]. It is therefore assumed that the transition of α-$Li_3N$ to β-$Li_3N$ occurs at 4.2 kbar and 300 K. Several pieces of evidence suggested a new structure was being formed such as two different Li site with quadrupolar coupling constants that did not correspond to the same two values as for the α-$Li_3N$, namely 406 and 164 kHz in contrast to 582 ±3 and 285 ±1 kHz in the α-$Li_3N$ system, measured with the field applied parallel to the *c*-axis. The evidence also seemed to suggest that the β-$Li_3N$ had a higher lithium ion mobility. Least squares calculation from powder diffraction studies assigned the unknown phase as being hexagonal but with a larger *c* parameter[11-12]. The new phase remains stable for several months and can be returned to the α-$Li_3N$ form at elevated temperatures and normal pressures[10]

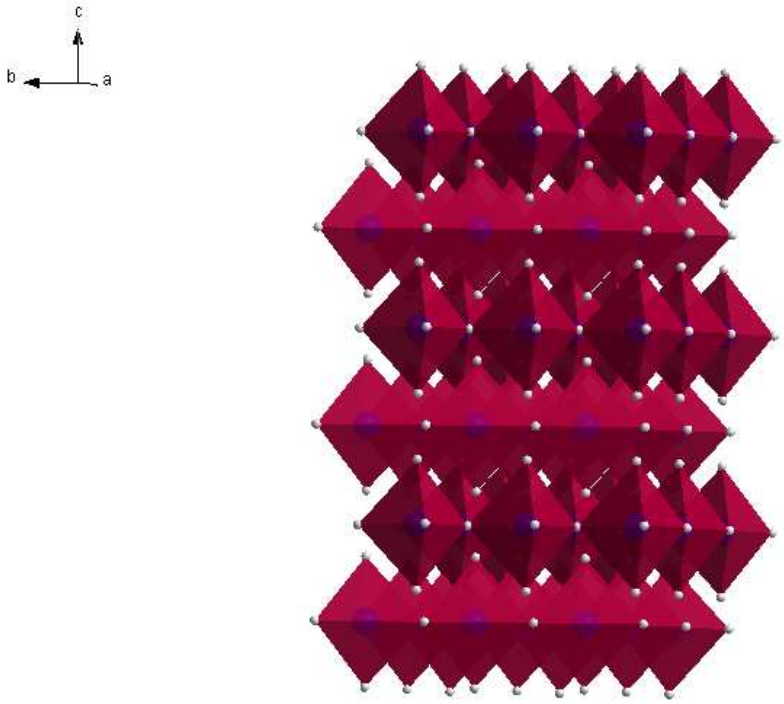


**Figure 1.5 A polyhedral representation of β-$Li_3N$ with the ruby red polyhedra, centred by blue spheres representing nitrogen atoms and white spheres representing lithium atoms.**

As seen in Figure 1.5, the previously [$Li_2N$] layers in α-$Li_3N$ are now transformed into [LiN] layers in the β-$Li_3N$ structure. This can be seen a lot clearer in Figure 1.6.

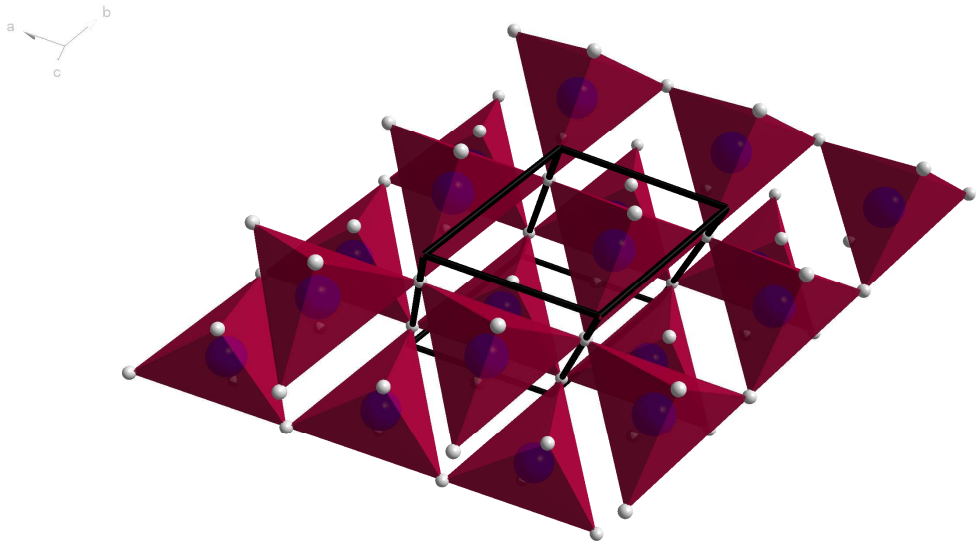


**Figure 1.6 Polyhedral representation of β-$Li_3N$ viewed along the *c*-axis. Ruby red polyhedra centred by blue spheres representing nitrogen ions, white representing lithium and the unit cell outlined in black.**

As can be seen, the nitrogen coordination has transformed from hexagonal bipyramidal to trigonal bipyramidal which is isostructural with that of $Li_3P$.

### *1.2.3 Ionic conductivity in $Li_3N$*

One of the main properties required for a material to be considered as a solid electrolyte for batteries is openness of the crystal structure. This makes lithium nitride a potential candidate due to the small levels of vacancy found naturally within the structure. Work initially carried out by Madsupuy in 1957 into the conductivity in $Li_3N$ appeared to indicate that it had a low ionic conductivity of only $\sigma_i = 5x10^{-12}$ $ohm^{-1}$ $cm^{-1}$. This was deemed to be due to the fact that his measurements had been carried out on loosely compacted powders. Further $^7Li$ NMR studies carried out appeared to indicate that $Li_3N$ actually had very high lithium ion conductivity[10, 13-14], and this then lead to further conductivity studies[15-19]. Boukamp and Huggins carried out research on pressed pellets of $L_3N$ in a cell, whereby it was used as the solid electrolyte between two electrode discs of molybdenum, and a much higher conductivity, $\sigma_i = 6x10^{-4}$ $ohm^{-1}$ $cm^{-1}$, was found[17]. Within this work, they were able to separate the effects of inter-crystalline and intra-crystalline conductivity on the overall conductivity of the material, and found that the lower of the two effects would be the controlling

factor on the overall conducting behaviour. Thus, as the material becomes more fully sintered, the temperature at which the crossover for the two behaviours occurs decreases, and sintering at 750 °C for 2 hours decreased the crossover temperature to 70 °C[17]. It was found that the reaction conditions used along with any thermal treating of the samples heavily affected the ionic conductivity of the material. Further conductivity measurements were carried out by von Alpen on highly pure bars of lithium nitride that had been synthesised by the Czochralski technique, and discovered that these bars were stable in a moist atmosphere[15]. This phenomenon was found to be due to a surface layer of LiOH, $Li_2O$ and $Li_2CO_3$ on the crystal, which was polished, sawn and chemically etched to prevent interference with the measurement of the physical properties of the bulk material. Conductivity values much higher than previously reported were observed in the sintered bulk $Li_3N$, $\sigma_i$ = 1-2x$10^{-3}$ $ohm^{-1}$ $cm^{-1}$, with measurements made on single crystals revealing a conductivity perpendicular to the *c* axis almost double of that parallel to it[15]. A comparison of conductivities and activation enthalpies for a variety of materials is shown in Table 1.1below.

**Table 1.1 Comparative conductivities (σ) and activation enthalpies ($E_A$) for $Li_3N$ and similar $Li^+$ ion conductors (s.c. means single crystal, ∥ means parallel and ⊥ means perpendicular)[15].**

| Material | $E_A$ (eV) | σ 300K ($ohm^{-1}$ $cm^{-1}$) | σ 400K ($ohm^{-1}$ $cm^{-1}$) | σ 500K ($ohm^{-1}$ $cm^{-1}$) |
|---|---|---|---|---|
| **$Li_3N$ s.c. ⊥ c** | 0.29 | 1.2x$10^{-3}$ | 8x$10^{-3}$ | 4x$10^{-2}$ |
| **$Li_3N$ s.c. ∥ c** | 0.49 | 1x$10^{-5}$ | 6x$10^{-4}$ | 8x$10^{-3}$ |
| **$Li_3N$ sinter** | 0.29 | 1.5x$10^{-3}$ | 1x$10^{-2}$ | 3x$10^{-2}$ |
| **Li-*β*-alumina s.c.** | 0.19 | 1.3x$10^{-4}$ | 6.02x$10^{-4}$ | 5.88x$10^{-3}$ |
| **LiI** | 0.434 | 5.5x$10^{-7}$ | 2x$10^{-5}$ | - |
| **LiI (40 mol% $Al_2O_3$)** | 0.44 | 1.2x$10^{-5}$ | 1x$10^{-3}$ | - |

For $Li_3N$, a conduction mechanism was proposed from the results of the NMR, XRD and DFT calculation, and was thought to be occurring via an intraplanar $Li^+$ hopping process at 300 K or lower, and interplanar hopping at temperatures of 400 K or higher. The high conductivity was found to have been induced by a vacancy at the Li(2) site. This vacancy concentration at the Li(2) site was recently confirmed by powder neutron diffraction[20] to be ~3 % with the Li(1) site fully occupied. The cause of these vacancies is proposed to be due to the

presence of hydrogen in the material[21]. Experiments carried out by Wahl in 1979 found that when infrared transmission measurements were made for samples of lithium nitride, sharp lines at 3130 $cm^{-1}$ and 6090 $cm^{-1}$ were observed[21]. These corresponded very well to the fundamental mode of 3131 $cm^{-1}$ and second harmonic of 6109 $cm^{-1}$ for $NH^{2-}$ in argon. This theory had further weight added to it by deuterated experiments being carried out, and the different frequencies for $ND^{2-}$ were also observed. This therefore led to the explanation that aliovalent doping of $NH^{2-}$ in place of the $N^{3-}$ ion was occurring, and in turn created lithium ion vacancies for the purpose of charge balancing. When Rabenau and Schulz reconfirmed, in 1976, the structure which had previously been postulated by Zintl and Brauer they refined the temperature factors which were profoundly anisotropic in the model.

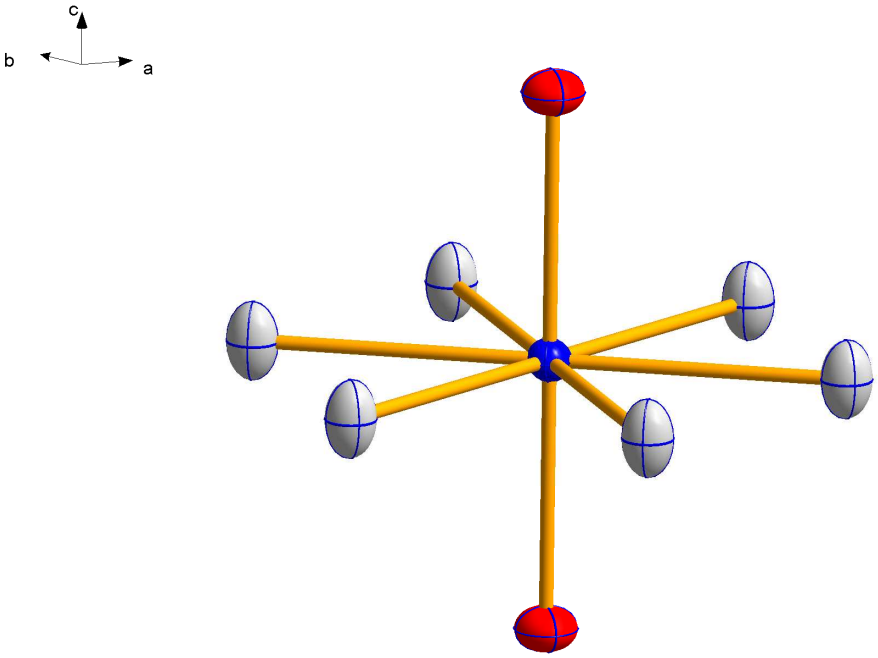


**Figure 1.7 Representation of 50 % probability thermal ellipsoids in $Li_3N$. Nitrogen represented by blue ellipsoid, intraplanar lithium (Li(2)) represented by white ellipsoids and interplanar lithium (Li(1)) represented by red ellipsoids.**

As can be seen in Figure 1.7 above, the thermal motion of the lithium atoms is perpendicular to the direction of the Li-N bonds. When this is taken into consideration along with the comparison of the bond lengths, 2.130 Å for Li(2)-N bond and 1.939 Å for the Li(1)-N bond, it would appear that the planar lithium

atoms are the more mobile species and conduction occurs due to a hopping process from Li(2) to Li(2). This was the accepted theory until in 1981 Messer *et al.* carried out some NMR studies into the diffusion mechanism in more detail[14]. Through a study of the temperature dependence of the quadrupolar splitting and the linewidths of the resonance lines, two different mechanisms were found to be in operation. At temperatures below 300 K, the previous mechanism remained true but, at temperatures above 300 K, a newer second mechanism appeared to be in operation. This diffusion mechanism was found to be operating parallel to the *c* axis and involved both the Li(1) and Li(2) atoms. They could not ascertain whether this second process involved direct jumps from Li(2) to Li(2) parallel to the *c* axis, or whether a pathway via the Li(1), Li(2) to Li(1) to Li(2) was occurring. This temperature dependence of the diffusion mechanism lends further explanation to the differing activation energies that are observed, 0.2 – 0.32 eV perpendicular to the *c* axis and 0.6 eV parallel to the *c* axis.

### *1.2.4 Hydrogen storage*

In recent times, with fossil fuel reserves becoming increasingly limited and minimisation of greenhouse effects in the atmosphere being a driver, greener, cleaner fuels are being investigated. As a result of this, one such area of keen interest for research is hydrogen energy sources. Fuel cells can be utilised to generate electricity from the reaction of $H_{2(g)}$ and $O_{2(g)}$ and as a result of this clean reaction, only water is produced as a by-product. The United States Department Of Energy (DOE) has set targets of 6.5 wt % storage by 2015 and 7.5 wt % by ultimately[22] for hydrogen storage to be considered as viable for use in motor vehicles. What should be noted about these targets is that the weight percentage given is for the entire storage system, and not just the solid state storage medium. Therefore, when the weight of the storage tanks, temperature and pressure control systems are considered, the amount of hydrogen a material would need to store would need to be a significant portion of its own weight.

With this in mind, there have been many potential materials researched and one of these is lithium nitride[23]. Through thermogravimetry, Chen *et al.* found that hydrogen absorption in lithium nitride began at 373 K and then a large uptake was evident at temperatures between 443 and 483 K, with a total adsorption of

9.3 wt % obtained after the sample was maintained at a temperature of 528 K for 30 minutes. The desorption was found to occur in two steps; below 473 K and with a high vacuum 6.5 wt % was released, and then at temperatures above 593 K the remaining 3 wt % could be removed. Pressure-composition (P-C) isotherms were performed on fresh samples of $Li_3N$, and were found to consist of two plateaus; one at low pressure, which was thought to correspond to the portion removed by high temperatures, and a slightly higher plateau ranging from 0.2 bar at 468 K to 1.5 bar at 528 K. Full desorption was not achieved and mass spectrometry indicated that hydrogen was the only gas being desorbed.

Samples were taken at different stages of the hydrogenation process and characterised by X-ray diffraction, and found that at half hydrogenation lithium imide and hydride were present, and lithium amide and an intensified lithium hydride phase were present at full hydrogenation. From all this information Chen *et al*. proposed that the following reaction path was occurring:

$$Li_3N + 2H_2 \leftrightarrow Li_2NH + LiH + H_2 \leftrightarrow LiNH_2 + 2LiH \qquad \textbf{1.4}$$

The high temperatures required for adsorption of hydrogen in lithium nitride, 6.5 wt % reversibly at 528 K, prevented it being applied as a potential hydrogen storage medium for the transport industry and achieving this at temperatures below 473 K remains a more favourable prospect.

## 1.3 Ternary Lithium Nitrides

Ternary lithium nitrides first appeared in the literature in 1928 when Frankenburger *et al*. reported the synthesis of the ternary nitride, $Li_3FeN_2$, and from this began research into comparisons of behaviours of ternary lithium nitrides compared to that of binary nitrides[24]. Work carried out by Juza and colleagues several decades ago categorised the ternary transition metal nitrides of the first period of the transition metals into two; those doped with the transition metals Ti through to Cr adopt an *anti*-fluorite superstructure and those doped with the transition metals Co to Cu adopt the $Li_3N$-type configuration[25]. The elements between these two regions, namely Mn and Fe, cannot be solely placed in either category as they will form both, forming the

*anti*-fluorite superstructures initially, but under high temperature, reductive conditions, will also form the $Li_3N$-type structure[19, 26].

## *1.3.1 $Li_3N$-type nitridometallates*

### 1.3.1.1 Structure

The majority of the founding research into materials of this type was conducted by Juza *et al.* over 50 years ago[27-29]. It was found that this group of nitridometallates, $Li_{3-x}M_xN$ (M= Ni, Cu and Co), contain the transition metals typically in +1 oxidation state, the transition metal substitutes partially at the interplanar Li(1) site and retains the $Li_3N$-type structure as seen in Figure 1.8.

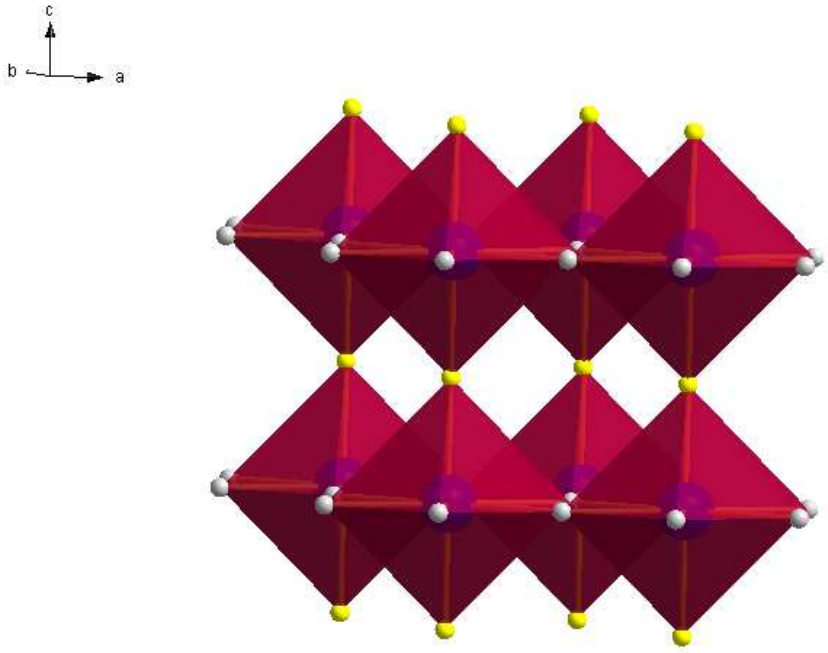


**Figure 1.8 Polyhedral representation of the $Li_3N$-type nitridometallate $Li_{3-x}M_xN$ structure. Ruby polyhedra centred by a nitrogen atom represented by the blue sphere, Li (2) represented by white spheres and mixed Li(1)/M sites represented by yellow spheres.**

$Li_3N$-type iron and manganese materials can also be prepared under thermal and reductive conditions starting from the *anti*-fluorite structures which they predominantly form[19, 26].

Several different methods of synthesis have been utilised and Juza *et al.* reported three; reacting lithium nitride with the transition metal under either $N_{2(g)}$ or $NH_{3(g)}$, nitriding of an alloy of the transition metal and lithium or reacting lithium nitride with the transition metal nitride under $N_{2(g)}$[25]. More recently synthesis by ball-milling of the reactants has also been reported[30].

Gregory *et al.* carried out studies, preferring to use the first method of synthesis but also reacting $Li_3N$ with cleaned foils of the respective transition metals to grow single crystals, and found that the metal substitutes at the interplanar sites. As a result, vacancies occur in the $[Li_2N]$ plane[31-32]. These vacancies can be either ordered or disordered, and as the metal substitution levels increase, so too does the tendency of the vacancies to ordering[33]. It was also found that by increasing the transition metal content the *a*-parameter, related directly to the Li(2)-N distance, increases whereas the *c*-parameter, which is directly related to double the Li(1)-N distance, decreases. This was observed to happen for all three of the transition metals, Co, Ni and Cu. Defect nitridometallates are of the form, $Li_{3-x-y}M_xN$, where x is the level of dopant metal and y is the level of lithium ion vacancy. For the nickel doped materials, it was found that when substitution levels went as high as x = 1, the vacancies ordered and this formed the variants $Li_5Ni_3N_3$ (x = 1, y = 0.33) and LiNiN[31] (x = 1, y = 1) (Figure 1.9).

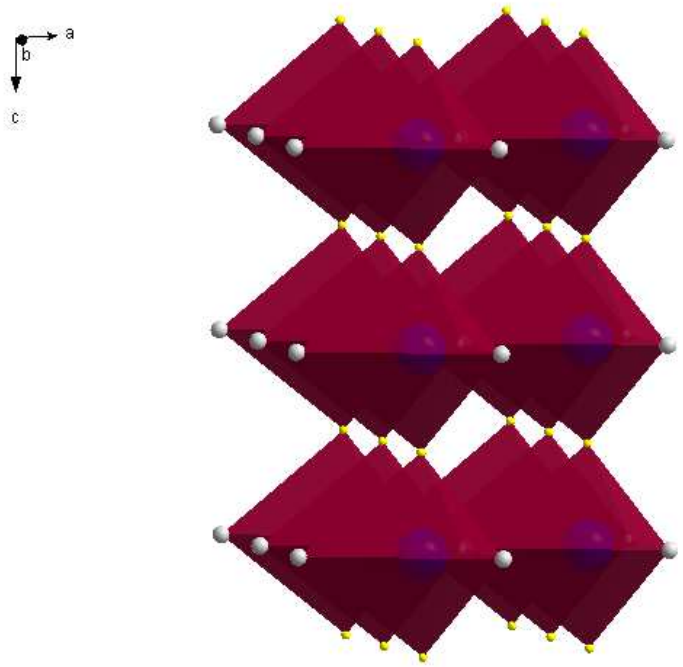


**Figure 1.9 Polyhedral representation of LiNiN with ruby polyhedra centred by a blue sphere representing a nitrogen atom, white spheres for Li atoms and yellow spheres for Ni atoms.**

In $Li_5Ni_3N_3$, $Ni^{1.33+}$ exists as a result of mixed $Ni^{+}$ and $Ni^{2+}$, and in LiNiN the nickel exists entirely as $Ni^{2+}$ [31].

Gregory *et al.* reported the synthesis of cobalt doped lithium nitride with a dopant level of x = 0.4, and also x = 0.43 and x = 0.79 for copper and nickel respectively[20]. Niewa et al. reported the synthesis of a material with a higher nickel dopant level of x = 0.85[34] and Weller *et al.* reported a high pressure synthesis of a copper doped lithium nitride which achieved a dopant level of x = 0.519[35]. Further discussion of the synthetic methods used to achieve these materials will be found in the background discussions of the consequent chapters.

As previously outlined, the iron and manganese ternary nitrides can form both the *anti*-fluorite type structures, and also the lithium nitride type via the thermal reduction of the *anti*-fluorite type materials.

In order to produce the manganese-containing $Li_3N$-type materials, $Li_7MnN_4$ was thermally treated at differing temperatures under an argon atmosphere in the

presence of cleaned lithium metal[19]. After thermal treatment at temperatures ranging from ≤1103 K to 1173 K there is a stage of intermediate materials namely, $Li_{24}[MnN_3]_3N_2$ and $Li_5[(Li_{1-x}Mn_x)N]_3$, before we achieve phase pure $Li_{3-x}Mn_xN$. In a similar way, Klatyk and Kniep synthesised a lithium nitride type iron ternary nitride from the *anti*-fluorite $Li_3FeN_2$ phase[26]. The material, $Li_{3-x}Fe_xN$ where x = 0.63, was obtained through heating mixtures of $Li_3FeN_2$ along with an alkali metal, sodium or lithium, in a one-to-one ratio with a very specific heating profile. Both of these materials were of the same space group as other $Li_3N$-type nitridometallates, P6/mmm.

#### 1.3.1.2 Properties

These materials have displayed some interesting physical and chemical properties including ionic conductivity, magnetism and some limited hydrogen storage properties.

##### *1.3.1.2.1 Electronic properties*

Gregory *et al*. carried out magnetic measurements on the nitridometallates $Li_{2.6-y}Cu_{0.4}N$, $Li_{2.6-y}Co_{0.4}N$, LiNiN and $Li_3N$ using a Quantum Design MPMS XL 5T SQUID magnetometer[33] in a temperature range of 5 -250 K and a field of 1000 Oe. Results of these measurements can be seen in Figure 1.10.

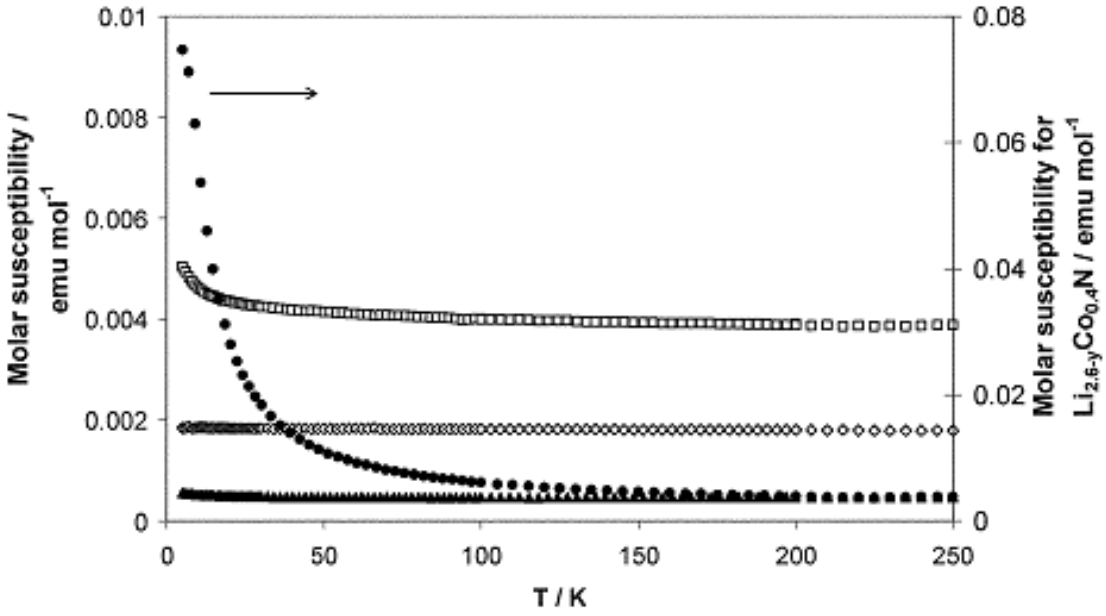


**Figure 1.10 Temperature dependence of molar susceptibility. Open diamonds represent $Li_3N$, open squares LiNiN, $L_{2.6-y}Cu_{0.4}N$ solid triangles and $L_{2.6-y}Co_{0.4}N$ solid circles[33].**

As can be seen from Figure 1.10, both $Li_3N$ and $Li_{2.6-y}Cu_{0.4}N$ display fairly weak Pauli paramagnetic behaviour, $Li_{2.6-y}Cu_{0.4}N$ shows a small Curie tail below 50 K and LiNiN also shows almost temperature-independent susceptibility but with a small tail below 50 K. $Li_{2.6-y}Co_{0.4}N$ displays behaviour archetypical to that of a Curie-Weiss paramagnet with the influence of localised magnetic moments from the Co atoms. These plots were fitted to a modified Curie-Weiss equation the parameters from which can be seen in Table 1.2.

**Table 1.2 Parameters from fitting of magnetic susceptibility to modified Curie-Weiss law.**

| Material | $\chi_0$ /$cm^3mol^{-1}$ | $C_M$ /$cm^3mol^{-1}$ | $\theta$ /K | $\mu_{eff}$ per M /$\mu_B$ |
|---|---|---|---|---|
| $Li_3N$ | 0.00182 | - | - | - |
| $Li_{2.6-y}Cu_{0.4}N$ | 0.00047 | 0.0005 | 0 | 0.15 |
| LiNiN | 0.00613 | 0.016 | -9.1 | 0.36 |
| $Li_{2.6-y}Co_{0.4}N$ | 0.00233 | 0.459 | 0 | 4.80 |

From the fitted data, Gregory *et al*. deduced that approximately 8.7% of the copper ions in $Li_{2.6-y}Cu_{0.4}N$ were $Cu^{2+}$. This would suggest that as there is a small percentage of aliovalent substitution of the $Li^+$ there will be a higher

concentration of vacancies present than in $Li_3N$ for the purpose of charge balance which was supported by variable temperature $^7$Li NMR. The $\mu_{eff}$ of 4.80 observed for the $Li_{2.6-y}Co_{0.4}N$ would appear to be a value that lies between the spin only value for a $Co^{2+}$ ion (3.87 $\mu_B$) and the value for a $Co^{2+}$ with a spin and orbital contribution (5.20 $\mu_B$) [36]. This would suggest that cobalt ions are present as $Co^{2+}$ with an orbital contribution to the overall magnetic moment. The magnetic susceptibility seen for LiNiN appears to suggest metallic behaviour, and DFT (Density Functional Theory) calculations and $^7$Li-NMR spectra indicated this was a type of behaviour that had been displayed previously by CaNiN[33].

#### *1.3.1.2.2 Ionic conductivity*

Another property of these materials which has gained a lot of interest as recently as just the last decade is their ionic transport properties and conductivities. In 1996 Asai *et al*. prepared a series of lithium nitridocuprates of the form $Li_{3-x}Cu_xN$ with a maximum value of x = 0.38[37].

Conductivity measurements were carried out by the ac impedance method on pellets of the materials which had been reacted at 500$^o$ C in order to sinter them, and were then evaporated. A gold blocking electrode was used. Asai *et al*. reported that upon substitution of the transition metal Cu, the conductivity decreased when compared to that of the parent material $Li_3N$, and this effect appeared to increase with increasing metal content. In addition, it was found that the activation energy for the material decreased with increasing metal content, and this could be directly attributed to a shift toward more covalent character in comparison to $Li_3N$.

The majority of the conductivity work carried out on transition metal ternary nitrides was carried out by two groups both in Japan in the mid 90's[38-41]. Shodai et al. carried out electrochemical studies on a series of transition metal ternary metals of the form $Li_{3-x}M_xN$ for M = Co, Ni and Cu with values of x = 0.1-0.6[40]. A disk of the material, acetylene black conductor and Teflon binding agent was pressed and assembled in a coin cell as the anode, with a disk of Li metal as the cathode and 1M solution of $LiClO_4$-ethylene carbonate/1,2-diethoxyethane as the electrolyte.

For the material $Li_{2.6}Co_{0.4}N$, cycling was carried out between 0 and 1.4 V with a current density of 0.5 mA/cm$^2$ and the charge-discharge profile can be seen in Figure 1.11 below.

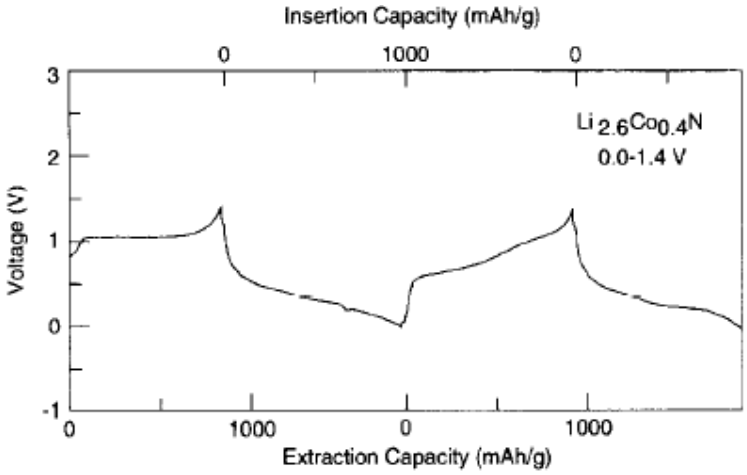


**Figure 1.11 Charge-discharge curve for $Li_{2.6}Co_{0.4}N$ sample[40].**

As can be seen, there is a plateau for the initial extraction of Li at around 1.1 V, and the Li insertion occurs at a voltage between 0 and 0.5 V, whereas for the second extraction of L there is less of a defined plateau and the extraction occurs between 0.6 and 1.1 V. The second insertion is almost identical to that of the first. The materials' function upon cycling was tested and was found to decrease slightly initially up to around 7 cycles whereby it stabilised at 760 mA h/g, which is more than double that of the theoretical capacity of $C_6Li$ (372 mA h/g). Shodai *et al.* attributed this initial decrease of capacity to reduction of the electrolyte at the anode surface due to lithium ions being extracted from the material and being incorporated in the electrolyte.

They studied how varying the amount of metal dopant, x, affected the extraction of lithium from the cell also, and found that as more transition metal was doped into the material, the lower the capacity of the first extraction. The effects of lithium extraction upon the materials structure was studied by X-ray diffraction progressively and can be seen in Figure 1.12.

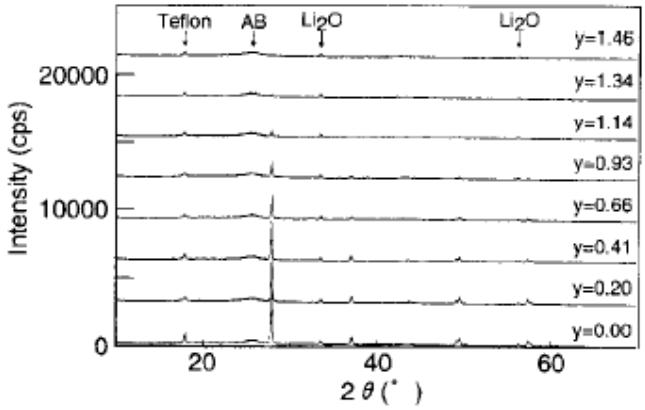


**Figure 1.12 X-ray diffraction patterns for $Li_{2.6-y}Co_{0.4}N$, where y = amount of extracted lithium[40].**

As can be seen, as lithium is extracted from the cell, the structure of the material gradually changes from a crystalline material when y = 0, to an amorphous structure at y = 1.46. However, it was found that the cycling capacity of the material actually increased with lithium extraction, and this would not be the case if the material was truly becoming amorphous. Shodai *et al*. therefore proposed that the shift to an amorphous phase identified in the XRD patterns is a manifestation of some short-range ordering.

Similar materials for copper and nickel were also synthesised. The material $Li_{2.6}Cu_{0.4}N$ showed similar initial behaviour for the extraction and insertion cycles as that of $Li_{2.6}Co_{0.4}N$, in that its capacity decreases to begin with then stabilises at a capacity of 650 mA h/g[40] when cycled between 0 and 1.3 V and was stable over 13 cycles. This is still a larger specific capacity than that of $C_6Li$, however $Li_{2.6}Ni_{0.4}N$ displayed a much lower stable specific capacity of only 180 mA h/g[40].

Nishijima *et al*. carried out electrochemical studies on similar materials and gauged the effects that cycling had upon their structures. The materials, $Li_{2.60}Co_{0.4}N$, $Li_{2.50}Ni_{0.5}N$ and $Li_{2.60}Cu_{0.4}N$ were used for the purposes of the electrochemical studies as these compositions appeared to give the highest stable capacities. For the first discharge it was found that for $Li_{2.60}Co_{0.4}N$ and $Li_{2.50}Ni_{0.5}N$ the amount of lithium being inserted, z, appeared to relate to the vacancy concentration of the material, $Li_{3-x-y-z}M_xN$, where y is the vacancy and for these two materials z for the initial extraction was equal to 0.3 Li[39]. The fact that it was lower than that of the copper containing material indicated that

there were fewer vacancies in that material, and this could be due to the fact that copper metal is quite commonly found in the $Cu^{+}$ oxidation state and would substitute for the Li monovalently. Whereas, $Ni^{+}$ and $Co^{+}$ are not quite so prevalent and are therefore more likely to exist in a higher oxidation state, they are more likely to allow aliovalent substitution to occur which will impart a greater number of vacancies.

For the $Li_{2.60}Co_{0.4}N$ and $Li_{2.50}Ni_{0.5}N$ materials, the charge-discharge cycling appears to be similar in that there are two steps to the charge process which can be seen in Figure 1.13.

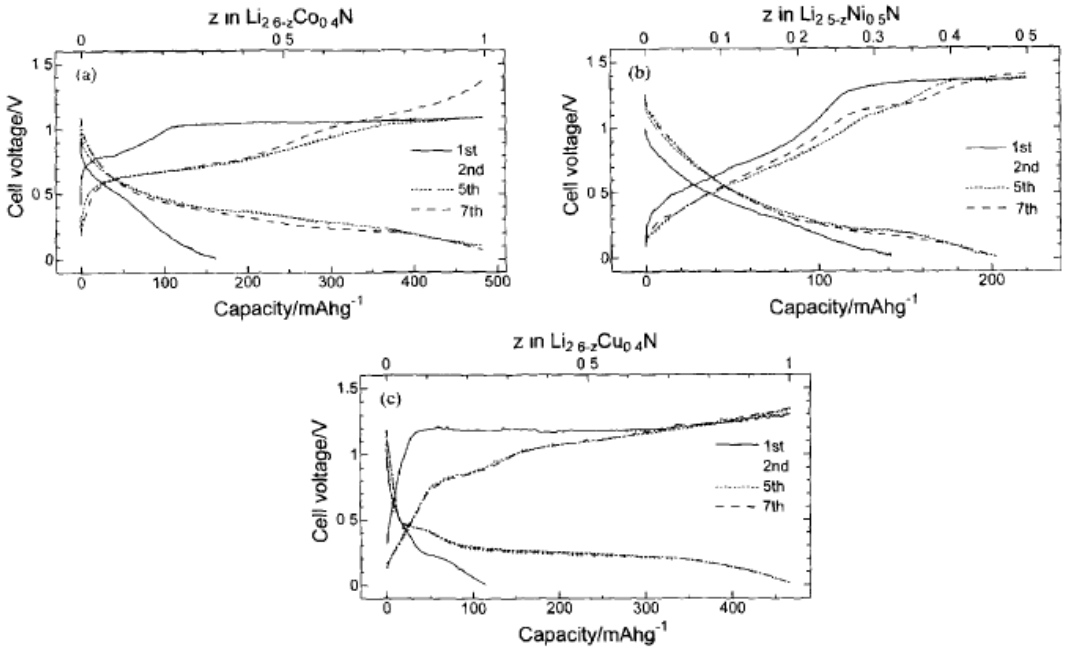


**Figure 1.13 The charge-discharge voltage curves for $Li_{2.6-z}Co_{0.4}N$, $Li_{2.5-z}Ni_{0.5}N$ and $Li_{2.6-z}Cu_{0.4}N$[39]**

As can be seen, the first part of the charge cycle corresponds to that of the first extraction of lithium for the two materials, z = 0.3. The plot for the second cycle was absent from the image in the original paper, and could not be obtained by contacting the author. After the second cycles the cell voltage gradually increases from 0.5 to 1.4 V, suggesting that the structure is changing as lithium is being inserted and extracted. This is supported by the structural changes which were observed upon cycling. For the cobalt containing material the *a*-parameter decrease and the *c*-parameter increases up to z = 0.3, suggesting that the lithium is being de-intercalated. However there is very little

change in the parameters of the copper containing material, and thus the sharp increase at the start of the voltage curve is attributed to the de-intercalation. Both materials form an amorphous phase upon lithium extraction, which is in agreement with the findings of Shodai *et al.*[40], and it is thought that it is this amorphous phase that is responsible for the electrochemical behaviour being observed in the consequent cycles, and thus why the capacities for these two materials are higher than that of the nickel material. Both these materials show a good reversibility of ~0.5 V, but over a small lithium extraction range, whereas the nickel material can extract between 0 and 0.5 lithium ions and is more stable structurally but has a higher reversibility voltage and lower capacity.

$Li_{2.60}Co_{0.4}N$ has gained the most interest as an anode material in lithium rechargeable batteries and many different papers on its electrochemical behaviour have been published[39, 41]. Attempts to improve the materials cyclability have been attempted[42] through the doping of the ternary nitride with Fe, and improvements on the capacity of the material have been achieved by varying the cathode material of the electrochemical cell[43]. In addition, this material has been used as a composite anode with tin oxides, graphites and silicates as many of them have favourable, but irreversible capacities and $Li_{2.60}Co_{0.4}N$ can counteract this.

#### *1.3.1.2.3 Hydrogen storage properties*

Another property of these materials which has begun to gain interest in recent times is their hydrogen storage properties. As the parent material, $Li_3N$, performed as a reversible hydrogen storage material, it was postulated that ternary nitrides could also behave as hydrogen stores. By modifying the material one might impart vacancies in the material and previous studies have shown that there is a correlation between vacancy concentration and hydrogen ion mobility. To date there is a very limited amount of research into this area. One study was carried out by Ma *et al.*[44] where the material of nominal stoichiometry $Li_{2.8-y}Co_{0.2}N$ was synthesised by ball-milling a reaction mixture of lithium nitride and cobalt powder of predetermined weights, for a duration of 5 hours under $N_{2(g)}$ (99.999%) with an initial pressure of ~1 MPa[44].

Ball-milling consists of putting the reactants in a sample jar with several balls, either stainless steel, agate or whatever the appropriate material would be, and clamping the jar inside the instrument which will rotate the jar, and thus the balls inside at a high speed. With synthesis by ball-milling, the reaction is aided through reducing the surface area of the reactants, increased temperature and pressure generated through the rotational speed of the apparatus and also increased contact between the reactants by ensuring thorough mixing. Some of the disadvantages of using this synthesis method are that due to the high rotational speed of the instrument, impurities from the sample container can occur and due to the synthesis method resulting in such a small particle size, it can lead to very broadened peaks in the X-ray diffraction pattern of the product.

For sufficient comparisons to be made, Ma *et al.* ball-milled lithium nitride as it was received, alongside the mixture of cobalt and lithium nitride, and also further ball-milled the cobalt containing sample under a hydrogen atmosphere. Iron impurity was present which was thought to have originated from the milling utensils and led to the formation of the structure $Li_{3-x-y-z}Co_xFe_yN$ (where z = vacancy). XRD of the sample further milled under a hydrogen atmosphere showed an alloy of the two transition metals precipitating from the $Li_3N$ lattice and coincided with the presence of $Li_2NH$. The composition of the alloy was proposed to be close to $Co_3Fe_7$[44]. Desorption behaviour of the materials can be seen in Figure 1.14.

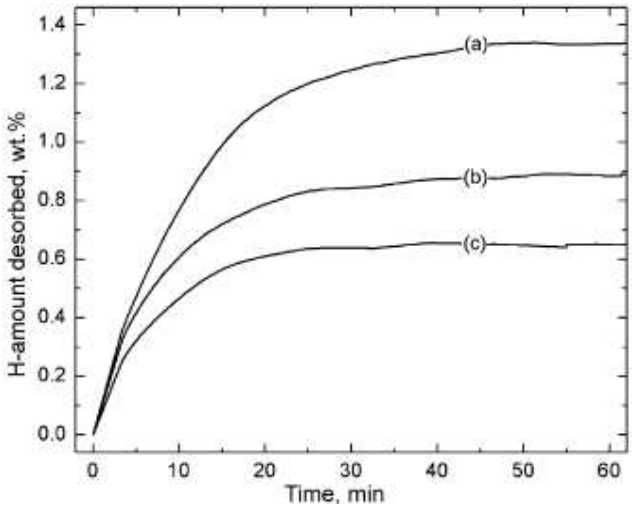


**Figure 1.14 First cycle hydrogen desorption curves at 255 $^oC$ for a) as-milled $Li_3N$ + Co sample b) with additional milling under $H_{2(g)}$ atmosphere and c) as-milled Li3N (all post-hydrogenation) [44].**

Previous work had indicated that doping of lithium manganates with Fe would help to reduce the Lewis acidity and improve the cycle life[42], however in Figure 1.14 the additionally milled sample contained more Fe than the as-milled sample and yet its desorption results were not as successful. As can be seen, the effect of $x = 0.2$ of the transition metal in the samples has a marked effect on the amount of hydrogen desorbed when compared to that of the lithium nitride desorption and at a much faster rate. The sample, additionally milled under a hydrogen atmosphere, gives a result that is intermediary, and this is proposed to be due to the partial precipitation of the Co-Fe alloy. The marked difference between the $Li_3N$ and the transition metal containing samples is less defined in the second sample, and again this is due to precipitation of the transition metals. This area remains a fairly untouched part of lithium nitridometallate chemistry.

## *1.3.2 Anti-fluorite type nitridometallates*

### 1.3.2.1 Structure

The majority of the work into these types of materials was first carried out in the 1940's by Juza *et al.*, and then revisited in the 1990's by groups led by Niewa and Gudat. These materials form superstructures of the *anti*-fluorite type which consist of the atoms in the reverse configuration to that of the fluorite structure. The fluorite structure consists of a face-centred cubic arrangement of the cations, typically the larger ion, with the anions in the tetrahedral holes. The *anti*-fluorite configuration consists of face-centred cubic packing of the anions with the cations situated in the tetrahedral holes. In fluorite, the fluorine ions are 4 coordinate and the calcium cations are 8 coordinate. Figure 1.15 displays this arrangement.

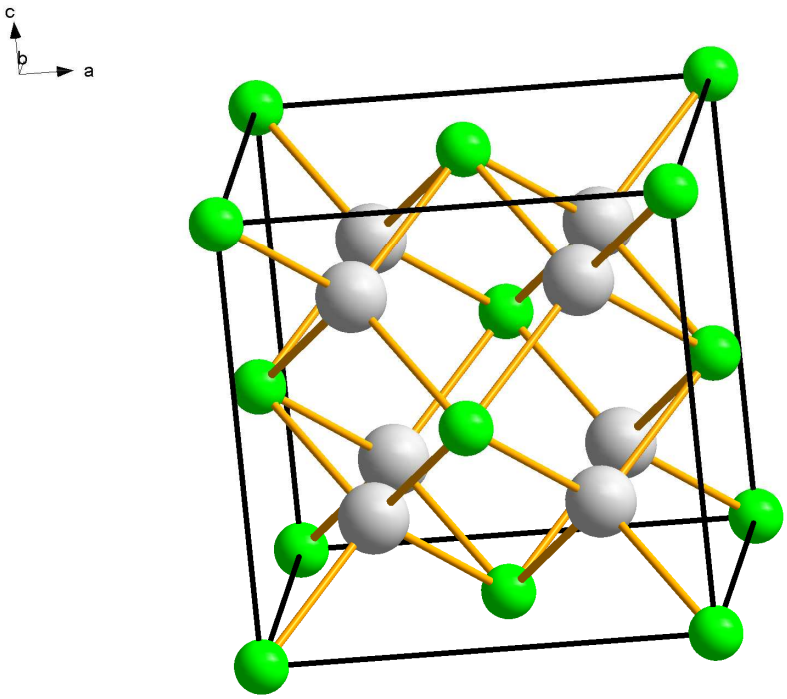


**Figure 1.15 Unit cell representation of fluorite $CaF_2$, white spheres represent $F^-$ ions and green spheres represent $Ca^{2+}$ ions.**

Materials which have been synthesised in this structural configuration include, $Li_5TiN_3$, $Li_7VN_4$, $Li_9CrN_5$, $Li_7MnN_4$ and $Li_3FeN_2$ whereby the transition metal is in a high oxidation state, +4, +5, +6, +5 and +3 respectively. Figure 1.16 illustrates the unit cell of $Li_5TiN_3$.

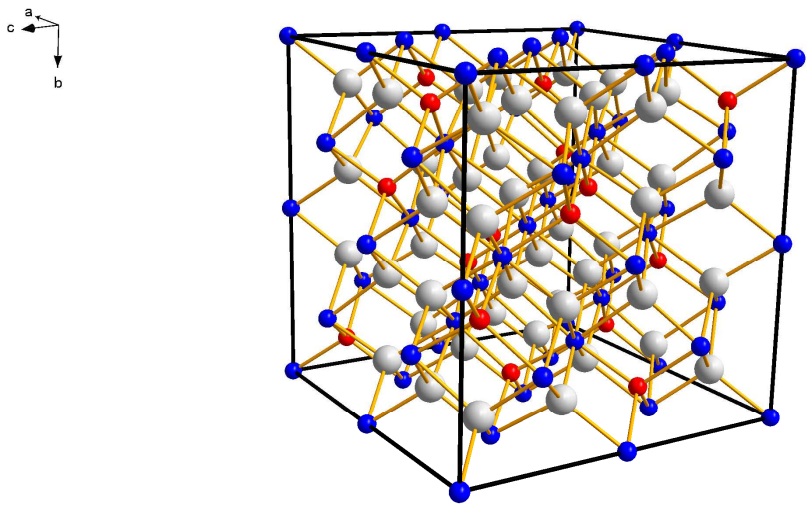


**Figure 1.16 Unit cell representation of $Li_5TiN_3$. Blue spheres represent $N^{3-}$ ions, white spheres represent the $Li^+$ ions and the red spheres represent the mixed Li/Ti site[28].**

This structure crystallises in the cubic space group Ia-3 with an *a*-parameter of 9.700 (2) Å. As can be seen, this is a 2a x 2a x 2a unit cell in comparison to that of $CaF_2$, brought about by Li-Ti ordering. If the unit cell is reduced down to an octant, i.e. one corner of the cell then we get the same representation as the *anti*-fluorite structure. Here, the nitrogen ions are eight coordinate and the lithium and titanium four coordinate. There are two metal sites, 48e occupied only by Li and the 16c site which is occupied by lithium ions and 2/3 by titanium ions.

$Li_7MnN_4$[45-46] and $Li_7VN_4$ crystallise in the cubic space group P -4 3 n[47]. These have the same arrangement with the nitride as the eight coordinate ion and the metals in four coordinate positions. In this space group the Li and Mn(v) occupy discrete sites within the structure, with Li occupying the 6b, 6d, 8e, 12f and 24i sites, and Mn at the 2a and 6c sites. $Li_5Cr_2N_9$[48] adopts the tetragonal space group P4/*nccz*.

$Li_3FeN_2$ adopts a distorted *anti*-fluorite structure and crystallises in the orthorhombic space group I b a m, with unit cell parameters *a* = 4.872(1) Å, *b* = 9.641(2) Å, *c* = 4.792(1) Å [49]. Again the metals occupy the four coordinate positions and the nitrogen the eight coordinate site and the structure consists of

infinite [$FeN_2$] chains as can be seen in Figure 1.17. The chains consist of Fe centred $FeN_4$ tetrahedra which share edges with the adjoining tetrahedra.

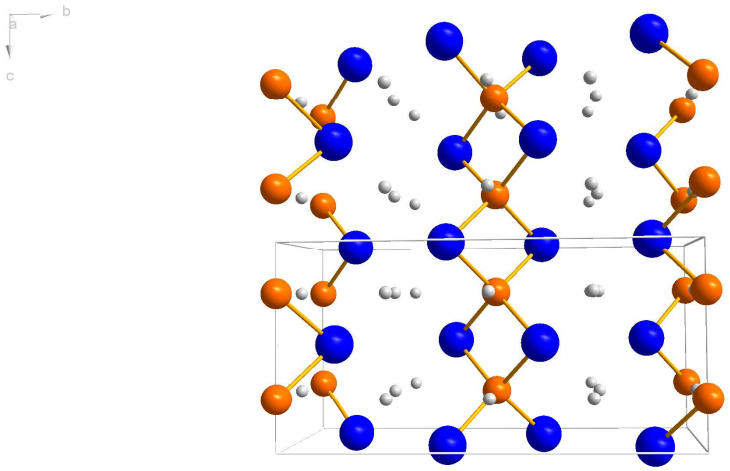

**Figure 1.17 Unit cell representation of $Li_3FeN_2$ displaying [$FeN_2$] chains. Blue spheres represent nitride ions, orange spheres iron ions and white spheres lithium ions[49].**

### 1.3.2.2 Properties

There have not been many investigations into the physical properties of these types of materials to date. Some magnetic property investigations have been carried out but the majority that have been investigated are electrochemical, and these were centred on two of the *anti*-fluorite materials, $Li_3FeN_2$ and $Li_7MnN_4$. One such investigation by Nishijima *et al.* looked into the electrochemical properties of $Li_3FeN_2$[50]. For the purposes of the investigation, the material was synthesised by the reaction of $Li_3N$ with $Fe_4N$ pressed into an 8mm pellet, and then heated under a 1% $H_{2(g)}$ - 99% $N_{2(g)}$ flow with a heating rate of 10 K/min to 873 K and then maintained at that temperature for a period of 12 hours[50].

For the material $Li_{3-x}FeN_2$, upon extracting Li for values of x from 0 to 1, there is a transition through four phases, all of which are orthorhombic. The phases change from $\alpha$-$\beta$ in the range $0 \leq x \leq 0.5$, then $\beta$-$\gamma$ for the range $0.5 \leq x \leq 0.75$ and finally $\gamma$-$\delta$ for the range $0.75 \leq x \leq 1.0$. For the transitions between these phases, the *b*-parameter decreases continually, but the *a*-parameter decreases

for α-γ but then increases for the final phase change to δ. The *c*-parameter decreases for the change of α-β phase, but then increases upon changing to the γ and again to the δ-phase. The unit cell volume decreases linearly as the phases change from the α-phase through to the δ-phase going from ~224.04 $Å^3$ to ~201.67 $Å^3$.

These phase changes had an effect on the observed OCV's (Open Cell Voltage) for this material, with steps in the voltages being observed for the changes from β-γ and γ-δ phases due to differences in Gibbs' free energy[50].

As lithium, x, was deintercalated between $0 \leq x \leq 1.0$, it was found that the electrical resistivity of the material decreased. Lithium was then intercalated back into the material to x = 1 and the potential difference between the charging and the discharging was small, which would indicate that this material could be highly reversible. The full amount of lithium deintercalated could not be re-intercalated and this material was found to have a specific capacity of 260 mA h $g^{-1}$. This would suggest that this material could be a potential candidate as an anode material when used in conjunction with a well performing cathode.

Similar to this study, $Li_7MnN_4$ was investigated for its electrochemical performance by Nishijima *et al.*[46]. In a similar way to $Li_3FeN_2$ a phase change was observed upon deintercalating lithium, from an α-phase to a ß-phase. The two phases co-exist in $Li_{7-x}MnN_4$ where $0 \leq x \leq 0.65$, beyond this from $0.65 \leq x \leq 1.25$ only the ß-phase exists. This material displays a specific capacity of 167.58 mA h $g^{-1}$, and although there are 5 potential lithium sites that the deintercalation could be occurring from over the $0 \leq x \leq 0.65$ range. Rietveld refinement revealed the best fit was achieved when allowing the occupancy of the Li(1) site to vary. For the range $0.65 \leq x \leq 1.25$ it is not known from which site Li is being deintercalated.

For the lithium reintercalation the reverse phase change occurs, and the ß-phase transforms back to the α-phase at x = 0.625 with full reversibility, i.e. the same amount of lithium deintercalated could be reintercalated. Upon cycling, a specific capacity of 210 mA h $g^{-1}$ with a cycling potential of 1.2 V was obtained and even though this capacity is much lower than that of lithium-carbon materials and with a higher operating potential, its good reversibility could make

it a promising candidate as an anode in lithium cells in tandem with a non-lithium cathode.

After this had been found Cabana *et al*. performed some NMR and powder neutron diffraction studies into this materials' structure and lithium mobility[45]. Rietveld refinement of the neutron diffraction data was in agreement with the previously confirmed structure, however variable temperature $^{6}$Li NMR suggested that the lithium ions at three of the five sites, Li(3), Li(4) and Li(5) were highly mobile, as opposed to the previous study which had found Li(1) the most mobile, and concluded that the hopping process involved these three ions as well as Li(1) in some way. It could not be concluded from their work whether or not the extraction of lithium was occurring consecutively from Li(1) then Li(5) or solely from the Li(5).

## 1.4 Other Alkali Metal Nitrides

For many years, it had been thought that there were no homologous binary nitrides of any other alkali metals, and although there had been a noted reaction between sodium metal and nitrogen gas through electrical discharge, there was no structural information obtained for the proposed materials that were synthesised. The noted presence of ammonia gas upon hydrolysis of the material was the only indicator that the nitride of sodium had been formed rather than an azide. Fischer and Jansen synthesised a material in 2002 by mixing the atomic gas phases of each component in a vacuum chamber, and then depositing the phases onto a cooled substrate and successfully characterised it as $Na_3N$[51]. The material was characterised by X-ray diffraction and was found to crystallise in a primitive cubic unit cell with $a$ = 4.7325(2) Å. Nitrogen ions are located at the eight corners of the unit cell with sodium ions connecting them on each edge of the unit cell. The structure of this material can be seen in Figure 1.18.

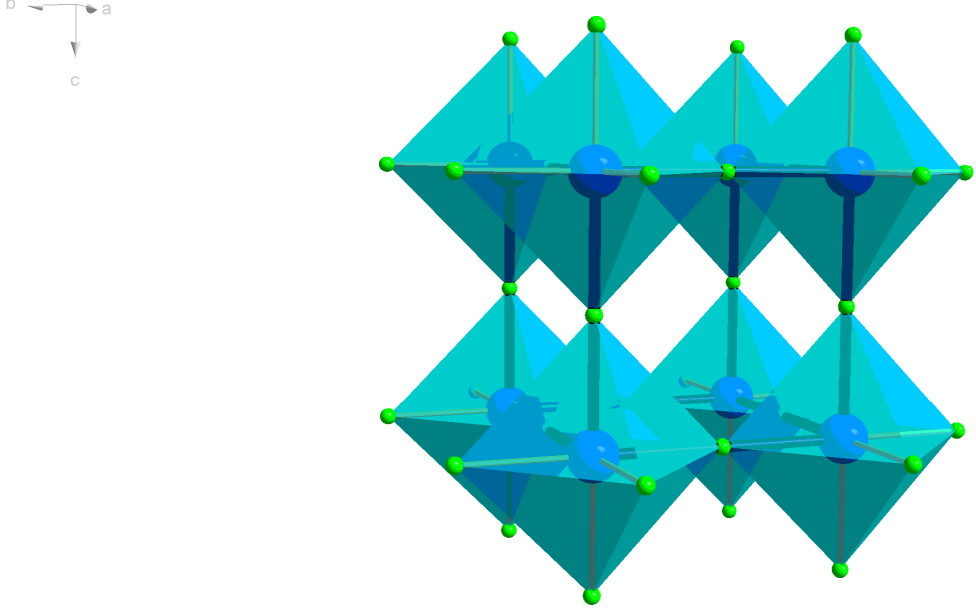


**Figure 1.18 Polyhedral representation of $Na_3N$. Blue octahedra are centred by blue spheres representing nitrogen atoms. Green spheres representing sodium atoms. Central black cube representing unit cell[51].**

As can be seen, the material forms $NNa_6$ octahedra with shared apices, in a way which is similar to that of $Li_3N$. The lower coordination of the nitrogen atom in this material is entirely due to the larger atomic radius of the sodium atoms, 2.33 Å, as opposed to that of lithium, 2.05 Å, and as such, a lower number of these atoms can pack around one nitrogen atom.

Variable temperature X-ray diffraction was performed and the material was found to be amorphous at 77 K and to then crystallise at 200 K and remain stable until 360 K. At temperatures above this, $Na_3N$ decomposes to Na and $N_2$. This indicated that there were no additional phases that could be accessed by increasing the temperature of the material, and to date no pressure induced phases have been identified.

Synthesised in a similar way, $K_3N$, was co-deposited onto a polished sapphire substrate at 77 K and then heated to room temperature, and the material characterised by X-ray diffraction and found to crystallise in the hexagonal space group $P6_3/mcm$, with a = 7.798(2) Å and c = 7.592(9) Å[52]. The structure of the material can be seen in Figure 1.19.

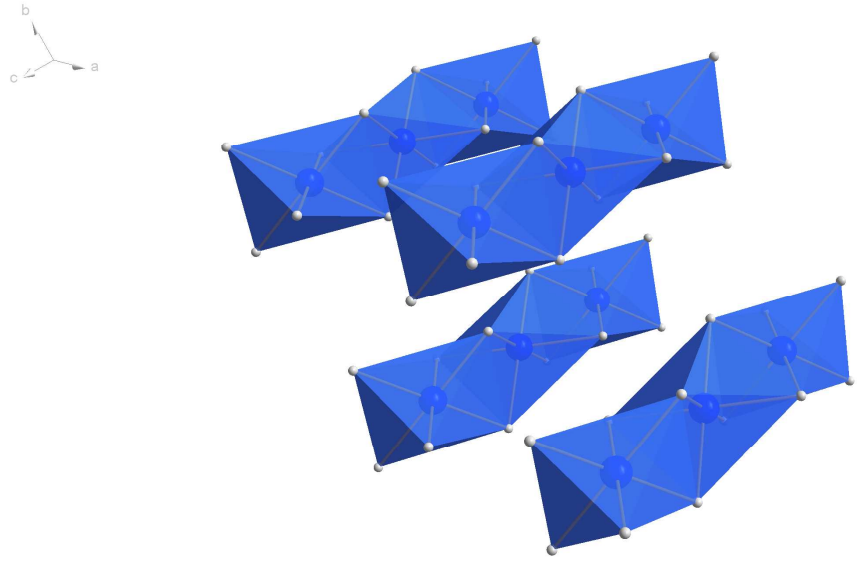


**Figure 1.19 Polyhedral representation of $K_3N$. Blue polyhedra centred by blue spheres represent nitrogen. White spheres representing potassium atoms[52].**

As can be seen, the structure is comprised of chains of $NK_6$ distorted octahedra which edge share. Heating this material to 233 K causes the structure to undergo a phase transformation to another $K_3N$ phase, which was characterised by XRD as having an orthorhombic unit cell. At 263 K the material decomposed and only elemental potassium remained.

Earlier reports of synthesis of rubidium and caesium nitrides through reaction of nitrogen with the corresponding metal hydride[53] were unsupported, and to date there remains no crystallographic evidence of such phases.

## 1.5 Alkaline Earth Metal Nitrides

Nitrides of the alkaline earth metals have been identified from the early 20$^{th}$ century and they tend to follow clear structural trends. As one descends the group, nitrides of beryllium and magnesium form salt-like compounds. These can be synthesised by a number of methods, but mainly through the reaction of the metal with nitrogen/ammonia gas or utilising sodium as a solvent for the reaction in a way similar to that of $Li_3N$. Calcium nitride is formed by a similar synthesis[54] and this material forms the ionic binary nitride but also forms metallic sub-nitrides (non-ideal stoichiometry) which are also formed by strontium and barium.

Beryllium nitride, α-$Be_3N_2$[55-56] (cubic, I a -3), was synthesised by the reaction of beryllium chips with nitrogen gas in a boron nitride furnace, and undergoes a phase change to ß-$Be_3N_2$[57] (Hexagonal, P63/*mmc*) at 1400 °C[58]. In the structure of the alpha phase, the beryllium is tetrahedrally coordinated to the nitrogen atoms and the nitrogen atoms are octahedrally coordinated to beryllium as shown in Figure 1.20. The beta phase adopts a hexagonal geometry.

Similarly $Mg_3N_2$ is synthesised through the reaction of magnesium metal and either nitrogen or ammonia gas[59], and although previous investigations by Mitchell[60] had reported two other phases along with the alpha phase, these were found to be all very similar in energy and could not be isolated, and so to date the only phase which has been substantiated is the α-$Mg_3N_2$ phase. Figure 1.20 shows the structure of this material[61].

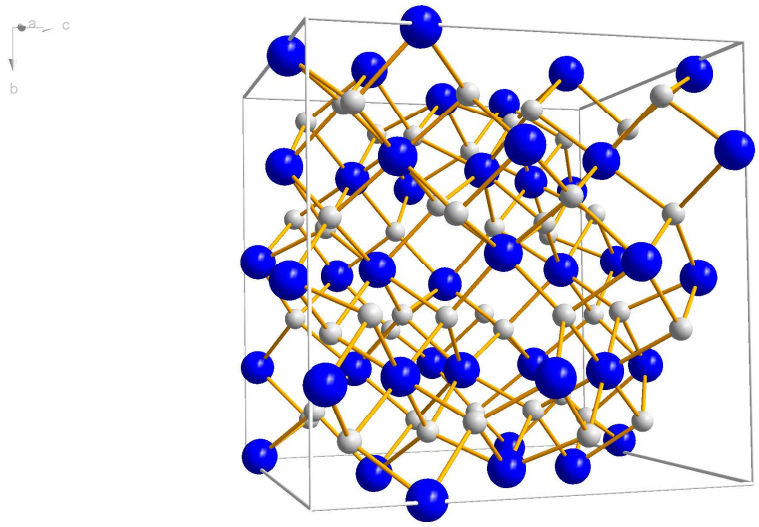


**Figure 1.20 Unit cell representation for α-$Be_3N_2$/ α-$Mg_3N_2$/ α-$Ca_3N_2$, where blue spheres represent nitrogen and white spheres represent beryllium/magnesium cations[61].**

As previously mentioned, calcium forms both ionic nitrides and metallic subnitrides. The ionic nitride is again formed at temperatures between 650 and 1150° C, through the reaction of nitrogen gas on the metal as with the previous alkaline earth nitrides[59]. The most well characterised phase is α-$Ca_3N_2$, which crystallises in the same space group as that of beryllium and magnesium as can be seen in Figure 1.20. In addition to this phase, there are two other phases that can be identified, the high temperature γ-$Ca_3N_2$ phase is formed at

temperatures above 1050° C[62] and the lower temperature ß-$Ca_3N_2$ phase formed at ~350° C[63]. The high temperature phase was found to crystallise in an orthorhombic unit cell, but this phase was later found to be a cyanamide containing material, namely $Ca_4N_2(CN_2)$[64], resulting from the carbon being leached into the material from the reaction vessel. The lower temperature phase indexed to a pseudo-hexagonal phase R-*3ch* where *a* = 6.18920 Å and *c* = 16.61115 Å [65].

Another nitride of calcium was discovered through the heating of α-$Ca_3N_2$ to temperatures of 1050° C in the presence of nitrogen, and this was thought to be of composition $Ca_{11}N_8$ but, similarly to the high temperature γ-$Ca_3N_2$ phase above, this was later characterised to be another cyanamide-containing phase. Again the presence of carbon was assumed to be from the same source of carbon, i.e. from the reaction vessel, and the material was reconfirmed to be $Ca_{11}N_6(CN_2)_2$[64].

A fourth calcium nitride was found to exist, a perinitride, and was of composition $Ca_3N_4$[66], and termed a perinitride due to the apparent excess of nitrogen. This material was synthesised via the decomposition of the azide of the alkaline earth metal under high vacuum, but at the time could not be isolated nor could it be confirmed by diffraction, but was well assigned using nitrogen elemental analysis later in 1966 by Okamoto *et al.* [67]. They synthesised the material in much the same way only this time carrying out the decomposition of the azide in decalin (Decahydronaphthaline) to give $Ca_3N_4$ and nitrogen gas. This material remains to date poorly understood and not very well investigated.

The lower metals in the alkaline earth period, strontium, barium and calcium do not form nitrides of the same type as beryllium and magnesium, of the form $A^{2+}{}_3N_2$, but instead form what are termed subnitrides.

Initially it had been thought that these metals did indeed form the conventional type of alkaline earth metal nitrides, $A^{2+}{}_3N_2$, and in the case of strontium, through the reaction of strontium metal and nitrogen gas it was reported that $Sr_3N_2$ had formed[68]. This was later found to be a mixture of $Sr_2N$ and SrNH[69] and the material $Sr_3N_2$ has never been observed and confirmed. Similarly $Ba_3N_2$ was thought to have been formed through the reaction of barium metal and nitrogen

gas by chemical analysis but the material could not provide clear X-ray diffraction patterns and although the pattern was indexed and chemical analysis provided the correct barium to nitride ratio, this structure remains close to that of BaNH.

The subnitrides, $A_2N$, have been synthesised through reductive heating of the purported $A_3N_2$ either under argon or in vacuum[70] at temperatures of ~ 900 – 1125 °C, but the subnitrides have been synthesised at lower temperatures through the direct reaction of the cleaned alkaline earth metal with nitrogen gas at temperatures of ~ 750 °C for $Sr_2N$[71], 480 – 500 °C for $Ca_2N$[70] and 1100 °C for $Ba_2N$[72]. They are all isostructural and crystallise in the trigonal *anti*-$CdCl_2$ space group R -3 m, as can be seen in Figure 1.20.

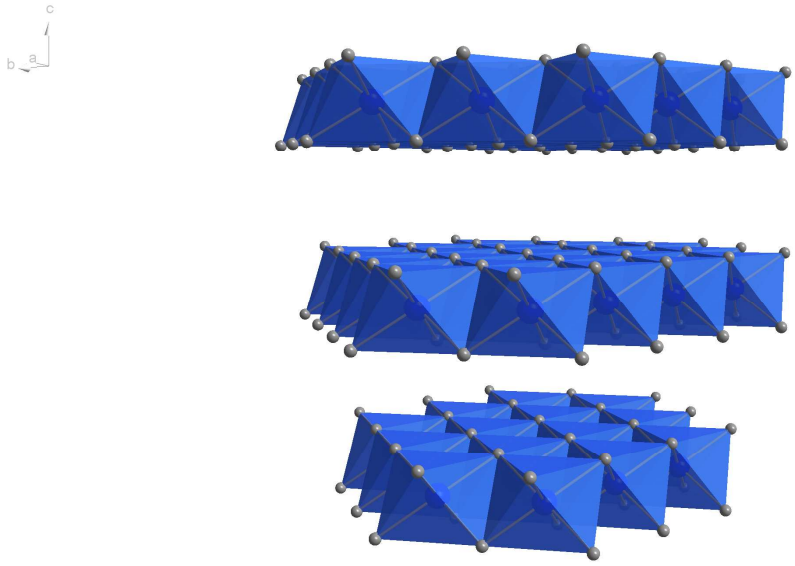


**Figure 1.21 Polyhedral representation of subnitrides $A_2N$. Blue $NA_6$ octahedra with blue spheres representing nitrogen atoms and grey spheres representing metal atoms, Ca, Ba or Sr[71].**

As can be seen from the figure, the structure consists of layers of edge sharing $NA_6$ octahedra, with large gaps between the layers into which other ions such as halides, F, Cl and Br, or metals, Au, Mn, Fe and Ga, can be inserted.

All of these alkali and alkaline earth metal nitrides form a number of ternary nitrides which potentially could have several different applications, and to date these are not all well characterised or understood.

## 1.6 Aims

The aims of the research performed and presented in this thesis were to synthesise lithium nitridometallates of the form $Li_{3-x-y}M_xN$, for M = Co, Ni and Cu where $x \leq 0.1$. These materials were to be synthesised under varying reaction conditions in order to gauge the effects that this had on the defect structure and stoichiometry of the materials, following on from strategies well defined from the study of the higher doped nitridometallates. Using different techniques, such as X-ray diffraction, powder neutron diffraction and scanning electron microscopy the reaction effects and metal dopant effects on the structures of these materials could be understood and fine-tuned. These investigations would allow us to see if trends and behaviours seen for the higher doped materials were observed at this low-doped level, such as aliovalent substitution and consequently vacancy incorporation. As a result this could potentially lead to materials with interesting magnetic behaviours due to changes of transition metal oxidation states for charge balancing. Also there is the potential that these low-doped materials could, as a consequence of their vacancies, show interesting $Li^+$ ion mobilities and / or charge storage properties as anode materials, and due to their lower densities compared to that of the higher doped nitridometallates, would maximise the gravimetric capacities. If vacancy incorporation in these materials is possible then, as previously postulated, $H^+$ ion mobility increases as vacancy concentration increases, and so these materials could provide interesting hydrogen storage properties with potential for the transition metal present having a catalytic effect on the adsorption and desorption of the gas, but again as these provide lower densities, gravimetric capacity would be maximised. The results of these investigations are presented herein.

## 1.7 References


1. L. Smart and E. Moore, *Solid State Chemistry An Introduction*, 2 edn.,137-146, Chapman and Hall, London 1995.
2. C. C. Addison and B. M. Davies, *Journal of the Chemical Society A - Inorganic Physical Theoretical*, (1969), 1827.
3. P. F. Adams, P. Hubberstey and R. J. Pulham, *Journal of the Less Common Metals*, **42**, (1975), 1.
4. R. C. Weast, *CRC Handbook of Chemistry and Physics*, 61 edn.,B-113, CRC Press Inc., Boca Raton, 1980.
5. L. Ouvrard, *Comptes Rendus Hebdomadaires Des Seances De L'Academie Des Sciences*, **114**, (1892), 120.
6. R. Brill, *Z. Kristallogr*, **65**, (1927), 94.
7. E. Zintl and G. Brauer, *Zeitschrift fuer Elektrochemie und Angewandte Physikalische Chemie*, **41**, (1935), 102.
8. A. Rabenau and H. Schulz, *Journal of Less-Common metals*, **50**, (1976), 155.
9. D. H. Gregory, *Coord. Chem. Rev.*, **215**, (2001), 301.
10. M. Mali, J. Roos and D. Brinkmann, *Phys. Rev. B*, **36**, (1987), 3888.
11. H. J. Beister, S. Haag, R. Kniep, K. Strossner and K. Syassen, *Angewandte Chemie-International Edition in English*, **27**, (1988), 1101.
12. S. V. Mitrokhina, K. P. Burdina and K. N. Semenenko, *Vestnik Moskovskogo Universiteta Seriya 2 Khimiya*, **31**, (1990), 612.
13. K. Differt and R. Messer, *J. Phys. C: Solid State Phys.*, **13**, (1979), 717.
14. R. Messer, H. Birli and K. Differt, *J. Phys. C: Solid State Phys.*, **14**, (1981), 2731.
15. U. V. Alpen, *J. Solid State Chem.*, **29**, (1979), 379.
16. U. V. Alpen, A. Rabenau and G. H. Talat, *Appl. Phys. Lett.*, **30**, (1977), 621.
17. B. A. Boukamp and R. A. Huggins, *Mater. Res. Bull.*, **13**, (1978), 23.
18. P. Hartwig, W. Weppner and W. Wichelhaus, *Material research bulletin*, **14**, (1979), 493.
19. R. Niewa, F. R. Wagner, W. Schnelle, O. Hochrein and R. Kniep, *Inorg. Chem.*, **40**, (2001), 5215.

20. D. H. Gregory, P. M. O'Meara, A. G. Gordon, J. P. Hodges, S. Short and J. D. Jorgensen, *Chem. Mater.*, **14**, (2002), 2063.
21. J. Wahl, *Solid State Commun.*, **29**, (1979), 485.
22. U. S. D. o. Energy, *Hydrogen, Fuel Cells & Infrastructure Technologies Program, Multi-Year Research, Development and Demonstration Plan, Planned program activities for 2005–2015*.
23. P. Chen, Z. Xiong, J. Luo, J. Lin and K. L. Tan, *Nature*, **420**, (2002), 302.
24. W. Frankenburger, L. Andissow and F. D. Luwigs, *Zeitschrift Fur Elektrochemie Und Angewandte Physikalische Chemie*, **34**, (1928), 632.
25. R. Juza, K. Langer and K. V. Benda, *Angew. Chem. internat. Edit*, **7**, (1968), 360.
26. J. Klatyk and R. Kniep, *Zeitschrift fuer kristallographie-new*, **214**, (1999), 447.
27. R. Juza and F. Hund, *Zeitschrift Fur Anorganische Chemie*, **257**, (1948), 1.
28. R. Juza, H. H. Weber and E. Meyersimon, *Z. Anorg. Allg. Chem.*, **273**, (1953), 48.
29. V. W. Saschsze and R. Juza, *Zeitschrift fur Anorganische Chemie*, **259**, (1949), 278.
30. J. Yang, K. Wang and J. Xie, *J. Electrochem. Soc.*, **150**, (2003), A140.
31. M. G. Barker, A. J. Blake, P. P. Edwards, D. H. Gregory, T. A. Hamor, D. J. Siddons and S. E. Smith, *Chem. Commun.*, (1999), 1153.
32. D. H. Gregory, P. M. O'Meara, A. G. Gordon, D. J. Siddons, A. J. Blake, M. G. Barker, T. A. Hamor and P. P. Edwards, *J. Alloys Compd.*, **317-318**, (2001), 237.
33. Z. Stoeva, R. Gomez, D. H. Gregory, G. B. Hix and J. J. Titman, *Dalton Trans.*, (2004), 3093.
34. R. Niewa, Z.-L. Huang, W. Schnelle, Z. Hu and R. Kniep, *Z. Anorg. Allg. Chem.*, **629**, (2003), 1778.
35. M. T. Weller, S. E. Dann, P. F. Henry and D. B. Currie, *J. Mater. Chem.*, **9**, (1998), 283.
36. F. A. Cotton and G. Wilkinson, *Advanced Inorganic Chemistry A Comprehensive Text*, 2nd edn.,637, Interscience, 1966.
37. T. Asai, K. Nishida and S. Kawai, *Mat. Res. Bull.*, **19**, (1984), 1377.

38. M. Nishijima, T. Kagohashi, M. Imanishi, Y. Takeda, Yamamoto and S. Kondo, *Solid State Ionics*, **83**, (1996), 107.
39. M. Nishijima, T. Kagohashi, Y. Takeda, M. Imanishi and O. Yamamoto, *J. Power Sources*, **68**, (1997), 510.
40. T. Shodai, S. Okada, S. Tobishima and J. Yamaki, *Solid State Ionics*, **86-8**, (1996), 785.
41. T. Shodai, S. Okada, S. Tobishima and J. Yamaki, *J. Power Sources*, **68**, (1997), 515.
42. Y. M. Kang, S. C. Park, Y. S. Kang, P. S. Lee and J. Y. Lee, *Solid State Ionics*, **156**, (2003), 263.
43. Y. Takeda, M. Nishijima, M. Yamahata, K. Takeda, N. Imanishi and O. Yamamoto, *Solid State Ionics*, **130**, (2000), 61.
44. L. P. Ma, P. Wang, H. B. Dai, L. Y. Kong and H. M. Cheng, *J. Alloys Compd.*, **466**, (2008), L1.
45. J. Cabana, N. Dupre, G. Rousse, C. P. Grey and M. R. Palacin, *Solid State Ionics*, **176**, (2005), 2205.
46. M. Nishijima, N. Tadokoro, Y. Takeda, N. Imanishi and O. Yamamoto, *J. Electrochem. Soc.*, **141**, (1994), 2966.
47. R. Juza, W. Gieren and J. Haug, *Z. Anorg. Allg. Chem.*, **300**, (1959), 61.
48. A. Gudat, S. Haag, R. Kniep and A. Rabenau, *Zeitschrift Fur Naturforschung Section B-a Journal of Chemical Sciences*, **45**, (1990), 111.
49. A. Gudat, R. Kniep and A. Rabenau, *Journal of Less-Common Metals*, **161**, (1990), 31.
50. M. Nishijima, Y. Takeda, N. Imanishi, O. Yamamoto and M. Takano, *J. Solid State Chem.*, **113**, (1994), 205.
51. D. Fischer and M. Jansen, *Angewandte Chemie-International Edition*, **41**, (2002), 1755.
52. D. Fischer, Z. Cancarevic, J. C. Schon and M. Jansen, *Z. Anorg. Allg. Chem.*, **630**, (2004), 156.
53. H. Moissan, *Comptes Rendus Hebdomadaires Des Seances De L Academie Des Sciences*, **136**, (1903), 587.
54. D. H. Gregory, M. G. Barker, P. P. Edwards and D. J. Siddons, *Inorg. Chem.*, **34**, (1995), 5195.
55. C. L. Hoenig and A. W. Searcy, *J. Am. Ceram. Soc.*, **50**, (1967), 460.

56. O. Reckeweg, C. Lind, A. Simon and F. J. DiSalvo, *Zeitschrift Fur Naturforschung Section B-a Journal of Chemical Sciences*, **58**, (2003), 159.
57. D. Hall, G. E. Gurr and G. A. Jeffrey, *Z. Anorg. Allg. Chem.*, **369**, (1969), 108.
58. P. Eckerlin and A. Rabenau, *Z. Anorg. Allg. Chem.*, **304**, (1960), 218.
59. M. von Stackelberg and R. Paulus, *Zeitschrift Fur Physikalische Chemie-Abteilung B-Chemie Der Elementarprozesse Aufbau Der Materie*, **22**, (1933), 305.
60. D. W. Mitchell, *Ind. Eng. Chem.*, **41**, (1949), 2027.
61. D. E. Partin, D. J. Williams and M. O'Keeffe, *J. Solid State Chem.*, **132**, (1997), 56.
62. Y. Laurent, J. David and J. Lang, *Comptes Rendus Hebdomadaires Des Seances De L'Academie Des Sciences*, **259**, (1964), 1132.
63. H. Hartmann and H. J. Frohlich, *Z. Anorg. Allg. Chem.*, **218**, (1934), 190.
64. O. Reckeweg and F. J. DiSalvo, *Angewandte Chemie-International Edition*, **39**, (2000), 412.
65. P. Hohn, S. Hoffmann, J. Hunger, S. Leoni, F. Nitsche, W. Schnelle and R. Kniep, *Chemistry-a European Journal*, **15**, (2009), 3419.
66. H. Hartmann and H. J. Frohlich, *Z. Anorg. Allg. Chem.*, **218**, (1934), 181.
67. Y. Okamoto and J. C. Goswami, *Inorg. Chem.*, **5**, (1966), 1281.
68. A. Guntz and F. Benoit, *Annales De Chimie France*, **20**, (1923), 5.
69. J. Gaude and J. Lang, *Revue De Chimie Minerale*, **9**, (1972), 799.
70. D. H. Gregory, A. Bowman, C. F. Baker and D. P. Weston, *J. Mater. Chem.*, **10**, (2000), 1635.
71. N. E. Brese and M. O'Keeffe, *J. Solid State Chem.*, **87**, (1990), 134.
72. O. Reckeweg and F. J. DiSalvo, *Solid State Sciences*, **4**, (2002), 575.

# 2. Experimental

## 2.1 Air Sensitive Handling Techniques

Due to the majority of the materials used in this research being highly air, and moisture, sensitive and pyrophoric, inert conditions had to be used for the purposes of handling. These inert conditions were obtained through the use of glove boxes containing inert gasses e.g. dry $N_2$ or Ar. Depending on the type of work needing to be carried out two types of glove box were available, evacuable and recirculating.

The use of an evacuable glove box is employed when an argon atmosphere is required, such as in the initial method of preparation of $Li_3N$ and also when TIG (Tungsten Inert Gas) welding is needed. The evacuable glove boxes are bespoke glove boxes, and consist of the box connected to a diffusion pump through an Edwards rotary vane pump. The front of the glove box contains a Perspex window through which all of the necessary equipment gets loaded, and two neoprene gloves with Perspex port covers for when evacuating. When using the box, the required equipment is loaded inside and the Perspex window, with o-ring to ensure a good seal, is fastened onto the front using eight butterfly screws. The rotary pump is switched on, the glove port covers are placed on and the air to the gloves is evacuated. The box is then also opened to the rotary pump and the air inside evacuated and the vacuum level is monitored at this stage using a Pirani gauge and when the vacuum has achieved ~$10^{-1}$ mbar the oil diffusion pump is evacuated and then the heater below the oil is switched on. Once the oil is hot the baffle valve at the top of the pump is opened to the box, and is left overnight to ensure complete de-gassing of the box has occurred, typically when a vacuum level of $10^{-4}$ mbar is observed. The next stage is to fill the box with $Ar_{(g)}$ that has been passed through a rare gas purifier (BOC) and molecular sieve in order to remove any oxygen or moisture. Once the gas has filled the box it is ready to be used. Once all manipulations have been carried out, the box is opened and the equipment removed in a reverse of the loading procedure.

The use of recirculating gloveboxes (Saffron Scientific Ltd.) are required when either $N_{2(g)}$ atmospheres or $Ar_{(g)}$ atmospheres are needed as in the case of the newer method for the $Li_3N$ preparation. The box has a cylindrical port for the transfer of all equipment and samples which is evacuated using a rotary vane pump (Edwards) and filled with the relevant gas supply from taps within the laboratory connected to the box. A recirculating pump within the box ensures the atmosphere remains good by passing the gas through a molecular sieve to remove water and BASF catalyst to remove oxygen. External oxygen and moisture meters display the levels within the box, ideally $O_{2(g)}$ <1 ppm and $H_2O$ <5ppm. Figure 2.1 below shows a schematic representation of the recirculating glove box.

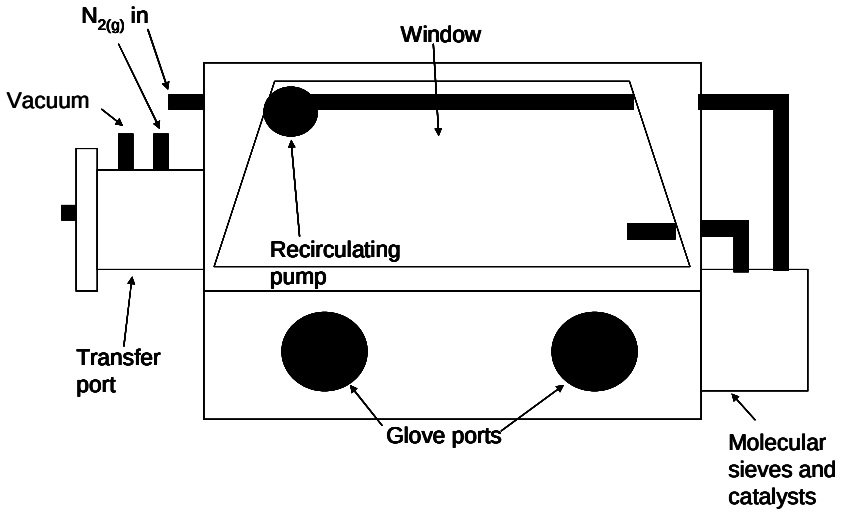


**Figure 2.1 Schematic representation of Saffron Scientific nitrogen recirculating glove box**

# 2.2 Syntheses

## *2.2.1 Preparation of Lithium Nitride*

There are a number of ways to synthesise lithium nitride[1-2], $Li_3N$, and the easiest conceivable way of doing so is by the direct reaction of solid lithium metal with gaseous nitrogen at elevated temperatures.

$$6Li + N_{2(g)} \xrightarrow{\Delta} 2Li_3N$$

However, use of this approach does have some disadvantages as discovered by previous members of the group, namely that the product often displays very poor crystallinity, is hard to grind and can contain impurities such as lithium oxide or hydroxide. A way of counteracting such problems is to synthesise the material using molten sodium metal as solvent for the reaction[3]. This has a number of advantages; above 653K sodium and lithium are completely miscible and, as no stable binary nitrides of sodium are formed under simple conditions, it leaves the lithium to completely react with the nitrogen giving products of high purity and crystallinity. Also, the presence of sodium can act as a scavenger for any residual oxygen thus reducing the likelihood of impurities forming with the product.

Due to the fact that Li will react at ambient conditions with $N_{2(g)}$, the use of an $Ar_{(g)}$ filled glove box is required. For the majority of the research an $Ar_{(g)}$ recirculating glove box was used for the purpose of these syntheses. A pool of Na was melted (m.p. 371 K) on a hotplate within the box and this keeps the atmosphere clean of any residual $O_{2(g)}$ or $H_2O$ that hasn't been removed by the sieve and catalyst. Once the Na is molten, any oxide or hydroxide that is present in the atmosphere reacts with the sodium and floats to the top of the pool and appears as a white or dulled layer. This can then be skimmed off the top of the pool using a knife or a spoon thus reducing the likelihood of obtaining impurity in the product. Once the atmosphere is cleaned, the sodium pool is moved to the side, and the stainless steel crucible containing the reaction Na (ca. 50g, Aldrich, 99 %) is placed on the hotplate to melt. Once molten, any oxide layer of the Na is skimmed off also, and then a piece of Li is cut (ca. 6g, Alfa, 99.9 %, < 0.1% trace metals) and cleaned using the knife and files for any parts that are smaller. The knife and spoon used are made of stainless steel and thus could potentially introduce carbon, iron and chromium impurities but due to the impact on the utensils being low and both were in good condition it wasn't thought likely that these impurities were being introduced. The Li is cut into several smaller pieces once cleaned and they are added to the molten reaction Na one at a time until each piece has dissolved. Then the hotplate is turned off and the crucible is allowed to cool and then sealed in a reaction vessel and run in a furnace as can be seen in Figure 2.2 below. The reaction is run at a temperature of 733 K for a period of 72 hours, during which time the sodium will

react with any residual oxygen or moisture as it has a greater affinity to do so, and thus the lithium will only react with the nitrogen to form $Li_3N$. Once the reaction has been run, it is switched off and allowed to cool to room temperature and then the cold finger filled with water, and the reaction is heated again to the same temperature of 733 K overnight, this time under dynamic vacuum. This allowed the solvent sodium to condense on the cold finger thus leaving only the product in the reaction crucible.

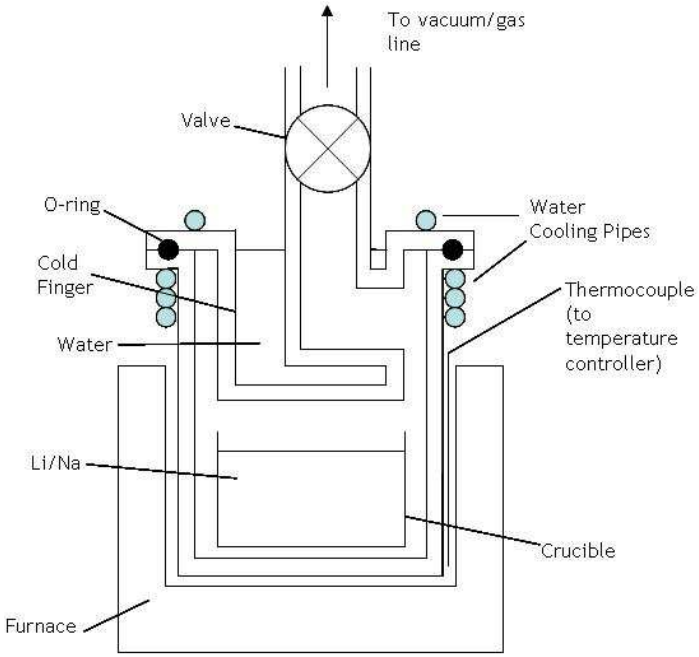


**Figure 2.2: Reaction vessel for $Li_3N$ preparation**

## *2.2.2 Lithium nitridometallates*

The synthesis of lithium nitridometallates of the general formula $Li_{3-x}M_xN$ are synthesised from the parent material lithium nitride, and can be synthesised in a number of ways previously discussed in the literature[4-7].

$$Li_3N + xM \longrightarrow Li_{3-x}M_xN$$

One of these methods is the reaction of the lithium nitride with the nitride of the transition metal, i.e. $Li_3N$ with $Cu_2N$. Another method that has been employed more recently in the literature is to ball mill $Li_3N$ with the powder of the corresponding transition metal. This has had only limited success and one

significant drawback of this method in terms of characterisation is the peak broadening seen in the diffraction pattern of the products due to reduced particle size. The synthesis that has been employed for the course of this research has been to react lithium nitride with the powder of the transition metal at elevated temperatures. The preparations for these syntheses are all carried out in an $N_{2(g)}$ recirculating glove box. The transition metal powder was pre-reduced in a horizontal tube furnace under a flow of 5% $H_2/N_{2(g)}$ overnight. The reduced powder is then transferred quickly to the glove box, and the required weight is mixed with the corresponding weight of the lithium nitride powder. The reactants are ground together for approximately five minutes in an agate mortar and pestle to ensure a homogeneous distribution. The reactant mixture is then pressed into a pellet of ~1g (or several pellets for larger sample quantities) using a 13mm stainless steel pellet die. The pellet(s) is placed inside of a stainless steel crucible which is turn sealed inside a stainless steel reaction vessel with a valve attached and run in a furnace as shown below in Figure 2.3. The temperature was set on the temperature controller for the furnace (most often 700$^o$ C) and also the length of time for which it was to be maintained at that temperature (typically 2 – 7 days) also programmed. The cooling water is tap fed through the copper cooling pipes at the bottom and out the top into the sink drain. When the programmer has stopped heating at the end of the reaction, and the vessel and furnace are both sufficiently cool, the vessel is removed from the furnace, the water pipes are removed from the copper pipes, and the copper pipes are dried using vacuum and acetone to allow the entire vessel to be transferred to the glove box. Once inside the glove box, the allen bolts are removed from the lid of the vessel and the lid taken off, the crucible can then be lifted out of the vessel using a pair of tongs, and the product collected from inside the crucible.

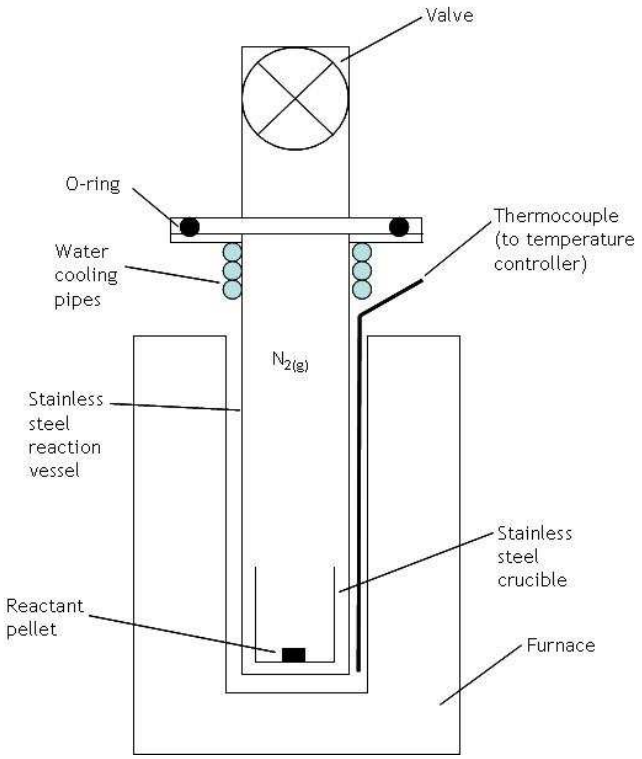


**Figure 2.3: Reaction vessel and furnace for the preparation of lithium nitridometallates**

The product can vary in colour from a dark green, through grey and black to even a brownish colour, and this is entirely dependant on the transition metal used, and the pellet can often be very hard when low levels of dopant metal are used, and very soft when higher transition metal levels are used.

# 2.3 Structure characterisation / Product characterisation

## *2.3.1 Powder X-ray diffraction*

### 2.3.1.1 Background

The explanation of X-ray diffraction that is most commonly used is that which was devised by Bragg[8-9] with respect to a crystal which is constructed from layers or planes of atoms which form a regularly repeating structure. The layers or planes within this crystal typically have an inter-atomic separation of ~2-3 Å. These planes can reflect a beam of incident radiation where the reflection angle is equal to the angle of incidence, and constructive diffraction will occur when

the wavelength of this radiation is close in size to that of the distance between the layers of the plane.

The reason why X-ray radiation is scattered is due to the fact that its wavelength is comparable to that of inter-atomic distances within a crystal, *e.g.* Cu $K_\alpha$ $\lambda$ = 1.5418 Å, Mo $K_\alpha$ $\lambda$ = 0.7107 Å.

From the situation in Figure 2.4 we can see that in order for the two X-ray beams, A and B, to constructively interfere they must be in phase. But, as can be seen, beam B must travel the additional distance of xyz in comparison to beam A. This is known as the path difference, and this must be equal to an integer number of wavelengths in order for beams A and B to be in phase:

$$xyz = n\lambda \qquad \mathbf{2.1}$$

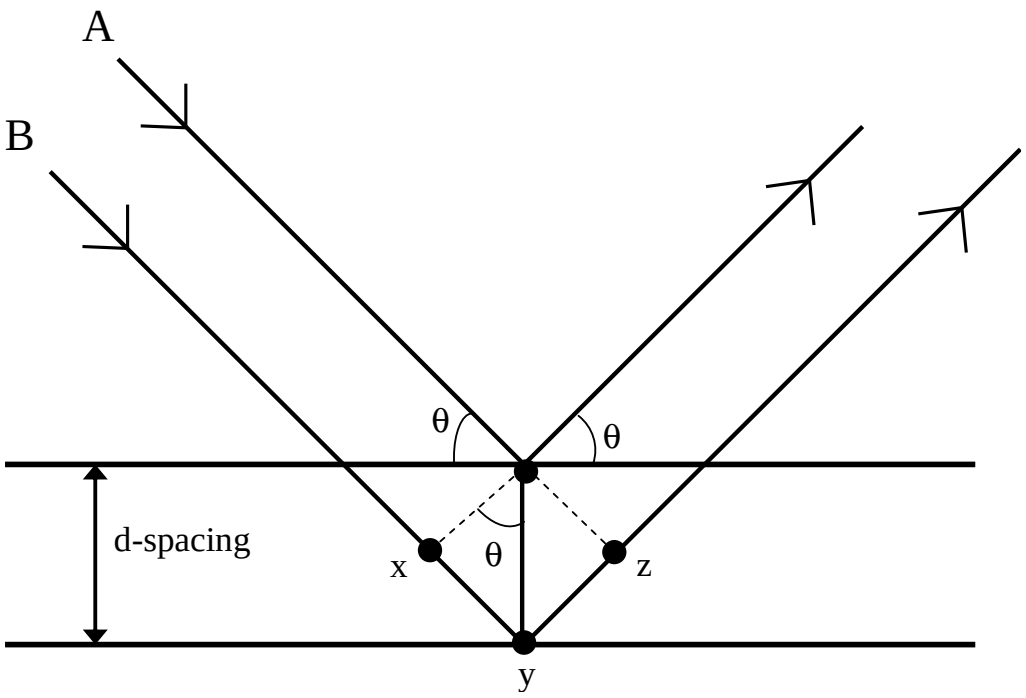


**Figure 2.4 Schematic representation of X-ray diffraction for derivation for Bragg's law.**

From Figure 2.4 it can be seen using simple geometry that the Bragg angle, $\theta$, and the d-spacing are related to the distances xy and yz as follows:

$$xy = yz = d \sin \theta \qquad \mathbf{2.2}$$

It therefore follows that:

$$xyz = 2d \sin \theta \qquad \mathbf{2.3}$$

By combining equations **1** and **3**, Bragg's law is derived:

$$n\lambda = 2d \sin \theta \qquad \mathbf{2.4}$$

This therefore means that allowed reflections will only be observed at specific angles, which are dependant on the unit cell size of the sample, *i.e.* the spacing between the interatomic planes of the sample, d. From these d-spacings the crystal system can be derived and the miller indices, hkl values, of the planes refer to the fractional coordinates where the plane intersects the a, b and c axes respectively. Table 2.1 below shows the specific expressions for each crystal system.

**Table 2.1 Equations for d-spacings in different crystal systems, where *a, b* and *c* are the unit cell parameters, *h, k* and *l* are the miller indices where the diffraction plane intersects the unit cell axes. *α, β* and *γ* are the angles of the unit cell, *d* is the interatomic plane distance and *V* is the unit cell volume.**

| ***Crystal system*** | ***Expression for $d_{hkl}$*** |
|---|---|
| **Cubic** | $\frac{1}{d_{hkl}^2} = \frac{h^2 + k^2 + l^2}{a^2}$ |
| **Tetragonal** | $\frac{1}{d_{hkl}^2} = \frac{h^2 + k^2}{a^2} + \frac{l^2}{c^2}$ |
| **Orthorhombic** | $\frac{1}{d_{hkl}^2} = \frac{h^2}{a^2} + \frac{k^2}{b^2} + \frac{l^2}{c^2}$ |
| **Hexagonal** | $\frac{1}{d_{hkl}^2} = \frac{4}{3}\left(\frac{h^2 + hk + k^2}{a^2}\right) + \frac{l^2}{c^2}$ |
| **Monoclinic** | $\frac{1}{d_{hkl}^2} = \frac{1}{\sin^2\beta}\left(\frac{h^2}{a^2} + \frac{k^2 \sin^2\beta}{b^2} + \frac{l^2}{c^2} - \frac{2hl\cos\beta}{ac}\right)$ |
| **Triclinic** | $\frac{1}{d_{hkl}^2} = \frac{1}{V^2}[h^2b^2c^2\sin^2\alpha + k^2a^2c^2\sin^2\beta + l^2a^2b^2\sin^2\gamma + 2hkabc^2(\cos\alpha\cos\beta - \cos\gamma) + 2kla^2bc(\cos\beta\cos\gamma - \cos\alpha) + 2hlab^2c(\cos\alpha\cos\gamma - \cos\beta)]$ **where** $V = abc(1 - \cos^2\alpha - \cos^2\beta - \cos^2\gamma + 2\cos\alpha\cos\beta\cos\gamma)^{1/2}$ |

The intensity that is observed from the diffraction is entirely dependent on what the contents of the unit cell are, *i.e.* which atoms and where within the unit cell they are found, as it is due to the electrons that the X-rays are scattered. X-ray diffraction acts as a function of atomic number, thus meaning that as you have heavier elements present, there are a greater number of electrons present and more scattering occurs. This leads to an increased intensity being observed.

In order for samples to strongly diffract, the crystallites are required to be aligned/oriented at random. If this is achieved then it means that there will always be some crystallites aligned at the Bragg angle,$\theta$, and diffraction from all the planes in this crystallite will occur. There are examples where the crystallites of particular materials have a tendency to either form a particular morphology or orient themselves in a particular way. This prevents random orientation and means that orientation is preferred in one manner opposed to others. This leads to 'preferred orientation' which can cause heightened intensities for some reflections which are attributed to a particular direction. $Li_3N$ is a perfect example of this as it forms flat hexagonal platelets which, as one would imagine, lie flat which in turn lead to an increase in intensity for the 00l peaks. In order to overcome this problem, all PXD experiments were carried out in the Debye-Scherrer (parallel beam) geometry for the purposes of this work.

Whereas single crystal X-ray diffraction leads to well defined single points of intensity from the planes of the crystal, X-ray diffraction from a powder (randomly oriented crystallites) leads to rings of diffraction intensity and the pattern seen at the end is the result of a one dimensional slice through these diffraction rings. This means that there will be regions of the pattern where diffraction intensities of different planes overlapped. This made early attempts at data analysis very difficult, and attempts were made to acquire individual structure factors from the peak envelopes and apply single crystal methods to obtain the structural information. This meant that early characterisation techniques were restricted mainly to trial and error comparisons of powder patterns to already known patterns and characterisation of the simplest of crystal structures (highest symmetry).

All this was changed by H.M. Rietveld[10-11]. He postulated that there was information attached to each intensity at each step in the pattern, and that even areas where no intensity or scrambled intensity was seen, some information could be elucidated. He did this by refining parameters, pertaining to specimen or instrument effects, in a model for the observed diffraction pattern. This has since allowed for Powder X-ray Diffraction (PXD) to become a

very powerful tool at the chemists disposal, and can allow for the determination of particle sizes, crystal structures, crystal defects and disorder.

#### 2.3.1.2 Preparation of PXD samples

Samples are ground well post-reaction in an agate mortar and pestle to ensure uniform distribution of the crystallites. The samples are then loaded into a silica glass capillary (ranging in width from 0.3mm to 0.7mm) using the end of a micro-spatula. The capillary is packed well to a height of ~4-5cm and then compacted further by tapping the base of the capillary holder on the base of the glove box, in which all this preparation takes place.

Once the sample has been packed sufficiently within the capillary, again using the end of the micro-spatula, a small amount of silicone grease is placed in the opening so as to plug the capillary. At this time, the capillary is deemed airtight and is removed from the glove box. It is then flame sealed using a standard lighter to ensure a more secure seal.

#### 2.3.1.3 Data collection

All measurements were made using a Bruker d8 advance $\theta$-$2\theta$ diffractometer. The radiation used was Cu K$\alpha$ ($\lambda$ = 1.5418 Å) with a monochromator in order to eliminate Cu K$\beta$ and K$\alpha$2 radiation. The tube operated at 40 kV and 40 mA. The standard setup used was a 1mm divergence slit and a pre-sample air scattering reducer, a post-sample beamstop. The sample was run under capillary rotation with a Vantec (PSD) detector.

A short scan was carried out for a $2\theta$ range of 5-85 degrees in steps of 0.017 $^{o}$ at a scan speed of 0.63 seconds per step, which equated to ~60 minutes. Longer scans in order to acquire data of Rietveld refinement quality were carried out over a $2\theta$ range of 5-90 degrees for a duration of approximately ten hours.

#### 2.3.1.4 Data analysis

The Bruker instrumental software produces a .raw file at the end of a measurement which contains information about the experiment such as the $2\theta$

positions, intensities and d-values. In order to display this graphically, the program PowderCell 2.4[12] is used and the pattern is viewed as a plot of intensity on the y-axis against 2θ on the x-axis. Then this pattern can be compared to databased powder patterns from the ICSD[13] (Inorganic Crystal Structure Database) in order to ascertain what impurities are present (if any) in addition to the product phase. Indexing of the powder pattern and extraction of the refined cell parameters and symmetry are done using the program "CELL" via minimization of the expression:

$$M = \sum_n W_n \left( \sin^2\theta_n^{obs} - \sin^2\theta_n^{calc} \right)^2 \qquad \textbf{2.5}$$

using an iterative least squares procedure. $W_n$ is a weighting factor, proportional to $tan\theta$. The cell parameters so produced are attributed estimated standard deviations (ESDs), although these reflect only the goodness of fit between the observed and calculated 2θ position and provide no indication of systematic experimental errors.

Rietveld refinement was carried out on the longer scanned data using von Dreele and Larson's GSAS (the General Structure Analysis System) program[14]. The model is compared to a known crystal system, and so the first phase is initially loaded, then the histogram for the recorded pattern is loaded and the usable data regions are selected and saved. Background parameters and scale factors are firstly introduced then followed by a correction for the lattice parameters, sample displacement and zero point. Then at this stage normal refinement of the peak shape parameters would be carried out followed by setting up of constraints for any shared sites. The fractional occupancies and isotropic temperature factors are allowed to refine. At this stage, if the refinement and atoms are stable, anisotropic temperature factors can be refined in both PND and XRD but if light atoms are present in the material then refinement of anisotropic temperature factors for XRD data is not very stable.

The quantity that is minimized during a least-squares refinement is the residual, $S_y$, by means of the expression:

$$S_y = \sum_i w_i (y_i - y_{ci})^2 \qquad \textbf{2.6}$$

where $w_i$ is a weighting factor corresponding to $1/y_i$, $y_i$ is the (gross) intensity at the *i*th step, and $y_{ci}$ is the calculated intensity at the *i*th step.

The calculated intensities, $y_{ci}$, are obtained from the $|F_K|^2$ values calculated from the structural model by summing of the calculated contributions from neighbouring Bragg reflections plus the background:

$$y_{ci} = s\sum_K L_K \left|F_K\right|^2 \phi(2\theta_i - 2\theta_K) P_K A + y_{bi} \qquad \textbf{2.7}$$

where, s is the scale factor, K represents the Miller indices *h k l,* for a Bragg reflection. $L_K$ contains the Lorentz polarisation and multiplicity factors, $\phi$ is the reflection profile function and $P_K$ is the preferred orientation function. A is an absorption factor, $F_K$ is the structure factor for the Kth Bragg reflection and $y_{bi}$ is the background intensity at the *i*th step.

The default background function that is selected in GSAS is the second function, which is a cosine Fourier series with a leading constant term:

$$y_{bi} = B_l + \sum_{j=2}^{N} B_j \cos\left[P * (j-1)\right] \qquad \textbf{2.8}$$

For constant wavelength, either X-ray or neutron, the P term is in degrees $2\theta$ and is merely the detector position for the step. For Time of Flight (TOF) data, the times are scaled by 180/TMAX, whereby the TMAX is the maximum allowed by the incident beam. The values of $B_l$ and $B_j$ are determined by least square during the Rietveld refinement of the powder pattern.

Due to the fact that the observed and calculated intensities are compared at each point it is imperative for the modelled profile functions to correspond to the Bragg reflections accurately. Peak shape tends to be a function of the instrument, and for the Bruker D8 the peak shape is best described by a pseudo-Voigt function:

$$\eta L + (1-\eta)G \qquad \textbf{2.9}$$

and the mixing parameter $\eta$, can be refined as a linear function of 2θ and the refineable variables *NA* and *NB:*

$$\eta = NA + NB * (2\theta) \qquad \textbf{2.10}$$

The pseudo-Voigt contributions to the peak shape from Gaussian (G) and Lorrentzian (L) peak shapes are governed by the respective equations:

$$G = \frac{(4\ln 2)^{1/2}}{H_K \pi^{1/2}} \exp\left(-4\ln 2(2\theta_i - 2\theta_K)^2 / H_K^2\right) \qquad \textbf{2.11}$$

and:

$$L = \frac{(4)^2}{\pi H_K} 1/\left[1 + 4\frac{(2\theta_i - 2\theta_K)^2}{H_K^2}\right] \qquad \textbf{2.12}$$

where $2\theta_K$ is the calculated position for the Kth Bragg peak corrected for the counter zero-point and $H_K$ is the full-width-at-half-maximum (FWHM) of the Kth Bragg reflection.

The dependence of the breadth *H* of the reflection profiles measured as full-width-at-half-maximum (FWHM) has typically been modelled as:

$$H_K^2 = U\tan^2\theta + V\tan\theta + W \qquad \textbf{2.13}$$

where $H^2_K$ is the full-width-at-half-maximum at the Kth Bragg reflection, and U, V and W are all the refineable parameters. X-ray instruments give a narrow profile and this therefore means that sample effects, such as microstrain and crystallite size, contribute a significant part to the total.

As has been indicated, the refinement process is a ‘best fit’ correlation between the observed diffraction intensities with the calculated intensities from the model. It is therefore important to gauge the goodness of the model and whether we have achieved a global minimum rather than a local (false)

minimum. The way in which this is done is through the use of several '*R*-values' shown below:

$$R_F = \frac{\sum \left| (I_K('obs'))^{1/2} - (I_K(calc))^{1/2} \right|}{\sum (I_K('obs'))^{1/2}} \qquad \textbf{2.14}$$

$$R_B = \frac{\sum \left| I_K('obs') - I_K(calc) \right|}{\sum I_K('obs')} \qquad \textbf{2.15}$$

$$R_P = \frac{\sum |y_i - y_{ci}|}{\sum y_i} \qquad \textbf{2.16}$$

$$R_{WP} = \left\{ \frac{\sum w_i (y_i - Y_{ci})^2}{\sum w_i (y_i)^2} \right\}^{1/2} \qquad \textbf{2.17}$$

$$R_e = \left\{ \frac{N - P}{\sum w_i (y_i)_2} \right\}^{1/2} \qquad \textbf{2.18}$$

where $R_F$ is the structure factor, $R_B$ the Bragg, $R_P$ the pattern, $R_{WP}$ the weighted pattern and $R_e$ the expected 'R-factors'. $I_K$ obs and calc are the observed and calculated intensities at the Kth Bragg reflection from the programme. Similarly, $y_i$ and $y_{ic}$ are the observed and calculated intensities at the ith step and $w_i$ is the inverse of $y_i$. Also N is the number of observations and P is the number of refineable parameters[14-15].

Due to the fact that $R_F$ and $R_B$ are deduced from the model and not the observed Bragg intensities, it means that they are weighted in favour of the model and therefore not the most mathematically reliable. The most meaningful factor to assess the progress of the refinement is $R_{WP}$. The final measure of the whole fit of the minimization is the goodness of fit parameter which is defined as:

$$\chi^2 = \left( \frac{R_{WP}}{R_e} \right)^2 \qquad \textbf{2.19}$$

The goodness of fit can also be viewed graphically by observing the created observed-calculated-difference (OCD) plot. This shows the measured pattern with the calculated one overlaid and shows a plot below of the difference between the two. A good fit would have a difference plot which was almost flat.

## *2.3.2 Time of Flight Powder Neutron Diffraction*

### 2.3.2.1 Background

The ToF PND that was carried out for the purpose of this thesis was carried out on the GEneral Materials diffractometer (GEM) at the ISIS facility at the Rutherford Appleton Laboratories which is a pulsed neutron source.

An 800 MeV proton accelerator produces pulses of protons at a frequency of 50 times a second, and this accelerates bunches of $H^-$ ions and then these are injected into the synchrotron where they are focused into a circle. Alumina foils then remove the electrons leaving only the protons which are then further accelerated, and after ~10000 revolutions are separated into two large bunches. These bunches are then extracted from the synchrotron and collide with a tungsten target and, through spallation, create neutrons. Hydrogenous moderators around the target slow the speed of the neutrons down to the speeds required, and then these travel to the sample and then onto the detector. The detector $2\theta$ angle is fixed and the arrival time of the neutrons at the detector is recorded.

The wavelength of a neutron is related to it's velocity by the de Broglie relationship:

$$\lambda = \frac{h}{mv} \qquad \textbf{2.20}$$

where, h = Planck's constant, m = mass of a neutron and v = velocity.

The typical velocity of a thermal neutron is ~2200 $ms^{-1}$, which corresponds to a wavelength of 1.8 Å. This is comparable to the inter-atomic distances between planes in a crystal and thus neutron diffraction can be used in crystalline solids.

The time of flight of the neutrons, t, is given by:

$$n\lambda = n\frac{ht}{mL} = 2d\sin\theta \qquad \textbf{2.21}$$

Since we can record the time at which the neutrons arrive at the detector, and we know Planck's constant, the mass of a neutron and the distance from the source to the sample, L, we can therefore calculate the wavelength of each neutron.

X-rays are diffracted by the electrons around the nucleus of an atom, and as a consequence of this, the scattering power increases with increasing atomic number. This has the drawback of light atoms being hard to detect. However, because neutrons are diffracted by the nucleus of an atom, there is no linear dependency of the diffraction with atomic number. This therefore gives the advantage that lighter atoms can now be located, and their temperature factors and site occupancies can be refined much more accurately.

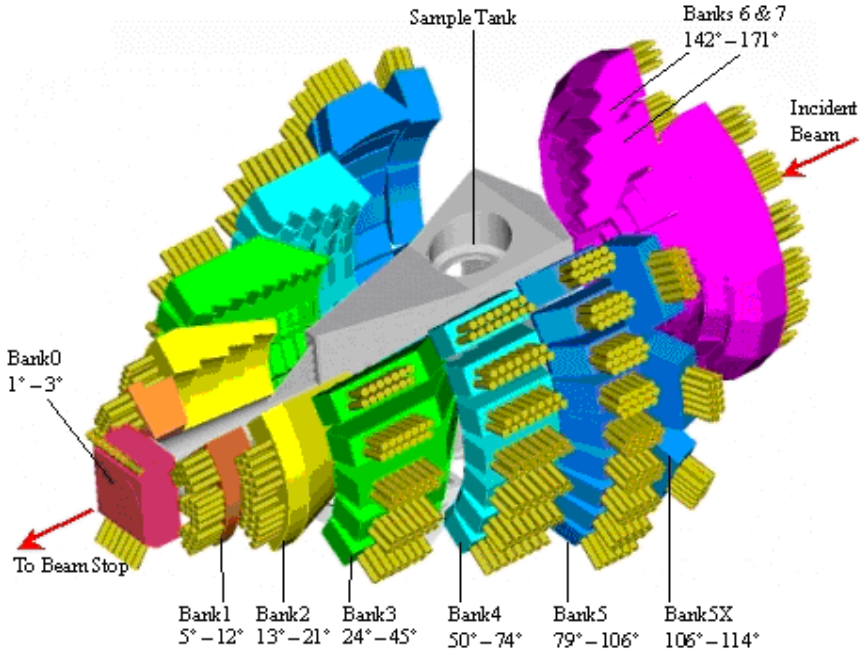


**Figure 2.5 Schematic representation of the GEM instrument**

The GEM instrument as can be seen in Figure 2.5 is a medium resolution high intensity powder diffractometer. This instrument offers a highly stable detector array, which covers a very wide range in scattering angles and a very large solid

angle, leading to a wide dynamic range and high count rate[16]. Low temperature diffraction can be performed through the use of a cryostat, and high temperature diffraction with a furnace. The data are collected on several banks at different angles all using ZnS/$^{6}$Li scintillator detectors and Table 2.2 shows the details for the different banks.

**Table 2.2 Detector specifications for POLARIS**

| Bank number | Scattering angle 2θ ° | No. of detector elements/ modules |
|---|---|---|
| **0** | 1.21 – 3.18 | 80 /4 |
| **1** | 5.32 – 12.67 | 330 /6 |
| **2** | 13.44 – 21.59 | 320 /4 |
| **3** | 24.67 – 45.61 | 900 /10 |
| **4** | 50.07 – 74.71 | 1400 /14 |
| **5** | 79.07 – 106.60 | 2160 /18 |
| **5x** | 106.02 – 114.19 | 720 /18 |
| **6** | 142.50 – 149.72 | 560 /14 |
| **7** | 149.98 – 171.40 | 800 /10 |

#### 2.3.2.2 Preparation of ToF samples

The samples are synthesised by the method previously detailed in section 1.2.2. Approximately 2g of the sample is ground and placed inside a vanadium canister inside a recirculating glove box at the ISIS facility. The lid is placed on the top of the canister with a turn of indium wire to help form the seal, then three small allen bolts are screwed down tight. The lid of the canister has a threaded hole for attaching it to the 'candlestick' then this is loaded into the instrument.

#### 2.3.2.3 Data collection

All of the ToF PND experiments in this thesis were carried out on GEM at the ISIS facility with the help of Dr. R. I. Smith. Data were collected from all four banks of detectors simultaneously as separated histograms. The experimental run times varied from ~1.5 hours to ~4 hours depending on sample quantity and crystallinity.

#### 2.3.2.4 Data analysis

Software manipulation was carried out at the GEM beam station in order to reduce the data to a usable form. The program GSAS is used to refine the data as described by the Rietveld method in section 1.3.1.4.

## *2.3.3 Constant Wavelength Powder Neutron Diffraction*

#### 2.3.3.1 Background

All constant wavelength powder neutron diffraction experiments presented in the course of this thesis were performed on D1A at the Institut Laue-Langevin (ILL) in Grenoble, the schematic of which can be seen in Figure 2.6. It is a large cold neutron source with ten guides each serving three or four instruments, and provides a high intensity flux of neutrons. This is a nuclear reactor site and produces free neutrons through the process of nuclear fission.

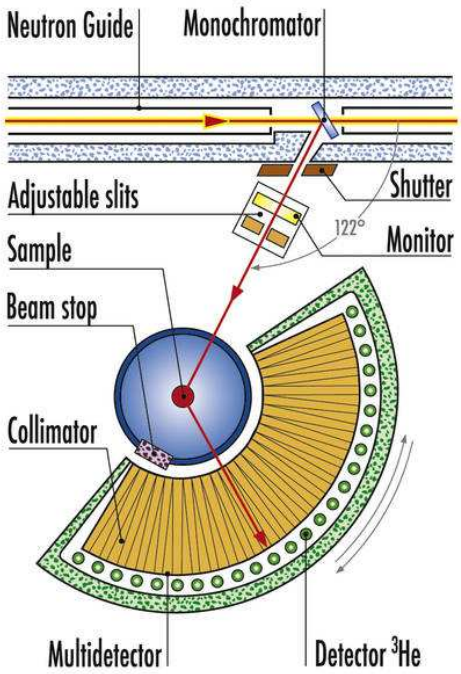


**Figure 2.6 Schematic representation of D1A instrument**

The monochromator consists of thirty germanium crystals thirty millimetres high. The take off angle is 122 degrees and the wavelength used is 1.911 Å corresponding to a germanium crystal *hkl* plane of 115. The angular range

available is a 2θ of 6 – 160 degrees. The detector consists of 25 $^{3}$He counters at 5 atmospheres of pressure each and there is a temperature range of 1.5 K to 600 K depending on whether the cryostat or the cryofurnace is used.

This facility was utilised in this course of research for the same reason as for with the ToF neutron diffraction, with the ability to probe lighter elements foremost, coupled with the higher flux of neutrons available makes it a useful tool.

#### 2.3.3.2 Preparation of CW PND samples

The materials were prepared by the method outlined in section 1.2.2. The samples were then prepared for the experiment using a glove bag at the ILL. The samples were placed inside of the glove bag which was then sealed, evacuated and then purged 5 times. The sample, ~2 g, was then funnelled into the vanadium canister using a small piece of paper as a funnel, and a copper gasket ring used to make a good seal with the lid of the canister. The lid was secured in place using three small allen bolts, and the threaded hole in the middle of the lid allowed the canister to be screwed onto the centrestick and then loaded into the cryofurnace.

All of the CW PND experiments presented in this thesis were carried out on D1A at the ILL with the help of Dr Clemens Ritter.

#### 2.3.3.3 Data collection

Samples were collected at approximately 6 hours per temperature per sample, thus equating to one day per sample. All of the CW PND experiments presented in this thesis were carried out on D1A at the ILL.

#### 2.3.3.4 Data analysis

The data were reduced to a GSAS compatible format at the end of the run, at the beam station. The program GSAS is used to refine the data as described by the Rietveld method in section 1.3.1.4.

## 2.4 Magnetic Measurements

The magnetic measurements were carried out using a Quantum Design MPMS SQUID (Superconducting QUantum Interference Device) magnetometer which measures the magnetic moment produced by the sample and from that the magnetic susceptibility can be calculated. A SQUID is a very sensitive magnetometer that can measure extremely small magnetic fields based on superconducting loops containing Josephson junctions, which are two superconductors linked by a non-conducting barrier allowing current to flow between them. The input current splits into the two branches and, if there is some external magnetism applied (from the sample), the current used to generate the magnetic field cancels out the external flux. Once the current in one of the branches exceeds the critical current, the loop becomes resistive and a voltage is generated across the junction. This voltage is then measured by the instrument. The SQUID is capable of measuring changes in external magnetic fields that approach $10^{-15}$ T even when operating in fields as large as 7 T.

The samples were prepared by the method described in section 1.2.2, and then ground using a mortar and pestle inside a recirculating glove box. The weight of the sample is measured and then, using a small piece of aluminium foil, it is transferred into one half of an empty medicinal gelatine capsule. The other empty half of the capsule is then inverted and pressed into the filled half. The join between the two halves is further secured using some non-magnetic Kapton tape. This tape serves a double purpose of being low-static and also it increases the width of the whole capsule. This allows the capsule to be just slightly wider than the drinking straw it is placed inside, and thus when under the vacuum will not be sucked out of the straw. The capsule is pushed half way down the straw, and then one inch of the straw is cut off the bottom, and a hole placed one inch from the top. The straw is then mounted onto the end of a sample rod, and the sample enters the loadlock in the SQUID. The sample is then evacuated and purged with clean $He_{(g)}$ and then passes through a lip seal into the sample space. Several different types of measurements are possible with the SQUID, but in the course of this thesis an M(T) scan has been performed, which is where the magnetisation of the sample is measured at a constant field but with a varying temperature. The field used was typically 100 Oe and the temperature ranged

from 4 to 200 K. For each sample, a Field Cooled (FC) and a Zero-Field Cooled (ZFC) measurement was made. A Field Cooled measurement consisted of the sample being cooled to 4 K in the field of 100 Oe and then the DC measurement being made upon warming up to 200 K. The Zero-Field Cooled measurement means cooling the sample down to 4 K in the absence of a field, and then the field is switched back on and the DC measurement taken upon warming the sample up to 200 K.

The magnetometer records the machine moment (*MM*) and this must then be corrected for the diamagnetic contributions of the gelatine capsule (*GC*). The correction can be done using the formula below:

$$GC = \left(\left(-1.8 + 1.83/T\right) \times 10\text{^}{-8}\right) \times H \times GCW / 0.0434 \qquad \textbf{2.22}$$

where, *T* is the temperature, *H* is the field and *GCW* is the weight of the gel-cap. The correction for the gelatine capsule alone could be found also by just running the empty gel-cap under normal experimental conditions. The sample machine moment (M), i.e. the magnetisation of the sample only, is then found by:

$$M = MM - DC \qquad \textbf{2.23}$$

The gram magnetic susceptibility, $\chi_g$, and molar magnetic susceptibility, $\chi_m$, are then found by:

$$\chi_g = \frac{M}{H \times SW} \qquad \textbf{2.24}$$

$$\chi_m = \chi_g \times MW \qquad \textbf{2.25}$$

where, *SW* is the sample weight and *MW* is the molecular weight. At this point a diamagnetic correction needs to be made for any ligands, non-magnetic atoms and also the (paired) lower shell electrons of the magnetic atoms. This is done using standard tables of constants, known as Pascal's constants, and are then subtracted from $\chi_m$. This then gives the corrected $\chi_m$, and from this the effective magnetic moment, $\mu_{eff}$, can also be found:

$$\mu_{eff} = \sqrt{3kCN/T} \qquad \textbf{2.26}$$

$$\mu_{eff} = 2.828(\chi_m T)^{1/2} \qquad \textbf{2.27}$$

For the equations above, *k* is Blotzmann's constant and *N* is Avogadro's number and plots of the reciprocal of the corrected molar susceptibility versus temperature can be made to confirm what types of magnetic behaviour are present, such as Curie law magnetic behaviour, whereby the susceptibility changes as a function of the Curie constant, *C*, divided by the temperature, *T*:

$$\chi = \frac{C}{T} \qquad \textbf{2.28}$$

Materials with transition metals could also display Curie-Weiss law which then also includes the Weiss constant $\theta$:

$$\chi = \frac{C}{T - \theta} \qquad \textbf{2.29}$$

The inclusion of this constant indicates that there is some interaction between the adjacent spins of the material, which could arise in ferro- or antiferro-magnetism at low temperatures. The temperature at which this change occurs is called the Curie temperature, $T_c$, when the transition is to a ferromagnetic state, and the Néel temperature, $T_N$, when the transition is to an antiferromagnetic state.

Once the effective magnetic moment is known, it can be compared to the known spin-only magnetic moment for transition metal ions. Ions can have both spin and orbital contributions to their overall magnetism, and the spin of an electron arises from it spinning on its axis and has a spin magnetic moment, $\mu_s$:

$$\mu_s = g\sqrt{s(s+1)} = 1.73BM\ , \qquad \textbf{2.30}$$

where:

$$1BM = \frac{eh}{4\pi mc} = 9.2732 \times 10^{-24}\, Am^2 \qquad \textbf{2.31}$$

where, *s* is spin of ½, *e* is the charge on one electron, *h* is Planck's constant, m is the mass of one electron and *c* is the speed of light.

When there is more than one unpaired electron to be considered within an atom, then the total spin magnetic moment becomes:

$$\mu_S = g\sqrt{S(S+1)} \qquad \textbf{2.32}$$

In this situation, *S*, is the sum of all of the individual unpaired electron spin quantum numbers and *g* is the gyromagnetic ratio (typically ~2.00). But we also need to take into consideration the orbital angular momentum quantum number, *L*, for an ion, and then the expression becomes:

$$\mu_{S+L} = \sqrt{4S(S+1)+L(L+1)} \qquad \textbf{2.33}$$

Comparison of the $\mu_{eff}$ values to pre-determined values for each metal ion in the material can give an indication as to the oxidation state.

## 2.5 Scanning Electron Microscopy

The technique of scanning electron microscopy (SEM) is used in the course of this research to probe the surface morphology and features of the materials. In contrast to a standard microscope which uses light to image the object, electron microscopes use a focused beam of electrons. The stream of electrons is formed in the electron gun under a high vacuum and then accelerated towards the specimen with a positive electrical potential. The stream of electrons is focussed and confined into a monochromated beam using metal apertures and magnetic lenses. The sample is then irradiated by the beam causing interactions which affect the beam and these effects and interactions are then in turn transformed into an image.

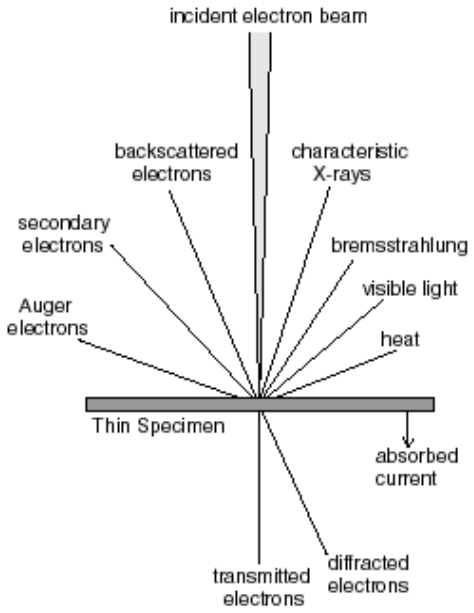


**Figure 2.7 Effects resulting from electron bombardment of a material**

In Figure 2.7 above, most of the effects that are seen at the top of the figure are inelastic effects, whereby the electron beam interacts with the electron shells of the atoms of the sample. However, the backscattering effects are considered to be elastic effects, and it is these that are utilized when examining samples for SEM. The backscattered (reflections bounced back in direction of incident beam) and secondary electrons (electrons generated as products of ionisation of the atom) are separated through the use of a detector in the sample chamber which is kept with a 10 KeV positive potential on its face, which specifically attracts the secondary electrons. A certain amount of these electrons are collected by a detector and are displayed by a cathode ray tube (CRT). Quantitative analysis of the elements present in the materials is possible through the use of Energy Dispersive X-ray analysis (EDX), whereby the energy of the electrons that are emitted by the sample are scanned and identified as the corresponding element. One drawback of using EDX is that, due to the fact it operates as a function of atomic number, it is difficult to detect lighter atoms accurately and also difficult to distinguish between elements which are similar in atomic number.

Samples were prepared by the method detailed in section 1.2.2 using a recirculating glove box as outlined in section 1.1. The samples are ground using

an agate mortar and pestle and an adhesive carbon tab is stuck onto an aluminium stub. There is a small plastic film on the top of the carbon tab, and this is removed to expose the upper adhesive part, and a small amount of the sample is sprinkled onto the tab. The stub is mounted into an SEM transporting box and a few lengths of parafilm are wound round the opening seal of the box to ensure as little contact with air as possible upon transporting the samples from the glove box to the SEM instrument. Once at the instrument, a bag is attached to a $N_{2(g)}$ cylinder, and gas is then flowed over the sample box while it is opened and the stub placed on the instruments carousel. This minimizes the effects of contact with the air.

A Philips XL30 SEM-FEG was used in the Chemistry Department of Glasgow University operating at 20 KV in high vacuum mode with a working distance of 10 mm. This was used with the assistance of Mr Jim Gallagher.

## 2.6 Electrochemical Measurements

### *2.6.1 Background*

These measurements were carried out with the use of a Swagelok-type cell, materials were synthesised by the method outlined in section 1.2.2. and measurements carried out at the Universitat Autònoma de Barcelona (UAB), in Barcelona. For the preparation of the Swagelok cells, ~10-15 mg of material is required and this includes 15 % of a carbon conductor additive. Several different types of carbon additive were used, mainly carbon sp, acetylene black and Printex.

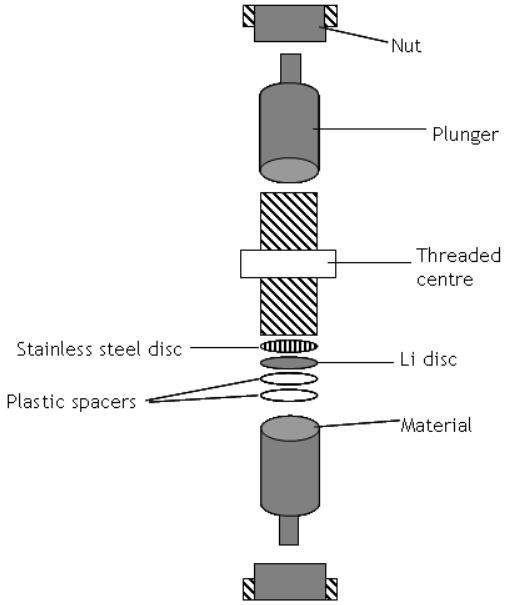


**Figure 2.8 Swagelok cell setup for electrochemical analysis**

The material (mixed with the carbon additive) is weighed inside a glass Pasteur pipette inside an argon recirculating glove box, and then placed inside one of the plungers, then the other discs are placed on top as shown in Figure 2.8. The plunger is slowly pressed down on top of the discs in order to prevent the sample jumping up and sticking to the sides, and the discs are pressed together. A few drops of $LiPF_6$ electrolyte were then added and allowed to absorb into the spacers. The whole cell is then sealed using spanners. Blanks were run of carbon additives, carbon sp, acetylene black and Printex, and also the active material to gauge their lithium insertion properties.

### *2.6.2Data collection*

The cells are connected to a potentiostat and run for C/20 sweeps, where 1/20 of the total capacity is discharged within an hour and thus would take 20 hours for a full discharge of the capacity, between 0 V and 2 V typically. All work was carried out with the help of Dr Rosa Palacin and Dr Frederic Gillot.

### *2.6.3Data analysis*

The data that was output from the potentiostat was converted on the instrument PC into a format for which it could be used for further analysis and manipulations. Analysis of the data and the graphical outputs produced were done using the program Kaleidagraph 3.52[17].

## 2.7 Pressure-Composition-Temperature Analysis

### *2.7.1Background*

These measurements were carried out in-house at the Department of Chemistry, The University of Glasgow using a PCTPro2000 from Setaram. The basis of this instrument is that it operates based on the Sievert's method of volumetric gas adsorption. The principle of the method is that a sample of known quantity is loaded and sealed within a sample vessel, and this vessels dead space is then measured using $He_{(g)}$. Once this is known, and the environment is connected to a reservoir of known volume of $H_{2(g)}$, the sample is heated to the required temperature. Once it achieves this temperature the valve is opened and the material adsorbs the hydrogen gas. The difference between the volume of gas in the hydrogen reservoir before and after can be calculated and the difference is the volume of gas that has been taken up by the sample. Figure 2.9 below shows the setup of the sample holder for the purposes of these experiments.

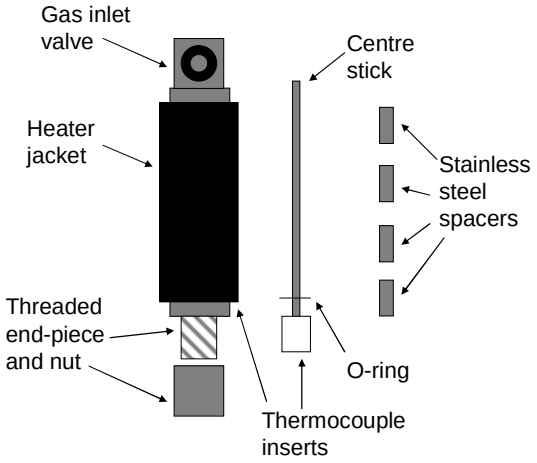


**Figure 2.9 PCTPro 2000 analysis sample holder configuration.**

In order to prepare a sample for the purpose of these experiments, all of the equipment above was loaded into the nitrogen recirculating glovebox after it had been cleaned and purged and gassed in the transfer port for 3 cycles. The materials were then brought into the glovebox, the correct weight of the preferred material weighed out, typically 200 – 300mg, and this was then ground finely using an agate mortar and pestle. The spacers were then placed on the centre stick with the O-ring at the bottom, and then loaded up through the bottom of the sample vessel, and screwed into place with the nut to fasten it. The valve was then removed from the top and the sample was loaded in from the top and then any space remaining between the top of the sample and the top of the vessel was plugged with a little silica wool. The valve fitting had an O-ring placed in it and it too was secured tightly at the top, the valve tap was closed, and the entire vessel removed from the glove box ready to be attached to the instrument.

### *2.7.2 Data collection*

For the purposes of the materials studied in the course of this thesis, the samples were heated to 250 $^{o}$C and the hydrogen pressure that was used in the reservoir was 20 bar for the purposes of the kinetic adsorption of the gas. For the kinetic desorption the reservoir pressure was set at zero and the sample temperature remained the same. These adsorptions and desorptions could be carried out for as many cycles as required, but in the case of these materials the

measurement was only carried out until the material had reached gas saturation and then full desorption.

### *2.7.3Data analysis*

The data was output from the PCTpro instrument in a .raw format which could be used directly on the built-in analysis software Igor Pro 6, or alternatively for making adjustments to scales etc Microsoft excel was used.

## 2.8 References


1. L. Ouvrard, *Comptes Rendus Hebdomadaires Des Seances De L'Academie Des Sciences*, **114**, (1892), 120.
2. R. Brill, *Z. Kristallogr*, **65**, (1927), 94.
3. C. C. Addison and B. M. Davies, *Journal of the Chemical Society A - Inorganic Physical Theoretical*, (1969), 1827.
4. D. H. Gregory, P. M. O'Meara, A. G. Gordon, J. P. Hodges, S. Short and J. D. Jorgensen, *Chem. Mater.*, **14**, (2002), 2063.
5. R. Juza, K. Langer and K. V. Benda, *Angew. Chem. internat. Edit*, **7**, (1968), 360.
6. R. Niewa, F. R. Wagner, W. Schnelle, O. Hochrein and R. Kniep, *Inorg. Chem.*, **40**, (2001), 5215.
7. V. W. Sachsze and R. Juza, *Zeitschrift fur Anorganische Chemie*, **259**, (1949), 278.
8. W. H. Bragg, *Proceedings of the Royal Society of London Series a-Containing Papers of a Mathematical and Physical Character*, **89**, (1913), 246.
9. W. H. Bragg and W. L. Bragg, *Proceedings of the Royal Society of London Series a-Containing Papers of a Mathematical and Physical Character*, **88**, (1913), 428.
10. H. M. Rietveld, *Acta Crystallographica*, **22**, (1967), 151.
11. H. M. Rietveld, *J. Appl. Crystallogr.*, **2**, (1969), 65.
12. W. Kraus and G. Nolze, Federal Institute for Materials Research and Testing, Berlin, Editon edn., 2000.
13. D. A. Fletcher, R. F. McMeeking and D. Parkin, *J. Chem. Inf. Comput. Sci.*, **36**, (1996), 746.
14. A. C. Larson and R. B. V. Dreele, Los Alamos National Laboratory Report LAUR 86-748, Los Alamos, Editon edn., 2004.
15. R. A. Young, *The Rietveld Method*,43-54, Oxford University Press, Oxford, 1995.
16. A. C. Hannon, *Nuclear Instruments and Methods in Physics Research A*, **551**, (2005), 88.

17. S. software, Synergy software, Reading, Editon edn., 2002.

# 3. Lithium nitridocobaltates

## 3.1 Introduction

As previously discussed in chapter 1, α-$Li_3N$ has a hexagonal structure which consists of a nitrogen atom bonded to six lithium atoms in a plane, and a further two lithium atoms in a plane above and below. This leads to hexagonal bipyramidal polyhedra which are edge sharing and [$Li_2N$] planes perpendicular to the *c*-axis. It was discovered that transition metals could be substituted into this structure forming nitridometallates of the general formula, $Li_{3-x}M_xN$ (where M is either Mn, Fe, Co, Ni or Cu), and that the substitution predominantly occurred with the interplanar lithium, Li(1), at the apices of the bipyramids rather than Li(2) as can be seen in Figure 3.1 below[1].

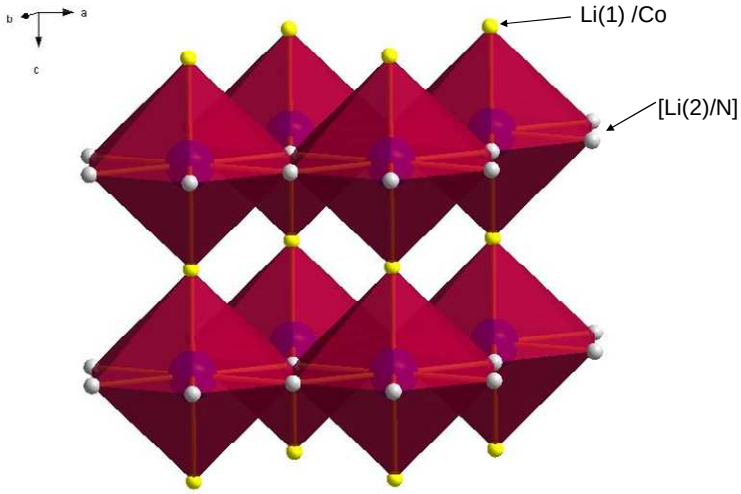


**Figure 3.1 Polyhedral representation of $Li_{3-x}M_xN$, ruby polyhedra centred by blue spheres representing nitrogen ions, white spheres representing intraplanar lithium ions and yellow spheres representing interplanar lithium or transition metal ions.**

As can be seen, substitution of these metals occurs with retention of the lithium nitride structure. In addition to isovalent substitution of the transition metals, i.e. replacement of $Li^+$ with $M^+$, the lithium nitride structure has been found to

be retained when aliovalent substitution occurs, i.e. when $Li^+$ is substituted by $M^{2+}$.

Lithium nitride was shown to display some anomalous properties, such as its colour and ionic conductivity[2-3], and it was these anomalous properties that spawned further research into the structure and bonding of the nitride and the nitridometallates.

The nitridometallates have been synthesised via a number of ways[4-6], with methods such as reacting the transition metal nitride with the lithium nitride in high temperature reactions, nitriding of a Li-M alloy, reaction of lithium nitride with transition metal powder at high temperatures and reaction of $Li_3N$ with a foil of the transition metal. The one most often reported is the reaction of the lithium nitride powder with transition metal powder at elevated temperatures.

It had been found that substitution of transition metals for the interlayer lithium atoms gave rise to structural behaviours that followed trends. It was found that with increasing the transition metal content, the *a*-parameter of the unit cell increases, and concurrently the *c*-parameter decreases and this was found to be consistent across all the nitridometallates. This can be seen in Figure 3.2 below[7].

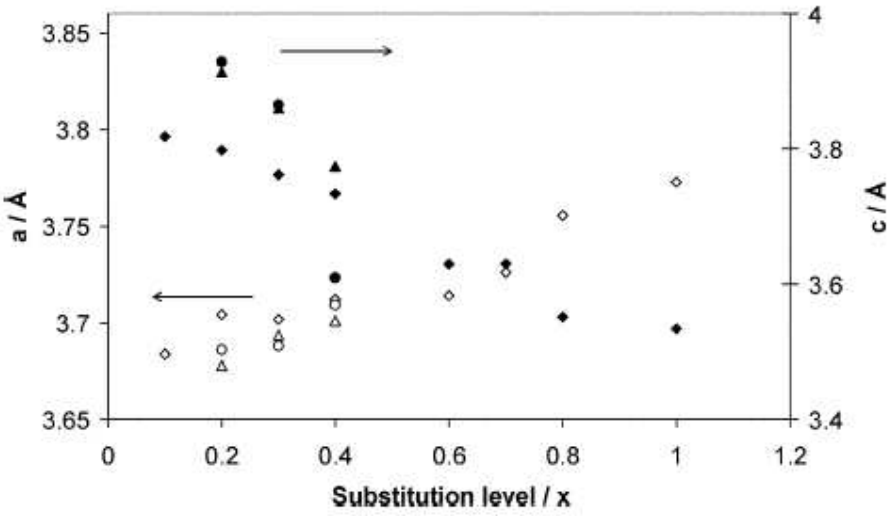


**Figure 3.2 Variations of unit cell parameters with transition metal substitution level for $Li_{3-x}M_xN$. Cu is represented by triangles, Co by circles and Ni diamonds. Full symbols represent *c*-parameter and empty symbols represent *a*-parameters[7].**

In addition to the structural effects that metal doping of lithium nitride with transition metals has on lithium nitridometallates, the effects on the physical properties of the materials has also drawn a great deal of interest. Some of the properties of these materials which have gained the most interest are their magnetic susceptibilities, ionic conductivities and hydrogen storage properties.

Gordon *et al* carried out a comprehensive structural and magnetic study into defective lithium nitridocobaltate materials[8]. Two materials $Li_{1.99}Co_{0.53}N$, and $Li_{1.95}Co_{0.6}N$ were synthesised producing single crystals of the former and bulk material of the latter. Both materials were investigated by powder neutron diffraction (PND) and the substitution levels of the transition metals and levels and location of the $Li^+$ vacancies were accurately assigned by Rietveld refinement against the data. The data from XRD and PND seemed to suggest that there were appreciable vacancies within the $[Li_2N]$ planes, and from the refinements it appeared that the number of vacancies approached a similar number to that of the transition metal occupancies. This appeared to suggest that aliovalent substitution was occurring and the stoichiometries could be refined closely to the general formulation $Li_{3-2x}Co_xN$.

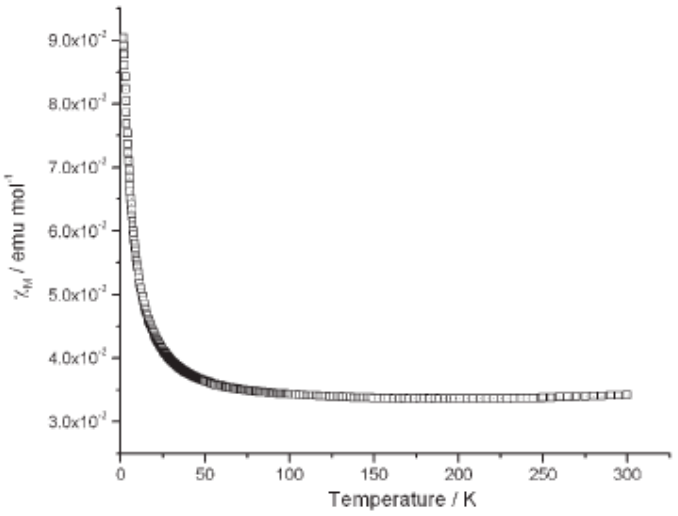


**Figure 3.3 Plot of molar magnetic susceptibility versus temperature for $Li_{1.99}Co_{0.53}N$[8].**

These materials were investigated for their magnetic susceptibilities and variable temperature measurements were carried out as can be seen in Figure 3.3 between temperatures of 2 and 300 K. From 300 to 100 K there was only small temperature dependence to the magnetic susceptibility. Below this

temperature a Curie tail was observed and the whole curve was fitted to a modified Curie-Weiss expression with values of $\chi_0$ = 0.0331(2) emu mol$^{-1}$, $C_M$ = 0.202(2) emu mol$^{-1}$ K and $\theta$ = 1.000(9) K. The $\chi_0$ value appears to suggest that there is a Pauli paramagnetic contribution to the magnetisation and delocalisation of the electrons gives infinite chains of (Li,Co)N in the direction of the *c*-axis. This type of behaviour is similar to that observed in nickel systems[9]. The localised magnetic moment on each cobalt atom is actually larger than that observed for Ni but less than that of Fe in the iron system where the large moment is thought to originate from a larger orbital contribution to the electron spin[10-11].

Another property of nitridocobaltates that has become of particular interest is their electrochemical properties as outlined in section 1.3.1.2, most importantly their ability to store $Li^+$ for potential application as an electrode. Within this series of nitridometallates, the material which has gained most attention due to its electrochemical performance has been $Li_{2.60}Co_{0.40}N$. The nitride has a high specific capacity of 760 mA h g$^{-1}$ which is more than double that of the theoretical capacity of $C_6Li$, 372 mA h g$^{-1}$ [12-13]. The material appeared to shift from a crystalline to amorphous state upon extracting lithium which was thought to be a rearrangement of the elements and this new arrangement was associated with the consequent cycles.

Improvements have been made to the capacity and cyclability in the last decade[14-15] and improvements to the capacity of the material have been achieved through its application in an electrochemical cell in conjunction with cathode materials which have also shown high electrochemical performance[15]. Three cells were constructed, one where a Li containing cathode material was chemically pre-extracted, $Li_{2.60}Co_{0.4}N/Li_{0.64}Mn_{1.96}O_4$, a second where a Li-free cathode was used, $Li_{2.60}Co_{0.4}N/a\text{-}Cr_3O_8$ and a third where the anode nitridometallate had a Li pre-extraction before being used with a high voltage cathode, $Li_{1.37}Co_{0.4}N/Li_{1.10}Mn_{1.90}O_4$. In the first cell, the charged cathode material is prepared by extracting lithium from $Li_{1.05}Mn_{1.95}O_4$ using $Br_2CH_3CN$ solution, and the electrochemical cells were constructed using the materials detailed above and acetylene black, Teflon binder and $LiClO_4$/PC+DME electrolyte. The weight ratio of $Li_{2.60}Co_{0.4}N/Li_{0.64}Mn_{1.96}O_4$ was 1/3 (30mg/90mg)

and the cathode was found to have vacancies equivalent to 50 mAh/g. Upon the initial discharge these vacancies were entirely occupied by lithium from the anode, resulting in vacancies of 150 mAh/g in the anode. The anode material had an intrinsic vacancy equivalent to 200 mAh/g after synthesis, so at the stage after the first discharge the anode has a total vacancy of 350 mAh/g.

The second cell was constructed using 140 mg of the anode material and 420 mg of a-$Cr_3O_8$[16] as the cathode material. The cell was cycled over a potential range of 4.0 V - 1.8 V with a current density of 0.3 mA/$cm^2$. The first discharge of this cell gives a higher capacity and lower potential than in consequent cycles, 124.6 mAh and 2.04 V respectively, and this is thought to be due to a transformation from a crystalline state to an amorphous state. The electric current efficiency remained close to 100 % upon cycling but the energy efficiency was only ~72 %.

The third cell was constructed using the anode material from which lithium had been chemically extracted using $I_2$-PC solutions, and it was found that, as lithium was chemically extracted, there was a transformation from a crystalline state to an amorphous state, similar to the situation observed during the electrochemical extraction of lithium. The material $Li_{1.37}Co_{0.40}N$ was tested in a cell with Li as the cathode material and, in comparison to $Li_{2.60}Co_{0.4}N$, it showed reduced cyclability but similar charge/discharge behaviour. An electrochemical cell was constructed using 25 mg $Li_{1.37}Co_{0.40}N$ as the anode and 100 mg of $Li_{1.10}Mn_{1.90}O_4$ as the cathode. Deterioration of the cyclability was observed but the capacity observed was similar to that of the first cell with the lithium extracted cathode. It was suggested that $Li_{2.60}Co_{0.40}N$ could be successfully applied as an anode for lithium secondary batteries.

Experiments to improve on the cycle life of the lithium nitridocobaltates were carried out by Kang *et al*[14], and upon carrying out variable temperature syntheses of materials of the series $Li_{3-x}Co_xN$ ($0.2 \leq x \leq 0.6$), and carrying out subsequent charge-discharge measurements, it was found that $Li_{2.60}Co_{0.4}N$ which had been synthesised at 650 $^{o}$C shows the best potential operation as an anode of around 1000 mAh/g after the first cycle. The first cycle of this material shows a potential plateau in it which seemed to suggest that a structural change was occurring, and this theory was then supported when XRD analysis of the material was carried out at different stages of lithium extraction. The XRD patterns

shifted from a defined crystalline pattern to an amorphous pattern. In addition to its high capacity, this material also showed an initial coulometric efficiency of 96% and its rate capability at rate of 1.0*C* was found to be 94.94% that of a 0.2*C* rate. All of these characteristics make this material a more attractive prospective commercial anode material than a conventional graphite anode, but the cycle life of the material (a capacity fade of 80 % after 20 cycles) made it unlikely to be applicable.

In order to improve the cycle-life of the material, the process by which it diminishes needed to be well understood, and whether the diminishing of the cycle life was due to structural or surface changes, as previously seen for similar materials, needed to be studied first. As the materials' XRD pattern became amorphous after the first cycle, any potential structural effects of the degradation of cycle life could not be studied this way. TEM was instead used and indicated that for the consequent cycles the material remained unchanged from that after the first cycle, i.e. amorphous, and so structural causes of the degradation were ruled out.

Resistance of the cell was found to increase as the capacity decreased upon cycling and, through SEM micrographs, this was found to be due to surface film formation. This was thought to occur due to reactions with the electrolyte upon contact and this was confirmed through IR and AES (Auger Electron Spectroscopy) whereby fluorine and phosphorus from the electrolyte were detected and carbonates also formed. It has previously been known that cycle life decay has been caused by degradation of the active components of the materials but analyses by EDX and ICP after 1 and 100 cycles show that the metal and nitrogen content of the material remain almost constant, and thus the surface film formation is thought to be the main cause of the cycle life degradation.

Previously, Lewis acidity of the transition metals has been shown to be the cause of surface film formation[14], and this lessened as the ionic radius of the metal increased and the oxidation number decreased, and as such Fe metal was a good candidate for doping the material. This appeared to have the desired effect as after the material was doped, the increase in surface resistivity was found to be less pronounced upon cycling, however there was a slight decrease in the overall

capacity of the material. The cycle life of the material was improved. However it remained too low to have a commercial application and thus further improvement of the material is required.

More recently, composite materials of $Li_{2.60}Co_{0.4}N$ and natural graphite have been made in order to try and improve on the initial coulombic effect of the graphite[17]. An increase from 69% to ~100% was achieved, along with an improvement on the cycle life of the composite anode material over that of natural graphite.

Until now, many investigations into nitridocobaltates have focussed on the maximum substitution levels, with in depth studies into the structure-property relationships arising in the resultant materials. The work contained here, however, is focussed on the structure-property effects induced by low levels of cobalt substitution in lithium nitride ( $Li_{3-x-y}M_xN$ with $x \leq 0.1$) which had previously been unstudied. Structural characterisation would be accomplished by different techniques, such as powder XRD, powder neutron diffraction (PND) and SEM. Resulting properties would be investigated through the use of SQUID magnetometry, pressure-composition isothermal investigations and also electrochemical studies. Of particular interest in these studies was to observe the oxidation state of the metal that was incorporated into the structure, and whether or not aliovalent substitution was occurring.

As has been shown in all the lithium nitridometallates with higher dopant metal levels, both time and temperature are what govern both the generation of vacancies and the level of vacancy seen[9], so if these materials are to follow this same trend then it is possible that a similar level of vacancy could be created in these low doped materials. $Li_{2.60}Co_{0.4}N$ to date has proven to be the best candidate as an anode material with a specific capacity of 760 mAh $g^{-1}$, and from the first discharge of this material it would appear that there are vacancies within it. Even for $Li_3N$, vacancy has been shown to relate to improved ionic conductivity through hydrogen doping, and therefore if the materials studied herein could have similar vacancy levels to that of $Li_{2.60}Co_{0.4}N$,then the volumetric capacity of the material could be maximised due to less heavy metal. This would then give the potential for application as anode material for lithium secondary batteries, dependant on the cycle life of the material. Similarly, the

creation of vacancies within these materials could potentially give rise to some interesting magnetism as a result of charge compensation on transition metals.

## 3.2 Lithium Cobalt Nitride

### *3.2.1 Experimental*

Polycrystalline samples of these materials were prepared through the reaction of cobalt powder (Aldrich 99.5 %) with $Li_3N$ (Aldrich ≥ 99.9% and synthesised in-house) in varying ratios in order to gauge the effects of differing metal content on these low-doped materials. These materials were synthesised by the method detailed in section 2.2.2. The ground mixed reactants were pressed into a 13 mm pellet and then placed inside a stainless steel crucible that had been sandblasted to remove any residual imperfections. In the lowest doped material, which was the first synthesised, the pellet was placed inside an alumina crucible within the stainless steel crucible in order to prevent reaction with the stainless steel, however the pellets were found to be stuck to the alumina post-reaction. All reactions were sealed in a stainless steel reaction vessel under $N_{2\,(g)}$ (99.999 %). The reactants were heated to 973 K for differing lengths of time (2 – 7 days) and the reactions were then allowed to cool by turning the furnace off and allowing the heat to dissipate. The pellets in most of the cases were dark grey with a metallic glint, and were very hard often requiring to be broken using a hammer.

For materials **[1]** and **[4]** (see Table 3.1), their magnetic behaviour was measured through the use of a SQUID (Superconducting Quantum Interference Device) magnetometer and the help of Dr Marek Jura at the ISIS facility at the Rutherford Appleton Laboratories. The samples were prepared for each measurement by the method outlined in Section 2.4 and were measured in a field of 100 Oe in each case. For these two materials, a Zero-Field Cooled (ZFC) measurement and also a Field Cooled (FC) measurement was carried out. The ZFC measurement was made by cooling the sample down to 2 K in the absence of a field and then turning the field on, and measuring the magnetisation upon warming the material to 200 K, and the FC measurement by cooling the sample

down in the presence of a 100 Oe field and then measuring the magnetisation upon warming back 200 K.

The electrochemical measurements that were performed on materials **[1]**, **[4]** and $Li_{2.60}Co_{0.4}N$ (which had been synthesised solely for the purpose of comparison reasons in the electrochemical measurements, as it was a well know successful anode material) were carried out at the Universitat Autònoma de Barcelona (UAB), in Barcelona for the Swagelok cells. The samples for these measurements were prepared by the method outlined in section 2.6, and a slow cycle rate of typically C/20 (whereby 100 % of the samples charge is consumed over a period of 20 hours) was utilised for the measurements in this Swagelok configuration. The material sample weight (~ 0.015g typically) was added to a 15 % carbon 'sp' additive in order to aid the conduction through the anode. Two polytetrafluoroethylene (PTFE) spacers were placed on top to create a space between the anode and cathode, a disc of lithium metal placed on top (cathode), followed by a stainless steel disc to create a good contact with the cell plunger. The full cell was then closed by tightening the nuts at the two ends of the cell. The cell was connected to and run on the potentiostat, with the potential cycled between 0 and 2 V typically and the resultant charge measured, and this was then corrected for the sample weight to give a weight specific capacity mAh/g.

## *3.2.2Results and Discussion*

Table 3.1 below shows the materials produced and the different reaction parameters for each.

**Table 3.1 Reaction setup and parameters for the series $Li_{3-x}Co_xN$.**

| Label | Nominal Stoichiometry | Temperature /K | Reaction Time | $Li_3N$ type |
|---|---|---|---|---|
| **[1]** | $Li_{2.95}Co_{0.05}N$ | 973 | 2 days | Aldrich |
| **[2]** | $Li_{2.90}Co_{0.1}N$ | 973 | 2 days | Aldrich |
| **[3]** | $Li_{2.95}Co_{0.05}N$ | 973 | 2 days | In-house |
| **[4]** | $Li_{2.95}Co_{0.05}N$ | 973 | 7 days | Aldrich |

Initial phase analysis was carried out by powder X-ray diffraction at room temperature on a Bruker d8 diffractometer using Cu $K_\alpha$ radiation (λ = 1.5406 Å). Patterns were analysed using PowderCell 2.4[18] with structures from the ICSD database. Typical observed and calculated patterns are shown in Figure 3.4 below.

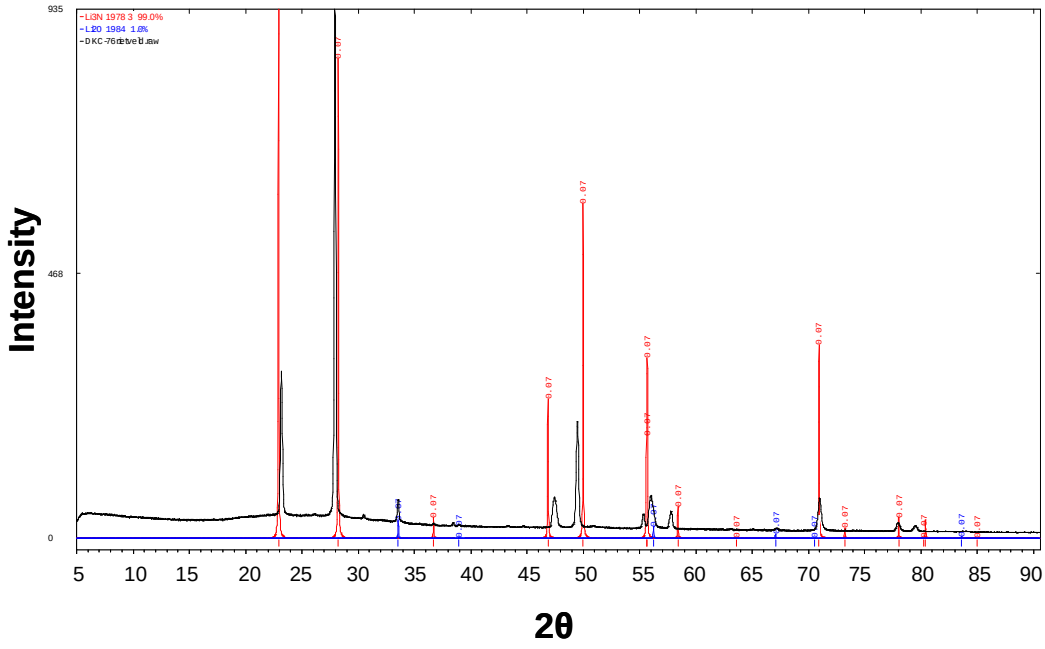


**Figure 3.4 XRD pattern of $Li_{2.90}Co_{0.1}N$ [2] (black) referenced against $Li_3N$ (red) and $Li_2O$ (blue).**

As can be seen from Figure 3.4 the X-ray diffraction pattern measured from sample **[2]**, of nominal stoichiometry $Li_{2.90}Co_{0.1}N$ which had been reacted for 2 days, is slightly shifted from the pattern of $Li_3N$[19] with an impurity phase of $Li_2O$ and this was the same for all four of the samples and a $Li_2NH$ impurity in **[2]** which became evident later. The observed shift in the peaks of the XRD measured nitride phase from the reference $Li_3N$ pattern is most likely due to the metal substitution.

Unit cell refinement of the measured XRD pattern against that of the reference pattern for $Li_3N$ was carried out using CELREF[20-21] and the calculated cell parameters for this material along with that of the reference material can be found in Table 3.2 below.

**Table 3.2 Comparison of cell parameters of $Li_3N$[19], $Li_{2.95}Co_{0.05}N$ [1], $Li_{2.90}Co_{0.1}N$ [2] and $Li_{2.95}Co_{0.05}N$ [3].**

| Material | a /Å | c /Å | V /Å$^3$ |
|---|---|---|---|
| $Li_3N$ | 3.648(1) | 3.875(1) | 44.66 |
| $Li_{2.95}Co_{0.05}N$ **[1]** | 3.673(5) | 3.857(1) | 45.06 |
| $Li_{2.90}Co_{0.1}N$ **[2]** | 3.682(3) | 3.832(1) | 44.99 |
| $Li_{2.95}Co_{0.05}N$ **[3]** | 3.667(4) | 3.8615(7) | 44.97 |

As can be seen from these parameters, there is an increase in the *a* parameter and a decrease in the *c* parameter compared to $Li_3N$, and this has previously been shown to be due to an increase in the covalent character of the Li(1)/M-N bond[22] upon substituting transition metal for the alkali metal, due to the larger ionic radii of transition metals ($Co^+$ 0.98 Å) in comparison to lithium ($Li^+$ 0.59 Å)[23]. Previous papers have indicated a linear relationship between the unit cell parameters and the metal substitution levels for lithium nitridometallates[7, 24], with a continuous increase of *a* and decrease of *c*-parameter with increasing metal content. Interestingly there appears to be a difference between the cell parameters for **[1]** and **[3]** where the only difference was the source of the $Li_3N$ starting material where **[1]** is synthesised with Aldrich $Li_3N$ which contains both alpha and beta phases of the nitride. **[3]** was synthesised using in-house synthesised $Li_3N$ which was all alpha phase. This could indicate that the nature of the starting material affects the structure of the final material but at this stage the refined site occupancies for the transition metals are not known, and so the effect of a longer *c*-parameter and a shorter *a*-parameter may be due to there being less cobalt present in **[3]**. Due to there being a lower cobalt content for these materials than in previously researched lithium nitridometallates, the unit-cell parameter change is less pronounced, but fits well with the previous trends.

As these materials contain late transition metals, quite often a high background was observed in the powder X-ray diffraction patterns from Cu $K_\alpha$ radiation due to fluorescence. This is due to the X-ray absorption wavelength for the transition metals being similar to that of the X-ray source. In order to overcome this problem powder neutron diffraction was utilised as this does not operate as a

function of atomic weight and so fluorescence of transition metals was not observed.

### *3.2.3 Constant-wavelength neutron diffraction*

Constant wavelength measurements were performed on D1A with the help of Dr Clemens Ritter at the ILL (Institut Laue Langevin) facility in Grenoble (section 2.3.4), which is a high flux powder neutron instrument. The samples were loaded into a 13 mm vanadium can and were then sealed using purpose-made copper gaskets (mp.1357.77 K). As the temperatures of these reactions were to reach 483 K, these gaskets were preferential to traditional indium wire seals (mp.429.75 K). In order to perform the measurements at variable temperatures, the use of a cryostat and cryofurnace was employed.

Rietveld refinement of the constant wavelength data was carried out using GSAS (General Structure Analysis System) through the Expgui interface[25]. Data were collected and the histogram was loaded in GSAS. The starting model was based upon that of the starting material, $Li_3N$, with the transition metal placed on the Li(1) shared site. The occupancies of the shared site were initially set at fixed values that reflect the nominal stoichiometry of the synthesised material. The background was fitted using function type 8 (a linear interpolation formula with greater partitioning at lower d-spacing) other than at 70 K in **[1]** and **[3]** where the background was fitted graphically. Peak profiles were fitted using function 4 (convolution of a pseudo-Voigt and asymmetry function along with microstrain broadening) and the lattice parameters were allowed to vary. Once the refinement stabilised, the fractional occupancies of the Li and the Co shared site were varied (while constrained to be equivalent, and the temperature factors were constrained to be the same), followed by the temperature factors of the shared site and finally the temperature factors of the remaining two atoms. The presence of $Li_2O$ impurity was noted in both materials and an additional $Li_2NH$ impurity in **[2]**. At this stage, the occupancy of the Li(2) site was allowed to vary freely and, in these materials, the occupancy settled at a value just above 1 and so the site occupancy factor (SOF) was set as 1. Finally, anisotropic temperature factors were introduced into the model, firstly for the constrained shared site, then the Li(2) site and finally for the nitrogen atom. Selected refinement data

and unit cell data from the refinements can be seen below in Table 3.3 and Table 3.4 and selected OCD (Observed-Calculated-Difference) plots can be seen in Figure 3.5-Figure 3.10. All OCD plots for materials at each temperature and full refinement data are included in the appendix.

**Table 3.3 Atomic parameters from Rietveld refinement of CW PND data for the series Li3-xCuxN. *occ denotes site occupancy. $U_{11} = U_{22} = 2U_{12}$; $U_{13} = U_{23} = 0$. Li occ = 1 – Co occ.**

| | $Li_{2.95}Co_{0.05}N$ **[1]** | $Li_{2.90}Co_{0.1}N$ **[2]** | $Li_{2.95}Co_{0.05}N$ **[3]** |
|---|---|---|---|
| **Space group** | P6/*mmm* (No. 191) | | |
| **Temperature /$^{o}$K** | 298 | 298 | 298 |
| **Calculated density, ρ/ g cm$^{-3}$** | 1.351 | 1.482 | 1.382 |
| ***a* / Å** | 3.6709(1) | 3.6805(1) | 3.6652(1) |
| ***c* / Å** | 3.8548(2) | 3.8343(2) | 3.8608(2) |
| ***V* / Å$^3$** | 44.985(4) | 44.981(4) | 44.916(3) |
| **Li(1)/M-N / Å** | 1.92737(9) | 1.91716(10) | 1.93040(8) |
| **Li(2)-N / Å** | 2.11950(6) | 2.12504(8) | 2.11621(6) |
| | Li(1)/M (1b) (0,0,0.5) | | |
| **Co occ*** | 0.034(9) | 0.102(10) | 0.049(9) |
| **100 x $U_{11}$/Å$^2$** | 1.94(17) | 2.19(28) | 1.86(19) |
| **100 x $U_{12}$/Å$^2$** | 0.97(8) | 1.06(14) | 0.93(10) |
| **100 x $U_{33}$/Å$^2$** | 0.17(25) | 0.58(36) | 0.43(26) |
| | Li(2) (2c) (3/8,1/3,0) | | |
| **occ*** | 1.000 | 1.000 | 1.000 |
| **100 x $U_{11}$/Å$^2$** | 1.35(13) | 1.82(17) | 1.54(12) |
| **100 x $U_{12}$/Å$^2$** | 0.68(7) | 0.91(8) | 0.77(6) |
| **100 x $U_{33}$/Å$^2$** | 2.79(27) | 3.14(35) | 1.86(23) |
| | N (1a) (0,0,0) | | |
| **occ*** | 1.000 | 1.000 | 1.000 |
| **100 x $U_{11}$/Å$^2$** | 0.48(3) | 0.47(4) | 0.73(3) |
| **100 x $U_{12}$/Å$^2$** | 0.24(2) | 0.24(2) | 0.37(2) |
| **100 x $U_{33}$/Å$^2$** | 0.41(5) | 0.74(6) | 0.67(5) |

**Table 3.4 Selected data from GSAS refinement of CW powder neutron diffraction for $Li_{2.95}Co_{0.05}N$ [1], $Li_{2.90}Co_{0.1}N$ [2] and $Li_{2.95}Co_{0.05}N$ [3].**

| Nominal Stoichiometry | Refined stoichiometry | Temp /K | Co | $wR_p$ | $R_p$ | $\chi^2$ |
|---|---|---|---|---|---|---|
| $Li_{2.95}Co_{0.05}N$ **[1]** | $Li_{2.95}Co_{0.05}N$ **[1]** | 70 | 0.032(8) | 0.0556 | 0.0514 | 2.212 |
| | | 298 | 0.034(9) | 0.0543 | 0.0474 | 1.870 |
| | | 389 | 0.037(10) | 0.0560 | 0.0466 | 1.803 |
| | | 483 | 0.032(11) | 0.0555 | 0.0438 | 1.763 |
| $Li_{2.90}Co_{0.1}N$ **[2]** | $Li_{2.90}Co_{0.1}N$ **[2]** | 70 | 0.093(9) | 0.0540 | 0.0426 | 1.917 |
| | | 298 | 0.102(10) | 0.0540 | 0.0435 | 1.970 |
| | | 388 | 0.108(11) | 0.0491 | 0.0388 | 1.694 |
| | | 482 | 0.109(12) | 0.0456 | 0.0361 | 1.476 |
| $Li_{2.95}Co_{0.05}N$ **[3]** | $Li_{2.95}Co_{0.05}N$ **[3]** | 70 | 0.044(8) | 0.0655 | 0.0510 | 3.480 |
| | | 298 | 0.049(9) | 0.0641 | 0.0495 | 3.407 |
| | | 393 | 0.058(9) | 0.0618 | 0.0487 | 3.160 |
| | | 493 | 0.038(10) | 0.0698 | 0.0556 | 2.919 |

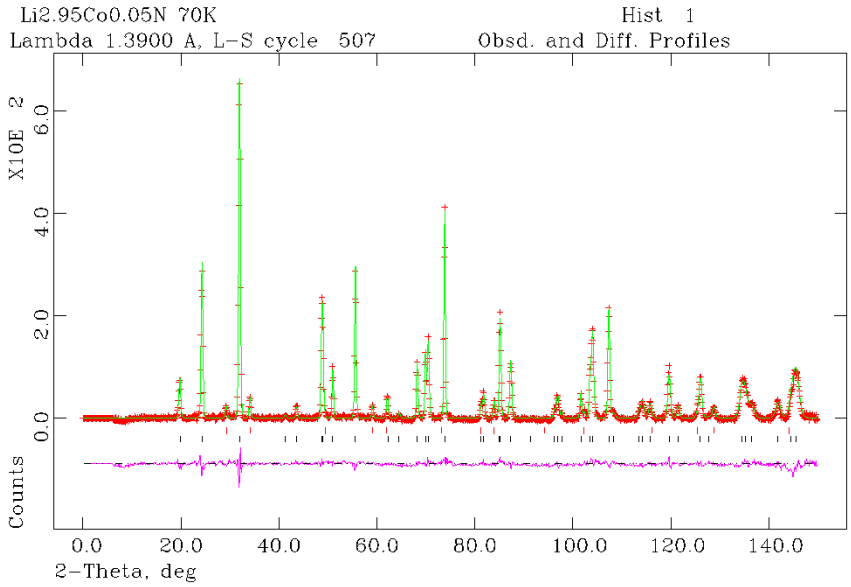


**Figure 3.5 OCD plot from GSAS Rietveld refinement of CW PND data for [1] at 70 K. Observed data is in red, calculated in green and the difference of the two profiles shown in pink. The nitride-type phase is assigned blue tickmarks and lithium oxide impurity phase red tickmarks.**

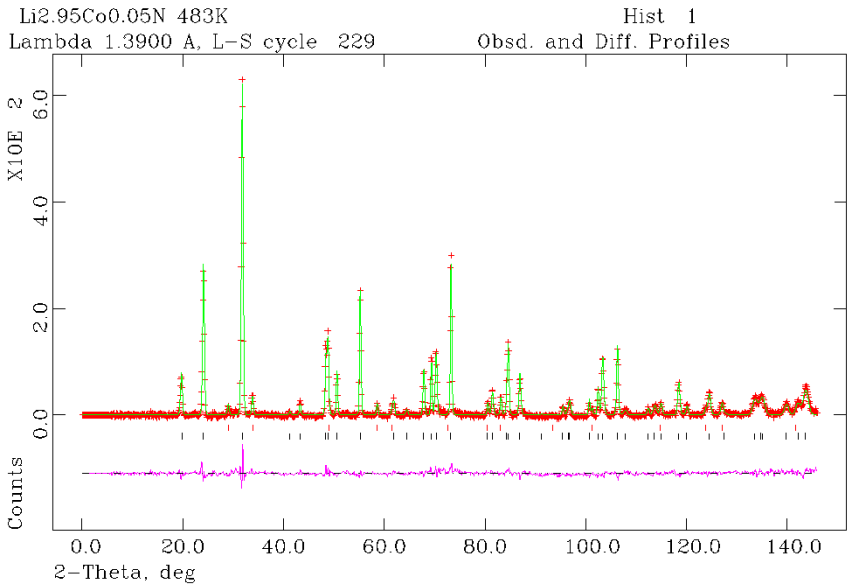


**Figure 3.6 OCD plots from GSAS Rietveld refinement of CW PND data for [1] at 483 K. Observed data is in red, calculated in green and the difference of the two profiles shown in pink. The nitride-type phase is assigned blue tickmarks and lithium oxide impurity phase red tickmarks.**

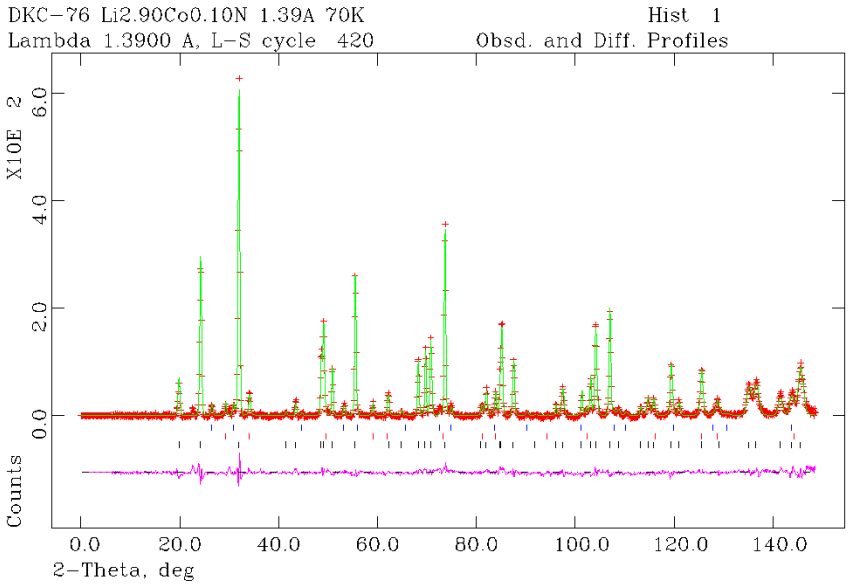


**Figure 3.7 OCD plots from GSAS Rietveld refinement of CW PND data for [2] at 70 K. Observed data is in red, calculated in green and the difference of the two profiles shown in pink. The nitride-type phase is assigned black tickmarks, lithium oxide impurity phase red tickmarks and lithium imide Impurity phase blue tickmarks.**

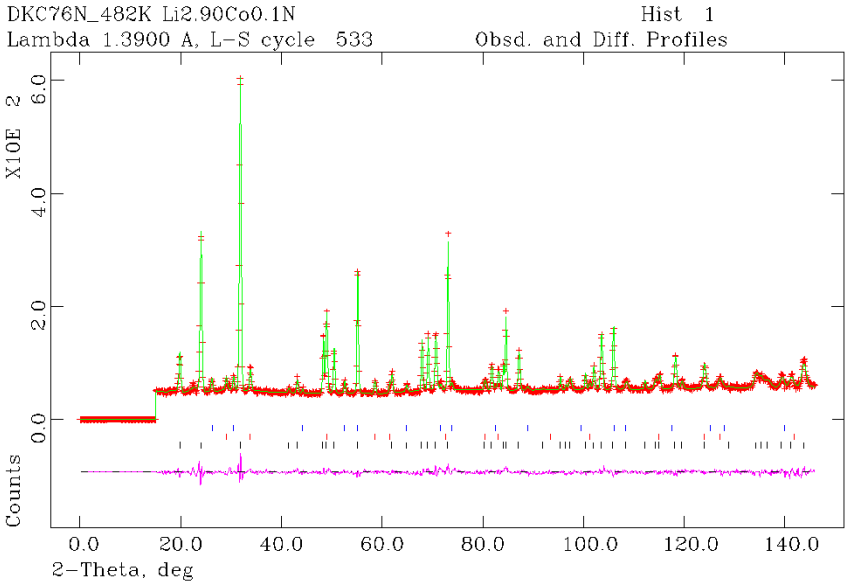


**Figure 3.8 OCD plots from GSAS Rietveld refinement of CW PND data for [2] at 482 K. Observed data is in red, calculated in green and the difference of the two profiles shown in pink. The nitride-type phase is assigned black tickmarks, lithium oxide impurity phase red tickmarks and lithium imide impurity phase blue tickmarks.**

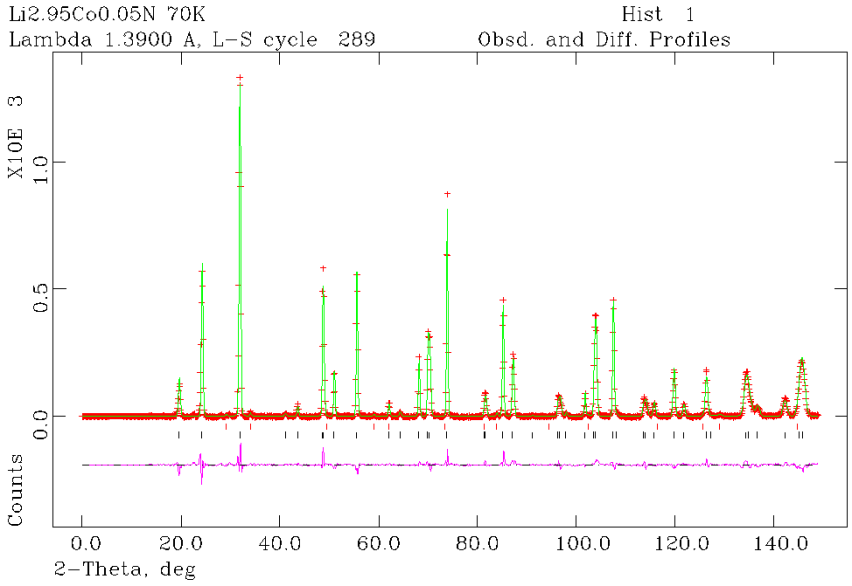


**Figure 3.9 OCD plots from GSAS Rietveld refinement of CW PND data for [3] at 70 K. Observed data is in red, calculated in green and the difference of the two profiles shown in pink. The nitride-type phase is assigned blue tickmarks and lithium oxide impurity phase red tickmarks.**

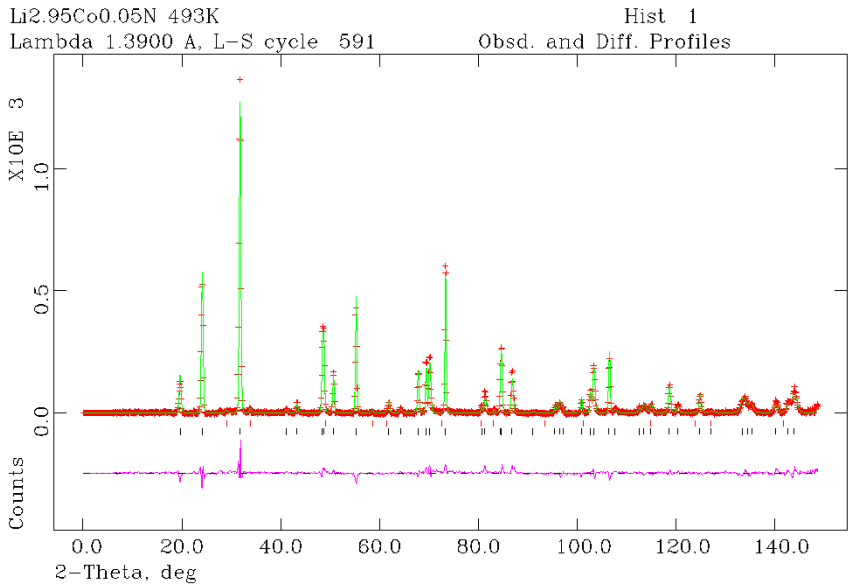


**Figure 3.10 OCD plots from GSAS Rietveld refinement of CW PND data for [3] at 493 K. Observed data is in red, calculated in green and the difference of the two profiles shown in pink. The nitride-type phase is assigned blue tickmarks and lithium oxide impurity phase red tickmarks.**

For all three of the materials, **[1]**, **[2]** and **[3]** the refinement indicates that they retain the $Li_3N$-type structure, and they refine across all four temperatures to be in accordance with the nominal stoichiometry, as at each temperature the cobalt site occupancy is within 3 x $\sigma$, which is the test for errors on a value.

From the refinement data in Table 3.3 and Table 3.4 it can be seen that the trends expected from the higher-doped materials[7], are seen from these materials at the lower-doped end of the scale. There is an overall decrease in *c*-parameter upon substituting more cobalt metal, and subsequently resulting in a lengthening of the *a*-parameter. However, the situation seen previously from the unit cell refinement of the materials using CELREF is still observed in the refined PND data, namely that materials **[1]** and **[3]** have different unit cell parameters despite being of the same nominal stoichiometry. This is made even more unexpected by that fact that for the two materials it is the one which has the lowest refined cobalt occupancy that is displaying the shortest *c*-parameter, **[1]**, whereas the converse would be expected. This would appear to suggest that the use of in-house synthesised lithium nitride as a reactant may be having an effect on the resultant structural characteristics of the product material. An observation that can be made from the OCD plots for the three materials is that

the difference plot for **[3]** is much flatter than that of the other two, and this is most likely to have arisen as a direct result of the in-house synthesised $Li_3N$ being much more crystalline, however the statistics for the Rietveld refinement do not reflect this. This is likely to be a consequence of the flatness of the background for **[3],** as when there are any small peaks on such a clean background, it becomes harder to fit the background to it in comparison to a noisy background, in which some small peaks would be lost, and the fit of the data would then be easier and the statistics would reflect so.

From the temperature factors it can be seen that the values of Li(2) show anisotropy of the temperature factors, and these are comparable with that of $Li_3N$[19] itself and of other lithium nitridometallates which have been studied[8, 26]. What is seen for these materials is that material **[1]** shows the greatest degree of elongation parallel to the *c*-axis, with **[2]** slightly less pronounced, and **[3]** shows almost isotropy to its temperature factors. This would suggest that for **[1]** and **[2]** there could be $Li^+$ mobility within the $[Li_2N]$ plane comparable to that of $Li_3N$. Figure 3.11 shows a comparison of all 3 materials with $Li_3N$[19].

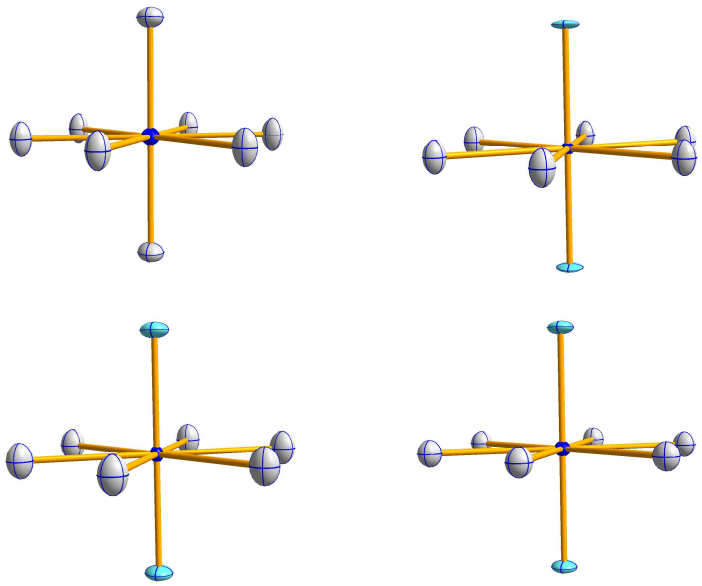

**Figure 3.11 50 % probability thermal ellipsoids for (moving clockwise from top left) $Li_3N$, $Li_{2.95}Co_{0.05}N$ [1], $Li_{2.90}Co_{0.1}N$ [2] and $Li_{2.95}Co_{0.05}N$ [3]. White ellipsoids represent lithium ions, blue ellipsoids represent nitrogen ions, and light blue ellipsoids represent Li(1)/M ions.**

Importantly, an observation that can be made is that there was no presence of any vacancies at the Li(2) site for any of the three materials. Vacancies in these materials have been previously shown to depend heavily on the temperature and time of reaction[9], and as there appears to be no vacancies in these materials, the length of reaction in this particular case was thought to be the basis. In order to gauge if this was in fact the case a second sample of $Li_{2.95}Co_{0.05}N$ was synthesised only this time extending the length of time for the reaction from 2 to 7 days. Temperature and all other reaction conditions were kept as they previously had been.

### *3.2.4 Time of Flight neutron diffraction*

Initial characterisation of the material was again carried out by powder X-ray diffraction at room temperature on a Bruker d8 diffractometer using Cu $K_\alpha$ radiation ($\lambda$ = 1.5406 Å) and with PowderCell 2.4[18] to analyse powder patterns. The measured diffraction pattern matched well to a shifted $Li_3N$ pattern and there was presence of ~1 % $Li_2O$ impurity also.

ToF (Time of Flight) powder neutron diffraction measurements were made on this material using the instrument GEM at ISIS facility at the Rutherford Appleton Laboratories with the help of Dr Ron I. Smith. ~ 2.0g of sample was placed inside a 6 mm vanadium can and the height marked on the can in order to align with the centre of the beam. The can was sealed using allen bolts and a small circle of indium wire to form a seal as the measurements were only to be carried out at room temperature. Rietveld refinement of the ToF data was once again carried out using GSAS (General Structure Analysis System) through the Expgui interface[25].

The starting model was based upon that of the starting material, $Li_3N$, with the transition metal placed at the Li(1) shared site. The occupancies of the shared site are initially set at fixed values that reflect the nominal stoichiometry of the synthesised material. Only the 3 highest angle banks of data were loaded in as separate histograms and the unit cell parameters and scale factor were refined initially across all of the three of the histograms in the same way. The background was refined using function type 7 (linear interpolation function) and 12 terms for bank 6 but 8 terms for the other two banks. The peak shapes were

then refined separately for each histogram using peak shape type 2 (Ikeda-Carpenter function with pseudo-Voigt convolution) for both the main phase and the impurity phase. Once the fit seemed to appear stable, the temperature factors were constrained and were refined isotropically along with the fractional occupancies of the shared site. Further terms for the peak shape were then introduced and the fractional occupancy of the Li(2) site was then allowed to vary freely. A term for sample absorption was introduced at this stage and finally the anisotropic temperature factors for all of the atoms were refined. Some selected refinement data for this material can be seen in Table 3.5, with Table 3.3 as a comparison. Full refinement data will be found in the appendix.

**Table 3.5 Atomic parameters from Rietveld refinement of ToF PND of $Li_{2.95}Co_{0.05}N$ [4]. *occ denotes site occupancy. $U_{11} = U_{22} = 2U_{12}$; $U_{13} = U_{23} = 0$. Li occ = 1 – Co occ.**

| | | $Li_{2.95}Co_{0.05}N$ **[4]** |
|---|---|---|
| **Refined stoichiometry** | | $Li_{2.781}Co_{0.055}N$ **[4]** |
| **Space group** | | P6/*mmm* (No.191) |
| **Temperature /°K** | | 298 |
| **Calculated density, ρ/ g cm$^{-3}$** | | 1.355 |
| ***a* / Å** | | 3.66371(6) |
| ***c* / Å** | | 3.85213(8) |
| ***V* / Å$^3$** | | 44.779(2) |
| **w$R_p$** | | 0.0318 |
| **$R_p$** | | 0.0344 |
| $\chi^2$ | | 3.026 |
| **Li(1)/M-N / Å** | | 1.92607(4) |
| **Li(2)-N / Å** | | 2.11524(3) |
| **Li(1)/M (1b) (0,0,0.5)** | **Co occ*** | 0.055(3) |
| | **100 x $U_{11}$/Å$^2$** | 1.94(7) |
| | **100 x $U_{12}$/Å$^2$** | 0.97(3) |
| | **100 x $U_{33}$/Å$^2$** | 0.75(8) |
| **Li(2) (2c) (3/8,1/3,0)** | **occ*** | 0.918(6) |
| | **100 x $U_{11}$/Å$^2$** | 1.20(5) |
| | **100 x $U_{12}$/Å$^2$** | 0.60(2) |
| | **100 x $U_{33}$/Å$^2$** | 3.13(8) |
| **N (1a) (0,0,0)** | **occ*** | 1.000 |
| | **100 x $U_{11}$/Å$^2$** | 0.819(8) |
| | **100 x $U_{12}$/Å$^2$** | 0.410(4) |
| | **100 x $U_{33}$/Å$^2$** | 1.09(4) |

Figure 3.12, Figure 3.13 and Figure 3.14 below show the OCD plots for the refinements of the three higher angle histograms from the ToF data for **[4]**.

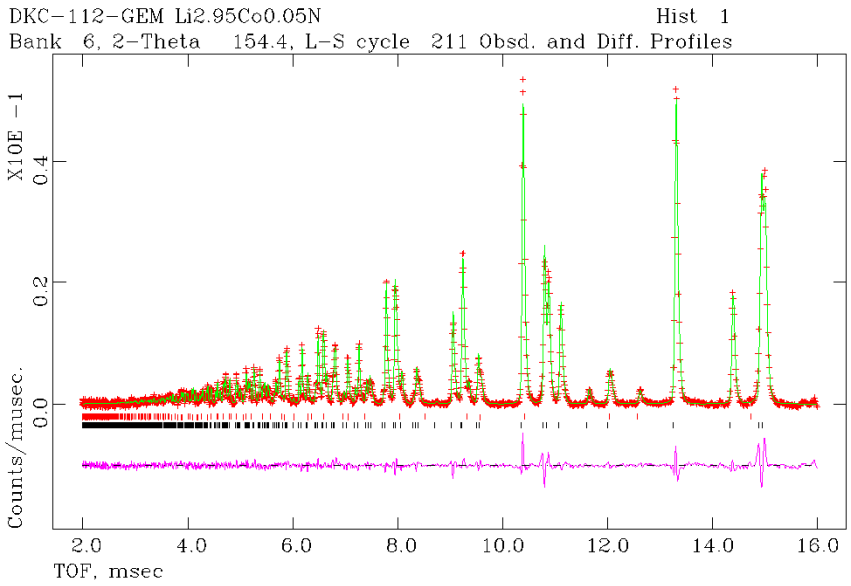


**Figure 3.12 OCD plots from GSAS Rietveld refinement of ToF PND data for [4] from the 2θ 154.4 $^{o}$ detector. Observed data is in red, calculated in green and the difference of the two profiles shown in pink. The nitride-type phase is assigned black tickmarks and lithium oxide impurity phase red tickmarks.**

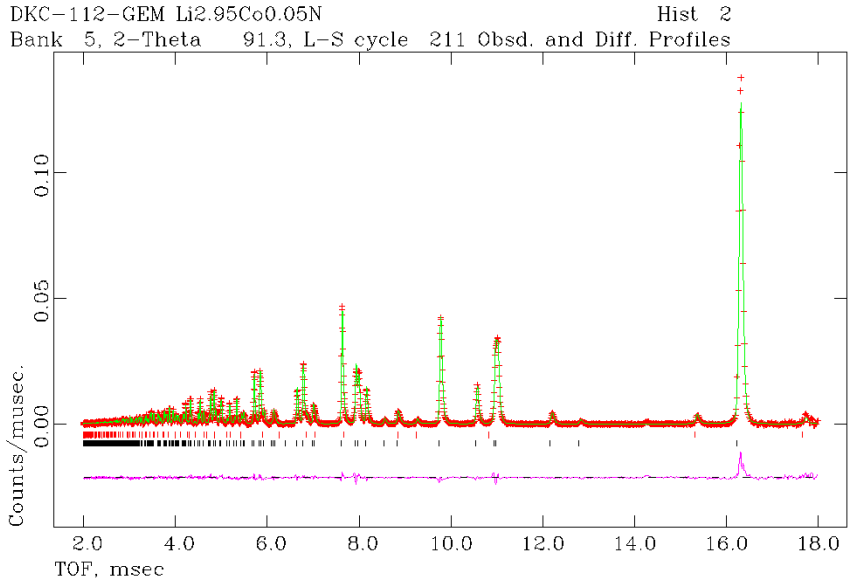


**Figure 3.13 OCD plots from GSAS Rietveld refinement of ToF PND data for [4] from the 2θ 91.3 $^{o}$ detector. Observed data is in red, calculated in green and the difference of the two profiles shown in pink. The nitride-type phase is assigned black tickmarks and lithium oxide impurity phase red tickmarks.**

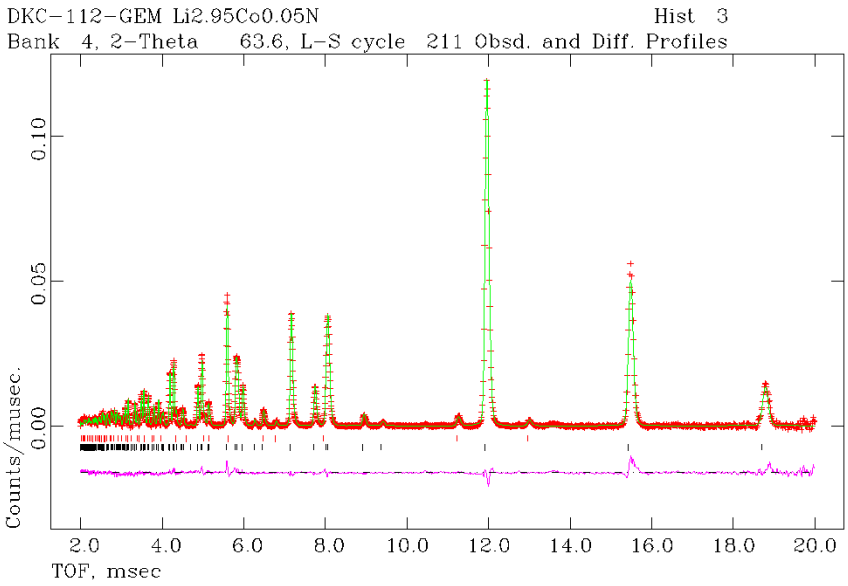


**Figure 3.14 OCD plots from GSAS Rietveld refinement of ToF PND data for [4] from the 2θ 63.6 ° detector. Observed data is in red, calculated in green and the difference of the two profiles shown in pink. The nitride-type phase is assigned black tickmarks and lithium oxide impurity phase red tickmarks.**

Comparing the refined model from **[1]** in which no vacancies were observed to that of the **[4]** which refined to give vacancies, it can be seen that there are important differences. Table 3.6 below shows how some of the low doped materials that have been studied compared to previously researched materials[1] from this series and in Figure 3.15 we can see the trend of how the unit cell parameters of these materials change as function of increasing metal content.

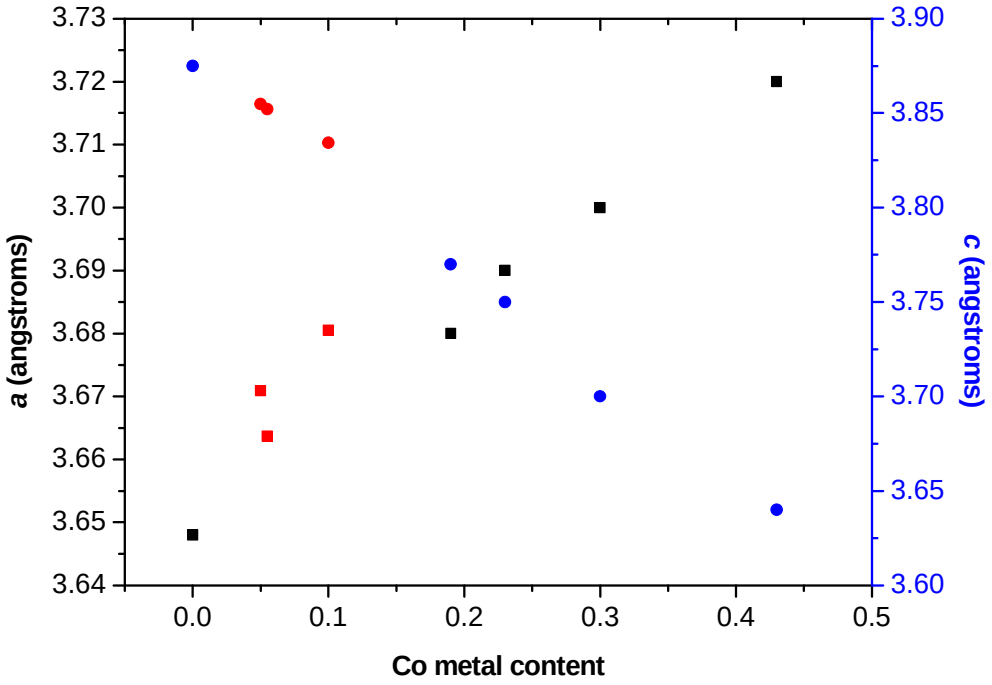


**Figure 3.15 Variation of unit cell parameters with increasing cobalt metal content. Blue markers denote unit cell *c*-parameters, black markers denote *a*-parameters, and red markers are values for materials [1], [2] and [4] from this work.**

**Table 3.6 Table of unit cell parameters for different cobalt lithium nitrides.**

| Material | x | a /Å | c /Å |
|---|---|---|---|
| $Li_3N$[19] | 0 | 3.648(1) | 3.875(1) |
| $Li_{2.95}Co_{0.05}N$ **[1]** | 0.05 | 3.6709(1) | 3.8547(2) |
| $Li_{2.781}Co_{0.055}N$ **[4]** | 0.055 | 3.66371(6) | 3.85213(7) |
| $Li_{2.9}Co_{0.1}N$ **[2]** | 0.1 | 3.6805(1) | 3.8343(2) |
| $Li_{2.81}Co_{0.19}N$[1] | 0.19 | 3.68(0) | 3.77(8) |
| $Li_{2.77}Co_{0.23}N$[1] | 0.23 | 3.69(2) | 3.75(8) |
| $Li_{2.70}Co_{0.30}N$[1] | 0.30 | 3.70(5) | 3.70(0) |
| $Li_{2.57}Co_{0.43}N$[1] | 0.43 | 3.72(1) | 3.64(7) |

As can be seen from the Table 3.6 and Figure 3.15, the materials which have been studied in the course of this research fit well with those which have been previously studied in the series. By comparing **[4]** with **[1]**, it would appear that we see for **[4]** a decrease in the atomic distance between the Li(1) and the nitrogen atom however the distance between the Li(2) and the nitrogen is also shorter than in **[1]**. The difference between Li(1)-N distance that is observed

could be explained by the difference in the cobalt content between the two materials (as this distance relates to half the unit cell *c*-parameter). Figure 3.15 indicates that *c*-parameter and hence Li(1)/Co-N decrease linearly with increasing metal content. In contrast to this the Li(2)-N distance, which relates to the unit cell *a*-parameter, cannot solely be attributed to the difference in the refined metal occupancies of the materials and thus could be due to the presence of Li(2) site vacancy.

The level of vacancies that are seen at the Li(2) site in **[4]** is 8.2 % at room temperature and the general formula for this compound, $Li_{3-x-y}M_xN$ (where x = 0.055 and y = vacancy = 0.164) which would suggest that the formula is in actual fact $Li_{3-4x}M_xN$. This would appear to indicate that aliovalent substitution of the transition metal is occurring and from the refined model it would appear that the cobalt oxidation state is +3.98, which would be higher than what has been previously seen in this series of materials and is an unrealistic oxidation state for this metal.

What is likely to be happening for this material **[4]**, is that the charge compensation from the lithium vacancy is not solely being attuned on the Co metal and that some of the charge is compensated on the nitrogen site also. For the material **[4]** if the nitrogen site was deficient by as little as 4 % it would give rise to a formal charge on the cobalt metal of + 1.8 for the purposes of charge balance, which is a far more reasonable value. A nitrogen vacancy of such a low level may even be below the detection levels of the neutron diffraction. This has been previously shown for the high-doped lithium nitridocobaltate $Li_{1.00}Co_{0.4}N$[27-28] where lithium had been electrochemically extracted from $Li_{2.60}Co_{0.4}N$. Through the use of electron energy-loss spectroscopy (EELS) it was noted that both the cobalt and nitrogen were playing a part in the charge balancing of the material when the vacancies were induced and this was manifested by holes in the nitrogen 2p orbital upon extraction. This is a possibility for what is happening for material **[4]** also, and may go some way to explaining why there is a shortening of the *a*-parameter seen in comparison to **[1],** as there is a change in the oxidation state of the nitrogen. Unfortunately in the materials examined by EELS, the material $Li_{1.0}Co_{0.4}N$ had become amorphous upon extraction of the lithium and thus crystallographic data could not be obtained to confirm how the unit cell parameters were affected by the nitrogen charge compensation.

Preliminary X-ray photoelectron spectroscopy (XPS) measurements were carried out on the materials at the National Centre for Electron Spectroscopy and Surface Analysis (NCESS) at Daresbury Laboratory. Through the use of a glove bag sealed around the loadlock of the spectrometer which was evacuated and flushed several times, the materials (sealed inside a box within a dessiccator) were introduced into the ultra-high vacuum chamber of the XPS spectrometer and their spectra collected. Unfortunately due to the highly air sensitive nature of the materials and the non-ideal setup for such materials, the main peaks of the spectra that were observed corresponded to that of oxidation products of the sample. Therefore this technique did not prove anything conclusive. Some X-ray absorption near-edge structure (XANES) analysis of this material would help to elucidate the true oxidation state of the cobalt, and dependant on the results of this, some further EELS analysis would be useful.

## 3.3 Scanning Electron Microscopy (SEM)

SEM was carried out for both **[1]** and **[4]** in order to gauge if reaction time had an effect on the surface morphology of the material. The sample is prepared for the SEM by crushing the product pellet and grinding the product to a powder and sprinkling onto a carbon tab. The corresponding two images for the materials can be seen in Figure 3.16 and Figure 3.17.

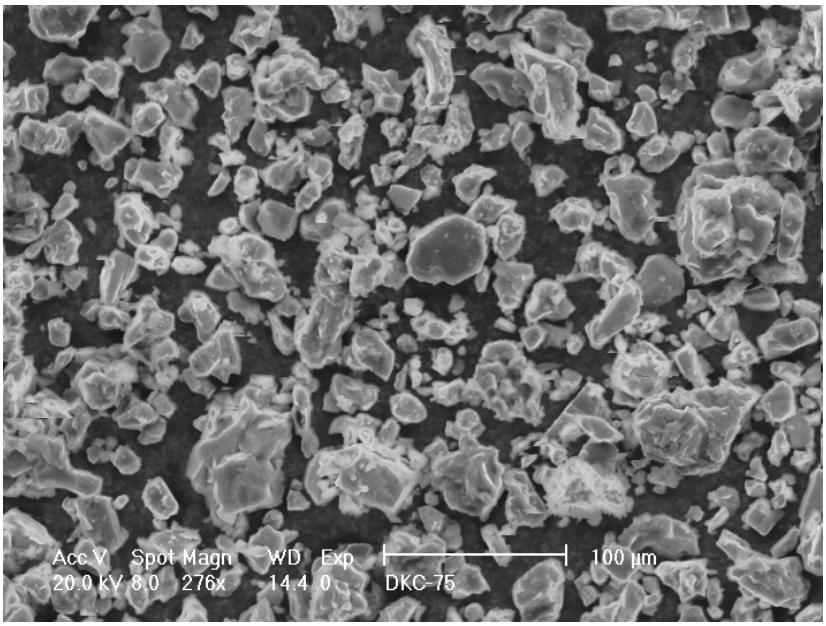


**Figure 3.16 SEM micrograph for $Li_{2.95}Co_{0.05}N$ [1]**

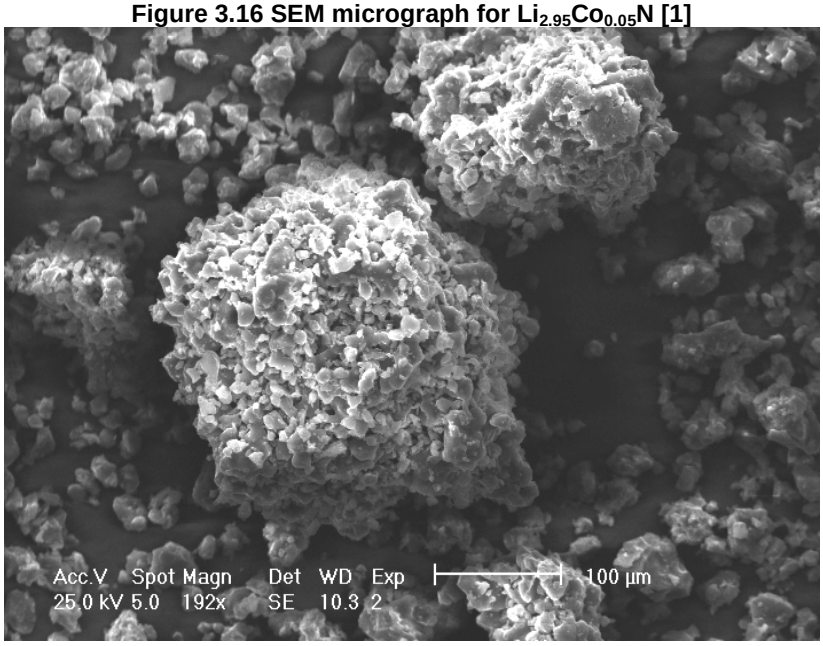


**Figure 3.17 SEM micrograph for $Li_{2.781}Co_{0.055}N$ [4]**

As can be seen in Figure 3.17 there are large aggregates of ~250 μm diameter, however these appear to consist of particles of much smaller sizes than those found in Figure 3.16 (individual particles typically ~40 μm) which actually look somewhat sintered. EDX spectroscopy (Energy Dispersive X-ray) was carried out on the two materials also and for $Li_{2.95}Co_{0.05}N$ **[1]** a cobalt : nitrogen ratio of 0.0499 : 1 which is close to agreement of the refined stoichiometry which was found from the PND results. For $Li_{2.781}Co_{0.055}N$ an cobalt : nitrogen ratio of 0.0634

: 1 which is in even closer agreement to the refined stoichiometry from the PND results. Results for EDX analysis are included in the appendix.

## 3.4 Magnetic Measurements

The measured moment output by the instrument was corrected for the diamagnetic effects of the lower shell paired electrons and for signals from the gelatine capsule. In Figure 3.18 and Figure 3.19 below we can see how the molar magnetic susceptibility varies with temperature for the two materials.

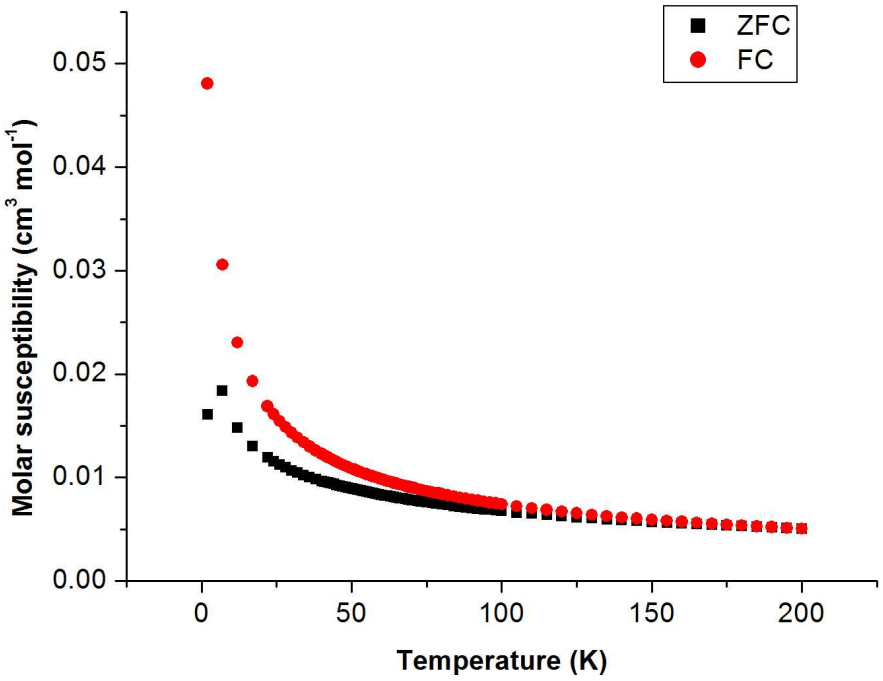


**Figure 3.18 Molar susceptibility as a function of temperature for $Li_{2.95}Co_{0.05}$ [1].**

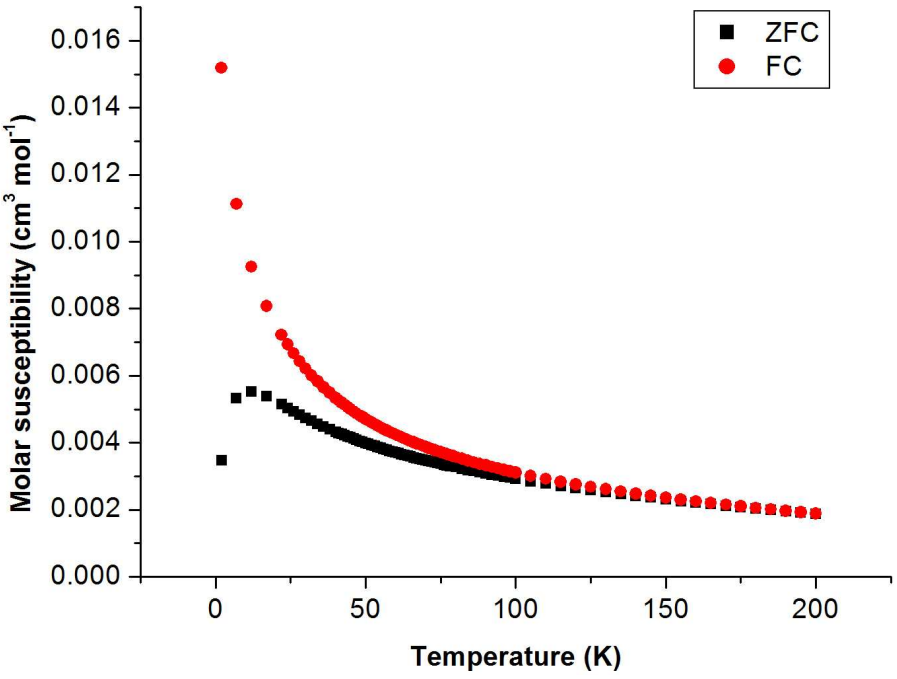


**Figure 3.19 Molar susceptibility as a function of temperature for $Li_{2.95}Co_{0.05}$ [4].**

As can be seen, the two materials display almost identical behaviour, with the only significant difference being the difference in the magnitude of the molar susceptibility values. These materials display fairly typical paramagnetic behaviour, with weak temperature dependant behaviour observed in both cases between 100 and 200 K. For both materials there can be a tail observed below 50 K which would be attributed to Curie type behaviour. The behaviour observed for these materials follows a modified Curie-Weiss law which has previously been used for explaining the magnetic behaviour of other materials in this series. Both of the materials displayed spin-glass type behaviour, and this is a type of behaviour that has previously been seen in this series of materials[29] and is suggested by the cusp that is seen in the zero-field-cooled measurement on both of the materials at ~2 K. The temperature at the maxima of these cusps is known as the freezing temperature, and it is widely understood that at temperatures below this that the atomic magnetic moments (spins) have no long-range magnetic order, but have static orientations which vary slightly over short distances[29]. In order to ascertain the spin-glass behaviour further, observation of ac susceptibility measurements would be required.

The inverse molar susceptibility was plotted versus temperature and a linear fit was carried out on the region of the plot which was temperature dependant. This can be seen in Figure 3.20 and Figure 3.21 below.

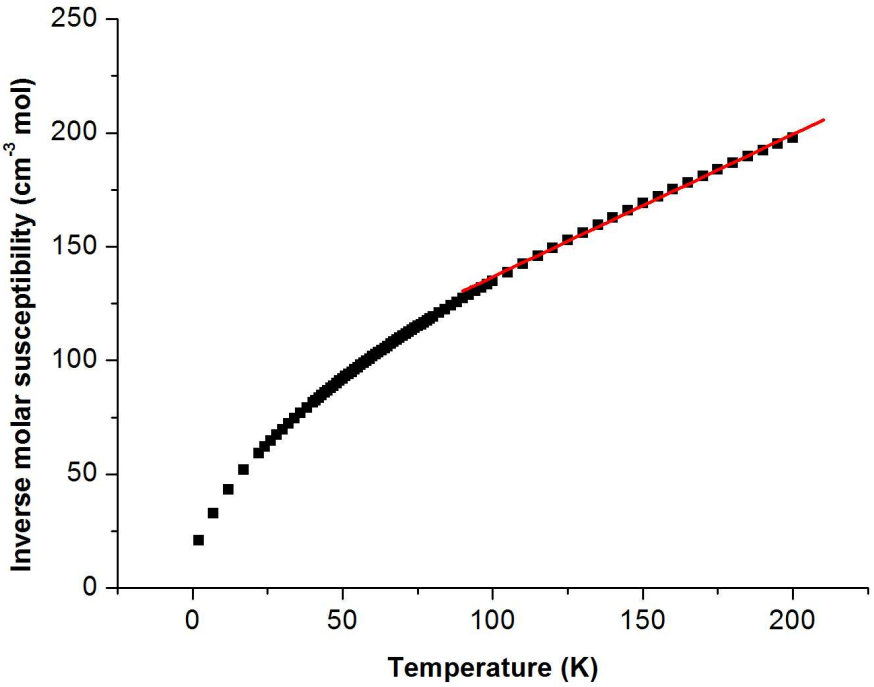


**Figure 3.20 Plot of field-cooled inverse molar susceptibility versus temperature for $Li_{2.966}Co_{0.034}N$ [1]. The red line is the linear fit for the temperature dependant region.**

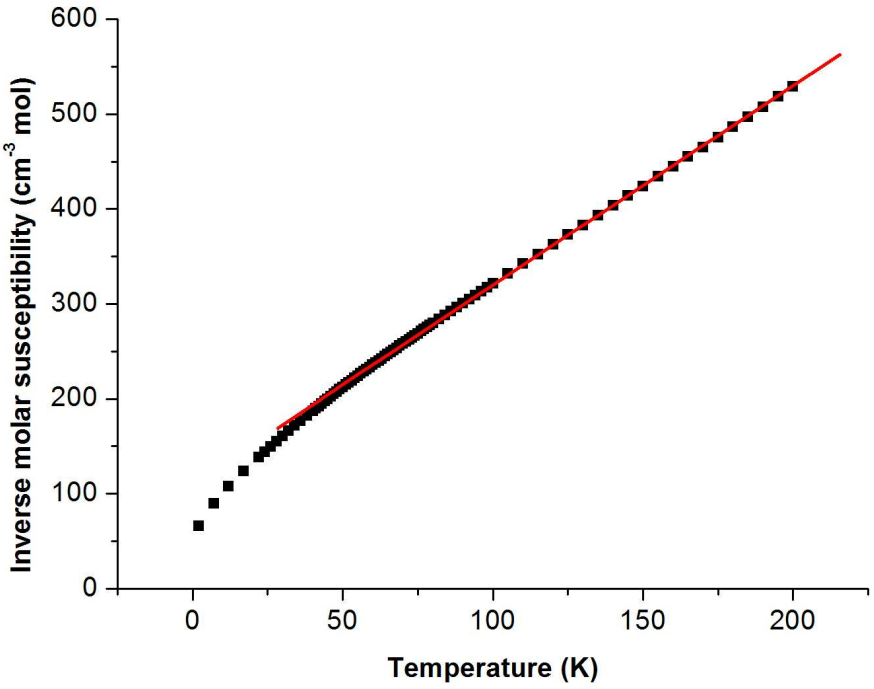


**Figure 3.21 Plot of field-cooled inverse molar susceptibility versus temperature for $Li_{2.781}Co_{0.055}N$ [4]. The red line is the linear fit for the temperature dependant region.**

For material **[4]**, it can be seen that it follows Curie-Weiss type behaviour above ~50 K, where it is linearly temperature dependent. The linear fit for the temperature dependant region yielded a Weiss and Curie constant of -52.240 K and 0.476 $cm^3\ mol^{-1}\ K$ respectively using the equation below which is a reordering of equation 25 from section 2.5:

$$1/\chi_m = (T+\theta)/C = (1/C)T + \theta/C$$

The effective molar magnetic moment for this sample can then be elucidated from the Curie constant by applying the equation from section 2.4. From this it would appear that the magnetic effects seen in the temperature dependant region equate to an effective magnetic moment of 4.099 Bohr Magnetons. As can be seen from the figure, material **[1]** has a larger temperature independent contribution, and from the linear fit for this sample, a Weiss constant of -120.961 K and a Curie constant of 1.611 $cm^3\ mol^{-1}\ K$ for the temperature dependant part (~100 - 200 K) was calculated. This Curie constant relates to an

effective molar magnetic moment for this sample of 3.532 Bohr Magnetons using the same equation as previously used.

For these two samples, the cobalt effective magnetic moments that are observed are relative to only 0.05 Co atoms for **[1]**, and 0.055 for **[4]**, and thus the effective moments per cobalt atom would be much higher, 70.64 and 74.527 BM respectively. These moments are far in excess of what would be calculated for a spin-only contribution from a $Co^{1+}$ ($d^8$), $Co^{2+}$ ($d^7$) or $Co^{3+}$ ($d^6$) ion.

As the cobalt ion is in the linear geometry, the splitting of the crystal field would be as in Figure 3.22 below:

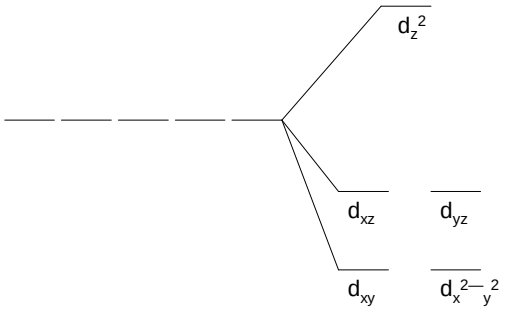


**Figure 3.22 Energy splitting for linear geometry of transition metals.**

From the neutron diffraction it would suggest that for **[1]** the cobalt is in the $Co^{1+}$ oxidation state and for **[4]** if all the charge is on the cobalt it would be in a $Co^{4+}$ oxidation state. These would be $d^8$ and $d^5$ electron configuration respectively. The $d^8$ configuration would give either 2 unpaired electrons or 0 unpaired electrons in high-spin and low-spin states respectively giving rise to a spin-only magnetic moment of $\sqrt{8}$ = 2.828 BM and diamagnetism.

Similarly for $d^5$, in a high-spin state there would be 5 unpaired electrons and a spin-only magnetic moment of $\sqrt{35}$ = 5.91 BM using the equation above. For low-spin there would be 1 unpaired electrons, a spin-only magnetic moment of $\sqrt{3}$ = 1.732 BM.

There has been previous evidence of a high orbital contribution to the magnetism seen for a lithium nitridoferrate[10-11], and as cobalt is beside iron in

the periodic table it could be argued that it too could experience the same effects, however the large effective moments that have been calculated would still be too large to be explained by this. It could be a possibility that the magnetism of these materials have been affected by either a paramagnetic or ferromagnetic impurity at the preparation stage. The same XANES experiments as outlined previously would again elucidate the oxidation state of the transition metal, but also would show the X-ray absorption edge for any other impurities.

## 3.5 Electrochemical measurements

The plots of specific capacity against varying cell voltage can be seen below in Figure 3.23 - Figure 3.25 for $Li_{2.60}Co_{0.4}N$, $Li_{2.95}Co_{0.05}N$ **[1]** and $Li_{2.90}Co_{0.1}N$ **[2]** respectively.

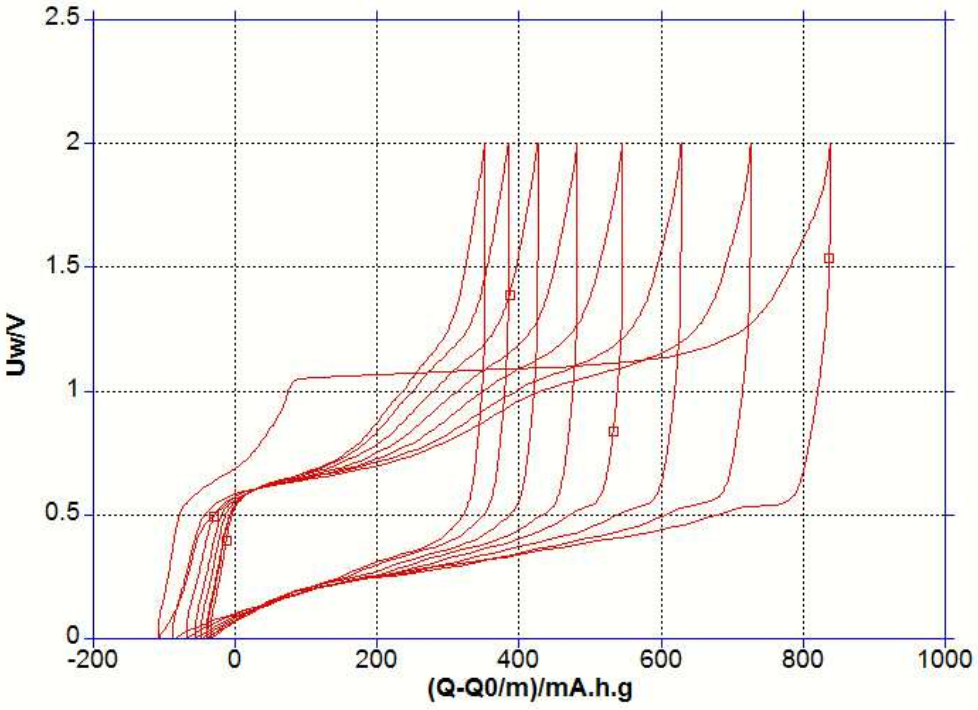


**Figure 3.23 Plot of cell voltage versus specific capacity for $Li_{2.60}Co_{0.4}N$.**

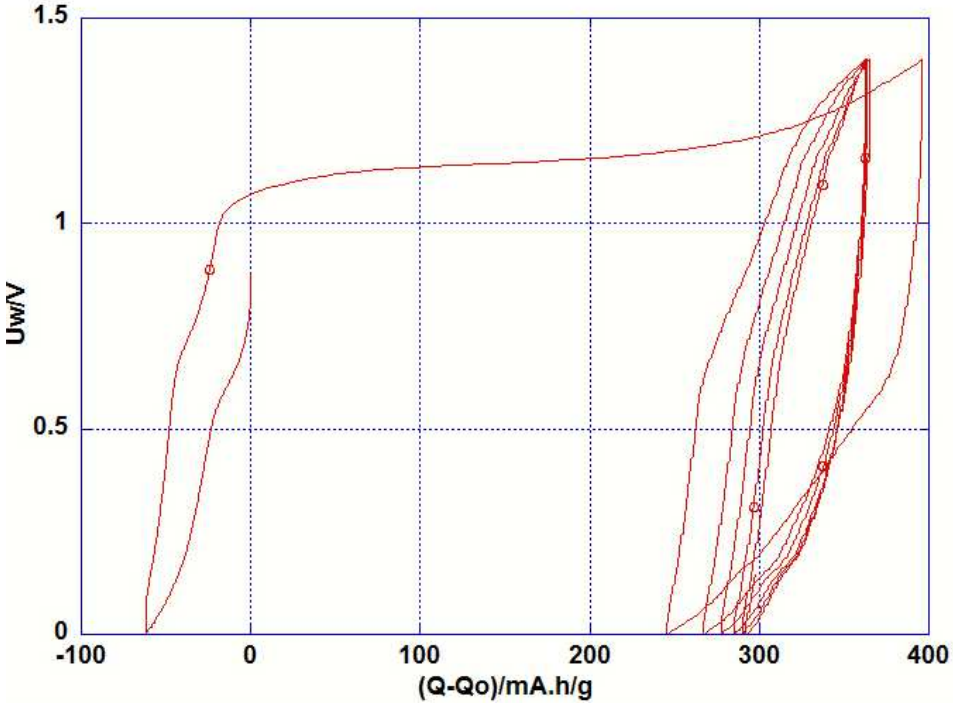


**Figure 3.24 Plot of cell potential versus specific capacity for $Li_{2.95}Co_{0.05}N$ [1].**

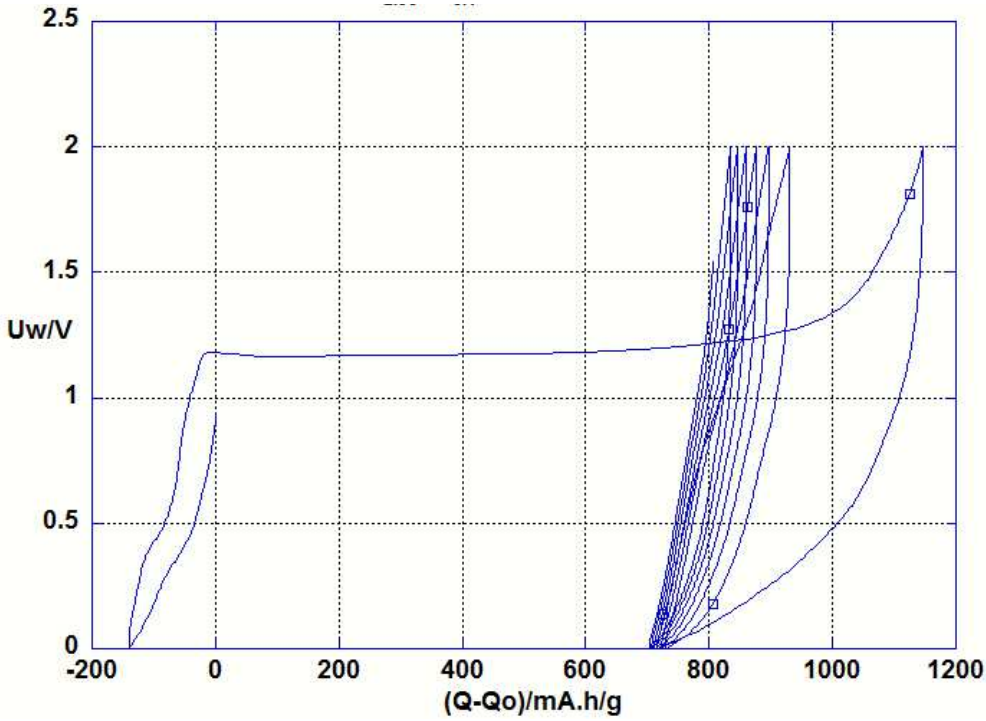


**Figure 3.25 Plot of cell potential versus specific capacity for $Li_{2.90}Co_{0.1}N$ [2].**

As can be seen there are similarities in the behaviour of these materials, most noticeably the large plateau during the first oxidation and a decrease in capacity

on subsequent charge cycles. For $Li_{2.60}Co_{0.4}N$ the capacity attained at the end of the first oxidation of the material was 838 $mAhg^{-1}$ which relates to the extraction of 1.966 lithium atoms. For $Li_{2.95}Co_{0.05}N$ **[1]** 396 $mAhg^{-1}$ and for $Li_{2.90}Co_{0.1}N$ **[2]** a specific capacity of 1147.20 $mAhg^{-1}$ was achieved.

From the plot of the specific capacity for $Li_{2.60}Co_{0.4}N$, it can be seen that there is reversibility to the charge and discharge cycling of the material, as after each reduction of the sample the specific capacity is close to that of the previous reduction endpoint. After the second oxidation the specific capacity of the sample had fallen by 13.38 % and by 25.09 % by the third and by the eighth and final oxidation there was an overall decrease in capacity from the initial oxidation by 57.99 %. As can be seen from the plot of the specific capacity for $Li_{2.95}Co_{0.05}N$ **[1]** the cyclability of this sample is not reversible for the first cycle, as after the first reduction step the capacity is at -61.961 $mAhg^{-1}$, but for subsequent cycles it is reversible with specific capacities in the region of ~250-290 $mAhg^{-1}$. The same type of behaviour is seen for $Li_{2.90}Co_{0.1}N$ **[2]** and upon cycling, this materials capacity decreased, by 18.84 % in the second cycle, 21.84 % in the third and by the eighth and final cycle the capacity has dropped by only 27.23 %.

The electrochemical measurements for these materials were carried out using lithium metal as the cathode material, lithium nitridocobaltate material as the anode material. From the two materials $Li_{2.95}Co_{0.05}N$ **[1]** and $Li_{2.781}Co_{0.055}N$ **[4]**, it can be seen that there is a plateau to the initial cycle. From previous work in this area, this plateau in the first step has been shown to be due to the sample moving from a crystalline to an amorphous character[30-31]. For the sample of $Li_{2.90}Co_{0.1}N$ **[2]**, it shows a stable capacity close to that of the well studied $Li_{2.60}Co_{0.40}N$, which is surprising as there is much less of the metal present and thus there shouldn't be anywhere near as many charge carriers (vacancies), and from the PND data it inferred that there were in fact no vacancies present at the Li2 site. In order to clarify how much of the lithium was potentially being inserted into the carbon additive, a blank experiment was run using only the carbon 'sp' and the lithium metal cathode. This can be seen in Figure 3.26 below.

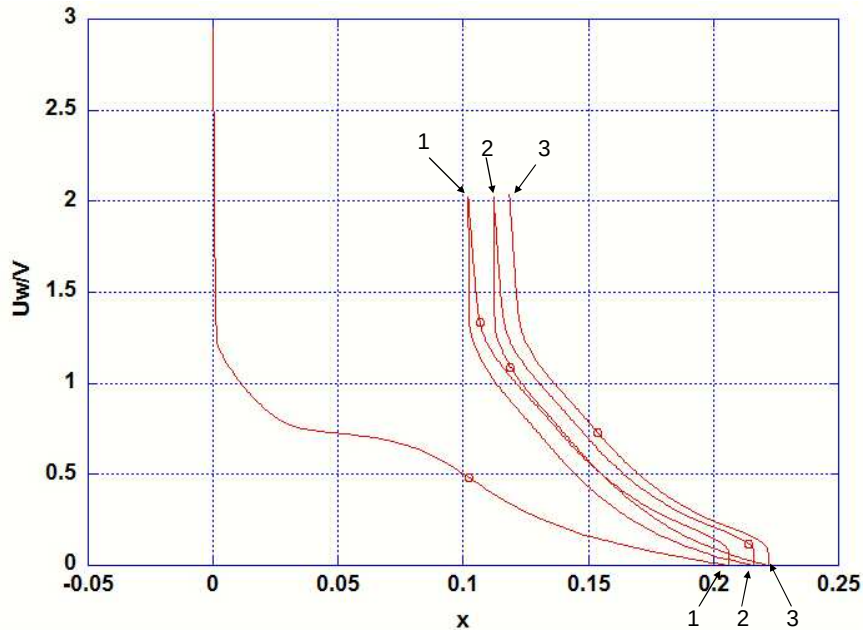


**Figure 3.26 Quantity of lithium inserted into carbon 'sp' additive and effects with cycling where x is lithium insertion/ extraction value. Arrowed numbers refer to cycle number.**

As can be seen there is a fairly small amount of the lithium inserted into the carbon additive and when this is compared to the initial insertion into the sample of $Li_{2.90}Co_{0.1}N$ **[2]** which was 0.2089 Li, it can be seen to be almost equal to the first insertion in the additive, therefore this could be where the lithium is being inserted initially and not into any vacancy in the material. After that the amount of lithium extracted from the two materials is governed by how easily it can be extracted, and this could be controlled by how weak the Li2-N bond is. The sample with the higher capacity, $Li_{2.90}Co_{0.1}N$ **[2]**, has a longer Li2-N bond (2.12505(7) Å) as compared to for $Li_{2.95}Co_{0.05}N$ **[3]** (2.11950(6) Å). These materials show good cyclability as compared to the previously studied $Li_{2.60}Co_{0.40}N$ and actually showed visible signs of improving with cycles which could give them a good potential application for lithium secondary batteries. The irreversibility seen could be a consequence of the material losing its long range structural order, and transforming to a different local structure, thus the lithium can never be reinserted back to the starting point.

As can be seen from the figures these materials appear to be fairly stable with cycling, even across the cycles that were performed it can be seen that there is a minimal drop in the capacity at the end of each. However there are some

similarities between **[1]**, **[2]** and $Li_{2.60}Co_{0.4}N$, the plateau which is present in the first oxidation step and also the increase of capacity with each insertion step but decrease after each extraction step. The oxidation step plateau has been seen previously in these materials and is thought to be due to the material undergoing a change from a crystalline material to an amorphous phase[13, 30].

## 3.6 Conclusions

These lithium nitridocobaltates, $Li_{2.95}Co_{0.05}N$ **[1]**, $Li_{2.9}Co_{0.1}N$ **[2]** and $Li_{2.781}Co_{0.055}N$ **[4]**, retain the lithium nitride-type structure even at this lower end of the metal occupancy scale. The changes which are observed in the unit cell parameters from that of the parent material, fit well with what has been previously seen for this series of materials with higher cobalt dopant levels x = 0.19 – 0.43[1], but only when the reaction time is comparable. An increase in the *a*-parameter and decrease in the *c*-parameter upon doping the material was observed and from Figure 3.11 this was shown to be in-line with previous materials containing higher quantities of cobalt metal[1]. This has previously been shown to be due to a shift towards more covalent character in the Li(1)-N bond, and as covalent bonds are shorter range than ionic bonds, a shorter Li(1)-N bond distance was measured. This consequently brought about a lengthening of the Li(2)-N bond due to a weakening effect and as these two bond lengths are directly related to the *a*-parameter and *c*-parameter, this explains the observed changes. For the material which had been reacted for longer, vacancies were found to be induced in the structure, and when the bond lengths and unit cell parameters are compared with the material which contained a similar metal content but no vacancy, it was found that the *c*-parameter varied only a little, however, the *a*-parameter was much shorter in the vacant material. This could be attributed to nitrogen of a higher oxidation state as a consequence of charge balancing.

SEM with EDX analysis for the materials **[1]** and **[4]** showed that as a result of longer reaction time, the particle size of the material had decreased but then agglomeration had begun to occur. The results of the EDX were in agreement with the ratio of ions found from the diffraction experiments.

These materials both displayed Curie-Weiss type behaviour and there was a spin-glass effect to the magnetism. From the inverse magnetic susceptibility plotted versus the temperature, we can see that there is a deviation from typical Curie-Weiss behaviour but by fitting the temperature-dependant part of the line (the straight part) to the Curie-Weiss equation, the Weiss and Curie constants were obtained, and from the Curie constant for both $Li_{2.966}Co_{0.034}N$ and $Li_{2.781}Co_{0.055}N$ a molar magnetic moment of 3.532 $\mu_B$ and 4.099 $\mu_B$ respectively. Since these

moments which are calculated are for a fraction of a cobalt atom, the moment which they would relate to for a whole atom of the metal would be extremely large, 70.64 and 74.527 respectively. These far exceed the moments that would be expected from the spin only moment for a $d^7$ or $d^6$ ion. A large orbital contribution to the overall magnetism could be accounting for the large moment seen, and this has previously been experienced for lithium nitridoferrates[10]. In the case of the iron containing ternary lithium nitride, the high magnetic moments which were observed were found to be due to spin-orbit coupling[11], and normally it would be thought that the crystal field quenches part of the orbital contribution, but for this material an orbital moment of L = 2 was possible for a linear crystal field. Also there is evidence for large hyperfine magnetic fields present in this material[10] arising from interactions between the nucleus and internally generated magnetic and electric fields. It could be assumed that similar effects are happening here in these lithium nitridocobaltates, as cobalt is beside iron in the periodic table and may be susceptible to similar magnetic behaviour. However, this would still not account for the effective moments seen for these materials, and as such an impurity in the preparation of the magnetic measurements has been assumed.

The electrochemical measurements that were carried out for the materials **[1]** and **[2]** showed that these materials could potentially perform as lithium anode materials, and in particular **[1]** showed a 34 % higher specific capacity than the material which to date has been classified as the best lithium anode material which is $Li_{2.60}Co_{0.4}N$ and has displayed a capacity of 760 $mAhg^{-1}$ [13, 27]. The lithium which is initially inserted into these materials electrochemically was assumed to be inserting into the carbon conductor and not the material themselves, as neither of the two had displayed any vacancy within their structure. After the insertion, the extraction of lithium was occurring as a result of weakened Li(2)-N bonds as a result of the cobalt which had been doped into these materials, and both materials showed promising cyclability.

## 3.7 Future work

XANES would be a useful tool to elucidate the oxidation state of the transition metal and any impurity within the material which could be causing the large

magnetic moments. In-situ electrochemical neutron diffraction could be useful to ascertain if these materials are becoming amorphous as has been previously seen, and if not then what structural changes are occurring during the reaction. Electrochemical analysis of the material with vacancies in its structure would be of interest to see how it performs with respect to those already studied, as in theory it should have a higher capacity, and some further studies of the cyclability of the materials would be of interest, over a larger cycle range.

## 3.8 References


1. V. W. Saschsze and R. Juza, *Zeitschrift fur Anorganische Chemie*, **259**, (1949), 278.
2. E. Zintl and G. Brauer, *Zeitschrift fuer Elektrochemie und Angewandte Physikalische Chemie*, **41**, (1935), 102.
3. U. V. Alpen, A. Rabenau and G. H. Talat, *Appl. Phys. Lett.*, **30**, (1977), 621.
4. M. G. Barker, A. J. Blake, P. P. Edwards, D. H. Gregory, T. A. Hamor, D. J. Siddons and S. E. Smith, *Chem. Commun.*, (1999), 1153.
5. D. H. Gregory, P. M. O'Meara, A. G. Gordon, D. J. Siddons, A. J. Blake, M. G. Barker, T. A. Hamor and P. P. Edwards, *J. Alloys Compd.*, **317-318**, (2001), 237.
6. J. Yang, K. Wang and J. Xie, *J. Electrochem. Soc.*, **150**, (2003), A140.
7. Z. Stoeva, R. Gomez, D. H. Gregory, G. B. Hix and J. J. Titman, *Dalton Trans.*, (2004), 3093.
8. A. G. Gordon, R. I. Smith, C. Wilson, Z. Stoeva and D. H. Gregory, *Chemistry Communications*, (2004), 2812.
9. Z. Stoeva, R. I. Smith and D. H. Gregory, *Chem. Mater.*, **18**, (2006), 313.
10. J. Klatyk, W. Schnelle, F. R. Wagner, R. Niewa, P. Novak, R. Kniep, M. Waldeck, V. Ksenofontov and P. Gutlich, *Phys Rev Lett*, **88**, (2002), 207202.
11. P. Novak and F. R. Wagner, *Physical Review B*, **66**, (2002).
12. T. Shodai, S. Okada, S. Tobishima and J. Yamaki, *Solid State Ionics*, **86-8**, (1996), 785.
13. T. Shodai, S. Okada, S. Tobishima and J. Yamaki, *J. Power Sources*, **68**, (1997), 515.
14. Y. M. Kang, S. C. Park, Y. S. Kang, P. S. Lee and J. Y. Lee, *Solid State Ionics*, **156**, (2003), 263.
15. Y. Takeda, M. Nishijima, M. Yamahata, K. Takeda, N. Imanishi and O. Yamamoto, *Solid State Ionics*, **130**, (2000), 61.
16. Y. Takeda, R. Kanno, Y. Tsuji and O. Yamamoto, *J. Electrochem. Soc.*, **131**, (1984), 2006.

17. D. Liu, F. Du, W. Pan, G. Chen, C. Wang and Y. Wei, *Mater. Lett.*, **63**, (2009), 504.
18. W. Kraus and G. Nolze, Federal Institute for Materials Research and Testing, Berlin, Editon edn., 2000.
19. A. Rabenau and H. Schulz, *Journal of Less-Common metals*, **50**, (1976), 155.
20. U. D. Altermatt and I. D. Brown, *Acta Crystallographica Section A*, **43**, (1987), 125.
21. J. Laugier and B. Bochu, Grenoble, Editon edn., 1987.
22. A. G. Gordon, D. H. Gregory, A. J. Blake, D. P. Weston and M. O. Jones, *Int. J. Inorg. Mater.*, **3**, (2001), 973.
23. R. D. Shannon, *Acta Crystallographica Section A*, **32**, (1976), 751.
24. R. Niewa, Z.-L. Huang, W. Schnelle, Z. Hu and R. Kniep, *Z. Anorg. Allg. Chem.*, **629**, (2003), 1778.
25. A. C. Larson and R. B. V. Dreele, Los Alamos National Laboratory Report LAUR 86-748, Los Alamos, Editon edn., 2004.
26. D. H. Gregory, P. M. O'Meara, A. G. Gordon, J. P. Hodges, S. Short and J. D. Jorgensen, *Chem. Mater.*, **14**, (2002), 2063.
27. T. Shodai, Y. Sakurai and T. Suzuki, *Solid State Ionics*, **122**, (1999), 85.
28. S. Suzuki, T. Shodai and J. Yamaki, *J. Phys. Chem. Solids*, **59**, (1998), 331.
29. D.-L. Liu, F. Du, Y.-J. Wei, C.-Z. Wang, Z.-F. Huang, X. Meng, G. Chen, Y. Chen and S.-H. Feng, *Mater. Lett.*, **63**, (2009), 133.
30. M. Nishijima, T. Kagohashi, M. Imanishi, Y. Takeda, Yamamoto and S. Kondo, *Solid State Ionics*, **83**, (1996), 107.
31. M. Nishijima, T. Kagohashi, Y. Takeda, M. Imanishi and O. Yamamoto, *J. Power Sources*, **68**, (1997), 510.

# 4. Lithium nitridocuprates

## 4.1 Introduction

These materials fall within the same group, lithium nitridometallates, as that of the lithium nitridocobaltates previously discussed in full detail in Chapter 3. As has been previously described, the transition metals Co, Ni and Cu form substituted variants of the parent material lithium nitride, $Li_3N$, through the transition metal being partially substituted at the interplanar Li(1) site, and as a result the hexagonal structure of lithium nitride is retained. When the metal is partially present at the Li(1) site, the structure of the resulting material consists of alternating layers of [LiN] and Li/M along the direction of the *c*-axis. These materials have been a focus of much interest since the first reports of their synthesis in the 1940's by Juza[1]. Previous work has been carried out regarding the upper limits of substitution in these lithium nitridometallates $Li_{3-x-y}M_xN$, and Gregory *et al.*[2] found that for Ni, x = 0.79 was the highest achievable for disordered nitrides as once the metal dopant levels reach x = 1, ordered variants of the lithium nitridometallates form, (e.g. when y = 0.333 for $Li_5Ni_3N_3$ and y =1 for LiNiN). The highest dopant level that has been achieved for nickel since the work of Gregory *et al.* with retention of the $Li_3N$ structure type is x = 0.85[3]. Similarly, the highest quantity of copper dopant that was achieved by both Gregory *et al.* and Niewa *et al.* is x = 0.43 synthesised at standard pressures, although a copper containing material has been synthesised by Weller *et al.* with a copper content of x = 0.519, by pressing a pellet of a mixture of lithium nitride and copper nitride and reacting it at 700 $^oC$ under a pressure of 200 bar for 16 hours[4]. For cobalt the highest accounted content of the metal was x = 0.6 and this was reported by Gordon *et al.*[5]. With all of these materials it was found that by introducing transition metal at the Li(1) site, there was a shortening of the bond length between the Li(1) and nitrogen and simultaneously a lengthening and weakening of the Li(2)-N bond which relate to the *c*-, and *a*-parameter respectively. This decrease in the *c*-parameter and Li(1)/M-N bond has been previously presumed to be due to a shift towards more covalent $\pi$-bond character and thus a formation of stronger bonds and this is evident from the shorter bond distance.

Lithium nitridocuprates gained a considerable amount of interest in the same wave of research as the previously detailed lithium nitridocobaltates in the wake of the discovery of large ionic conductivity in the parent material, lithium nitride. It had been previously postulated that by introducing transition metal at the Li(1) site, a weakening of the Li(2)-N bond would occur and this could in effect cause the activation energy for the ionic conductivity to decrease and thus facilitate ionic mobility and improve on the materials' electrochemical performance. In addition, it had been postulated that if the transition metal being substituted at the Li(1) site was of a higher oxidation state than the lithium (aliovalent substitution), then in order to maintain charge neutrality a greater number of vacancies could be introduced and that this could also improve the ionic conductivity of the substituted materials with respect to $Li_3N$.

As has been previously detailed for cobalt lithium nitrides, these materials have displayed interesting magnetic properties. Previously these materials have been known to display Curie-Weiss, Pauli paramagnetic, and spin-glass magnetic behaviour.

### *4.1.1 Lithium nitridocuprates*

Lithium nitridocuprates have been known since their first reported synthesis by Juza *et al.*[1, 6-7]. There have been many methods employed to synthesise these materials; reacting lithium nitride with copper metal under $N_{2(g)}$ or $NH_{3(g)}$, nitriding of an alloy of lithium metal and copper metal, reaction of lithium nitride with copper nitride[8], reacting lithium nitride with copper metal foil[9] and in more recent times, ball-milling of the copper metal with the lithium nitride[10]. Each of these have had varied success but the most successful have been the reaction with the metal foil and the reaction with the metal using lithium nitride and these have previously provided the purest and most crystalline samples.

As previously defined, the material where Cu = 0.43 was the highest amount of metal dopant that was possible under standard conditions without having any metal impurity post reaction[2-3]. When the metal is substituted at the Li(1) site the changes to the unit cell of the material which were observed are in line with what was expected for these materials and Table 4.1 shows this by comparing the unit cell data for the two materials.

**Table 4.1 Bond lengths and unit cell parameters for lithium nitride and copper lithium nitride.**

| Material | Space group | Li(2)-N /Å | Li(1)-N /Å | *a* /Å$^2$ | *c* /Å$^2$ | V /Å$^3$ |
|---|---|---|---|---|---|---|
| $Li_3N$[11] | P6/MMM | 2.1063(6) | 1.9375(5) | 3.648(1) | 3.875(1) | 44.66(2) |
| $Li_{2.57}Cu_{0.43}N$[3] | P6/MMM | 2.1200(6) | 1.8898(5) | 3.6717(11) | 3.7796(11) | 44.13(2) |

Niewa *et al*. did not report the presence of any lithium vacancies at the Li(2) site for this material, however Gregory *et al*. had also synthesised the same material and reported a 16 % vacancy at the Li(2) site[2]. There were several differences between the syntheses of each material, the main differences being that Niewa *et al*. reacted the $Li_3N$ with copper foil in a tantalum crucible under ambient back-pressure of $N_{2(g)}$ for 20 – 40 hours at 500 – 600 $^oC$, however Gregory *et al*. had reacted the $Li_3N$ with the copper foil in a stainless steel crucible under $N_{2(g)}$ pressure for 5 days at 750 $^oC$. As has been previously mentioned, the determining factors in the creation of lithium vacancies are both length of reaction time and reaction temperature, and so it would seem that this is the cause of the difference in the two materials' unit cells. For the copper containing nitride with a vacant Li(2) site, there is a slight increase in the *a*-parameter (3.6791(1) Å), and a slightly larger decrease of the *c*-parameter (3.7725(1) Å).

The previously mentioned lithium nitridocuprate with x = 0.519 was achieved through the use of high pressure synthesis[4]. The copper content was confirmed through Rietveld refinement from powder X-ray diffraction data, and this also yielded the presence of 14 % vacancies at the Li(2) site, which was slightly less than the vacancy level which had been reported when less metal was substituted[2]. There was a significant decrease in bond length for the Li(1)/M-N bond in comparison for that of the parent material, $Li_3N$, from 1.938 to 1.875 Å. This can yet again be attributed to the greater degree of covalency of the Li(1)/M-N bond due to more copper being present, which gave rise to an *a*-parameter of 3.67922(3) Å and a *c*-parameter of 3.75095(4) Å.

As previously discussed, these structural changes to the parent material brought about by the transition metal substitution can have consequent effects on the

physical properties of these materials. Gregory *et al*. carried out magnetic susceptibility measurements on $Li_{2.60}Cu_{0.4}N$[9], using SQUID magnetometry and for comparative reasons, $Li_3N$, which between the temperatures of 4 and 120 K displayed weak, temperature independent Pauli paramagnetic behaviour. $Li_{2.60}Cu_{0.4}N$ however showed a temperature dependant magnetic behaviour, whereby the susceptibility decreased quickly from 4 K to ~20 K. This was equated to be equivalent to 1.9 $\mu_B$ at 300 K and Gregory *et al*. attributed this to being the influence of $Cu^+$ and $Cu^{2+}$ ions.

Niewa *et al*.[3] also investigated the magnetic behaviour of lithium nitridocuprates, and the measurements were carried out between 1.8 and 400 K. A series of nitridocuprates were measured for $Li_{3-x-y}Cu_xN$ where x = 0.6, 0.12, 0.22, 0.32 and 0.43. Figure 4.1 shows a plot of the magnetic susceptibility for each of these materials as a function of varying temperature.

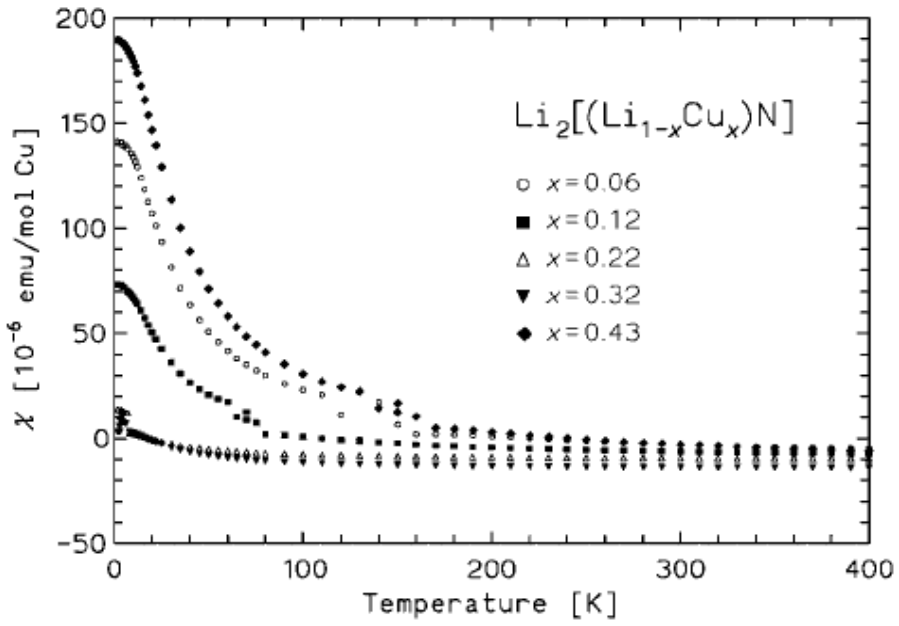


**Figure 4.1 Plot of field-cooled molar magnetic susceptibilities with varying temperature for the series $Li_{3-x-y}Cu_xN$[3].**

As can be seen from Figure 4.1, the materials which displayed the highest molar susceptibilities were those which contained both the highest and the lowest transition metal content. All of the materials in the series shown in Figure 4.1 follow a modified Curie equation of magnetic susceptibility:

$$\chi(T) = \chi_0 + C/T \qquad \textbf{4.1}$$

where $\chi_0$ is the temperature independent susceptibility, *C* is the Curie constant, T is the temperature and $\chi(T)$ is the susceptibility at a given temperature. Fitting of the measurements to the equation above gave rise to the parameters listed in Table 4.2 below. H is the applied field and $T_g$ is the maxima that are seen for the zero-field cooled plots for each material.

**Table 4.2 Parameters from fitting of modified Curie-law to lithium nitridocuprate series[3].**

| x(Cu) | $\mu_{eff}$/M-atom/$\mu_B$ | $\chi_0$/ $10^{-6}$ emu/ mol | $T_g$ / K |
|---|---|---|---|
| 0.06(1) | 0.66 | -14 | 4.0 |
| 0.12(1) | 0.28 | -10 | 3.0 |
| 0.22(1) | 0.10 | -11 | 7.0 |
| 0.32(1) | 0.09 | -14 | 6.5 |
| 0.43(1) | 0.29 | -18 | 4.0 |

As can be seen from the parameters presented in Table 4.2, the largest effective magnetic moment per metal atom is seen for the material which contains the lowest copper content. The moments that are observed for the materials in this series do not all correlate to the spin-only magnetic moments that would be expected for a $3d^{10}$ ion as in linear geometry this would lead to pairing of all the electrons and one would expect to see diamagnetism, and in fact only the two materials with x = 0.22 and 0.32 conform to this. For the other materials in this series the large moments that are seen would be attributed to a large orbital contribution to the magnetic behaviour. The same materials in the series had their susceptibilities measured after being cooled in the absence of the magnetic field, before being warmed again with the field on and measuring (ZFC). When these materials' FC and ZFC curves are plotted together, there is a deviation between the two curves whereby there is a point where the susceptibility drops off as the temperature decreases. This type of behaviour is indicative of a spin-glass type of behaviour. It is assumed that the spins that are on the metal centres are separated along the Li/M-N-Li/M chain sufficiently so that there is no long range ordering, and as such there is a level of frustration associated with the spins. When the temperature drops below a certain point, the freezing temperature, the orientation of the spins on these atoms are fixed.

Asai *et al.*[12] made some investigations into how the doping of copper metal into lithium nitride would affect the $Li^+$ conduction of the material and found that upon increasing the dopant level, the conductivity of the material decreased and the activation energy decreased. The latter was attributed to the greater degree of covalency in the Li(1)/M-N bond, and thus aiding the ion migration between the layers. The reduction in conductivity was ascribed to being due to a reduction in the number of charge carriers (vacancies) and can be explained through the equation below:

$$\sigma \propto n_V \exp(-E_a/RT) \qquad \mathbf{4.2}$$

as can be seen if the activation energy of the materials' ionic migration decreases with increasing metal dopant, and the number of charge carriers remains constant, it would be assumed that the conductivity of the material would increase, so as the conductivity was found to decrease it could only be due to a decrease in the charge carrier concentration (vacancies). Asai *et al.* reported a negative effect on the conductivity but concluded that the reduction of the activation energy could still have a possibility of improving the conductivity if the charge carrier concentration could be controlled.

Nishijima *et al.*[13] carried out some electrochemical investigations into materials in the series $Li_{3-x-z}M_xN$ where M = Co, Ni and Cu and x = 0.1, 0.2. 0.3 and 0.4. Coin cells of 50 mg of sample with 10 mg acetylene black carbon binder were pressed into 12 mm diameter pellets under a 1 MPa pressure, used as the cathode with a disc of Li sheet as the anode and 1M $LiClO_4$/PC + DME as the electrolyte. The material $Li_{2.60}Cu_{0.4}N$ was found to have the highest discharge capacity in cycle 1. Figure 4.2 below the closed-cell voltage curves for this material.

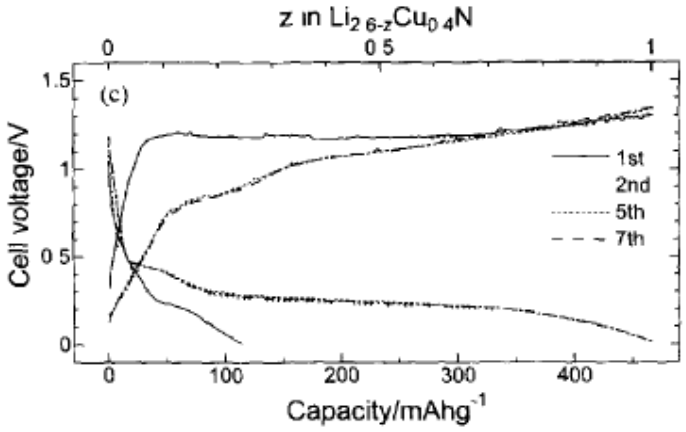


**Figure 4.2 Charge and discharge curves for $Li_{2.6-z}Cu_{0.4}N$ at a current density of 0.3 mA/cm$^2$ [13].**

The initial discharge capacity seen for this material was small in comparison to that of Ni and Co. As lithium is deintercalated during the early stage of the first charge there is a steep part to the curve which corresponds to the first step of the discharge, and this is a consequence of the $Cu^+$ oxidation state being a favourable one, whereas for Ni and Co, there is no similar part to their charge curve, as they can accommodate the vacancies created more easily through oxidising to the 2+ oxidation state.

As can be seen in Figure 4.2, after the first discharge of the cell, the cell capacity remains stable at ~460 mAh/g, and also shows very good reversibility. The second cycle was absent in the original copy and could not be obtained from the author. There is a significant plateau to the first charge curve for the sample and this has been seen previously for the material $Li_{2.60}Co_{0.4}N$[14], and was postulated to be due to a shift from a crystalline phase to an amorphous one. Shodai *et al*. reported a higher capacity for their lithium nitridocobaltate of the same stoichiometry, and this was thought to be due to the use of a different electrolyte which could be influencing different surface chemistry such as surface film formation, and thus the formation of the amorphous phase has been thought to arise from sample/electrolyte interactions[15]. When Nishijima *et al*. used the same electrolyte, they reported similar capacities[13].

From this previous research it can be seen that these materials have been well studied and characterised at the structural level, and have had their resultant properties measured. The course of this study is aimed at investigating the opposite end of the metal dopant scale for these materials, gauging whether

similar structural trends to the rest of the series are observed and fully characterising the structural effects that are caused by such low levels of dopant metal. This will be achieved through the use of conventional synthetic methods and characterisation using different techniques such as X-ray diffraction (XRD), Powder Neutron Diffraction (PND) and Scanning Electron Microscopy (SEM) with Electron-Dispersive X-ray (EDX) spectroscopy.

The potential presence of Li(2) vacancies in these materials will be studied, and as a consequence their resultant magnetic behaviour could be affected, as a result of oxidation of the copper for maintaining charge neutrality. As Asai *et al.*[12] reported for the copper lithium nitrides at the higher end of the scale that the ionic conductivity of these materials decreased with increasing copper content, these materials with low content could prove to have interesting $Li^+$ mobility properties in the future and so full characterisation of the behavioural trends is necessary.

# 4.2 Lithium Copper Nitride

## *4.2.1 Experimental*

Bulk samples of lithium copper nitride were prepared through the synthesis which was detailed in section 2.2.2. Stoichiometric quantities of both copper metal powder (Aldrich 99.5 %) and lithium nitride powder (Aldrich ≥ 99.9% and synthesised in-house for **[5], [7], [9], [11]** and **[14]** from Table 4.3) were ground together and then each pressed into three approximately equal 13 mm diameter pellets. Pellets were stacked one upon the other inside a sandblasted stainless steel crucible or within an acid cleaned copper foil holder within the crucible, which was in turn lowered inside a stainless steel reaction vessel using a nichrome wire cage and sealed under $N_{2(g)}$ (99.999 %). Each of the samples were heated to 973 K for differing lengths of time (2 – 7 days) and then once reacted, the furnace switched off and the reaction allowed to cool to room temperature. The vessels were opened inside a nitrogen-filled glove box and the samples were removed from the crucible, ground and collected into sample vials. The majority of the samples were a black/brown colour.

The magnetic properties of **[6]** and **[13]** (see Table 4.3) were measured by a SQUID (Superconducting Quantum Interference Device) magnetometer at the ISIS facility at the Rutherford Appleton Laboratories with the help of Dr Marek Jura. The samples were prepared for each measurement by the method outlined in Section 2.4 and were measured in a field of 100 Oe in each case. For the two materials, a Zero-Field Cooled (ZFC) measurement and also a Field Cooled (FC) measurement was carried out. The ZFC measurement was made by cooling the sample down to 2 K in the absence of a field and then turning the field on, and measuring the magnetisation upon warming the material to 200 K, and the FC measurement by cooling the sample down in the presence of a field and then measuring the magnetisation upon warming to 200 K.The measured moment output by the instrument was corrected for the diamagnetic effects of the core electrons and also the gelatine capsule.

## *4.2.2 Results and Discussion*

Table 4.3 below shows an overview of the reactions carried out by the method above for the research purposes of this work.

**Table 4.3 Reaction conditions and setup for bulk synthesis of materials.**

| Label | Nominal Stoichiometry | Temperature /K | Reaction Time | Setup |
|---|---|---|---|---|
| **[5]** | $Li_{2.971}Cu_{0.029}N$ | 973 | 2 days | Foil + Crucible |
| **[6]** | $Li_{2.95}Cu_{0.05}N$ | 973 | 2 days | Crucible |
| **[7]** | $Li_{2.939}Cu_{0.061}N$ | 973 | 2 days | Foil + Crucible |
| **[8]** | $Li_{2.90}Cu_{0.1}N$ | 973 | 2 days | Crucible |
| **[9]** | $Li_{2.971}Cu_{0.029}N$ | 973 | 3 days | Foil + Crucible |
| **[10]** | $Li_{2.95}Cu_{0.05}N$ | 973 | 3 days | Foil + Crucible |
| **[11]** | $Li_{2.939}Cu_{0.061}N$ | 973 | 3 days | Foil + Crucible |
| **[12]** | $Li_{2.90}Cu_{0.1}N$ | 973 | 3 days | Foil + Crucible |
| **[13]** | $Li_{2.95}Cu_{0.05}N$ | 973 | 7 days | Crucible |
| **[14]** | $Li_{2.939}Cu_{0.061}N$ | 973 | 4 days | Foil + Crucible |

Samples were prepared for XRD characterisation as per section 2.3.1.2. Simple phase characterisation of the samples was carried out room temperature on a Bruker d8 diffractometer using Cu $K_\alpha$ radiation ($\lambda$ = 1.5406 Å) and phase comparisons made using the ICSD database and PowderCell 2.4. A typical powder pattern is shown in Figure 4.3.

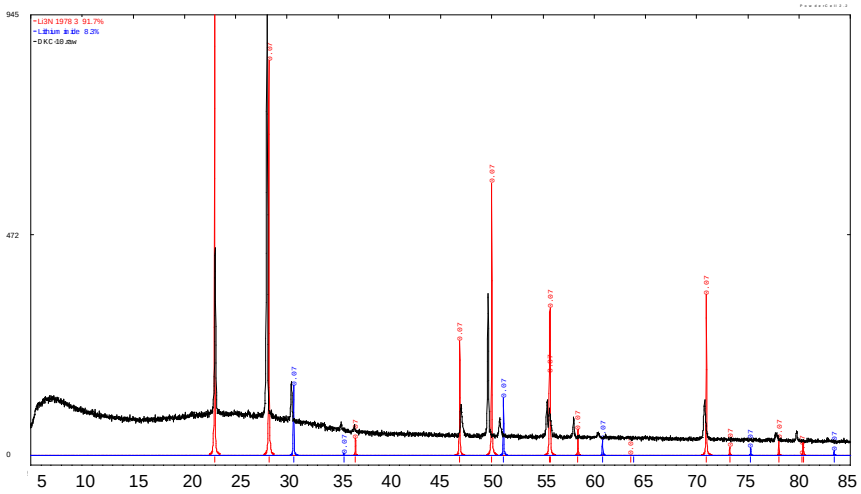


**Figure 4.3 XRD pattern of $Li_{2.971}Cu_{0.029}N$ [9] (black) referenced against $Li_3N$ (red) and $Li_2NH$ (blue). X-axis is 2θ and y-axis is intensity.**

As can be seen from the XRD pattern for the material above, this particular sample matches closely to the pattern of $Li_3N$ the slight shift in the peak positions is indicative of Cu substitution. There is also presence of ~9 vol % lithium imide impurity in the sample and the same impurity is present in samples **[11]**, **[5]**, **[7]** and **[14]**. For samples **[10], [12], [8]** and **[13]** lithium oxide is the only impurity. Sample **[6]** contains both oxide and imide impurity but only a very small amount of the latter. The presence of these impurities is likely to be as a consequence of exposure to air, either in the glove box due to a poor transfer chamber seal or catalysts / sieves needing regenerated, or through a poor seal from the O-ring of the reaction vessel. The lack of lithium hydroxide as an impurity suggests the impurities were a consequence of air rather than moisture.

### 4.2.2.1 Refinement of XRD data

Capillaries were run on the Bruker d8 for 12 hours over a 2θ range of 5 – 90 for data of quality viable for Rietveld refinement. Rietveld refinement was carried out with the use of GSAS (General Structure Analysis System) through the Expgui interface[16]. Starting models for the samples were based upon that of the parent material, lithium nitride, with the copper metal placed on the Li(1) site such that the sum of copper and lithium at that site was constrained to unity. The occupancies for the two metals were set to correspond to the nominal stoichiometries for the materials. Firstly the background of the model was

fitted, using function type 1 (Chebyschev polynomial of the first kind), and then the zero-point was allowed to refine freely. Lattice parameters were subsequently allowed to vary, followed by peak profiles (profile type 2, which is a multiterm Simpson's rule integration of the pseudo-Voigt function, in all cases) and once stabilised the fractional occupancy of the Li(1) site was refined. At this point, the Li(2) site was varied, however the site occupancy refined to an unrealistic value of 55 -67 % for each of the four, and thus it was set to 1. The temperature factors for the shared Li(1) site were then allowed to vary followed by the temperature factors of the other two positions, Li(2) and N. Observed-calculated-difference (OCD) plots for selected materials are shown below in Figure 4.4 – Figure 4.7. OCD plots for all the materials discussed in this chapter are presented in the appendix.

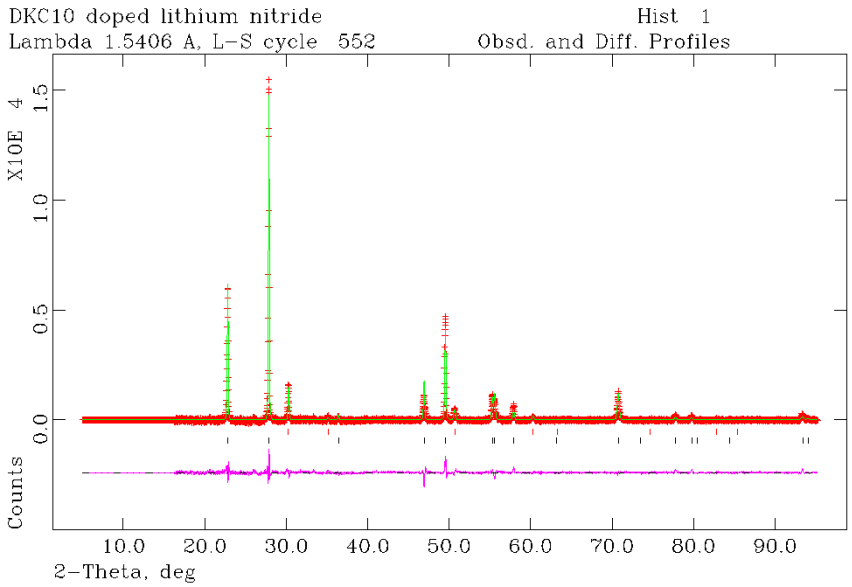


**Figure 4.4 OCD plot from GSAS refinement of XRD data for $Li_{2.971}Cu_{0.029}N$ [9]. Observed data is in red, calculated in green and the difference of the two profiles is shown in pink. The nitride-type phase is assigned blue tickmarks and imide impurity phases red tickmarks.**

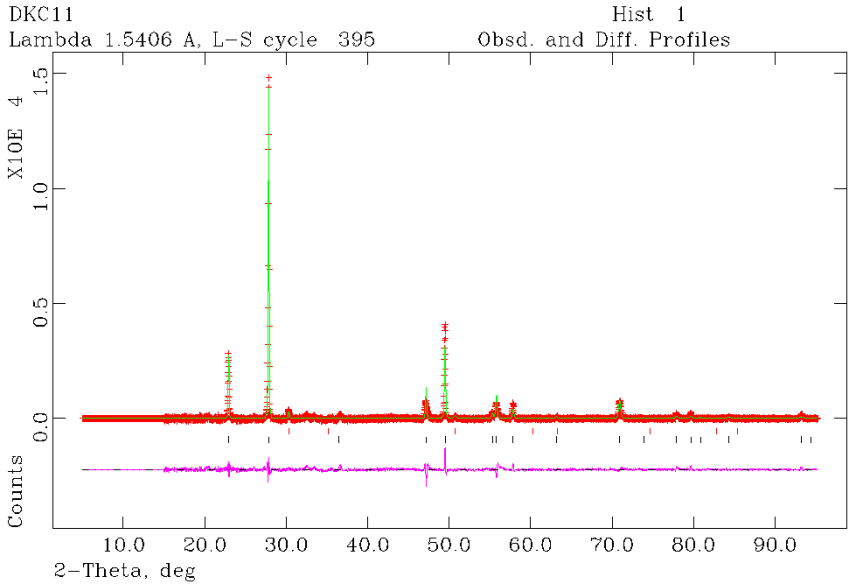


**Figure 4.5 OCD plot from GSAS refinement of XRD data for $Li_{2.939}Cu_{0.061}N$ [11].Observed data is in red, calculated in green and the difference of the two profiles is shown in pink. The nitride-type phase is assigned blue tickmarks and imide impurity phases red tickmarks.**

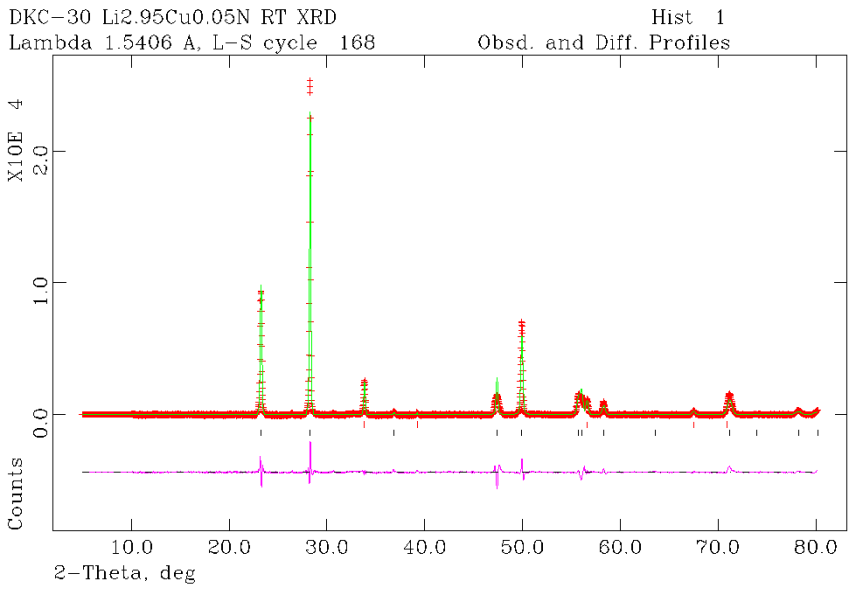


**Figure 4.6 OCD plot from GSAS refinement of XRD data for $Li_{2.95}Cu_{0.05}N$ [10]. Observed data is in red, calculated in green and the difference of the two profiles is shown in pink. The nitride-type phase is assigned blue tickmarks and oxide impurity phases red tickmarks.**

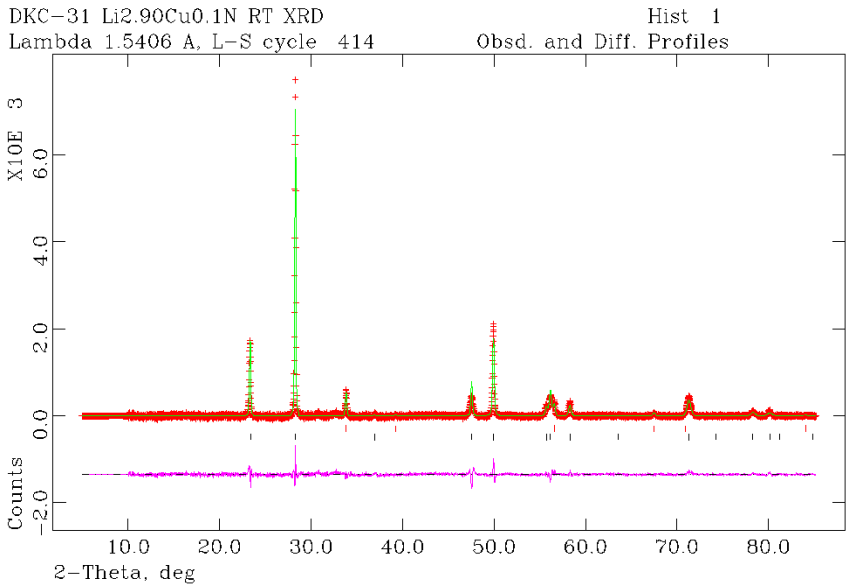


**Figure 4.7 OCD plot from GSAS refinement of XRD data of $Li_{2.90}Cu_{0.1}N$ [12]. Observed data is in red, calculated in green and the difference of the two profiles is shown in pink. The nitride-type phase is assigned blue tickmarks and oxide impurity phases red tickmarks.**

The refinements confirm that these materials retain the $Li_3N$-type structure. The materials above were selected for comparison reasons as they were all reacted for the same temperature, length of time and with the same reaction setup, the only difference being the metal dopant level. Selected data from these refinements can be found in Table 4.4 below, and again full details can be found for these refinements in the appendix.

**Table 4.4 Selected data from GSAS for Rietveld refinement of XRD measurements for materials in the series $Li_{3-x-y}Cu_xN$. *occ denotes site occupancy**

| **Sample nominal stoichiometry** | $Li_{2.971}Cu_{0.029}N$ **[9]** | $Li_{2.939}Cu_{0.061}N$ **[11]** | $Li_{2.95}Cu_{0.05}N$ **[10]** | $Li_{2.90}Cu_{0.1}N$ **[12]** |
|---|---|---|---|---|
| **Reaction T /K** | 973 | 973 | 973 | 973 |
| ***a* / Å** | 3.6609(1) | 3.66601(6) | 3.6627(2) | 3.6632(2) |
| ***c* / Å** | 3.8516(1) | 3.8334(1) | 3.8479(2) | 3.8364(2) |
| **Cu (x) occ*** | 0.074(1) | 0.122(2) | 0.054(1) | 0.097(1) |
| **Li(2) occ*** | 1.000 | 1.000 | 1.000 | 1.000 |
| $\chi^2$ | 2.714 | 3.530 | 6.489 | 1.960 |
| $R_p$ | 0.0343 | 0.0411 | 0.0561 | 0.0499 |
| $wR_p$ | 0.0498 | 0.0601 | 0.0854 | 0.0675 |

From the data presented above it can be seen that for **[9]** and **[11]** there is a higher copper content than would be expected from the amount of copper metal reactant that was added at the start of the reaction. There are some factors that could lead to this observation, the possibility of evaporation of the $Li_3N$, reaction with the copper metal foil (which is supported by the presence of a dark layer on the foil post reaction) and also user errors are more prominent when working with such small quantities of metal. The most likely is the reaction with the copper foil, as the foil used for **[9]** and **[11]** was fresh and the same foils were then used for **[10]** and **[12]**, and as can be seen, for the latter two there was a copper content much closer to that which was expected. This would appear to suggest that the copper metal that was present in the fresh foils had leeched out in the first two reactions and by the second set there was no reaction then with the foil. Table 4.5 below shows interatomic distances for the refined model for the materials above and Figure 4.8 shows a comparison of bond lengths as a function of copper dopant level.

**Table 4.5 Interatomic distances from Rietveld refinement against XRD data for selected samples from the series $Li_{3-x-y}Cu_xN$.**

| Sample refined stoichiometries | Li(1)/M-N | Li(2)-N | Li(1)/M-Li(2) |
|---|---|---|---|
| $Li_{2.926}Cu_{0.074}N$ **[9]** | 1.92581(6) | 2.11372(6) | 2.85947(6) |
| $Li_{2.878}Cu_{0.122}N$ **[11]** | 1.91670(6) | 2.11668(4) | 2.85553(5) |
| $Li_{2.946}Cu_{0.054}N$ **[10]** | 1.92401(8) | 2.11474(8) | 2.85901(8) |
| $Li_{2.903}Cu_{0.097}N$ **[12]** | 1.91819(9) | 2.11504(9) | 2.85508(9) |

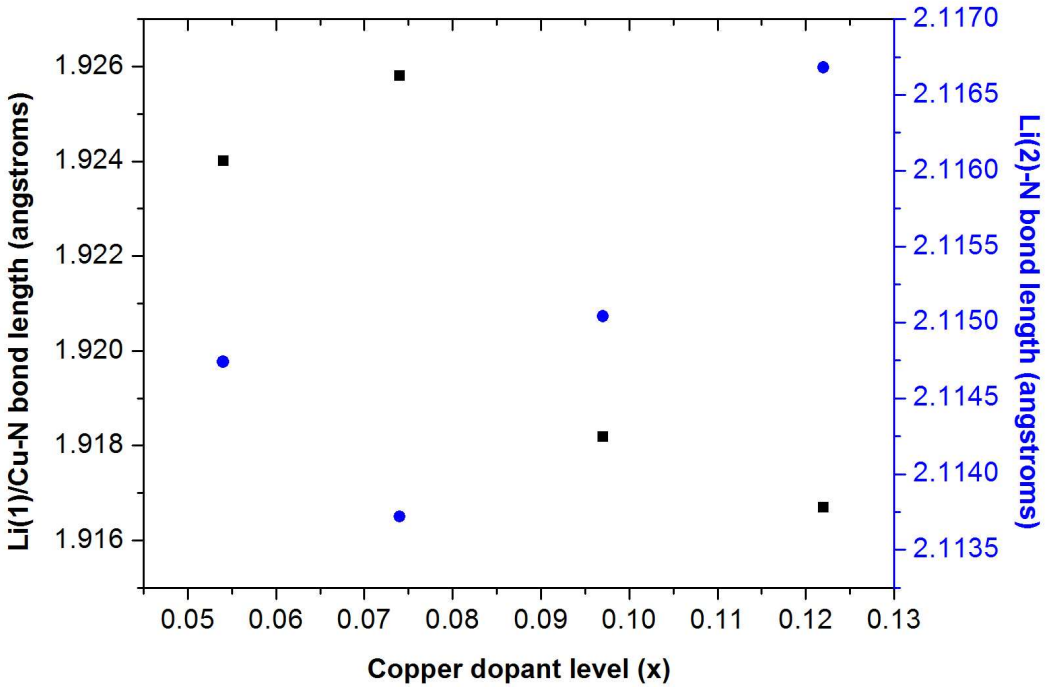


**Figure 4.8 Variation of bond lengths from Rietveld refinement against XRD data for selected samples from the series $Li_{3-x-y}Cu_xN$. Blue dots represent Li(2)-M bond lengths and black squares represent Li(1)/Cu-N bond lengths.**

From the information shown above, it can be seen that the unit cell parameters and atomic distances for this series of materials, other than **[10],** follow the general trend of a decreasing Li(1)/Cu-N bond length and increasing Li(2)-N bond length with increasing copper content. It would almost suggest that for these materials, the trend of a constant decreasing Li(2)-M and increasing Li(1)/M-N bond does not hold true as you go towards lower copper dopant levels, $x \leq 0.075$. At this stage, site occupancy factors and possible vacancies can not be

well gauged, as X-ray diffraction is a technique that is based upon the electrons of an element and consequently operates as a function of atomic number. Light atoms such as lithium and any potential vacancies will be hard to accurately place or quantify.

#### 4.2.2.2 Refinement of CW neutron data

A more accurate way to assess information from materials of this type is through the use of neutron diffraction. In order to have high enough quantities of the materials to be able to run neutron diffraction experiments, fresh samples were synthesised (materials **[6]**, and **[8]**) and used for these measurements

Constant wavelength measurements were carried out at D1A at the ILL (Institut Laue Langevin) facility in Grenoble (section 2.3.4), which is a high flux powder neutron instrument. The samples for CW measurements were loaded into 13 mm vanadium cans and were then sealed using purpose-made copper gaskets (mp.1357.77 K). As the temperatures of these reactions were to reach 483 K, these gaskets were preferential to traditional indium wire seals (mp.429.75 K). In order to carry the measurements out at variable temperatures, a cryostat and a cryofurnace were employed.

Rietveld refinement against the constant wavelength data was carried out using GSAS (General Structure Analysis System) through the Expgui interface[16] for **[6]** and **[8]**. Data were collected at each temperature using the only detector bank. The starting model was based upon that of the starting material, $Li_3N$, with the transition metal factored in on the Li(1) shared site. The occupancies of the shared site were initially set at fixed values that reflected the nominal stoichiometry of the synthesised material. The background was fitted using function type 1 (Chebyschev polynomial of the first kind) for **[6]** at 389 and 482 K using 10 terms, but fitted graphically for 70 and 293 K using 12 and 10 terms respectively. For sample **[8]** the background was fitted using function type 8 (a linear interpolation formula with greater partitioning at lower d-spacing) for all the temperatures using 20 terms, other than at 70 K which was fitted graphically using 10 terms. Different fits for the background are used as a certain level of pragmatism is required in order to achieve a good model. This is standard practice in crystallography as there may be diffuse scattering and other similar

effects which are more prominent at some temperatures than at others and thus require to be fitted to different equations. For both samples, the peak profiles for the main phase were fitted using peak profile type 4 (convolution of pseudo-Voigt and asymmetry with microstrain broadening) and using profile type 2 (a pseudo-Voigt formula) for the impurity phases. The temperature factors for the atoms were allowed to vary sequentially and then fractional occupancies for the shared Li(1) site were varied. The site occupancy factor of the Li(2) was varied freely and finally once stable, anisotropic temperature factors for all four atoms varied sequentially. The refinement was run through several cycles until it stabilised. Some selected OCD plots from these refinements can be seen below in Figure 4.9-Figure 4.12 where the observed data are in red, the calculated in green and the difference of the two profiles is shown at the bottom with a pink line. Also the tickmarks for the phases present are shown, with the nitride-type phase assigned blue tickmarks and impurity phases red tickmarks. All OCD plots for the refinements are included in the appendix.

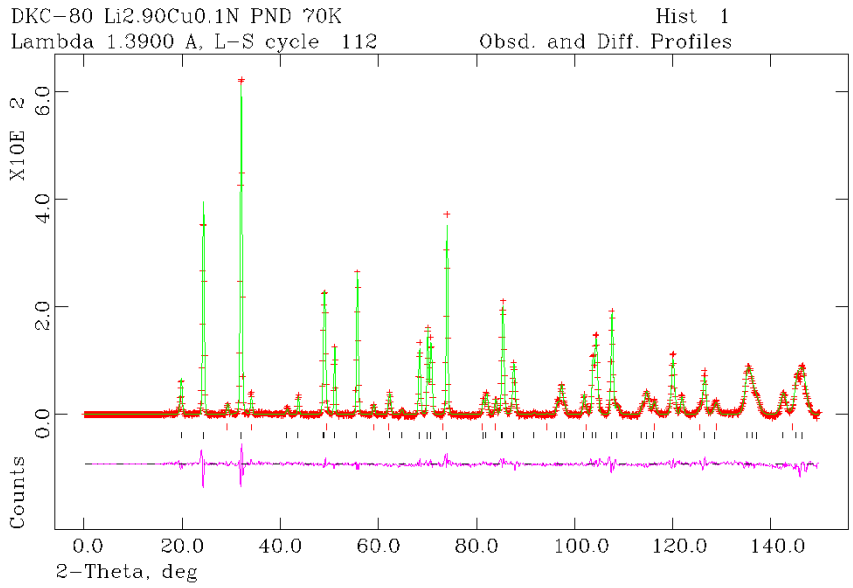


**Figure 4.9 OCD plot from GSAS refinement of PND data for Li2.90Cu0.1N [8] at 70 K. Observed data is in red, calculated in green and the difference of the two profiles is shown in pink. The nitride-type phase is assigned blue tickmarks and oxide impurity phases red tickmarks.**

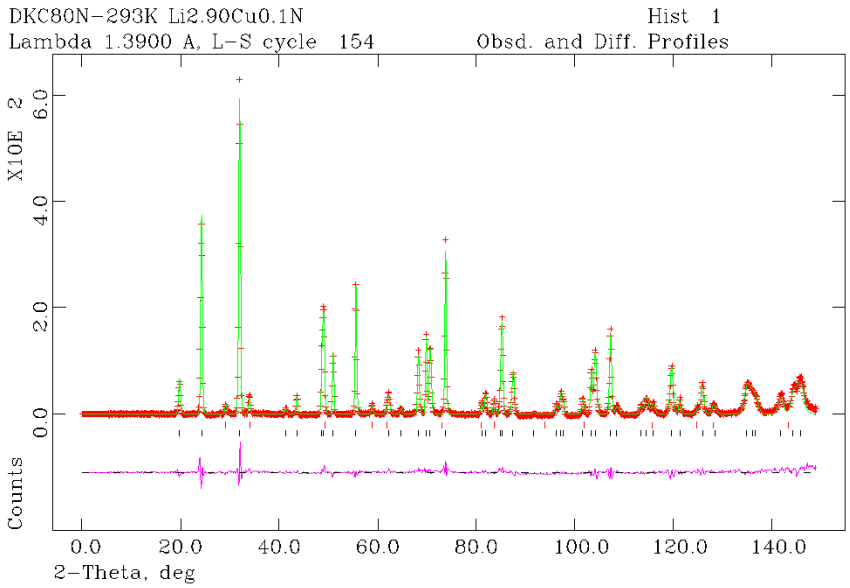


**Figure 4.10 OCD plot from GSAS refinement of PND data for $Li_{2.90}Cu_{0.1}N$ [8] at 293 K. Observed data is in red, calculated in green and the difference of the two profiles is shown in pink. The nitride-type phase is assigned blue tickmarks and oxide impurity phases red tickmarks.**

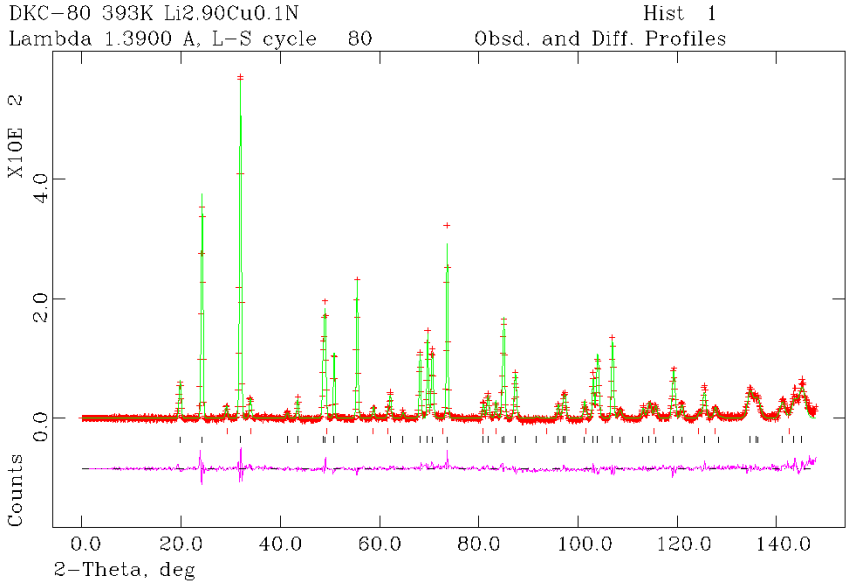


**Figure 4.11 OCD plot from GSAS refinement of PND data for $Li_{2.90}Cu_{0.1}N$ [8] at 393K. Observed data is in red, calculated in green and the difference of the two profiles is shown in pink. The nitride-type phase is assigned blue tickmarks and oxide impurity phases red tickmarks.**

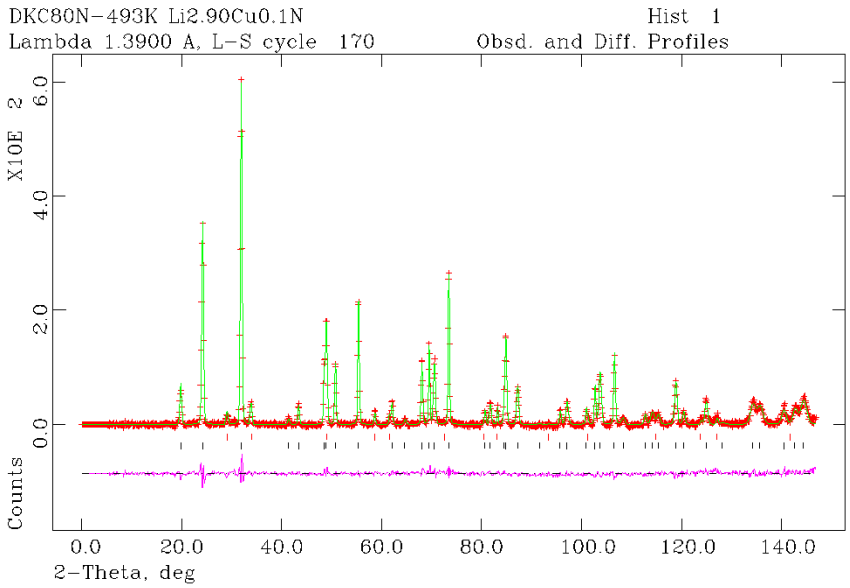


**Figure 4.12 OCD plot from GSAS refinement of PND data for Li2.90Cu0.1N [8] at 493K. Observed data is in red, calculated in green and the difference of the two profiles is shown in pink. The nitride-type phase is assigned blue tickmarks and oxide impurity phases red tickmarks.**

Some selected refinement data **[6]** and **[8]** at various temperatures can be found below in Table 4.6 and Table 4.7 below.

**Table 4.6 Selected data from GSAS refinement of PND measurement of $Li_{2.95}Cu_{0.05}N$ [6] and $Li_{2.90}Cu_{0.1}N$ [8].**

| Sample nominal stoichiometry | Sample refined stoichiometry | T /K | Cu occ* | $R_P$ | $wR_P$ | $\chi^2$ |
|---|---|---|---|---|---|---|
| $Li_{2.95}Cu_{0.05}N$ **[6]** | $Li_{2.95}Cu_{0.05}N$ | 70 | 0.047(5) | 0.0562 | 0.0673 | 2.762 |
| | | 293 | 0.051(5) | 0.0543 | 0.0647 | 2.531 |
| | | 389 | 0.040(5) | 0.0452 | 0.0582 | 1.847 |
| | | 482 | 0.047(5) | 0.0435 | 0.0574 | 1.786 |
| $Li_{2.90}Cu_{0.1}N$ **[8]** | $Li_{2.90}Cu_{0.1}N$ | 70 | 0.087(4) | 0.0488 | 0.0608 | 6.953 |
| | | 293 | 0.094(4) | 0.0429 | 0.0510 | 4.746 |
| | | 393 | 0.100(5) | 0.0433 | 0.0542 | 1.505 |
| | | 493 | 0.096(5) | 0.0441 | 0.0559 | 1.291 |

*occ denotes site occupancy

**Table 4.7 Unit cell and interatomic distance data from GSAS refinement of PND measurement of $Li_{2.95}Cu_{0.05}N$ [6] and $Li_{2.90}Cu_{0.1}N$ [8].**

| Sample | T /K | *a* /Å | *c* /Å | V /Å$^3$ | Li(1)/Cu-N /Å | Li(2)-N /Å |
|---|---|---|---|---|---|---|
| $Li_{2.95}Cu_{0.05}N$ **[6]** | 70 | 3.6610(2) | 3.8545(2) | 44.741(5) | 1.92723(12) | 2.11381(9) |
| | 293 | 3.6612(2) | 3.8548(2) | 44.748(5) | 1.92738(12) | 2.11389(9) |
| | 389 | 3.6703(2) | 3.8587(2) | 45.016(6) | 1.92934(12) | 2.11914(10) |
| | 482 | 3.6787(2) | 3.8610(3) | 45.250(6) | 1.93051(14) | 2.12400(12) |
| $Li_{2.90}Cu_{0.1}N$ **[8]** | 70 | 3.6556(1) | 3.8409(2) | 44.451(4) | 1.92047(9) | 2.11065(7) |
| | 293 | 3.6644(1) | 3.8421(2) | 44.860(4) | 1.92105(10) | 2.11576(8) |
| | 393 | 3.6730(1) | 3.8447(2) | 44.920(5) | 1.92233(10) | 2.12073(8) |
| | 493 | 3.6812(2) | 3.8471(2) | 45.149(5) | 1.92356(11) | 2.12547(8) |

From these refinements it can be seen that these materials are of the lithium nitride structure type with the formula $Li_{2.95}Cu_{0.05}N$ for **[6]** and $Li_{2.90}Cu_{0.1}N$ for **[8]**. The copper content x (and site occupancy factor for Li(1)) are all within three times the deviation of the nominal figure, 3σ, which is a well defined way of quoting a standard deviation from statistics and is often used for the purposes of crystallography. Quoting of a standard deviation to 3σ comes from a bell curve distribution for a value which has been defined statistically accounts for 99.73 % of all the values then being within these limits. Therefore the refined stoichiometries all agree well with the nominal stoichiometries across the four temperatures for each of the materials.

One of the most important observations that can be made from these variable temperature experiments is that there is no evidence of formation of new phases at lower temperatures. The refined metal occupancies for these materials at room temperature correspond well to the occupancies from the refinement of the room temperature XRD measurement for both materials and both display an increase in the *a*-parameter and decrease in *c*-parameter upon increase of copper content with comparison to that of the parent compound $Li_3N$[11]. There is a larger variation in the *a*-parameter at higher temperatures than is seen for the *c*-parameter and this shows anisotropic thermal expansion is present for these materials, which has been seen previously in both lithium

nitride and nitridometallates, and this can be seen in Figure 4.13 and Figure 4.14 below.

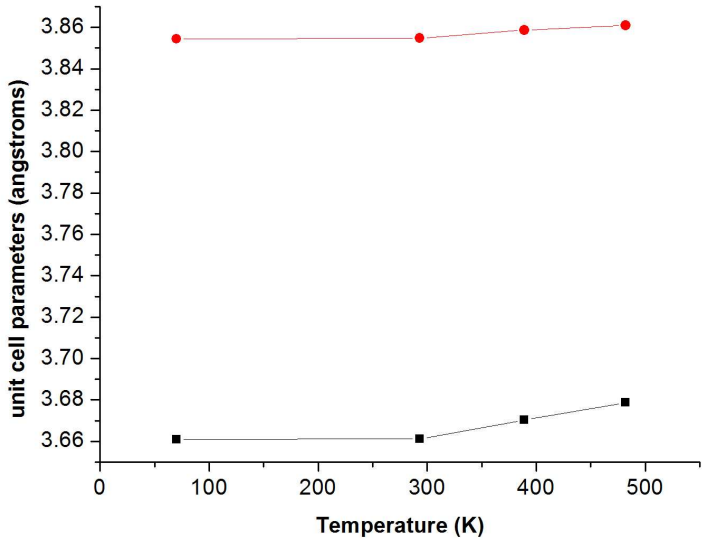


**Figure 4.13 Variation of unit cell parameters as a function of temperature for [6]. Black markers represent the *a*-parameter and red markers represent the *c*-parameter.**

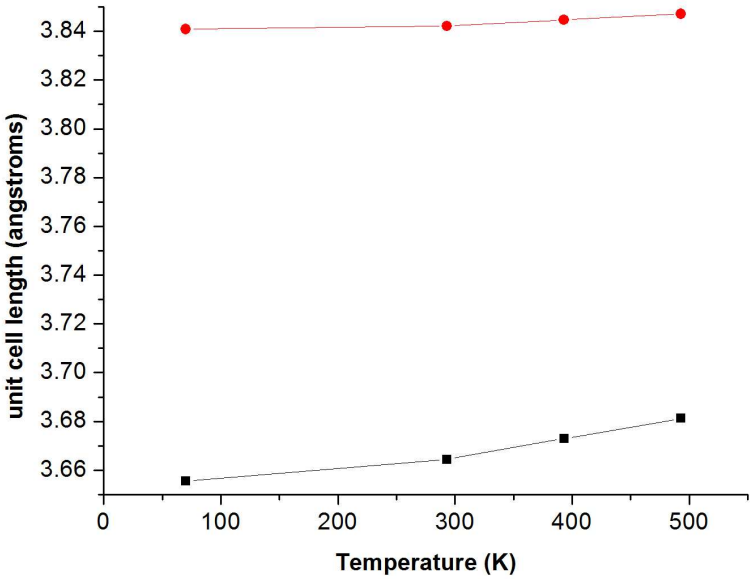


**Figure 4.14 Variation of unit cell parameters as a function of temperature for [8]. Black markers represent the *a*-parameter and red markers represent the *c*-parameter.**

For these refinements, when the occupancy of the Li(2) site was allowed to vary freely, the refined value settled at a value just above one, and therefore it was fixed as one. This would suggest that there are no vacancies present in these

materials, and that isovalent substitution of the copper metal has taken place and it is thus in the $Cu^{+}$ oxidation state. Given the previously observed trends in vacancy concentration with time and temperature[17] lack of vacancy generation is likely to be due to the short reaction time of 2 days. Thus it is likely that a longer length of reaction time is required to induce vacancies in these materials. In order to gauge if these trends operate similarly at this lower level of metal doping, a material of a similar composition to $Li_{2.95}Cu_{0.05}N$ **[6]** was synthesised under the same reaction conditions only this time with a longer reaction time of 7 days, $Li_{2.95}Cu_{0.05}N$ **[13].**

#### 4.2.2.3 Refinement of ToF neutron data

ToF (Time of Flight) powder neutron diffraction measurements were made on **[13]** using the instrument GEM at the ISIS facility at the Rutherford Appleton Laboratories. The sample was placed inside a 13 mm vanadium can and the height marked on the can in order to align with the centre of the beam. The can was sealed using allen bolts and a small circle of indium wire to form a seal. Rietveld refinement of the ToF data was once again carried out using GSAS (General Structure Analysis System) through the Expgui interface[16].

The starting model was based upon that of the starting material, $Li_3N$, with the transition metal factored in on the Li(1) shared site. The occupancies of the shared site were initially set at fixed values that reflect the nominal stoichiometry of the synthesised material and constrained to total 100 % occupancy. Only the 3 highest angle banks of data were loaded in as separate histograms and the unit cell parameters and scale factor were refined initially across all of the three of the histograms in the same way. The background was refined using function type 7 (a linear interpolation function) and 12 terms for bank 6 but 8 terms for the other two banks. The peak shapes were refined separately for each histogram using peak shape type 2 (Ikeda-Carpenter function with pseudo-Voigt convolution) for both the main phase and the impurity phase. Once the fit was stable, the temperature factors were constrained and refined isotropically along with the fractional occupancies of the shared site. Further terms for the peak shape were then introduced and the fractional occupancy of the Li(2) site was then allowed to vary freely. A term for sample absorption was introduced at this stage and finally the anisotropic temperature factors for all of

the atoms were refined. The OCD plots for the three histograms can be seen below in Figure 4.15 - Figure 4.17.

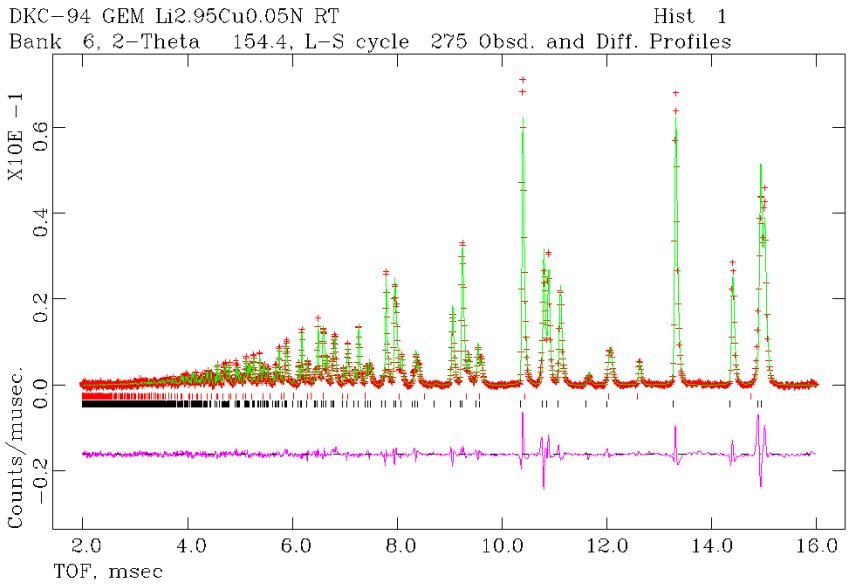


**Figure 4.15 OCD plot from GSAS refinement of ToF data for $Li_{2.95}Cu_{0.05}N$ [13] from 2θ 154.4° detector. Observed data is in red, calculated in green and the difference of the two profiles is shown in pink. The nitride-type phase is assigned blue tickmarks and oxide impurity phases red tickmarks.**

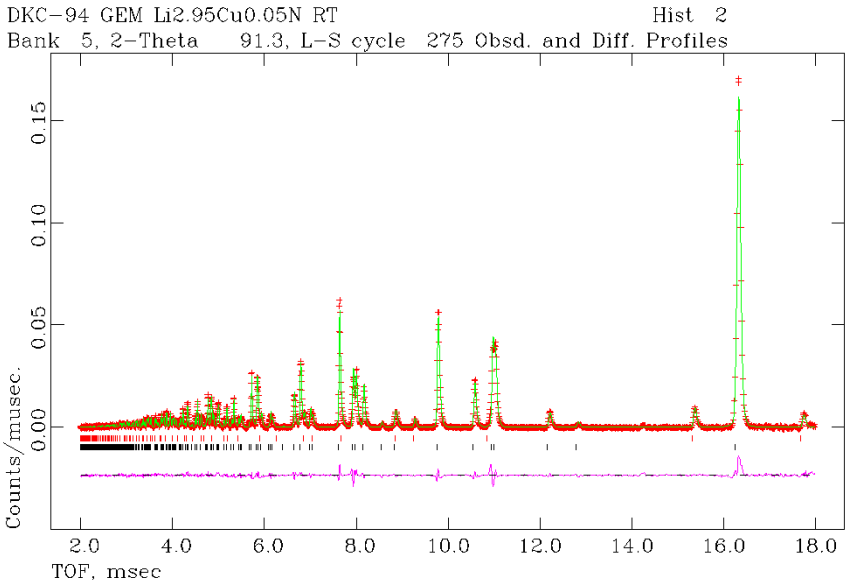


**Figure 4.16 OCD plot from GSAS refinement of ToF data for $Li_{2.95}Cu_{0.05}N$ [13] from 2θ 91.3° detector. Observed data is in red, calculated in green and the difference of the two profiles is shown in pink. The nitride-type phase is assigned blue tickmarks and oxide impurity phases red tickmarks.**

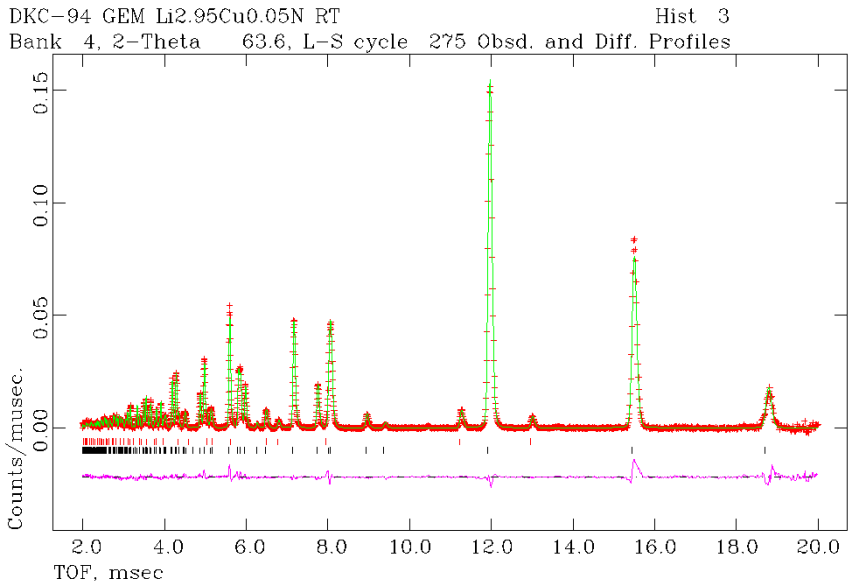


**Figure 4.17 OCD plot from GSAS refinement of ToF data for $Li_{2.95}Cu_{0.05}N$ [13] from 2θ 63.6° detector. Observed data is in red, calculated in green and the difference of the two profiles is shown in pink. The nitride-type phase is assigned blue tickmarks and oxide impurity phases red tickmarks.**

Some selected data from the refinements are shown below in Table 4.8 and Table 4.9.

**Table 4.8 Selected data from GSAS refinement of ToF data for $Li_{2.95}Cu_{0.05}N$ [13].**

| Sample nominal stoichiometry | Refined stoichiometry | Hexagonal, P6/*mmm* | | | | |
|---|---|---|---|---|---|---|
| | | Li(2) occ* | Cu occ* | $R_P$* | $wR_P$* | $\chi^{2}$* |
| $Li_{2.95}Cu_{0.05}N$ **[13]** | $Li_{2.765}Cu_{0.057}N$ **[13]** | 0.911 (8) | 0.057 (2) | 0.0361 | 0.0378 | 5.218 |

*occ denotes site occupancy

**Table 4.9 Selected unit cell data from GSAS refinement of ToF data for $Li_{2.95}Cu_{0.05}N$ [13].**

| Sample | *a* /Å | *c* /Å | V /Å$^3$ | Li(1)/Cu-N /Å | Li(2)-N /Å | Li(1)/Cu-Li(2) /Å |
|---|---|---|---|---|---|---|
| $Li_{2.765}Cu_{0.057}N$ **[13]** | 3.66709(6) | 3.85199(8) | 44.860(2) | 1.92600(4) | 2.11730(4) | 2.86224(4) |

The higher copper content in **[13]** in comparison to **[6]**, manifests itself with a slightly shorter Li(1)-N bond due to a greater extent of covalent character now in the bond, (*c* is 3.8548(2) Å in **[6]** as opposed to 3.85199(8) Å in **[13]** which has been reacted longer. This material also displays a much longer Li(2)-N bond and unit cell *a*-parameter, 3.6612(2) Å in material **[6]** as opposed to 3.66709(6) Å in material **[13].** The increase in the *a*-parameter is likely to arise from an increased copper content couple with the presence of vacancies in this material (a vacancy concentration at the Li(2) site of 8.9 %). This vacancy would give rise to the material being of the formula $Li_{2.765}Cu_{0.057}N$ when the general formula is $Li_{3-x-y}Cu_xN$, and thus x = 0.057 and y = 0.178. This would suggest that the nominal oxidation state of the copper metal in this material is +4.12 in order to maintain charge neutrality and consequently suggests that aliovalent substitution is taking place in this particular material. If this were a true representation of the oxidation state of the metal then this would be a very rare situation as $Cu^{4+}$ is very rarely found in other areas of chemistry and is the highest permissible oxidation state of copper. This would appear to suggest that this oxidation state is not a true representation of what is taking place and as with the studies in other sections of this work. As has been described previously, for the lithium nitridocobaltate $Li_{2.60}Co_{0.4}N$[18-19], when this material had lithium extracted from it creating the material $Li_{1.0}Co_{0.4}N$, if it were to be assumed that the lithium were compensating for all of the charge, then this would lead to an oxidation state of +5. This is clearly unrealistic, and through the use of electron energy-loss spectroscopy (EELS), it was found that there were significant holes in the nitrogen 2p orbital, and as a result, the nitrogen could be taking part in some of the charge balancing mechanism that was taking place in the material.

It is therefore not completely unlikely that a similar mechanism is taking place for the materials studied here. It is a strong possibility that for these materials both nitrogen and copper are counterbalancing the charge that remains as a result of the lithium vacancies. The use of core X-ray absorption near-edge spectroscopy (XANES) would be an extremely useful tool for the further study of the materials of this series, as this would elucidate the true oxidation state of the transition metal. If these were to be coupled with some EELS studies, then the oxidation state of both species could be better identified and a more suitable mechanism for the charge balancing of these materials defined.

Figure 4.18 and Figure 4.19 below shows the thermal ellipsoids for the two materials, and what can be seen from this figure is that the ellipsoids for Li(2) in **[13]** are much more elongated in the direction of the *c*-parameter than that of **[6]**, and it has previously been found that Li(2) is the mobile species in $Li^+$ ion conductivity[20-22]. As such, from the thermal ellipsoids it would suggest that the Li(2) atoms in **[13]** are more mobile than that of **[6]** and this could be attributed to the greater vacancies present in the former.

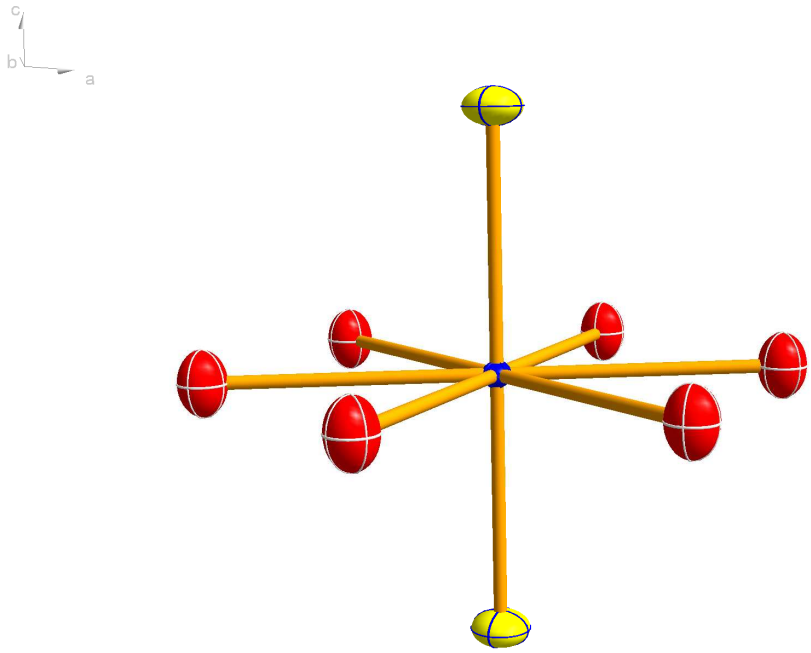


**Figure 4.18 50 % probability thermal ellipsoid representation from PND data for $Li_{2.95}Cu_{0.05}N$ [6].**

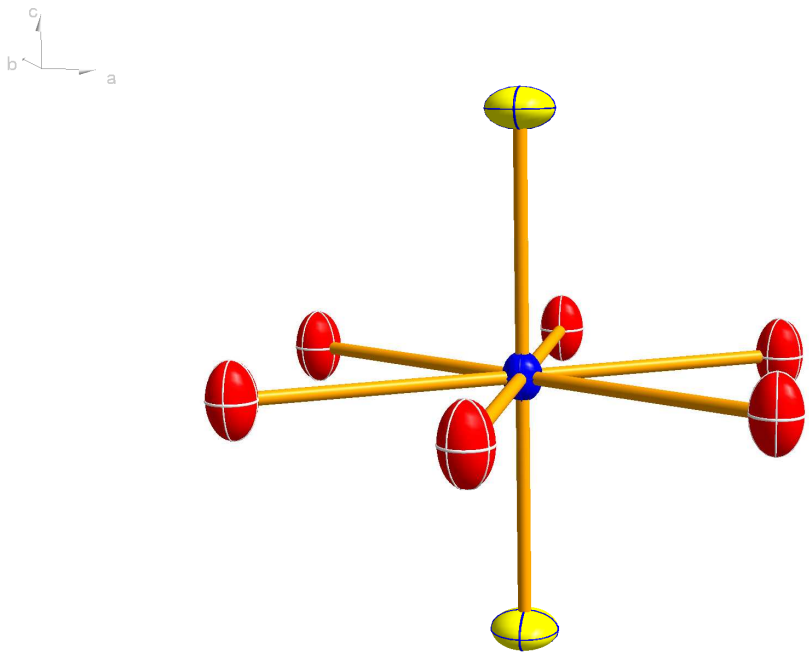


**Figure 4.19 50 % probability thermal ellipsoid representation from PND data for $Li_{2.765}Cu_{0.057}N$ [13].**

As a result of the thermal ellipsoids being elongated parallel to the *c*-plane, and thus the suggestion that the Li(2) ions in these materials are mobile, then these materials could potentially have some interesting electrochemical properties, as it has been previously shown that by doping $Li_3N$ with transition metal you decrease the activation energy, thus facilitating ion migration, but also as there is a greater number of vacancies in these materials there would also be a larger number of charge carriers[12]. From the work of Asai e*t al*. it was shown for the lithium nitridocuprates that, as the copper metal content increased, the ionic conductivity for the resultant material consequently decreased. Altogether this makes these lithium nitridometallates interesting materials electrochemically.

## 4.3 SEM

Scanning Electron Microscopy (SEM) was performed for **[13]** and **[6]** with Energy Dispersive X-ray (EDX) spectroscopy for **[6]** using a Philips XL30 SEM-FEG, and the samples were prepared from a powder of the product pellet post-reaction. The voltage was set at 20 kV in high vacuum mode with a working distance of 10 mm

as outlined in Section 2.5. and Figure 4.20 - Figure 4.22 below show micrographs for these materials taken at different magnifications.

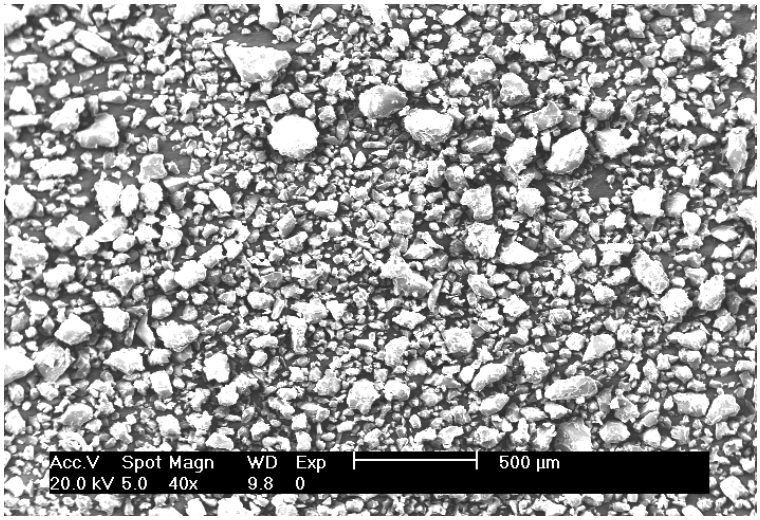


**Figure 4.20 SEM micrograph for [13] at 40x magnification.**

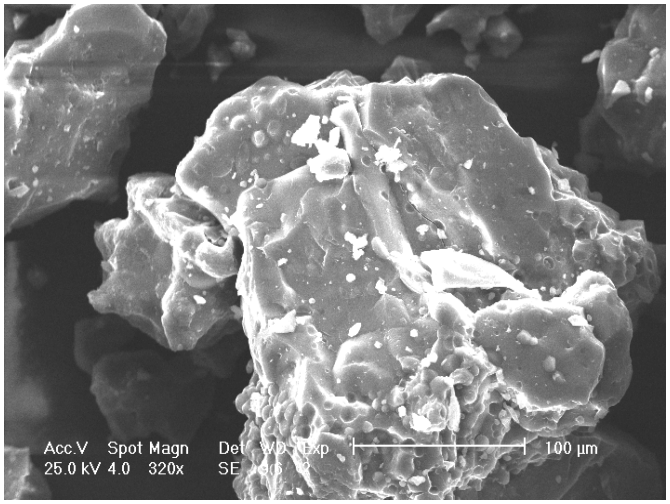


**Figure 4.21 SEM micrograph of [13] at 320 x magnification.**

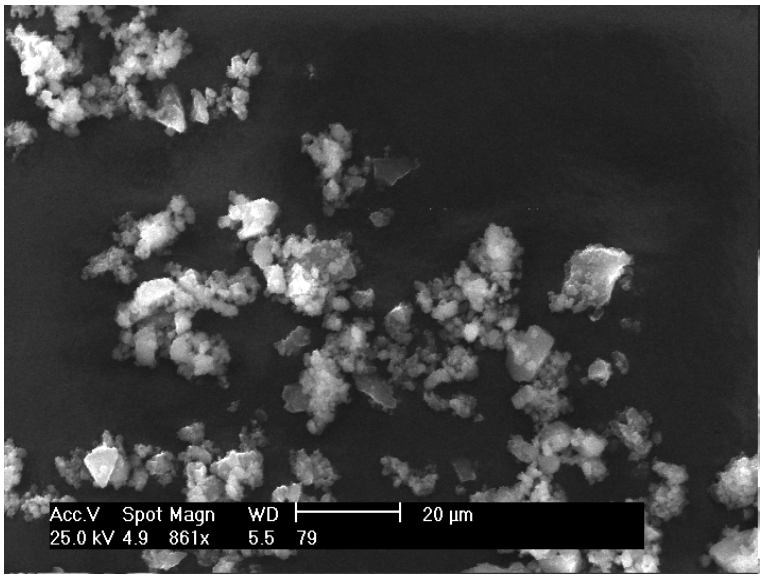


**Figure 4.22 SEM micrograph of [6] at 861 x magnification.**

From the micrographs it would seem that both are granular powders with large grains, ~100 µm in width on average for **[13]**, and ~5 µm in width on average for **[6]**. For **[13]** the grains do not appear to be agglomerates of smaller granules, as was seen in section 2.2.5 for **[4]** which had been reacted for 7 days also. However it does once again show that the longer reaction time yields a larger particle size.

For EDX analysis of these materials, it is difficult to differentiate between oxygen and nitrogen atoms as they are close in atomic weight, and due to the fact that the SEM tabs get exposed to the air for a brief moment upon transfer to the SEM carousel, there will be a slight presence of oxygen in the sample. As such, the nitrogen and oxygen content are considered to be as one and this is then compared to the copper metal content to find the Cu : N ratio. For $Li_{2.95}Cu_{0.05}N$ **[6]** the Cu : N ratio was found to be in close agreement to the refined metal occupancies with 5.95 : 94.05. EDX was not possible for **[13]** as there was an instrument failure which has yet to be resolved. Full data from EDX analysis for **[6]** is provided in the appendix.

## 4.4 Magnetic measurements

A plot of molar susceptibility as a function of temperature for both FC and ZFC measurements for **[6]** and **[13]** can be seen in Figure 4.23 and Figure 4.24.

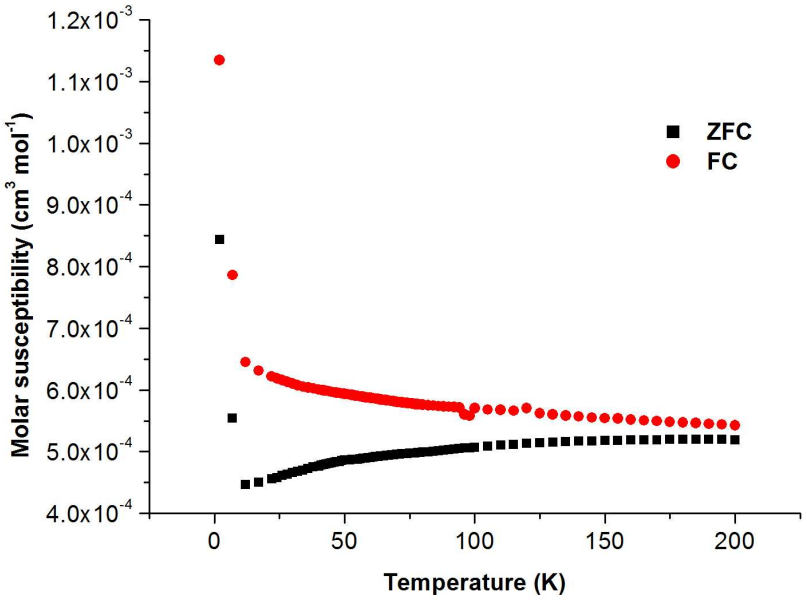


**Figure 4.23 Field-Cooled and Zero-Field Cooled plots of molar susceptibility with varying temperature for $Li_{2.95}Cu_{0.05}N$ [6].**

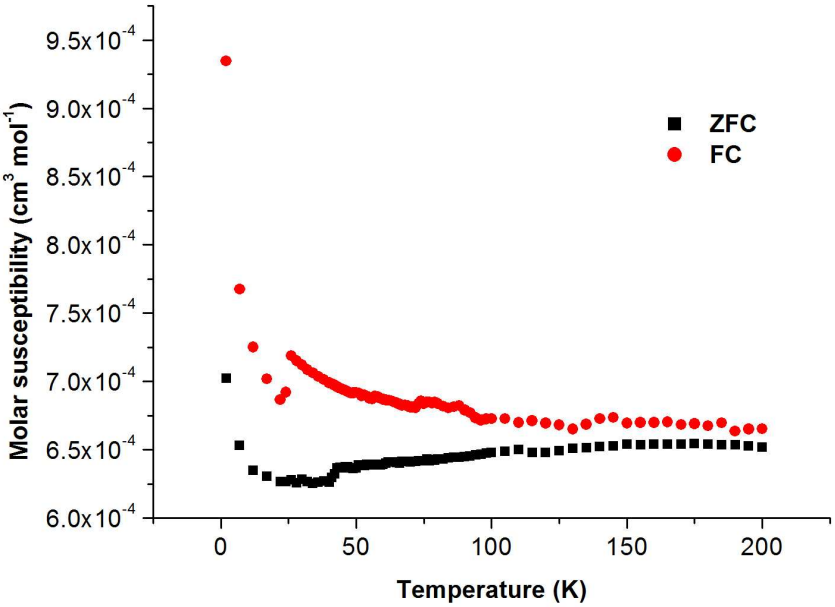


**Figure 4.24 Field-Cooled and Zero-Field Cooled plots of molar susceptibility with varying temperature for $Li_{2.765}Cu_{0.057}N$ [13].**

As can be seen for both the materials [6] and [13], the plot of magnetisation as a function of temperature is markedly different to that of the lithium nitridocobaltates seen from section 3.0 as there is no cusp to the ZFC which is indicative of the spin-glass type behaviour which had been observed. Also for the

FC and ZFC plots for [6] and [13] both display an increase in magnetisation with decreasing temperature which for the ZFC plot is the opposite to what was observed for the lithium nitridocobaltates.

For materials [6] and [13] the plot of magnetisation as a function of temperature is temperature independent other than a Curie-Weiss contribution to the magnetisation at lower temperatures. The value for the magnetisation itself is relatively small, and thus the changes in the magnetisation that are seen are also small. This is fairly indicative of behaviour dominated by Pauli paramagnetism and is similar behaviour to that previously seen for this series of materials at higher copper content[9]. At low temperatures there appears to be an ordering transition at ~ 15 K for **[6]** and ~ 22 K for **[13]**. It should be noted, however, that there are a number of apparently anomalous data points in both measurements. It is likely that this is due to errors with the instrument at the time of measurement rather than an impurity in the sample from the preparation, as the samples for magnetic measurements in each chapter of this work were prepared at the same time and the same anomaly does not appear in all of them. The inverse magnetic susceptibility for the two materials as a function of temperature can be seen in Figure 4.25 and Figure 4.26 below.

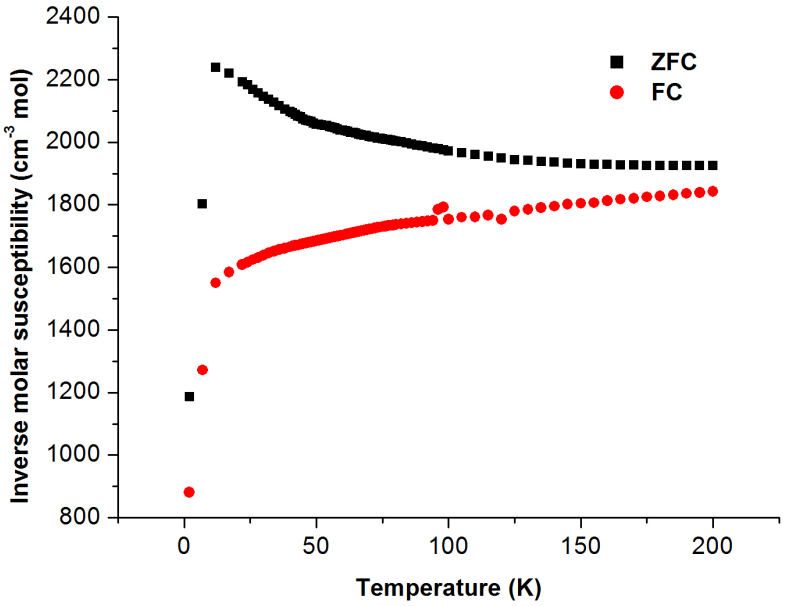


**Figure 4.25 Plot of molar effective magnetic moment versus temperature for $Li_{2.95}Cu_{0.05}N$ [6].**

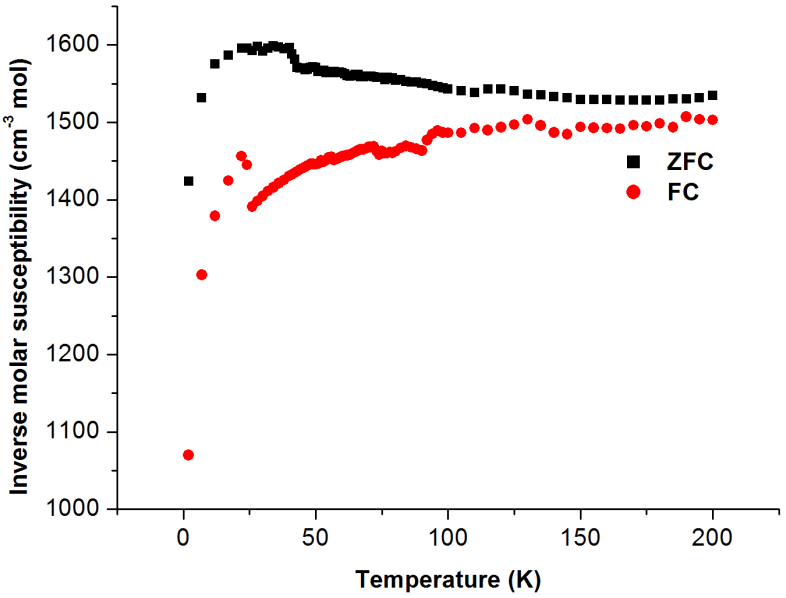


**Figure 4.26 Plot of molar effective magnetic moment versus temperature for $Li_{2.765}Cu_{0.057}N$ [13].**

What this Pauli paramagnetism would seem to be suggesting is that the moments that are seen arise as a consequence of electrons delocalised in a broad band

rather than in orbitals, however this is a feature of magnetism that is more common to materials with higher levels of transition metal, as there are a greater number of Cu ions in the chains that run in the direction of the *c*-axis. This makes them more likely to form a continuous band.

A different consideration could be that the magnetic behaviour that is observed for these materials is as a result of diamagnetism, with a low level of either paramagnetic or ferromagnetic impurity.

## 4.5 Conclusions

The work that has been presented herein has shown that materials doped with low levels of copper retain a $Li_3N$-type phase (hexagonal P6/*mmm*). This was ascertained by X-ray diffraction and both Constant Wavelength and Time of Flight neutron diffraction. The aim of the work was to ascertain what structural effects were induced in these materials by doping low quantities ($x \leq 0.1$) of copper metal and whether the effects that were seen were in line with the trends of what is seen in the previously studied higher-substituted materials[2, 9, 12].

The materials proved difficult to synthesise as pure phase, and this resulted in the presence of some impurities such as lithium oxide and lithium imide. From the X-ray diffraction it seems to suggest that the low-doped materials of this series conformed to the previously seen trends for the high-doped materials, in that as the transition metal is doped into the parent material $Li_3N$ there is an observed decrease in the *c*-parameter, and a consequent increase in the *a*-parameter[3]. This has been previously ascribed to a more covalent character in the Li(1)/M-N bond and also a consequent weakening of the Li(2)-N bond.

The materials were then further analysed by variable temperature neutron diffraction, and the model for the fit of the materials was improved. Most importantly it was found that for these low-doped materials there was no evidence of vacancies within materials that had been synthesised for only 2days at 700 $^{o}$C. However, ToF neutron diffraction was performed on a material which had been synthesised for 7 days at the same temperature and it was found that this material displayed a large lithium vacancy at the Li(2) (8.9 %)site in comparison to the copper content. This would give rise to a potentially large nickel oxidation state of +4.12 which would not be a reasonable oxidation state for the transition metal in this material. As with the lithium nitridocobaltates from section 3.0, a vacancy of 4 % at the nitrogen site, which could be below the detection limits for the powder neutron diffractometer, would lead to a nickel oxidation state of +2.02 which is a more commonly observed oxidation state.

This alternative charge balancing mechanism has been thought to be taking place within this material [13], where the nitrogen is also being oxidised and counterbalancing some of the charge through holes being formed in the 2p orbital, and this has been previously shown to occur for lithium nitridocobaltates[14, 19]. When the two materials of similar copper content were compared, **[6]** and **[13]**, both were found to have a less pronounced difference in the *c*-parameter and Li(1)/Cu-N bond length, but a more pronounced difference observed in the Li(2)-N bond length and subsequently *a*-parameter. This could be as a consequence of the change in the oxidation state of the nitrogen, as in previous materials it has thought that the presence of vacancy should lengthen the Li(2)-N bond length.

Both materials **[6]** and **[13]** showed elongation of the thermal ellipsoids for the Li(2) site parallel to the *c*-axis which suggests that this species is mobile for both materials. This could have a potential benefit for electrochemistry, and could yield a material with a high ionic conductivity. Unfortunately there was not enough time to test this premise. The two materials also displayed magnetic susceptibilities that could be described by paramagnetic dominated by Pauli behaviour, however there is also a possibility that the magnetism seen is a consequence of diamagnetism with either a paramagnetic or ferromagnetic impurity.

It would be interesting to see how these materials perform electrochemically in the future and also to gauge their hydrogen uptake potential, as this has been thought to increase with increased $Li^+$ ion mobility. EELS and XANES measurements would be important also to confirm the oxidation states of the species and help to understand the charge balance mechanism.

## 4.6 References


1. V. W. Saschsze and R. Juza, *Zeitschrift fur Anorganische Chemie*, **259**, (1949), 278.
2. D. H. Gregory, P. M. O'Meara, A. G. Gordon, J. P. Hodges, S. Short and J. D. Jorgensen, *Chem. Mater.*, **14**, (2002), 2063.
3. R. Niewa, Z.-L. Huang, W. Schnelle, Z. Hu and R. Kniep, *Z. Anorg. Allg. Chem.*, **629**, (2003), 1778.
4. M. T. Weller, S. E. Dann, P. F. Henry and D. B. Currie, *J. Mater. Chem.*, **9**, (1998), 283.
5. A. G. Gordon, R. I. Smith, C. Wilson, Z. Stoeva and D. H. Gregory, *Chemistry Communications*, (2004), 2812.
6. R. Juza and F. Hund, *Zeitschrift Fur Anorganische Chemie*, **257**, (1948), 1.
7. R. Juza, H. H. Weber and E. Meyersimon, *Z. Anorg. Allg. Chem.*, **273**, (1953), 48.
8. R. Juza, K. Langer and K. V. Benda, *Angew. Chem. internat. Edit*, **7**, (1968), 360.
9. A. G. Gordon, D. H. Gregory, A. J. Blake, D. P. Weston and M. O. Jones, *Int. J. Inorg. Mater.*, **3**, (2001), 973.
10. J. Yang, K. Wang and J. Xie, *J. Electrochem. Soc.*, **150**, (2003), A140.
11. A. Rabenau and H. Schulz, *Journal of Less-Common metals*, **50**, (1976), 155.
12. T. Asai, K. Nishida and S. Kawai, *Mat. Res. Bull.*, **19**, (1984), 1377.
13. M. Nishijima, T. Kagohashi, Y. Takeda, M. Imanishi and O. Yamamoto, *J. Power Sources*, **68**, (1997), 510.
14. T. Shodai, S. Okada, S. Tobishima and J. Yamaki, *Solid State Ionics*, **86-8**, (1996), 785.
15. Y. M. Kang, S. C. Park, Y. S. Kang, P. S. Lee and J. Y. Lee, *Solid State Ionics*, **156**, (2003), 263.
16. A. C. Larson and R. B. V. Dreele, Los Alamos National Laboratory Report LAUR 86-748, Los Alamos, Editon edn., 2004.
17. Z. Stoeva, R. I. Smith and D. H. Gregory, *Chem. Mater.*, **18**, (2006), 313.

18. T. Shodai, S. Okada, S. Tobishima and J. Yamaki, *J. Power Sources*, **68**, (1997), 515.
19. S. Suzuki, T. Shodai and J. Yamaki, *J. Phys. Chem. Solids*, **59**, (1998), 331.
20. U. V. Alpen, *J. Solid State Chem.*, **29**, (1979), 379.
21. P. Hartwig, W. Weppner and W. Wichelhaus, *Material research bulletin*, **14**, (1979), 493.
22. R. Messer, H. Birli and K. Differt, *J. Phys. C: Solid State Phys.*, **14**, (1981), 2731.

# 5. Lithium nitridonickelates

## 5.1 Introduction

These materials belong to the same general group as those reported in the previous two chapters, namely lithium nitridometallates of the form $Li_{3-x-y}M_xN$, where M = Ni and typically $x \geq 0.1$. As with all of the previously studied materials of the lithium nitridometallate type $Li_{3-x-y}M_xN$, transition metal substitution of the parent metal $Li_3N$ occurs partially at the Li(1) site as can be seen illustrated in Figure 5.1 below.

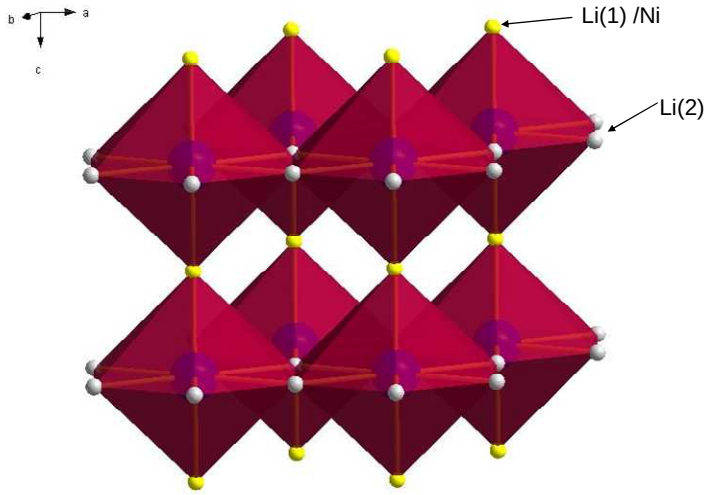


**Figure 5.1 Polyhedral representation of lithium nitridonickelate, $Li_{3-x}Ni_xN$. Ruby polyhedra with blue nitrogen atoms, white intraplanar lithium atoms and yellow interplanar lithium or nickel metal atoms.**

For these materials, similarly to the previous materials, either univalent substitution can take place, whereby the nickel replaces the Li(1) in the +1 oxidation state and thus does not induce any additional vacancies for charge balancing purposes, or aliovalent substitution, whereby the nickel replaces the Li(1) in oxidation states higher than +1, and in the process creates vacancies in order to maintain charge neutrality. In all of these nitridometallates which have been previously studied, vacancies occur at the Li(2) site.

These materials gained much interest during the late 40's and early 50's through the work of Juza *et al.*[1] where the area of interest was to principally investigate

the structural effects that would occur as a result of doping these materials with the transition metals[2-4], whether structural or property. In later years research groups shifted their interest to extending the transition metal substitution levels and in particular Gregory *et al*. studied the high doped materials in depth[5-10]. For the nickel-containing nitridometallates, as the metal dopant level approaches 1 then these materials have a greater tendency to form ordered lithium nitride type structures. As previously discussed in section 1.3.1.1 when the nickel replaces the lithium at the Li(1) site entirely then it forms $Li_5Ni_3N_3$ when y = 0.333 and LiNiN when y = 1 for $Li_{3-x-y}Ni_xN$ and for these two materials the nickel exists in $Ni^{1.33+}$ and the $Ni^{2+}$ oxidations states respectively, and for the former this is a mixing of the +1 and the +2 oxidation states.

Synthesis of these ordered phases has been achieved through controlling synthetic conditions and, in particular, for LiNiN it was achieved through the reaction of $Li_3N$ powder with nickel foil which had been pre-treated with a stream of 20% $H_2$/80% $N_2$ at 873 K for 24 h. The pre-treated foil was reacted for a period of 7 days under $N_{2(g)}$ in a temperature range of 973 – 1023 K and then cooled at 100 K $h^{-1}$ [11]. These reaction conditions give rise to the ordered structure of LiNiN which can be seen in Figure 5.2 and Figure 5.3.

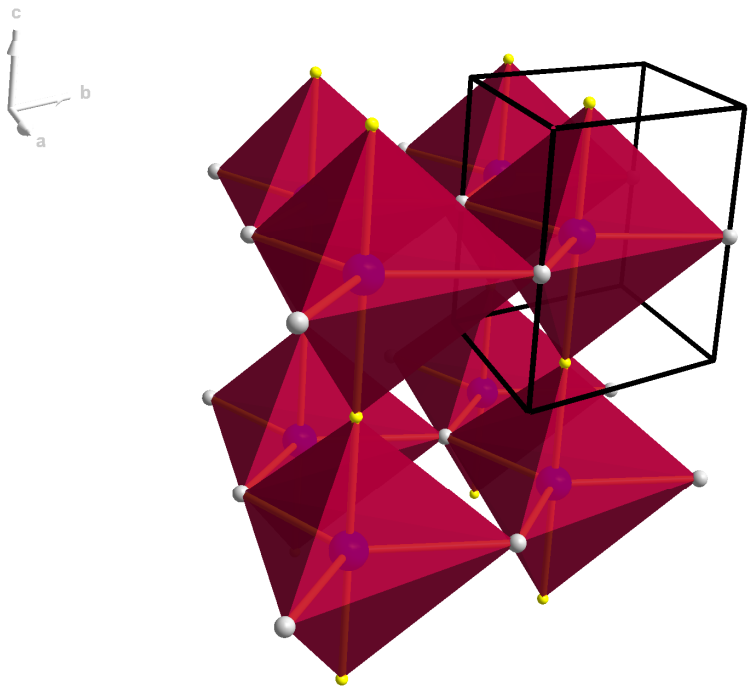


**Figure 5.2 Polyhedral representation of LiNiN, with ruby polyhedra, centred by blue N atoms with white Li atoms and yellow Ni atoms and the unit cell outline in black.**

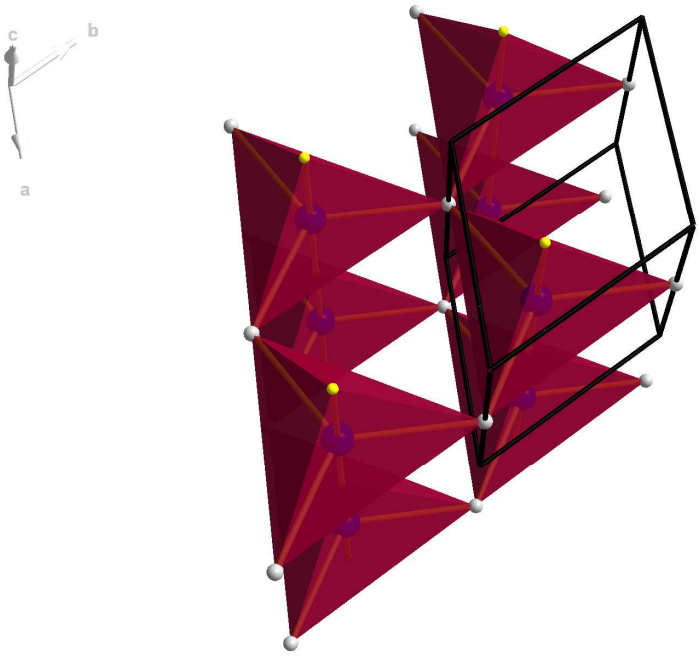


**Figure 5.3 Polyhedral representation of LiNiN, with ruby polyhedra centred by blue N atoms, with white Li(2) atoms and yellow Ni atoms. View skewed along the *c*-axis of the unit cell, with unit cell outlined in black.**

As can be seen from the Figures above, the ordering of the vacancies in this particular nickel-containing nitridometallate leads to the formation of nitrogen centred trigonal bipyramids, with three planar lithium atoms and nickel atoms both above and below the plane at the apices of the bipyramid.

Some of the resultant properties of these materials were investigated, and in particular the $Li^+$ ion diffusion was elucidated by $^7Li$ NMR studies. In lithium nitride, a $^7Li$ NMR study revealed that two separate diffusion pathways occurred at different temperatures[12-13], intralayer diffusion at temperatures up to ~300 K, and at temperatures above this interlayer diffusion takes place either through Li(2)-Li(1)-Li(2) jumps, or through the movement of vacancies or interstitials through the system[14-16]. For LiNiN solid state $^7Li$ NMR experiments revealed that there was only one diffusion mechanism taking place as there was only one spin-lattice relaxation seen, whereas in $Li_3N$ there are two, relating to the intralayer and interlayer diffusion process. The intralayer diffusion parameter obtained from linewidth measurements was in close agreement to that of the spin-lattice relaxation, and so it was thought to be intralayer diffusion taking place in LiNiN[11].

Magnetic studies of the material LiNiN revealed almost temperature independent paramagnetism with a small Curie tail at temperatures below 50 K[10]. These results and a low electrical resistivity at room temperature suggest LiNiN is metallic[10, 17]. The source of this metallic behaviour has been thought to have originated from the presence of infinite $[NiN_{2/2}]$ chains, and thus formation of continuous bonding and anti-bonding bands. The origin of the Curie tail in the susceptibility is likely to be due to partial substitution of $Li^+$ ions for the $Ni^{2+}$ ions at the apices.

The electrochemical performance of LiNiN as an anode material[6] was investigated. Li metal as the cathode material with a C/20 cycle rate and initial discharge capacity of 160 mAh/g. The maximum specific capacity for this material was 420 mAh/g with a voltage cut-off of 1.65 V and after 40 cycles the specific capacity was 341 mAh/g. This high capacity was found to be higher than that of the most well studied disordered nickel nitridometallates. This suggests that this material could be a potential candidate for application as an anode

material for lithium secondary batteries only once its reaction conditions are fine tuned, as currently the high operating voltage would not be advantageous for use in a battery cell.

Several different methods of synthesising the disordered materials have been utilised. The most common methods have been: (i) reactions between the lithium nitride and a transition metal nitride, (ii) reactions between $Li_3N$ powder and a transition metal foil and (iii) reaction of transition metal powders with the lithium nitride powder. The most successful synthesis method for a wide range of compositions has been the third of these above. Gregory *et al*. synthesised a material $Li_{3-x-y}Ni_xN$ where x = 0.79 and y = 0.85[8]and although Niewa *et al*. achieved a single phase nitridometallate with x = 0.85[18], vacancy levels were negligible and the transition metal was deemed to be predominantly univalent i.e. $Li^+$ were replaced by $Ni^+$ as opposed to $Ni^{2+}$ with creation of vacancies.

The main difference between the synthetic methods used by each group was the use of higher reaction temperatures by Gregory *et al*. Niewa *et al*. studied the entire nitridonickelate series from $0 \leq x \leq 0.93$ and a trend was observed, whereby with increasing metal concentration, x, there was a linear decrease in the unit cell *c*-parameter and a slight increase in the *a*-parameter. The cell parameters can be directly related to the Li(1)/Ni-N bond length and the Li(2)-N bond lengths respectively. Figure 5.4 and Table 5.1 below show the evolution of the cell parameters with varying nickel concentration.

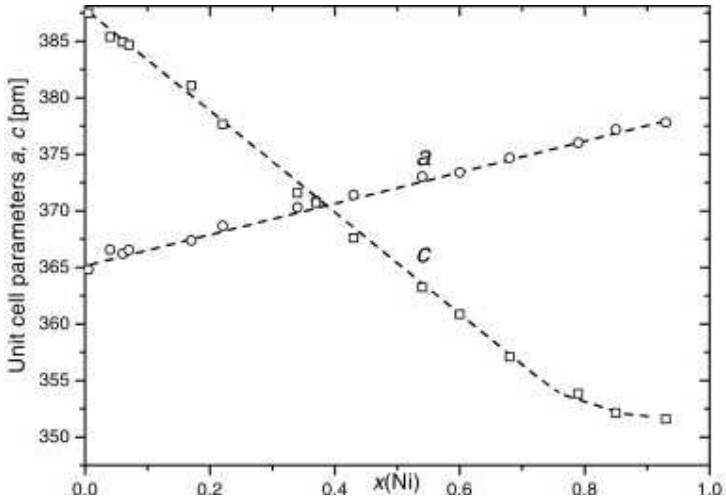


**Figure 5.4 Graph of variation of unit cell parameter *a* and *c* with increasing nickel metal substitution. *a*- unit cell parameters in open circles *c*-parameters open squares[18].**

**Table 5.1 Table of change of unit cell parameters with increasing nickel metal dopant, x, for the material $Li_{3-x}Ni_xN$[18].**

| x(Ni) | *a* / Å | *c* / Å | V / Å $^3$ |
|---|---|---|---|
| **0** | 3.648(1) | 3.875(1) | 44.66(2) |
| **0.04(1)** | 3.6657(14) | 3.8537(14) | 44.84(2) |
| **0.06(1)** | 3.6621(6) | 3.8491(6) | 44.70(1) |
| **0.07(1)** | 3.6654(16) | 3.8469(15) | 44.76(3) |
| **0.17(1)** | 3.6739(18) | 3.8107(18) | 44.54(3) |
| **0.22(1)** | 3.6868(18) | 3.7767(17) | 44.46(3) |
| **0.34(1)** | 3.703(1) | 3.716(1) | 44.13(2) |
| **0.37(1)** | 3.7090(20) | 3.7070(19) | 44.17(3) |
| **0.43(1)** | 3.714(1) | 3.676(1) | 43.91(2) |
| **0.54(1)** | 3.7302(14) | 3.6324(12) | 43.77(2) |
| **0.60(1)** | 3.7338(10) | 3.6085(7) | 43.56(2) |
| **0.68(1)** | 3.7467(14) | 3.7510(9) | 43.41(3) |
| **0.79(1)** | 3.7601(12) | 3.5384(6) | 43.32(2) |
| **0.85(1)** | 3.7719(9) | 3.5214(6) | 43.36(1) |
| **0.93(1)** | 3.7781(10) | 3.5158(6) | 43.46(2) |

A similar behaviour to that of the materials above is also seen in the series studied by Gregory *et al*. where additionally there are vacancies at the Li(2) site. This work concluded that not only is there a dependence of the Li(2)-N bond length on x, but that also this bond length appears to increase with increasing vacancy concentration. Previous work by Gregory *et al*. showed that lithium nitridonickelates in which there were similar dopant levels of nickel but different $Li^+$ vacancy concentrations within the material yielded no significant differences in the unit cell parameters and bonds lengths for the respective nitrides[19].

Both Gregory *et al*. and Niewa *et al*. recorded magnetic susceptibility data for materials in these series and similar magnetic behaviour was observed[8, 18]. All materials displayed magnetic behaviour dominated by Pauli paramagnetism, particularly at higher values of x. Both groups found evidence of anti-

ferromagnetic exchange interactions between corresponding nickel atoms, which was evident from a negative Weiss constant when the data were fitted to a modified Curie-Weiss expression. Nitridonickelates display a decreasing effective magnetic moment as the nickel metal content increases, which can be attributed increased delocalisation in the [Li/M-N] chain, and thus transition to a metallic state. Niewa *et al.*[18] found low x-value materials produced a higher effective magnetic moment than the expected spin-only value for $Ni^{+}$ and this was attributed to a large orbital contribution to the overall magnetisation as seen in lithium nitridoferrates[20-21] and other studies of nitridonickelates. [22] However Gregory *et al.* found that the effective magnetic moments for the metal ions were smaller in all materials than the expected spin-only values[8]. Gregory *et al.* postulated that the magnetic moment was more dependent on the nickel content than vacancy concentration, and that the latter had a relatively small effect on the magnetism of the materials[8].

Nishijima *et al.* studied the electrochemical performance of materials of the series $Li_{3-x}Ni_xN$ where $0 \leq x \leq 0.5$[23] and analysed the first discharge for x = 0.1, 0.2, 0.3, 0.4 and 0.5 with a current density of 300 $\mu A/cm^2$ and found that the amount of lithium that could be inserted into the material increased with increasing nickel metal content. The sample with x = 0.5 was used for testing the cyclability of the materials as this showed the highest capacity upon first discharge, equivalent to 200 mAh /g, and the cycles were also carried with a current density of 300 $\mu A/cm^2$. The amount of lithium that could be extracted, z, was limited to 0.5 $Li^{+}$ giving $Li_{2.5-z}Ni_{0.5}N$, and the potential 0.01 – 1.5 V for the charge / discharge cycles, and Figure 5.5 shows the capacity curves over 7 cycles.

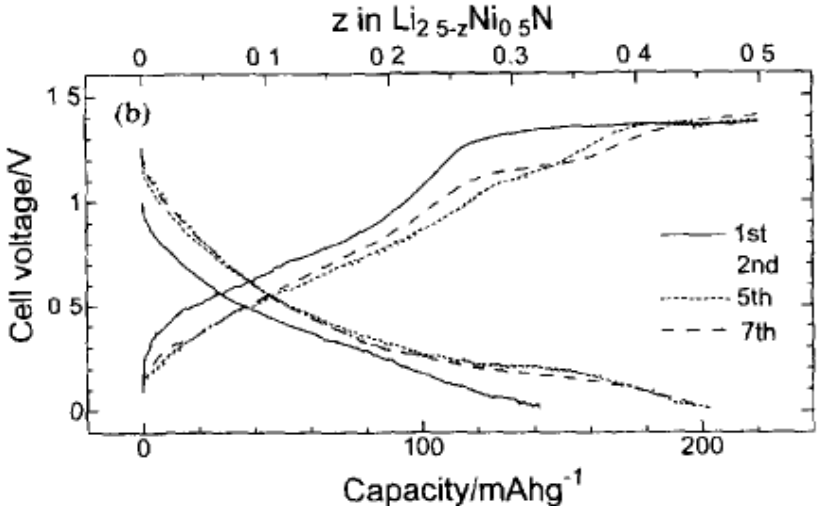


**Figure 5.5 Charge / discharge capacities for $Li_{2.5-z}Ni_{0.5}N$ upon cycling[23].**

As can be seen, the first discharge corresponds to the intercalation of 0.3 $Li^+$ and the first charge takes place over two regions, the first of which is an increase of voltage up to ~0.3 $Li^+$. The subsequent plateau would appear to correspond to the de-intercalation of the lithium ions which were intercalated during the first discharge. Once again, the second cycle was absent from the original copy of the paper and could not be obtained from the author. For nitridometallates of copper and cobalt the second cycle and consequent cycles curves are almost exactly the same as one another but very different to that of the first cycle and the reason for this was found to be that during the first cycle, there is a change from a crystalline to an amorphous phase with de-intercalation of lithium. The difference in the curves between the first and subsequent cycles for $Li_{2.5}Ni_{0.5}N$ is less pronounced than for other nitridometallates and the reason for this was that $Li_{2.5}Ni_{0.5}N$ undergoes less structural changes with de-intercalation of lithium. Lithium could be extracted up to z = 0.5 with little change to the unit cell and the sample remained in a crystalline state.

This series of lithium nitridometallates has been studied at higher levels of metal substitution and the characterisation of the structure and property relationships have been examined closely[5-6, 11, 17-19, 22, 24-25]. As can be seen in Figure 5.2 and Figure 5.3, the structural conformation of lithium nitridonickelates differs from that of cobalt and copper at the higher levels of substitution, when x = 1, and the aim of this work was to investigate whether any deviations from structural trends could be observed for these materials at

much lower values of x. This would be achieved through synthesis of the materials by standard conventional methods and characterisation techniques including; X-ray diffraction (XRD), powder neutron diffraction (in order to ascertain the structural occupancy factors (SOF's) of lighter elements such as lithium, and obtain a definitive model). From these experiments it should be possible to see how the lower substitution levels affect the structures and resulting properties of the materials.

Magnetic susceptibility of the synthesised materials would be assessed by SQUID magnetometry, to show how the nominal transition metal oxidation states in may influence the magnetism. If these low-doped materials have similar defect structure to the high-doped counterparts then they may show equally interesting magnetic properties.

A similar defect structure (vacancies) in these materials to that in previously studied materials, would allow the potential for better application as anode materials due to a lower nickel content and thus maximisation of the volumetric capacity.

Until now, the hydrogen adsorption properties of substituted nitrides of this series have not been analysed and so through the measurement of Pressure-Composition-Temperature behaviour it will be possible to assess the hydrogen adsorption and desorption properties and compare to lithium nitride itself. If these low doped nitridonickelates can be synthesised and vacancies created, then there is a potential for improving on the ionic mobility with respect to the high doped materials. Since increased ion mobility may correspond to increased hydrogen ion mobility then these materials could yield interesting properties as hydrogen storage materials due to better kinetics of adsorption /desorption, and the presence of a transition metal could also have a catalytic effect. These factors added to the fact that these materials would contain less heavy metal, would maximise the gravimetric capacity and make them of particular interest for study.

# 5.2 Lithium Nickel Nitride

## *5.2.1 Experimental*

### 5.2.1.1 Synthesis of $Li_{3-x-y}M_xN$

Bulk samples of lithium nickel nitride were prepared through the synthesis which was detailed in section 2.2.2. Stoichiometric quantities of both nickel metal powder (Aldrich 99.5 %) and lithium nitride powder (Aldrich ≥ 99.9% and for some materials in-house synthesised $Li_3N$, as seen in Table 5.2) were ground together and then pressed into three approximately equal 13mm diameter pellets, then stacked one upon the other inside a sandblasted stainless steel crucible or within an acid-cleaned nickel foil holder within the crucible, which was in turn lowered inside a stainless steel reaction vessel using a nichrome wire cage and sealed under $N_{2(g)}$ (99.999 %). Each of the samples were heated to 973 K for differing lengths of time (2 – 7 days) and then, once reacted, the furnace switched off and the reaction allowed to cool to room temperature. The vessels were opened inside a nitrogen-filled glove box and the samples were removed from the crucible, ground and collected into sample vials. The majority of the samples were grey/black in colour.

For characterisation samples were prepared by the method outlined in section 2.3.1.2, and then once the glass capillary was filled and flame sealed, was examined on the diffractometer. Simple phase characterisation of the samples was achieved through room temperature X-ray powder diffraction (XRD) on a Bruker d8 diffractometer using Cu $K_\alpha$ radiation ($\lambda$ = 1.5406 Å). Scans were collected over a $2\theta$ range of 5-85 ° in steps of 0.017 ° at a scan speed of 0.63 seconds per step, giving a total scan time of 1 h. Assessment of the phases present was carried out using PowderCell 2.4[26] in combination with the ICSD (Inorganic crystal structure database) in order to reference against know structures.

#### 5.2.1.2 Magnetic measurements

The magnetic behaviour of **[17]** was measured through the use of a Superconducting Quantum Interference Device (SQUID) magnetometer as described in section 2.4, with the help of Dr Marek Jura at the ISIS facility at the Rutherford Appleton Laboratories. The sample was prepared for measurement by the method outlined in Section 2.4 and was measured in a field of 100 Oe. Zero-Field Cooled (ZFC) measurement and Field Cooled (FC) measurements were carried out. The ZFC measurement was made by cooling the sample to 2 K in the absence of a field, turning the field on, and measuring the magnetisation upon warming the material back up to 200 K. The FC measurement was performed by cooling the sample in the presence of a field and then measuring the magnetisation upon warming to 200 K. The measured moment was corrected for the diamagnetic effects of the core electrons and the gelatine sample capsule.

#### 5.2.1.3 Electrochemical studies

The electrochemical measurements that were performed on materials **[17]** and **[20]** were carried out at the Universitat Autònoma de Barcelona (UAB), in Barcelona using Swagelok cells as described in section 2.6. Samples for these measurements were prepared as per the method outlined in section 2.6 using a 15 % carbon 'sp' additive, which was used as a conductor, and a slow cycle rate of typically C/20 (whereby 100 % of the samples charge is consumed over a period of 20 hours) . The cell was run on a potentiostat, with the potential cycled between 0 and 2 V (typically) and the resultant charge measured. The data were corrected for the sample weight to give a weight specific capacity in mA h $g^{-1}$.

#### 5.2.1.4 Pressure-composition-temperature analysis (PCT)

The PCT measurements were performed on material **[17]** using a HyEnergy PCTPro2000 from Setaram as described in section 2.7. The instrument operates based on the Sievert's method of volumetric gas adsorption. All manipulations were performed in a nitrogen-filled glove box. O.322g of the material was weighed, ground and transferred into the sample holder on top of four spacers, and the remaining space above the sample was plugged with silica wool. Once

sealed, the vessel was connected to the PCTpro instrument and leak tested using $He_{(g)}$ The internal volume was calculated using four calibrations. The volume calculated was 10.134 ml. The temperature was set to 250 $^{o}$C and the pressure in the hydrogen reservoir was set to 20 bar.

## *5.2.2 Results and Discussion*

### 5.2.2.1 XRD characterisation

Table 5.2 below shows an overview of the reactions carried out by the method from section 5.2.1.1 above and a typical powder pattern with the reference phases can be seen below in Figure 5.6.

**Table 5.2 Reaction conditions and setup for the synthesis of lithium nitridometallates of the form $Li_{3-x-y}M_xN$.**

| Label | Nominal Stoichiometry | Temp /K | Reaction Time | Setup | $Li_3N$ used |
|---|---|---|---|---|---|
| **[15]** | $Li_{2.95}Ni_{0.05}N$ | 973 | 2 days | Foil + Crucible | In-house |
| **[16]** | $Li_{2.90}Ni_{0.1}N$ | 973 | 2 days | Foil + Crucible | In-house |
| **[17]** | $Li_{2.95}Ni_{0.05}N$ | 973 | 2 days | Crucible | Aldrich |
| **[18]** | $Li_{2.90}Ni_{0.1}N$ | 973 | 2 days | Crucible | Aldrich |
| **[19]** | $Li_{2.95}Ni_{0.05}N$ | 973 | 2 days | Crucible | In-house |
| **[20]** | $Li_{2.95}Ni_{0.05}N$ | 973 | 7 days | Crucible | Aldrich |

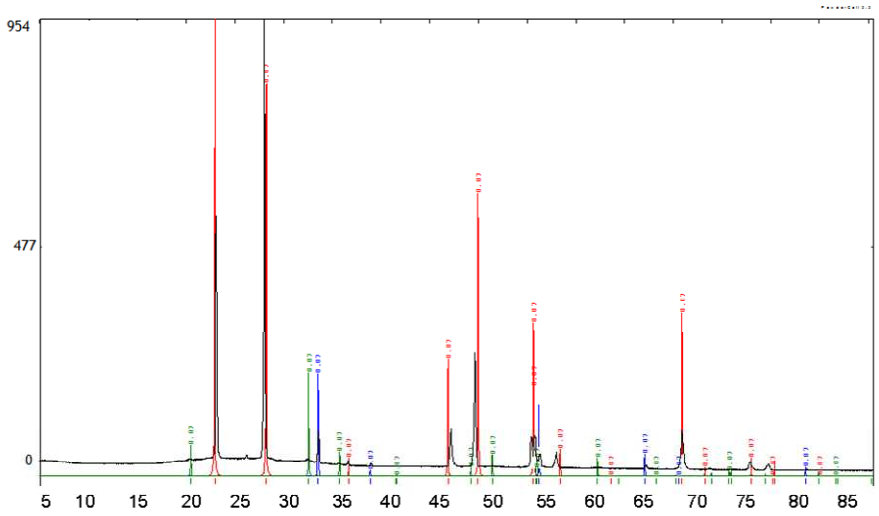


**Figure 5.6 X-ray diffraction pattern for [20] in black from Powdercell, $Li_3N$ in red, $Li_2O$ in blue and LiOH in green, all from ICSD. x-axis shows 2θ and the y-axis shows intensity.**

As can be seen above, the synthesis of these materials can be difficult to achieve without the presence of some impurity, but the majority of the samples contain only small levels of impurities. For **[20]** there was presence of small levels of lithium hydroxide and lithium oxide. For **[15]**, **[16]** and **[19]** there was presence of lithium oxide and lithium imide impurity, and for **[17]** and **[18]** there was only presence of a small lithium oxide impurity.

### 5.2.2.2 Refinement of XRD data

Once the phases present were identified a longer scan over a 2θ range of 5-90 degrees for a duration of approximately 10 h was performed in order to obtain high quality data for Rietveld refinement. This was done using the GSAS (the General Structure Analysis System) program with the EXPGUI user interface[27]. The starting model for the main phase was based upon that of the parent material $Li_3N$ and the initial occupancies were set to reflect the nominal stoichiometry of the material. Any areas at the extremities of the powder pattern were excluded and the background was fitted using function type 1 in all cases, which is a Chebyschev polynomial of the first kind. At this point, zero point correction was introduced, and the unit cell was also varied. Once the refinement appeared to be stable, peak shapes were introduced and allowed to

vary, using peak profile type 2 in all cases, which is a multiterm Simpson's rule integration of the pseudo-Voigt function. The constrained temperature factors and occupancies for the Li/Ni(1) site were allowed to vary in turn, and then the temperature factors for the nitrogen and the Li(2), however for **[19]** the temperature factors were found to be correlating with the site occupancy factor, and so this was not refined for this material. Finally the Li(2) site occupancy was allowed to vary freely, however, this gave a physically unreasonable value and so this was fixed at 1. This was not entirely unexpected as site occupancies for light elements such as lithium are not easy to refine using X-ray diffraction. Figure 5.7 - Figure 5.10 below show OCD (Observed Calculated Difference) plots for **[15]**, **[17]**, **[19]** and **[20],** which contain the same nominal nickel content but were synthesised under differing reaction conditions. OCD plots for all of the samples are included in the appendix.

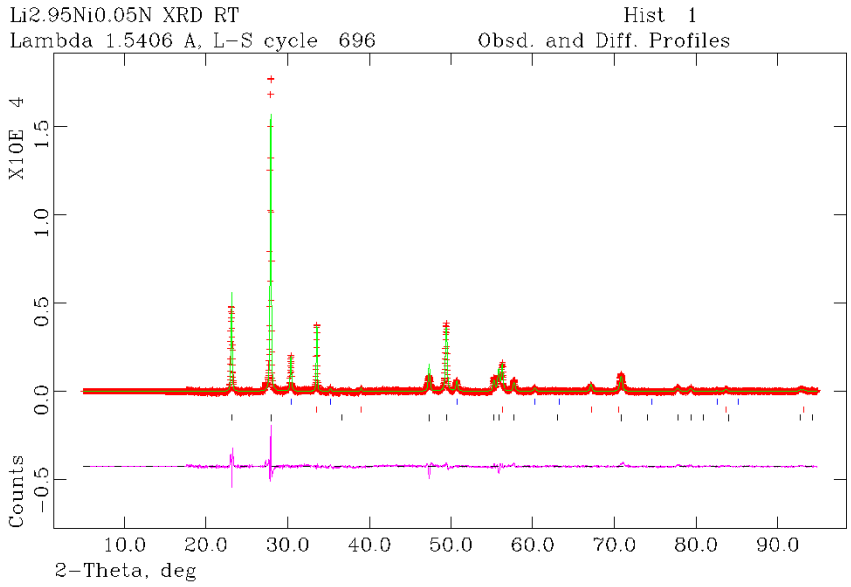


**Figure 5.7 OCD plot from GSAS refinement of XRD of $Li_{2.95}Ni_{0.05}N$ [15]. Observed data are in red, calculated in green and the difference of the two profiles is shown in pink. The nitride-type phase is assigned black tickmarks, lithium imide phase blue tickmarks and lithium oxide phase red tickmarks.**

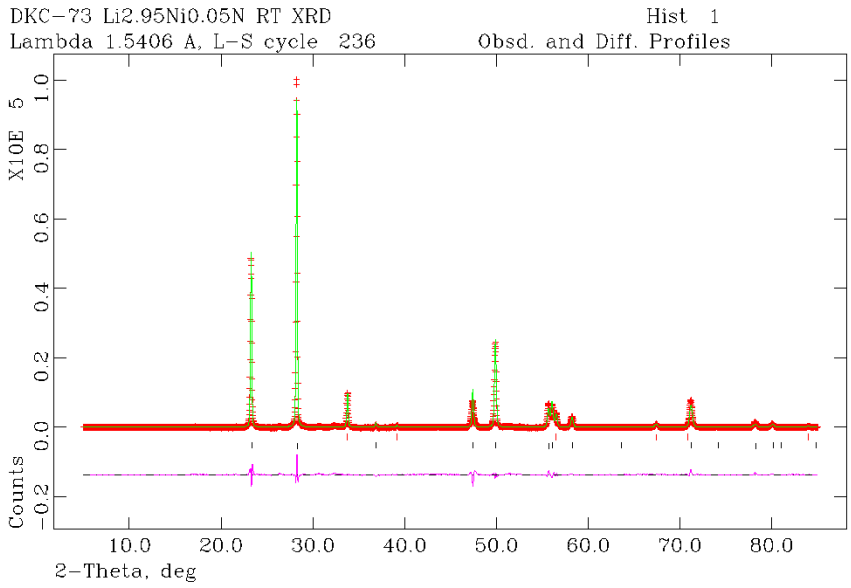


**Figure 5.8 OCD plot from the refinement against XRD data for $Li_{2.95-y}Ni_{0.05}N$ [17]. Observed data are in red, calculated in green and the difference of the two profiles shown in pink. The nitride-type phase is assigned blue tickmarks and lithium oxide impurity phase red tickmarks.**

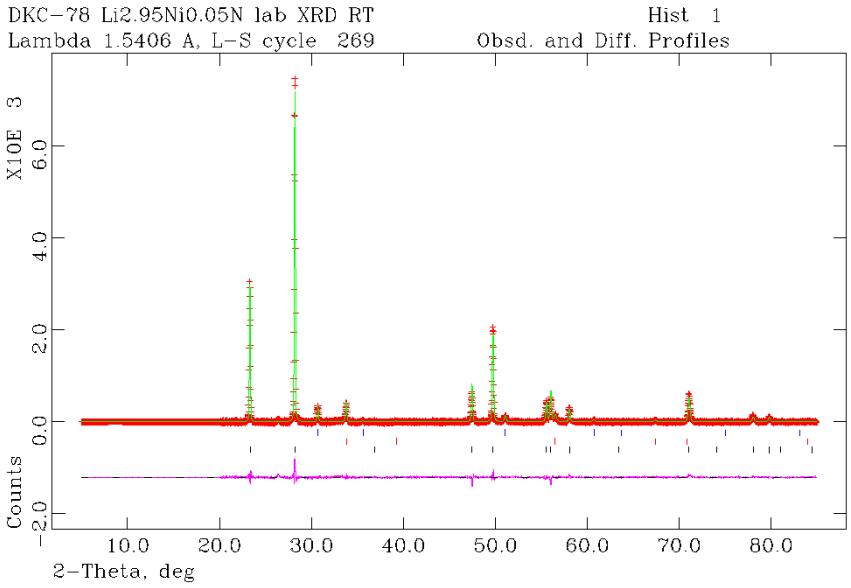


**Figure 5.9 OCD plot from GSAS refinement of XRD of $Li_{2.95}Ni_{0.05}N$ [19]. Observed data are in red, calculated in green and the difference of the two profiles shown in pink. The nitride-type phase is assigned black tickmarks, lithium imide blue tickmarks and lithium oxide phase red tickmarks.**

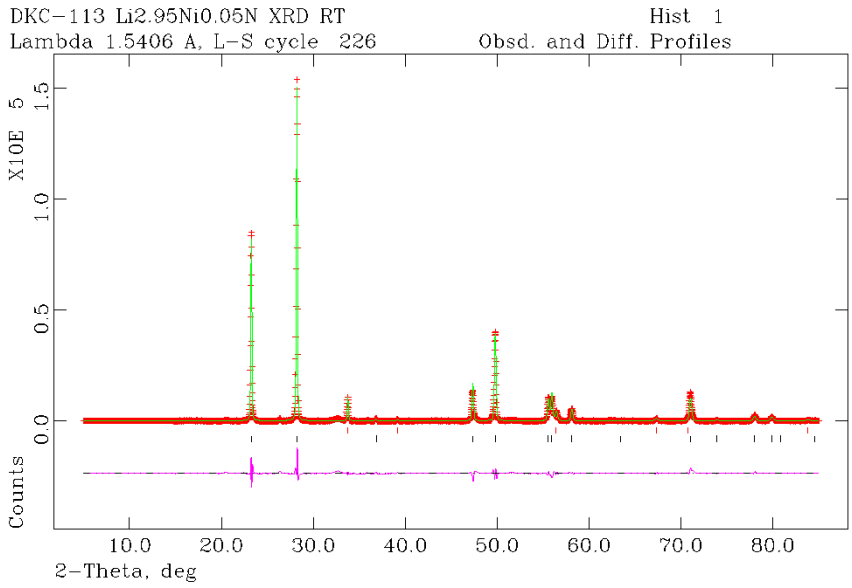


**Figure 5.10 plot from GSAS refinement of XRD of $Li_{2.95}Ni_{0.05}N$ [20]. Observed data are in red, calculated in green and the difference of the two profiles shown in pink. The nitride-type phase is assigned blue tickmarks and lithium oxide impurity phases red tickmarks.**

As can be seen from the OCD plots above, the observed data fit very well to the calculated profiles. There is a slight mismatch to the intensity for the largest peaks of the main phase which could not be resolved through changing the way the temperature factors vary, allowing for adsorption effects or through allowing for preferred orientation. Table 5.3 and Table 5.4 show selected refinement data and refined interatomic distances respectively for the materials. Full refinement details are included in the appendix.

**Table 5.3 Selected GSAS refinement data from XRD for $Li_{3-x}Ni_xN$, where nominally x = 0.05.**

| **Sample-nominal** | $Li_{2.95}Ni_{0.05}N$ **[15]** | $Li_{2.95}Ni_{0.05}N$ **[17]** | $Li_{2.95}Ni_{0.05}N$ **[19]** | $Li_{2.95}Ni_{0.05}N$ **[20]** |
|---|---|---|---|---|
| **Crystal system** | Hexagonal | | | |
| **Space group** | P6/*mmm* | | | |
| ***a* / Å** | 3.6875(1) | 3.6636(6) | 3.6754(5) | 3.6726(1) |
| ***c* / Å** | 3.8416(2) | 3.8424(6) | 3.8425(5) | 3.8515(1) |
| **Ni (occ)** | 0.098(1) | 0.055(1) | 0.060(1) | 0.059(1) |
| $\chi^2$ | 3.758 | 12.45 | 1.480 | 16.49 |
| $R_p$ | 0.0422 | 0.0421 | 0.0705 | 0.0389 |
| $wR_p$ | 0.0604 | 0.0631 | 0.0908 | 0.0598 |

*occ denotes site occupancy

**Table 5.4 Interatomic distances from Rietveld refinement against XRD data for the series $Li_{3-x-y}Ni_xN$.**

| Sample-refined stoichiometry | Li(1)/M-N | Li(2)-N | Li(1)/M-Li(2) |
|---|---|---|---|
| $Li_{2.945}Ni_{0.055}N$ **[17]** | 1.92121(23) | 2.1153(4) | 2.85756(34) |
| $Li_{2.941}Ni_{0.059}N$ **[20]** | 1.92574(4) | 2.12047(4) | 2.86442(4) |
| $Li_{2.92}Ni_{0.06}N$ **[19]** | 1.92124(27) | 2.12209(28) | 2.86259(27) |
| $Li_{2.902}Ni_{0.098}N$ **[15]** | 1.92080(9) | 2.12910(8) | 2.86750(8) |

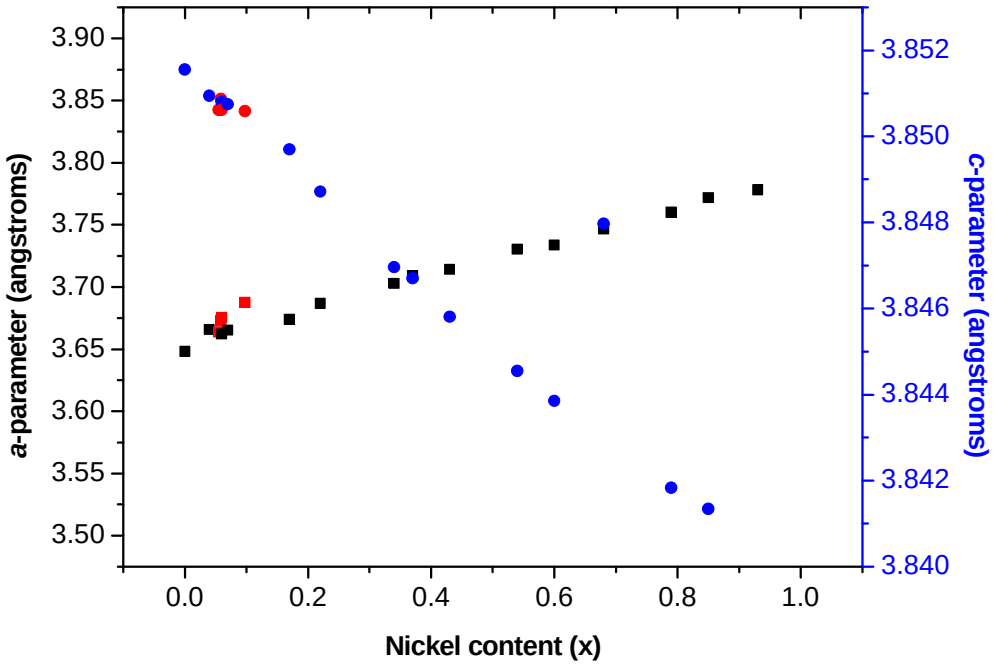


**Figure 5.11 Comparison of *a*- and *c*-parameter with varying nickel content, x, for the series $Li_{3-x}Ni_xN$. Black markers denote *a*-parameters, and blue markers denote *c*-parameters from the work of Niewa *et al.* [18] Red markers denote materials from Table 5.3.**

From Figure 5.11 and the data, it would appear that as the Ni content increases the *c*-parameter decreases as is expected and the results from Table 5.3 correspond with those recorded by Niewa *et al.*[18]. However, the *a*-parameter does not follow the same trend as the *a*-parameter from Niewa *et al.*[18] As can be seen the *a*-parameter does indeed increase as would be expected but this increase is much more pronounced than in their data. The data for the series from Niewa *et al.* was obtained from X-ray diffraction, and it would appear that they hadn't varied the Li(2) site, and the difference seen in the *a*-parameter between the two data sets could be due to vacancies being present in the data

from this work, this has previously been thought to influence the *a*-parameter. This cannot be ascertained accurately through the use of X-ray diffraction alone due to the presence of light atoms.

## *5.2.3 PND characterisation*

Powder neutron diffraction (PND) is a method that provides stronger diffraction from the lighter atoms. For this series of materials both Constant Wavelength (CW) and Time of Flight (ToF) were used. ~2.0g of sample was required for these experiments, and so new bulk material had to be synthesised. The constant wavelength measurements being carried out for **[17]**, **[18]** and **[19]** on D1A at the Institut Laue-Langevin (ILL) in Grenoble as described in 2.3.4.1 with the help of Dr Clemens Ritter, and the ToF measurements for **[20]** were made at ISIS at the Rutherford Appleton Laboratory on the instrument GEM with the help of Dr Ron. I. Smith as described in 2.3.3.1.

### 5.2.3.1 Constant Wavelength PND refinement

Diffraction data were collected for each sample at 70 K, 293 K, 389 K and 482 K respectively, collecting for approximately 6 h at each temperature. Copper gaskets were required to seal the vanadium cans to permit data collection at elevated temperatures. A modified $Li_3N$ structure was used as a starting model as for the X-ray refinements and the initial occupancies were set to reflect the nominal stoichiometry of the material. Background function type 8 (linear interpolation function with segments) was selected for **[17]**, **[18]** and **[19]**, other than for the 70 K measurement in **[19]** where the background was fitted graphically. The utilisation of different background fits is once again due to being pragmatic with the refinement and is standard practice in crystallography. Once the background was fitted, the unit cell for the main phase was allowed to vary, followed by the zero-point. Once these were stable the peak shapes were modelled. For all measurements, the peak profile function used was type 4 (convolution of pseudo-Voigt and asymmetrical peak shape with microstrain broadening). The impurity phases (**[17]** and **[18]** contained lithium oxide and **[19]** contained lithium imide and lithium oxide) were introduced once the peak shapes had refined. Peak profile function 2 (multiterm pseudo-Voigt function) was used to model the peak shape of the impurity phases. Again, similarly to the

XRD refinements, the site occupancies for the Li(1)/Ni shared site were constrained together so that they totalled 1 and their temperature factors constrained to be equal to one another, but the occupancy of the Li(2) site was then allowed to vary freely and, for all three of the materials studied here, the value of the occupancy fluctuated close to unity, and so was fixed at 1. The temperature factors for **[19]** for the two high temperature measurements were again not varied as per the XRD refinement as they were found to be correlating closely to the site occupancy factor. Figure 5.12 – Figure 5.17 below show OCD plots for the highest and lowest temperatures for each of the three samples.

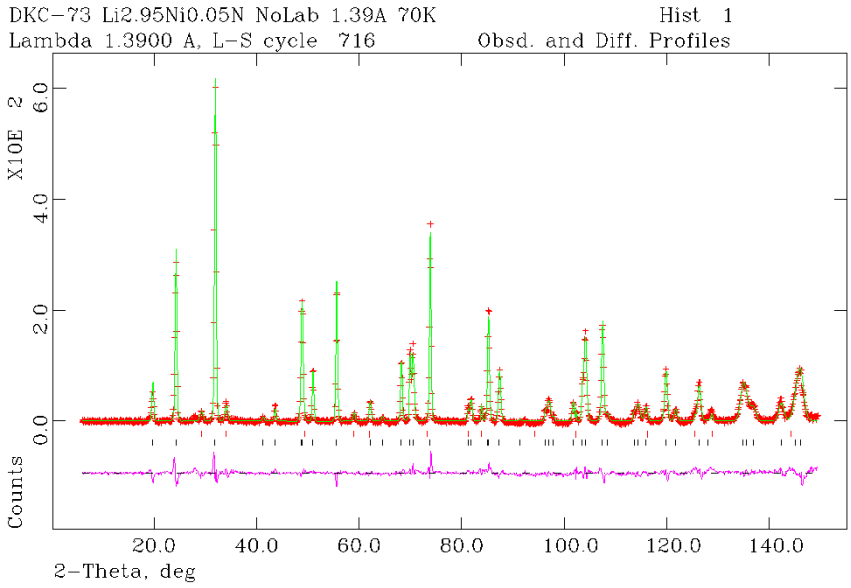


**Figure 5.12 OCD plot from GSAS Rietveld refinement of CW data for [17] at 70 K. Observed data is in red, calculated in green and the difference of the two profiles shown in pink. The nitride-type phase is assigned blue tickmarks and lithium oxide impurity phase red tickmarks.**

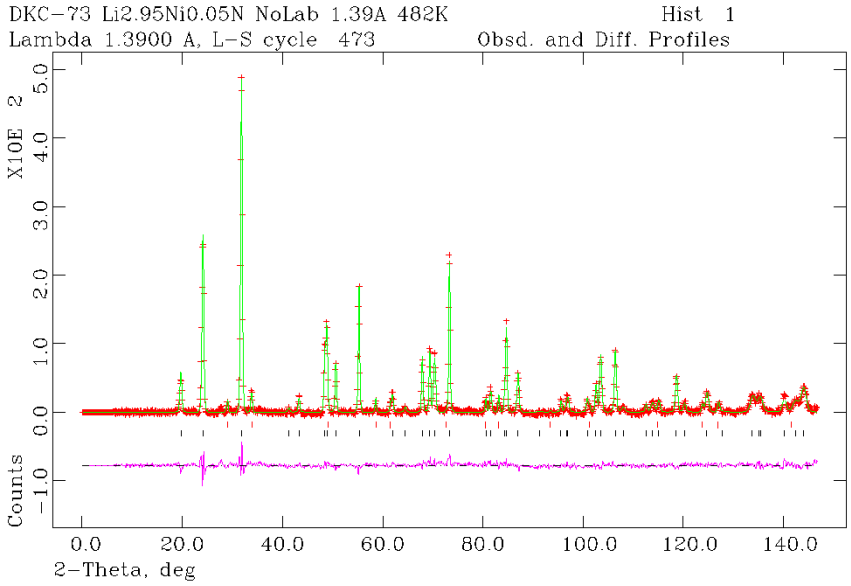


**Figure 5.13 OCD plot from GSAS Rietveld refinement of CW data for [17] at 482 K. Observed data is in red, calculated in green and the difference of the two profiles shown in pink. The nitride-type phase is assigned blue tickmarks and lithium oxide impurity phase red tickmarks.**

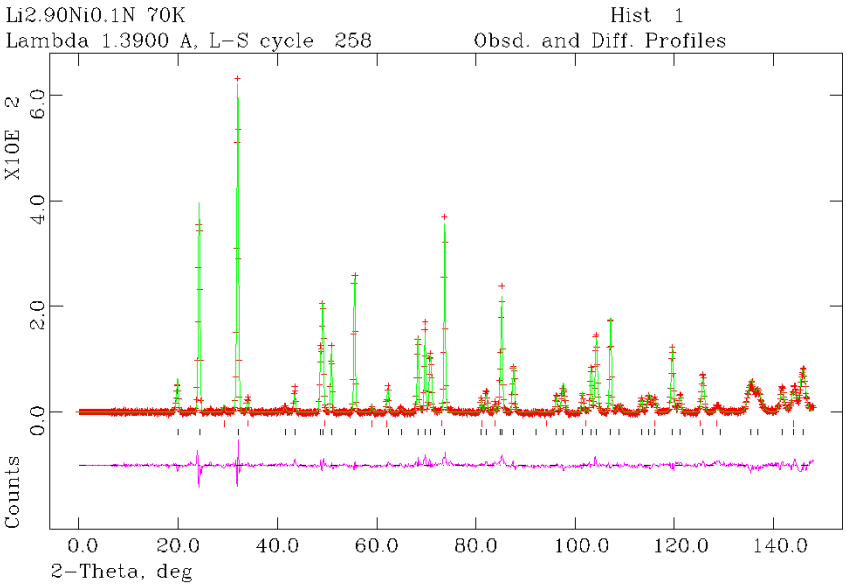


**Figure 5.14 OCD plot from GSAS Rietveld refinement of CW data for [18] at 70 K. Observed data is in red, calculated in green and the difference of the two profiles shown in pink. The nitride-type phase is assigned blue tickmarks and lithium oxide impurity phase red tickmarks.**

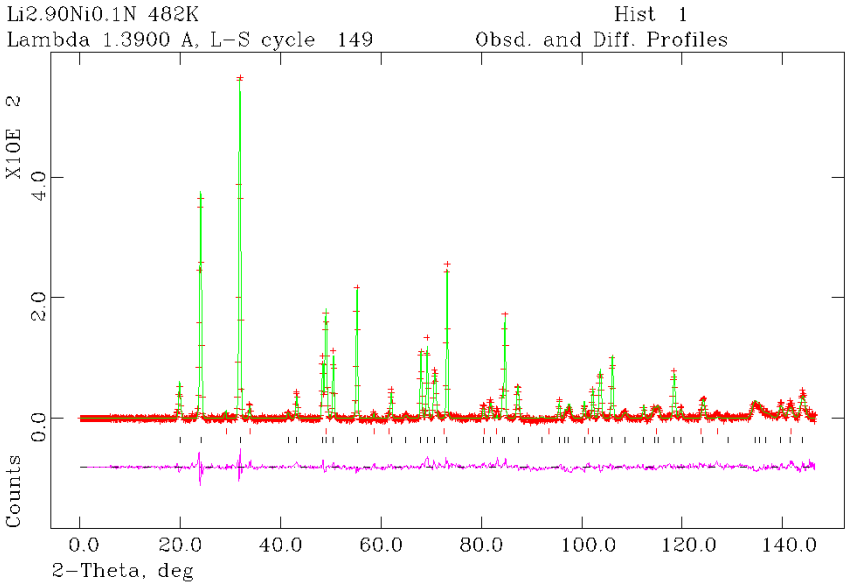


**Figure 5.15 OCD plot from GSAS Rietveld refinement of CW data for [18] at 482 K. Observed data is in red, calculated in green and the difference of the two profiles shown in pink. The nitride-type phase is assigned blue tickmarks and lithium oxide impurity phase red tickmarks.**

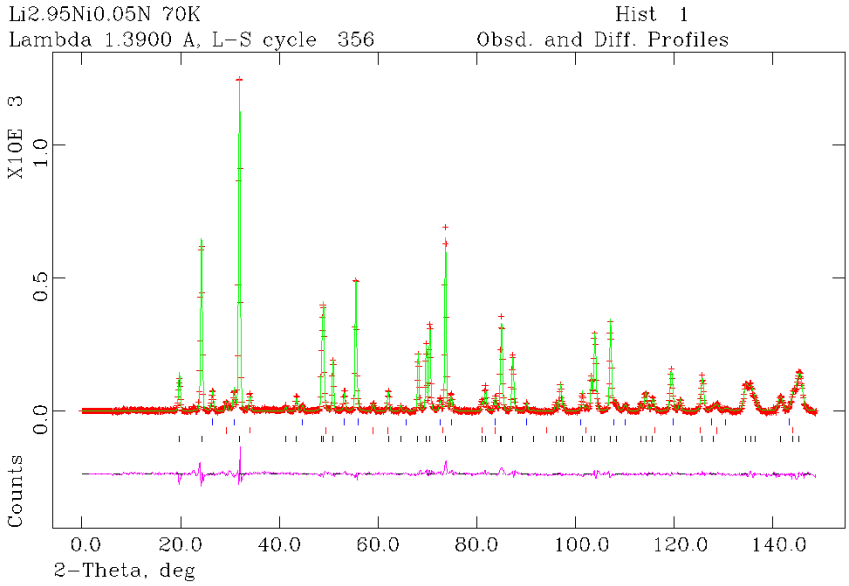


**Figure 5.16 OCD plot from GSAS Rietveld refinement of CW data for [19] at 70 K. Observed data is in red, calculated in green and the difference of the two profiles shown in pink. The nitride-type phase is assigned black tickmarks, lithium oxide impurity phase red tickmarks and lithium imide impurity phase blue tickmarks.**

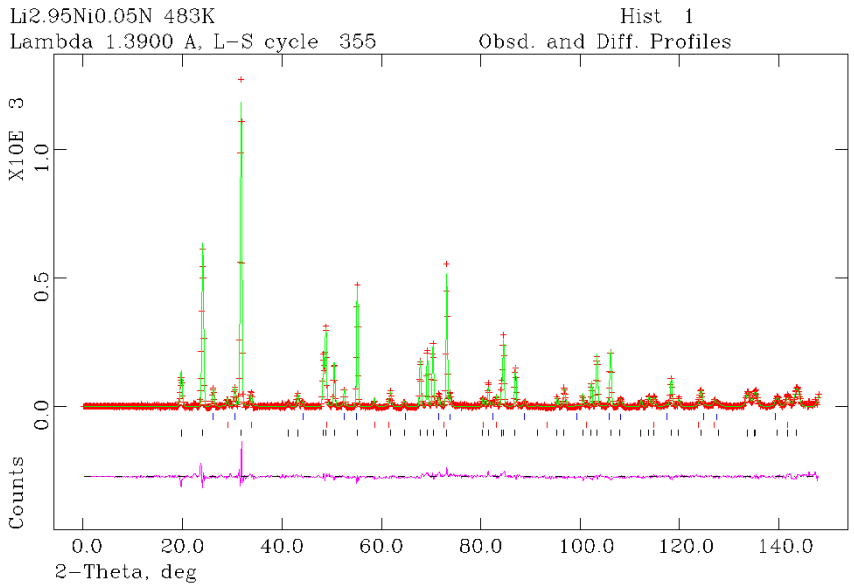


**Figure 5.17 OCD plot from GSAS Rietveld refinement of CW data for [19] at 483 K. Observed data is in red, calculated in green and the difference of the two profiles shown in pink. The nitride-type phase is assigned black tickmarks, lithium oxide impurity phase red tickmarks and lithium imide impurity phase blue tickmarks.**

As can be seen, there was no evidence of any phase changes during cooling or heating, each sample retained the $Li_3N$-type structure throughout the temperature range which was measured. Table 5.5 and Table 5.6 show some selected refinement data from the GSAS Rietveld refinements and refined unit cell and interatomic distance data respectively. Full data for the samples are included in the Appendix.

**Table 5.5 Selected data from PND refinements of $Li_{2.95}Ni_{0.05}N$ [17], $Li_{2.90}Ni_{0.1}N$ [18] and $Li_{2.95}Ni_{0.05}N$ [5].**

| Sample nominal stoichiometry | Sample refined stoichiometry | Temp /K | Ni Occ*. | $R_P$ | $wR_P$ | $\chi^2$ |
|---|---|---|---|---|---|---|
| **Hexagonal** | | | | | | |
| **P6/*mmm*** | | | | | | |
| $Li_{2.95}Ni_{0.05}N$ **[17]** | $Li_{2.95}Ni_{0.05}N$ **[17]** | 70 | 0.046(3) | 0.0557 | 0.0708 | 3.431 |
| | | 293 | 0.049(3) | 0.0428 | 0.0521 | 1.525 |
| | | 389 | 0.042(4) | 0.0435 | 0.0553 | 1.610 |
| | | 482 | 0.049(4) | 0.0426 | 0.0537 | 1.517 |
| $Li_{2.90}Ni_{0.1}N$ | $Li_{2.90}Ni_{0.1}N$ | 70 | 0.090(4) | 0.0478 | 0.0594 | 2.127 |

| | | | | | | |
|---|---|---|---|---|---|---|
| **[18]** | **[18]** | 293 | 0.089(3) | 0.0416 | 0.0480 | 1.773 |
| | | 389 | 0.083(4) | 0.0439 | 0.0534 | 1.952 |
| | | 482 | 0.097(5) | 0.0433 | 0.0544 | 1.909 |
| $Li_{2.95}Ni_{0.05}N$ **[19]** | $Li_{2.95}Ni_{0.05}N$ **[19]** | 70 | 0.050(3) | 0.0373 | 0.0488 | 2.267 |
| | | 293 | 0.053(3) | 0.0389 | 0.0493 | 2.432 |
| | | 388 | 0.043(2) | 0.0390 | 0.0490 | 2.485 |
| | | 483 | 0.048(2) | 0.0371 | 0.0475 | 2.437 |

*Occ denotes site occupancy

**Table 5.6 Unit cell and interatomic distance data from PND refinements of $Li_{2.95}Ni_{0.05}N$ [17], $Li_{2.90}Ni_{0.1}N$ [18] and $Li_{2.95}Ni_{0.05}N$ [19].**

| | | | | | | |
|---|---|---|---|---|---|---|
| **Sample** | **T /K** | ***a* /Å** | ***c* /Å** | **V /Å$^3$** | **Li(1)/Ni-N /Å** | **Li(2)-N /Å** |
| $Li_{2.95}Ni_{0.05}N$ **[17]** | 70 | 3.65634(8) | 3.8479(2) | 44.549(3) | 1.92393(9) | 2.11109(4) |
| | 293 | 3.6680(1) | 3.8510(2) | 44.871(4) | 1.92549(9) | 2.11751(7) |
| | 389 | 3.6755(2) | 3.8519(2) | 45.065(5) | 1.92596(12) | 2.12215(9) |
| | 482 | 3.6846(2) | 3.8549(2) | 45.324(6) | 1.92746(12) | 2.12740(10) |
| $Li_{2.90}Ni_{0.1}N$ **[18]** | 70 | 3.6678(1) | 3.8310(2) | 44.632(4) | 1.91549(9) | 2.11769(6) |
| | 293 | 3.67705(9) | 3.8311(2) | 44.859(3) | 1.91554(8) | 2.12305(5) |
| | 389 | 3.6852(1) | 3.8319(2) | 44.067(4) | 1.91592(10) | 2.12776(8) |
| | 482 | 3.6940(2) | 3.8328(3) | 45.290(5) | 1.91639(13) | 2.13275(9) |
| $Li_{2.95}Ni_{0.05}N$ **[19]** | 70 | 3.6660(1) | 3.8479(1) | 44.785(3) | 1.92395(7) | 2.11665(6) |
| | 293 | 3.6736(1) | 3.8471(2) | 44.963(3) | 1.92356(7) | 2.12108(6) |
| | 388 | 3.6829(1) | 3.8502(2) | 45.225(4) | 1.92510(8) | 2.12640(7) |
| | 483 | 3.6917(1) | 3.8519(2) | 45.463(4) | 1.92594(9) | 2.13151(7) |

From the refinements of these PND measurements, it can be seen that the content of the nickel metal for all three of the materials is within good agreement to that of the nominal stoichiometry from the reactants, and this is true across all four temperatures. The most important observation that can be made from the PND experiments is the absence of vacancies at the Li(2) site. When the site was allowed to vary freely, in all cases the value levelled out at a figure just slightly greater than 1, and thus it was considered that 1 was the

occupancy of the lithium at this site. As seen from the other lithium nitridometallates studied in previous sections, the short reaction time combined with low quantity of metal apparently constrains the production of vacancies. For **[17]** and **[19]** when the nickel metal occupancy is compared with that of the refinement of the Rietveld refinement of the XRD data, it can be seen that there is a large difference between the two. This is likely to be due to lithium being a lighter element and thus not so well diffracted by X-rays and, as the nickel metal is constrained to the same site as the Li(1), then the uncertainty is attuned on Ni, however for the PND Rietveld refinement, both atoms diffract neutrons well and therefore their individual occupancies are correctly assigned. Table 5.7 shows a comparison between XRD and PND results for both **[17]** and **[19]**.

**Table 5.7 Comparison of unit cell data from GSAS refinement of XRD and PND data respectively for [17] and [19].**

| Sample | Ni occ* | *a* /Å | *c* /Å | Li(1)/Ni-N /Å | Li(2)-N /Å |
|---|---|---|---|---|---|
| $Li_{2.945}Ni_{0.055}N$ **[17]** XRD | 0.055(1) | 3.6636(6) | 3.8424(6) | 1.92121(23) | 2.1153(4) |
| $Li_{2.95}Ni_{0.05}N$ **[17]** PND | 0.049(3) | 3.6680(1) | 3.8510(2) | 1.92549(9) | 2.11751(7) |
| $Li_{2.92}Ni_{0.06}N$ **[19]** XRD | 0.060(1) | 3.6754(5) | 3.8425(5) | 1.92124(27) | 2.12209(28) |
| $Li_{2.95}Ni_{0.05}N$ **[19]** PND | 0.053(3) | 3.6736(1) | 3.8471(2) | 1.92356(7) | 2.12108(6) |

*Occ denotes site occupancy

For both of these materials, there is a difference between the nickel metal occupancy from XRD Rietveld refinement in comparison to PND Rietveld refinement and for the two materials the difference is almost the same. The unit cell parameters do not show much change between the two types of diffraction, and the there is a larger difference in the *c*-parameter than there is in *a*. One other important observation that can be made for these materials above is that there is only a negligible difference in unit cell parameters between the material which has been synthesised using in-house $Li_3N$, **[19]**, and

the material synthesised using Aldrich $Li_3N$. The slight difference that is observed is likely to be due to the different refined nickel occupancies for the two room temperature refinements.

Using the nickel occupancy obtained from PND Rietveld refinement of **[17]** this value was then put back into the XRD Rietveld refinement and fixed at that value (not allowed to vary) and the Li(1) and Li(2) allowed to vary freely. This lead to the same values as when the Li(2) site was allowed to vary during the course of the XRD Rietveld refinement as previously stated, and this would correspond to vacancies at the Li(2) site of an unreasonable size, and thus the refinement appears to have an issue with the site occupancies.

#### 5.2.3.2 Refinement of ToF neutron data

In light of the negligible vacancies found in the samples above, a material was synthesised, **[20],** with the same nominal stoichiometry as **[17]** and **[19]** with the exception that a longer reaction time of 7 days as opposed to 2 days was employed.

Room temperature ToF (Time of Flight) powder neutron diffraction measurements were made on this material using the instrument GEM at the ISIS facility at the Rutherford Appleton Laboratories. The samples were placed inside a 13 mm vanadium can and the height marked on the can in order to align with the centre of the beam. The can was sealed using allen bolts and a small circle of indium wire was used as a gasket. Rietveld refinement against the ToF data was once again carried out using GSAS (General Structure Analysis System) through the Expgui interface[27].

The starting model was based upon that of the starting material, $Li_3N$, with the transition metal occupying the Li(1) site. The occupancies of the Li(1) site were initially set at fixed values that reflect the nominal stoichiometry of the synthesised material. Only the 3 highest angle banks of data were used and the unit cell parameters and scale factors were refined initially across all of the three of the histograms in the same way. The background for the three histograms were all fitted using function 7 (linear interpolation function) with 8 terms, peak shapes were then refined separately for each histogram using peak

shape type 2 (Ikeda-Carpenter function with pseudo-Voigt convolution) for both the main phase and the lithium oxide impurity phase. The lithium imide that was identified from XRD could not be seen in the ToF PND, and thus must have arisen as a consequence of the preparation of the glass capillary for the collection of the powder pattern. Once the fit seemed to appear stable, the temperature factors were constrained and refined isotropically along with the fractional occupancies of the shared site. Further terms for the peak shape were then introduced and the fractional occupancy of the Li(2) site was then allowed to vary freely. A term for sample absorption was introduced at this stage and finally the anisotropic temperature factors for all of the atoms were refined. The OCD plots for the three histograms can be seen below in Figure 5.18 – Figure 5.20.

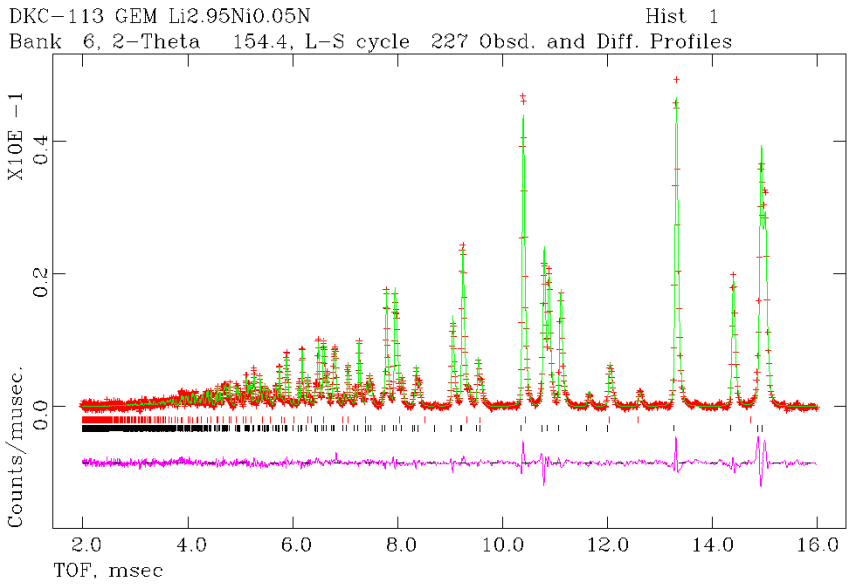


**Figure 5.18 OCD plot from GSAS refinement of ToF data for $Li_{2.95}Ni_{0.05}N$ [20] from 2θ 154.4° detector. Observed data is in red, calculated in green and the difference of the two profiles shown in pink. The nitride-type phase is assigned blue tickmarks and lithium oxide impurity phase red tickmarks.**

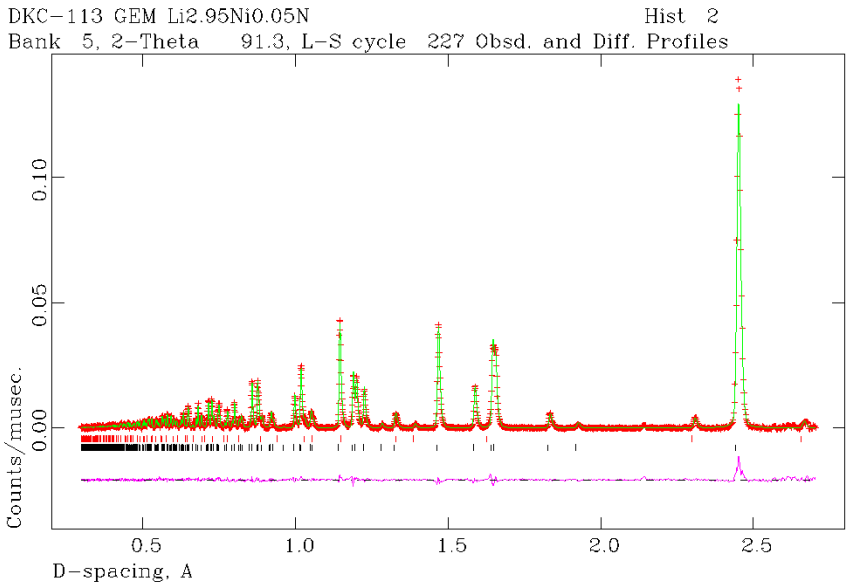


**Figure 5.19 OCD plot from GSAS refinement of ToF data for $Li_{2.95}Cu_{0.05}N$ [20] from 2θ 91.3° detector. Observed data is in red, calculated in green and the difference of the two profiles shown in pink. The nitride-type phase is assigned blue tickmarks and lithium oxide impurity phase red tickmarks.**

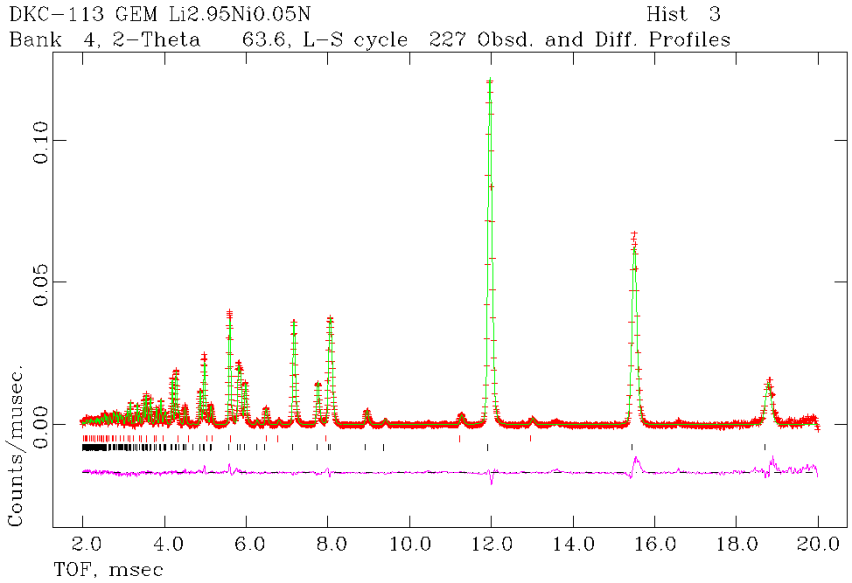


**Figure 5.20 OCD plot from GSAS refinement of ToF data for $Li_{2.95}Cu_{0.05}N$ [20] from 2θ 63.6° detector. Observed data is in red, calculated in green and the difference of the two profiles shown in pink. The nitride-type phase is assigned blue tickmarks and lithium oxide impurity phase red tickmarks.**

From the OCD plots for the three detector banks, it can be seen that there is a good fit between the model and that of the observed data. Table 5.8 and

Table 5.9 below show some selected refinement data for **[20]** with data for **[17]** included for comparative reasons.

**Table 5.8 Comparison of PND Rietveld refinement data for [17] (CW) and [20] (ToF).**

| **Crystal system** | | Hexagonal | | | | | |
|---|---|---|---|---|---|---|---|
| **Space group** | | P6/*mmm* | | | | | |
| **Nominal Stoichiometry** | **Refined Stoichiometry** | **Temp /K** | **Li(2) Occ*** | **Ni Occ*.** | **$R_P$** | **$wR_P$** | **$\chi^2$** |
| $Li_{2.95}Ni_{0.05}N$ **[17]** | $Li_{2.95}Ni_{0.05}N$ **[17]** | 293 | 1.000 | 0.049(3) | 0.0428 | 0.0521 | 1.525 |
| $Li_{2.95}Ni_{0.05}N$ **[20]** | $Li_{2.762}Ni_{0.05}N$ **[20]** | 293 | 0.906(6) | 0.050(1) | 0.0339 | 0.0302 | 2.794 |

**Table 5.9 Comparison of unit cell and interatomic distance data from PND refinements of [17] and [20].**

| Sample | T /K | *a* /Å | *c* /Å | V /Å$^3$ | Li(1)/Ni-N /Å | Li(2)-N /Å |
|---|---|---|---|---|---|---|
| $Li_{2.95}Ni_{0.05}N$ **[17]** | 293 | 3.6680(1) | 3.8510(2) | 44.871(4) | 1.92549(9) | 2.11751(7) |
| $Li_{2.762}Ni_{0.05}N$ **[20]** | 293 | 3.6664(1) | 3.84978(8) | 44.817(2) | 1.92489(4) | 2.11679(3) |

From the Rietveld refinement data for **[20]** from ToF neutron diffraction, the nickel metal occupancy is identical within error to that of **[17]** from CW data. The main difference that can be seen between the two materials however is the presence of vacancies now at the Li(2) site in **[20]**, which equate to 9.4 % at the Li(2) site. In order to maintain charge neutrality for the overall material, the nickel would need to be in an oxidation state of +4.76. This is an oxidation state which is far in excess of what would be either expected or permitted, and at this stage one would have to assume that this is not correct and that some other form of charge compensation is taking place within the material.

Previous work has been carried out to reveal some of the redox chemistry that takes place in the lithium nitridometallates when vacancies are created. In particular the lithium nitridocobaltate, $Li_{2.60}Co_{0.4}N$, has been studied by electron energy-loss spectroscopy (EELS) to ascertain which species balances the charge when lithium is extracted making the defect material, $Li_{1.0}Co_{0.4}N$[28-29]. Their situation was similar; if the entire vacancy was to be balanced by the transition metal then this would lead to $Co^{5+}$ which would have been an unimaginably high oxidation state for this metal. From their results they revealed that both cobalt and nitrogen play a part in the charge balancing, and therefore it is a possibility that in the materials studied in this work that the same is also true.

Another possibility for the balancing of the charge that remains from the vacancies in these materials is the presence of hydrogen bonded to the nitrogen, creating a localised imide, $Li_{3-x}Ni_xNH_y$. This would not be easily detected in XRD measurements as hydrogen is a light element, and often it is not easily resolved

in PND either hence why much research is carried out on deuterated materials. A good way to further probe if this is a possibility of the charge balancing would be to perform either infrared or Raman spectroscopy.

## 5.3 Magnetic measurements

These measurements were carried out as described earlier in section 5.2.1.2, and the sample preparation carried out as described in section 2.4. Figure 5.21 and Figure 5.22 show how the magnetic susceptibility varies as a function of temperature for both **[17]** and **[20]**.

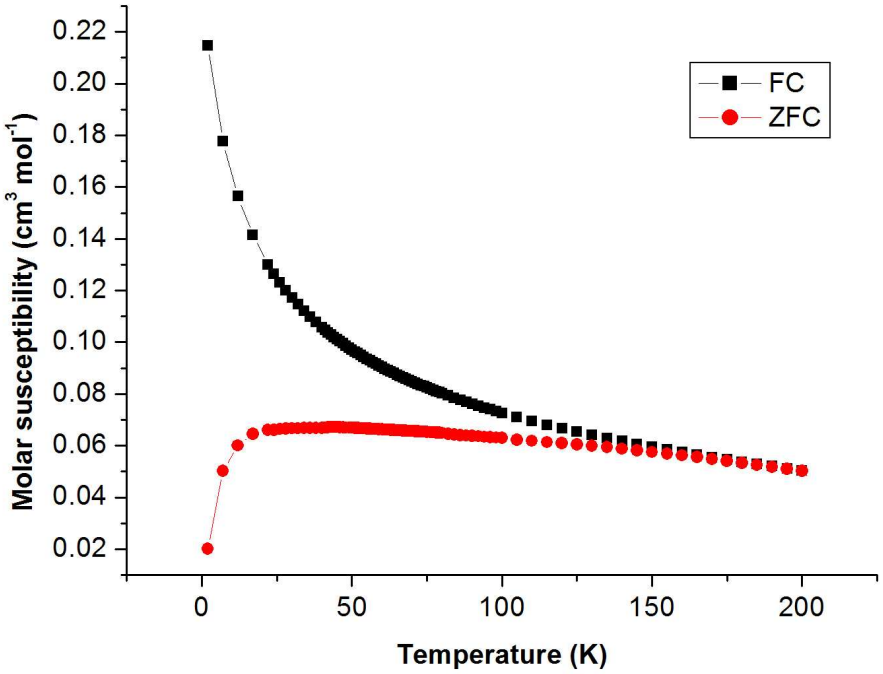


**Figure 5.21 Zero Field Cooled (ZFC) and Field Cooled (FC) plot of magnetic susceptibility as a function of temperature for [17].**

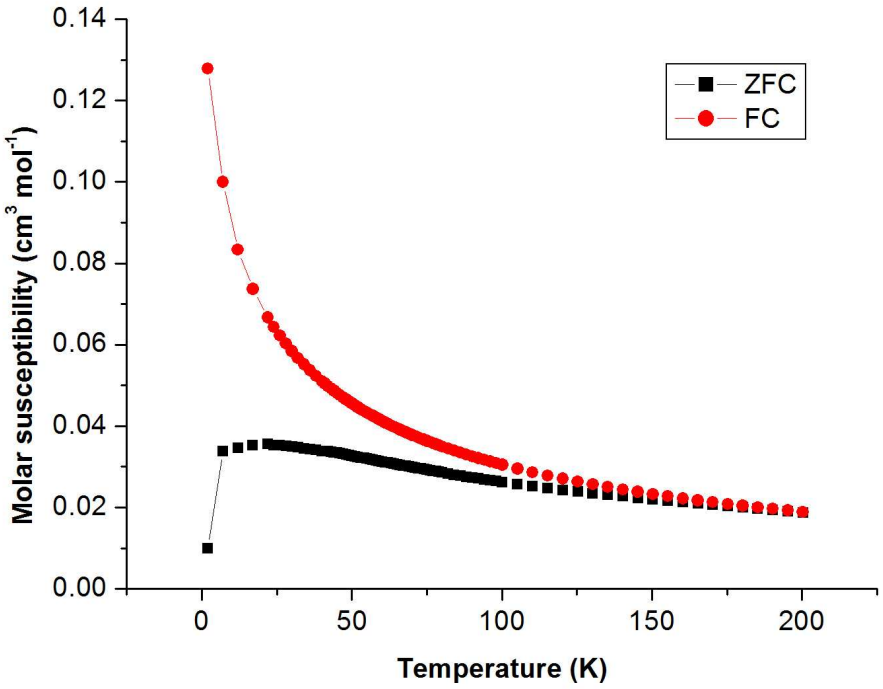


**Figure 5.22 ZFC and FC plot of magnetic susceptibility as a function of temperature for [20].**

From these plots, one can see that the two materials display fairly similar magnetic behaviour, with both showing a paramagnetic susceptibility that was temperature dependent in the FC measurement. This would suggest that the materials are displaying a typical localised paramagnetic behaviour with a Curie-Weiss temperature dependence; however the size of the magnetisation is rather large in comparison to what would be expected for a typically paramagnetic material. The divergence of the magnetisation for the FC and ZFC measurements for the two materials is indicative of spin-glass type behaviour. In the ZFC plot for both materials, it can be seen that there is a significant cusp to the plot as the temperature rises from 2 K, which is known as the freezing temperature for the reordering of the spins. For both materials it occurs at ~ 20 K and above this temperature the frustration of spins, from the remnant magnetisation after removing the external field, is overcome as a result of the thermal energy and the spins reorder. In the FC plots as the samples are cooled, the spins attempt to order in the direction of the field, thus creating a larger magnetisation, but as the temperature increases, the magnetisation begins to decrease as the spins are thermally disordered. This type of magnetic behaviour has been previously

observed for lithium nitridometallates of copper[18] and cobalt[30], but not previously for nickel. In order to observe the effects of this spin-glass behaviour in greater detail, the use of ac susceptibility would be required. By measuring the field dependence of the ac susceptibility measurements this can yield the criterion parameter for spin-glass behaviour. This has been previously used successfully for $Li_{2.50}Co_{0.5}N$[30]. Figure 5.23 and Figure 5.24 show plots for the reciprocal magnetisation as a function of temperature for both **[17]** and **[20]** respectively.

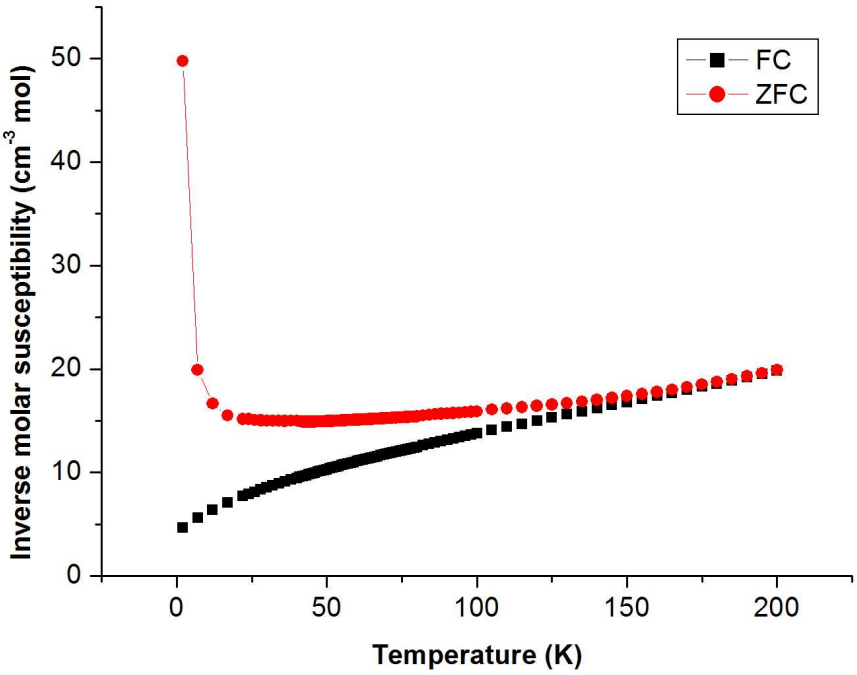


**Figure 5.23 ZFC and FC plot of inverse magnetic susceptibility as a function of temperature for [17]**

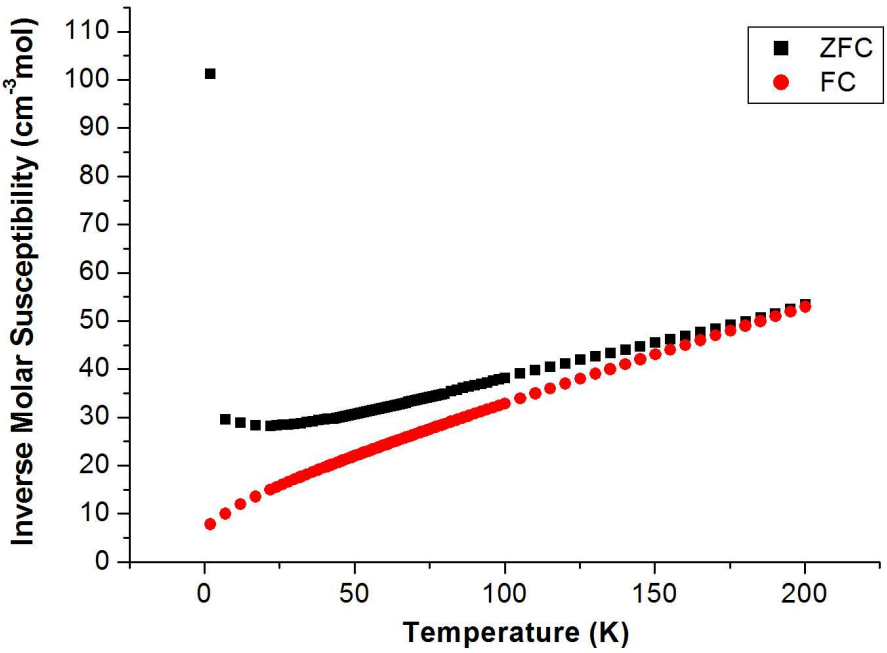


**Figure 5.24 ZFC and FC plot of inverse magnetic susceptibility as a function of temperature for [20].**

As can be seen from Figure 5.23 and Figure 5.24, the ZFC plots if extrapolated back to the x-axis would appear to indicate that there is an antiferromagnetic contribution to the magnetisation as the Weiss constant for both materials would be a negative value.

## 5.4 Electrochemical studies

The electrochemical performance of **[17]** was studied. The sample was prepared for testing as outlined in section 5.2.1.2 above and previously in section 2.6. The data preparation was carried out using the program Kaleidagraph 3.52[26] which is a data handling program for science and engineering purposes. The data that is output from the potentiostat records the voltage change applied across the sample Swagelok cell along with time, and outputs the current recorded as a function of time and how this relates to the intercalation/ deintercalation of lithium. Figure 5.25 below shows how the specific capacity of **[17]** varies as a function of applied voltage.

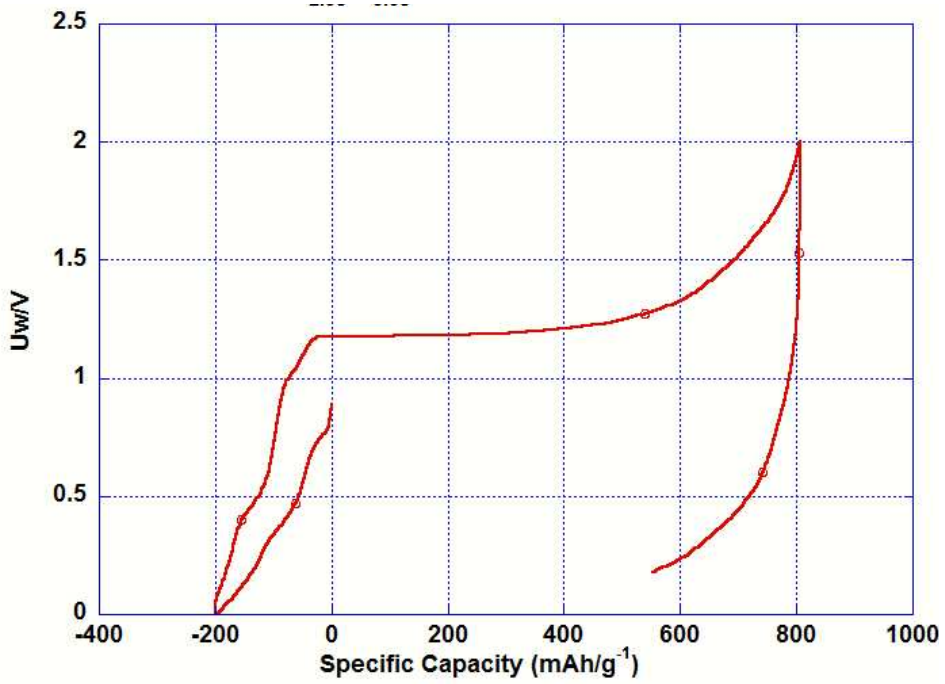


**Figure 5.25 Specific capacity for fist cycle for $Li_{2.95}Ni_{0.05}N$ [17] with varying applied voltage.**

The voltage limits were set to cycle between 0 and 2 V, but as can be seen the experiment was halted before the end of the first cycle due to a fault with the controller program, and so the stage of cycling was unknown upon regaining the program, therefore the measurement was stopped. The open cell voltage for this material when used as an anode was 0.892 V and the cycle was initially began by inserting lithium (discharge), and 0.28 $Li^+$ was achieved which corresponded to the decrease of the capacity to -200 mAh $g^{-1}$.

Even though this would appear to suggest that this material has vacancies into which lithium is initially being inserted, the carbon 'sp' conductor that was added to the anode material during the construction of the cell was found to insert approximately 0.25 $Li^+$. Three different types of carbon conductor were a possibility for use in conjunction with the anode material **[17]** and as each had only small differences in conductivity, the one which intercalated the lowest amount of lithium was used. This can be seen in Figure 5.26.

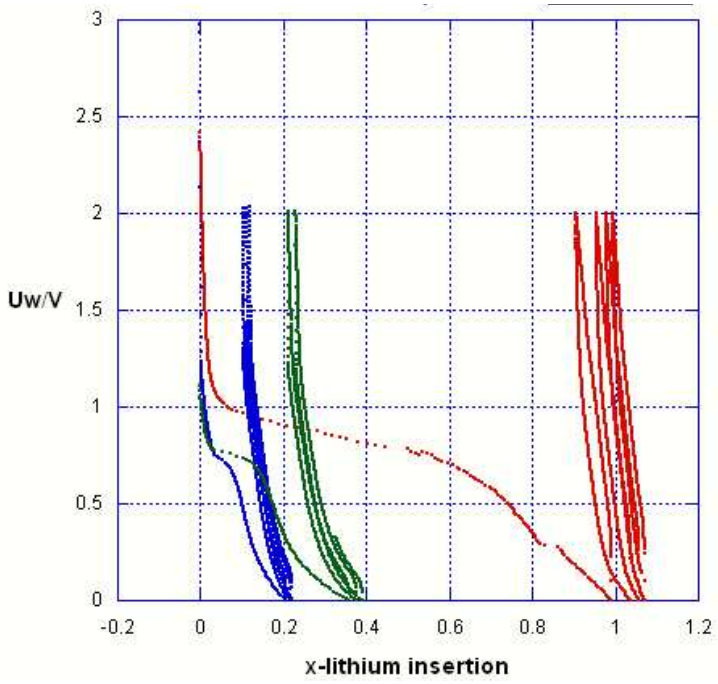


**Figure 5.26 Plot of applied cell voltage against lithium insertion for three types of carbon conductor. The blue line represents carbon 'Sp', the red represents 'Printex' and the green line represents acetylene black.**

For the first charge, 1.41 $Li^+$ were deintercalated from the material until 2 V had been applied to the cell, and this resulted in a specific capacity of 806.27 mA h $g^{-1}$. From the Figure above it is evident that there is a distinct region upon deintercalating the lithium, whereby the voltage being applied plateaus. In similar materials examined previously this has proven to be due to a shift from a crystalline material to an amorphous one[31]. The specific capacity here is far in excess of what has been previously seen for any other nickel nitridometallates and is even larger than that of the material which had previously and consistently been the best specific capacity to date, $Li_{2.60}Co_{0.4}N$ (760 mA h $g^{-1}$)[28, 31] and also has a lower density, 1.369 g/ $cm^3$ compares with 2.1 g/ $cm^3$. The fact that this material has shown such a high specific capacity upon it's first lithium extraction should perhaps come as no surprise, as Shodai *et al*. discovered in their $Li_{3-x}Co_xN$ series[32] that as the substitution level of cobalt increased in the material, then the capacity of the initial extraction decreased and so too did the cyclability capacity. This may be true for the lithium nitridonickelates also.

It is unfortunate that the cycling of the material could not be concluded as this would have ascertained whether the large capacity is achievable over many

cycles and this is something that would certainly be useful to look at for this particular material in the future.

## 5.5 Pressure-composition-temperature analysis

These measurements were carried out through the method outlined above in section 5.2.1.4 and also in section 2.7. The plot of the adsorption of hydrogen as a function of time for **[17]** can be seen in Figure 5.27.

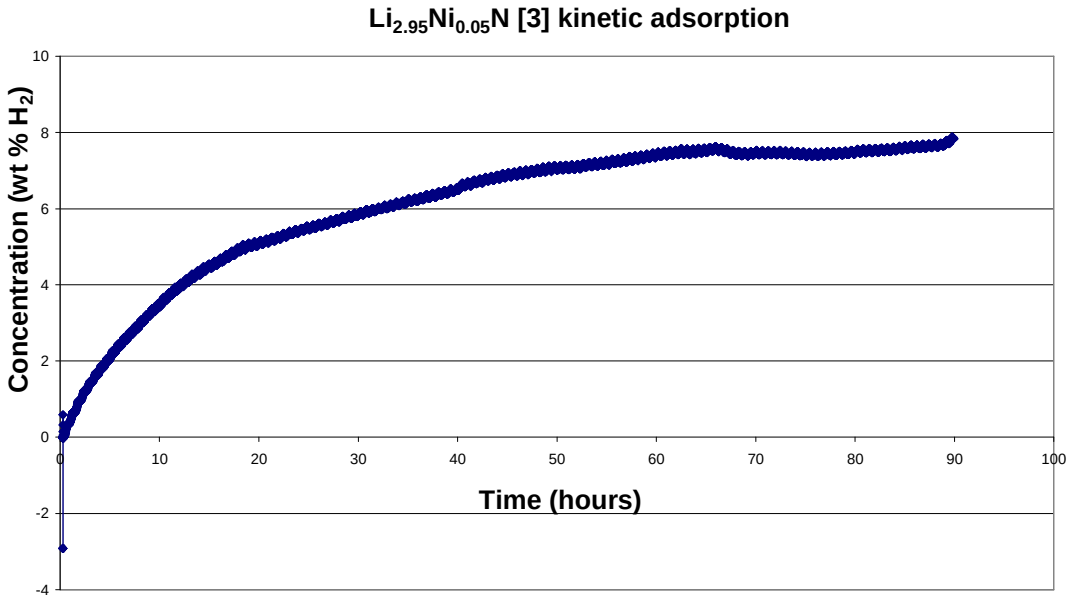


**Figure 5.27 Plot of $H_{2(g)}$ adsorption as a function of time for $Li_{2.95}Ni_{0.05}N$ [17]**

From the figure above it can be seen that 7.839 wt % of hydrogen is adsorbed by this material over a period of 90 hours. This is equivalent to 0.0252 moles of $H_{2(g)}$ being adsorbed by 0.0086 moles of $Li_{2.95}Ni_{0.05}N$, which is significant when compared to that of $Li_3N$ itself which has been shown to uptake 9.2 wt % but due to the formation of $Li_2NH$ means only 6.5 wt % can be stored reversibly at temperatures of 255 $^oC$ or above[33]. The desorption of the material was performed by cooling the sample down, evacuating any residual gas from the sample holder, and then heating the sample back up to the same temperature as before but with the pressure of the hydrogen reservoir set at 0 bar, so as to drive the desorbed gas out of the sample vessel. Desorption of the material can be seen below in Figure 5.28.

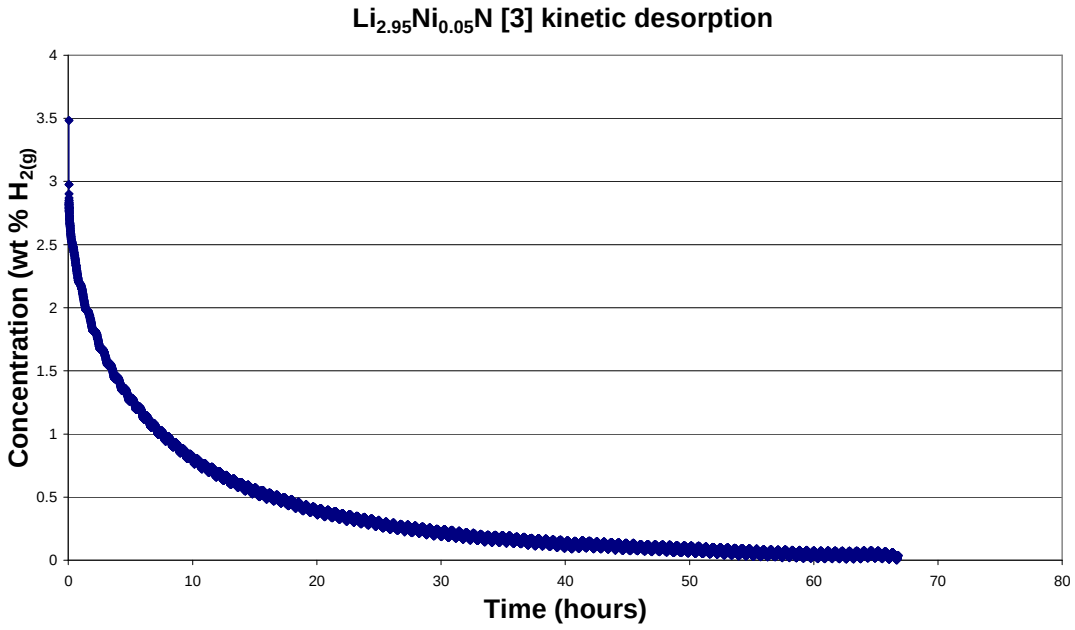


**Figure 5.28 Kinetic desorption of $H_{2(g)}$ as a function of time for $Li_{2.95}Ni_{0.05}N$ [17].**

As can be seen from the figure above, the full amount of hydrogen which has been adsorbed was not fully desorbed thereafter (3.5 wt %) and thus, it is quite likely that this material follows a similar adsorption/desorption process to $Li_3N$ whereby it initially forms lithium imide and hydride which then uptakes further hydrogen to from lithium amide and hydride. On desorption, the hydrogenated material loses hydrogen to form the imide and dehydrogenation proceeds no further under these conditions. If this material adsorbs hydrogen by the same mechanism as that of $Li_3N$, then the reaction equation would be as below:

$$Li_{2.95}Ni_{0.05}N + 2H_{2(g)} \rightarrow Li_{1.95}Ni_{0.05}NH + LiH + H_{2(g)} \rightarrow Li_{0.95}Ni_{0.05}NH_2 + 2LiH$$

If this is indeed the reaction mechanism by which this material uptakes hydrogen then it would yield a theoretical uptake of 10.77 wt %, which is more than that found experimentally. This would suggest that a different mechanism takes place for the uptake of the hydrogen for this material. The XRD pattern for the post-reaction material can be seen in Figure 5.29.

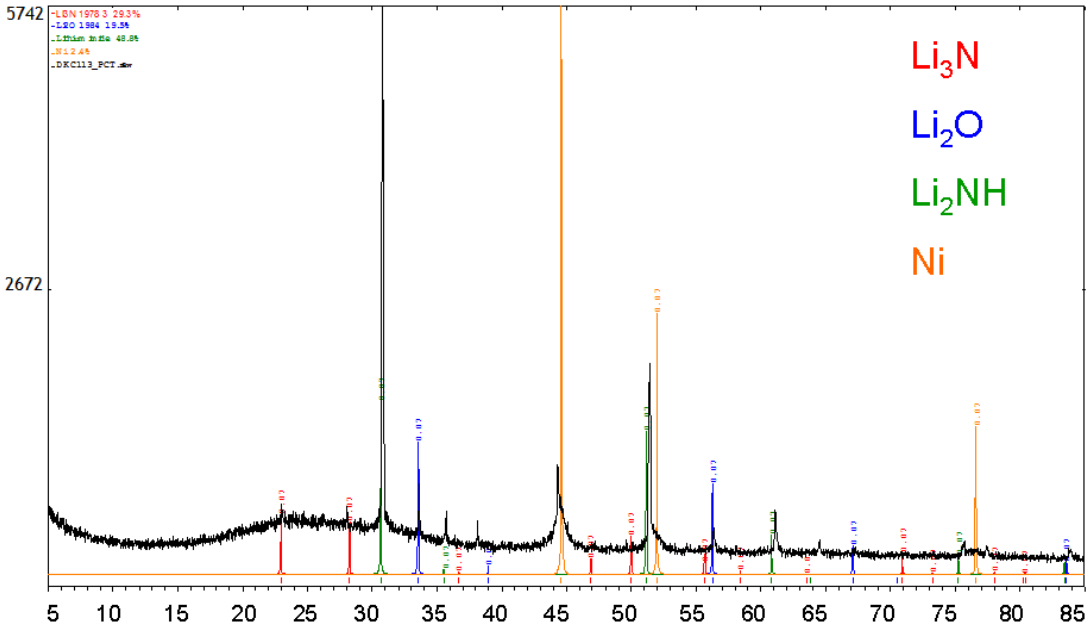


**Figure 5.29 Post PCT cycle XRD of $Li_{2.95}Ni_{0.05}N$ [17] with phase identification.**

From the Figure we see that the main phases which remain after one cycle (adsorption and desorption) are nickel metal, the $Li_3N$-type phase of **[17],** lithium imide, hydride and oxide. The fact that there is evidence of nitride in the post-reaction XRD would appear to suggest that not all of the starting material had adsorbed hydrogen. However given the presence of lithium imide, it can be argued that hydrogenation to a lithium amide-type phase followed by dehydrogenation returning to lithium imide has occurred. It is possible that a nitridometallate with a higher vacancy concentration such as **[20]** would have improved kinetics of adsorption and desorption as it has been argued previously that the presence of a vacancy can improve on $H^+$ ion mobility. Unfortunately there was not enough time to test this premise.

## 5.6 Conclusions

The work that has been presented herein has shown that materials doped with low levels of nickel retain a $Li_3N$-type phase (hexagonal P6/*mmm*). This was ascertained by both X-ray diffraction and neutron diffraction. The aim of the work was to ascertain what structural effects were induced in these materials by doping low quantities ($x \leq 0.1$) of nickel metal and whether the effects that were seen were in line with the trends of what is seen in the previously studied higher-substituted materials. Then the resultant properties of these materials could be ascertained and fine tuned in the future for optimisation.

Rietveld refinement against the XRD data seemed to indicate that, as expected, as the level of the nickel substituent is increased then there is a contraction along *c*, a decrease in the Li/M (1) – N bond length and a greater degree of $\pi$ character in the bond between the transition metal and the nitrogen. Also as x increases, so does the Li(2)-N bond length manifested in a longer *a*-parameter. The results of the work presented herein can be seen in the context of previous work by Niewa *et al.* in Figure 5.30.

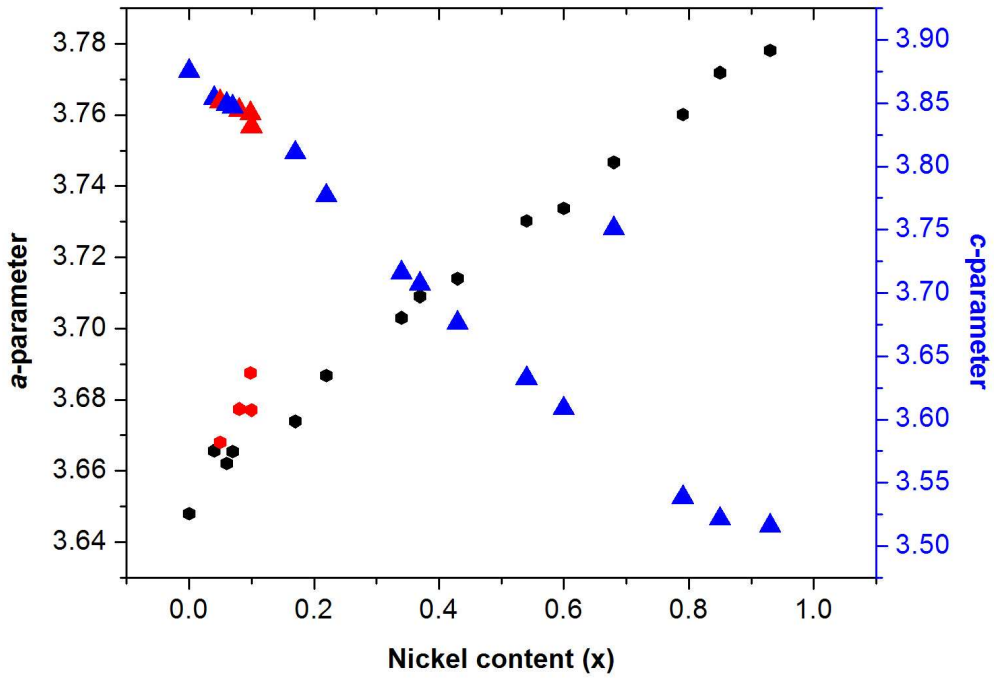


**Figure 5.30 Variation of *a* and *c*-parameter with increasing nickel content, x. Red markers denote materials [15], [17], [19] and [20], black markers represent *a*-parameters and blue markers represent *c*-parameters from Niewa *et al*[18].**

As can be seen, the materials **[15]**, **[17]**, **[19]** and **[20]** fit well to the previous trend, and even though material **[20]** contained vacancies at the Li(2) site there were no significant differences in the unit cell parameters of this material as compared to that of the material with the same nickel content but no vacancies **[17]**. This situation had also been previously documented by Gregory *et al.*[19].

In the lithium nickel nitrides of high x which have been studied previously (e.g. x > 0.5)[8, 18], it was found that the presence of vacancies depended on the quantity of dopant metal, the reaction temperature and length of reaction time[19]. This was also found to be true for the materials of low x here and for the materials which were reacted for a period of only 2 days, **[17]**, **[18]** and **[19]** there was no evidence of vacancies at the Li(2) site from Rietveld refinement against powder neutron diffraction data. Once the length of reaction was increased to 7 days for material **[20],** neutron diffraction provided evidence of vacancies (9.4 %) at the Li(2) site. This would lead to a nickel oxidation state of +4.76 if the transition metal were to be responsible for the full charge compensation of the material.

A transition metal oxidation state of this magnitude is not feasible and as such a different mechanism for charge balance must be taking effect. It was previously shown through EELS experiments, that in vacant lithium nitridometallates, there are significant holes in the nitrogen p-orbital and this mechanism for charge balance could be in effect in these materials also, or alternatively there could be the presence of some hydrogen bonded to the nitrogen forming a localised imide.The materials displayed localised Curie-Weiss paramagnetic behaviour and from FC and ZFC plots it could be seen that the compounds exhibit spin-glass like behaviour.

**[17]** was found to display a very high specific capacity in the first cycle, far in excess of that of the higher doped lithium nickel nitrides, and even in excess of that of the archetypal lithium anode material, $Li_{2.60}Co_{0.4}N$, with a high specific capacity of 806.27 mAh $g^{-1}$. Unfortunately the cyclability of the material could not be measured as the potentiostat stopped due to issues with the controller program and it cannot be ascertained whether this large specific capacity that is seen is only an effect of the first discharge or whether this is repeated in

consequent cycles. It has been previously reported[32, 34-36] that lithium nitridometallates display a much higher specific capacity for their first discharge in comparison to the following cycles. A characteristic flattened region was seen for the electrochemical study which corresponds to a change from a crystalline material to an amorphous one in the previously studied materials. The electrochemical cell that was utilised for these tests was of such a small capacity that not enough material could be recovered afterwards to perform XRD.

It had been previously postulated that the vacancies within these materials could improve $H^+$ ion mobility and that the presence of the transition metal could even catalyse the adsorption and desorption of hydrogen[37]. **[17]** displayed a significant hydrogen uptake. Under a pressure of 20 bar of hydrogen and heated to 250 $^oC$, 0.322g of sample was found to uptake 7.83 wt % over a period of 90 hours. The same temperature was used for the desorption of the hydrogen also, and it was found to be possible to desorb 3.5 wt % over a period of 67 h. This suggests that the hydrogen uptake isn't fully reversible, as for $Li_3N$-$Li_2NH$-$LiNH_2$, and cannot be completely desorbed to the starting material. In the Li-N-H system, the reversible step cycles between lithium imide and lithium amide. In this work it was intended to test whether this type of mechanism might apply to this material also. On one level, this theory was backed up by the presence of lithium imide in the post desorption XRD of the sample. The kinetics for the reaction appeared to be very slow, and as such it would appear that the presence of the transition metal did not have any catalytic effect.

These materials have proven to be intriguing, and their resultant properties would merit some further investigation. In order to ascertain the true transition metal oxidation state, X-ray Absorption Near-Edge Structure (XANES) would be a useful tool as it would show the excitations of the electrons from the specific electron shells, giving clarification. In addition, it would be interesting to study **[17]**'s electrochemical properties on cycling to see if the high specific capacity either diminishes or improves with further cycles, and possibly to carry out some in-situ X-ray diffraction experiments to get a better understanding of the process by which the material becomes amorphous and what happens with the material after the first extraction. It could prove interesting to study material **[20]** for its hydrogen uptake properties, as this material has a similar nickel content as **[17]**

but with vacancies present, and this could show the effect that these vacancies truly have on the $H^+$ ion mobility.

## 5.7 References


1. V. W. Saschsze and R. Juza, *Zeitschrift fur Anorganische Chemie*, **259**, (1949), 278.
2. R. Juza and F. Hund, *Naturwissenschaften*, **33**, (1946), 121.
3. R. Juza and F. Hund, *Zeitschrift Fur Anorganische Chemie*, **257**, (1948), 1.
4. R. Juza, H. H. Weber and E. Meyersimon, *Z. Anorg. Allg. Chem.*, **273**, (1953), 48.
5. M. G. Barker, A. J. Blake, P. P. Edwards, D. H. Gregory, T. A. Hamor, D. J. Siddons and S. E. Smith, *Chem. Commun.*, (1999), 1153.
6. J. Cabana, Z. Stoeva, J. J. Titman, D. H. Gregory and M. R. Palacín, *Chem. Mater.*, **20**, (2008), 1676.
7. A. G. Gordon, R. I. Smith, C. Wilson, Z. Stoeva and D. H. Gregory, *Chemistry Communications*, (2004), 2812.
8. D. H. Gregory, P. M. O'Meara, A. G. Gordon, J. P. Hodges, S. Short and J. D. Jorgensen, *Chem. Mater.*, **14**, (2002), 2063.
9. D. H. Gregory, P. M. O'Meara, A. G. Gordon, D. J. Siddons, A. J. Blake, M. G. Barker, T. A. Hamor and P. P. Edwards, *J. Alloys Compd.*, **317-318**, (2001), 237.
10. Z. Stoeva, R. Gomez, D. H. Gregory, G. B. Hix and J. J. Titman, *Dalton Trans.*, (2004), 3093.
11. Z. Stoeva, R. Gomez, A. G. Gordon, M. Allan, D. H. Gregory, G. B. Hix and J. J. Titman, *Journal of American Chemistry Society*, **126**, (2004), 4066.
12. U. V. Alpen, A. Rabenau and G. H. Talat, *Appl. Phys. Lett.*, **30**, (1977), 621.
13. R. Messer, H. Birli and K. Differt, *J. Phys. C: Solid State Phys.*, **14**, (1981), 2731.
14. M. J. Aragón, B. León, C. Pérez Vicente and J. L. Tirado, *J. Power Sources*, **189**, (2009), 823.
15. M. L. Wolf and C. R. A. Catlow, *Journal of Physics C-Solid State Physics*, **17**, (1984), 6635.
16. M. L. Wolf, J. R. Walker and C. R. A. Catlow, *Journal of Physics C-Solid State Physics*, **17**, (1984), 6623.

17. Z. Stoeva, B. Jager, R. Gomez, S. Messaoudi, M. Ben Yahia, X. Rocquefelte, G. B. Hix, W. Wolf, J. J. Titman, R. Gautier, P. Herzig and D. H. Gregory, *J. Am. Chem. Soc.*, **129**, (2007), 1912.
18. R. Niewa, Z.-L. Huang, W. Schnelle, Z. Hu and R. Kniep, *Z. Anorg. Allg. Chem.*, **629**, (2003), 1778.
19. Z. Stoeva, R. I. Smith and D. H. Gregory, *Chem. Mater.*, **18**, (2006), 313.
20. J. Klatyk, W. Schnelle, F. R. Wagner, R. Niewa, P. Novak, R. Kniep, M. Waldeck, V. Ksenofontov and P. Gutlich, *Phys Rev Lett*, **88**, (2002), 207202.
21. P. Novak and F. R. Wagner, *Physical Review B*, **66**, (2002).
22. W. Schnelle, R. Niewa and F. R. Wagner, *J. Magn. Magn. Mater.*, **272-276**, (2004), 828.
23. M. Nishijima, T. Kagohashi, Y. Takeda, M. Imanishi and O. Yamamoto, *J. Power Sources*, **68**, (1997), 510.
24. J. Klatyk, P. Hohn and R. Kniep, *Zeitschrift Fur Kristallographie-New Crystal Structures*, **213**, (1998), 31.
25. J. B. Ducros, S. Bach, J. P. Pereira-Ramos and P. Willmann, *Electrochim. Acta*, **52**, (2007), 7035.
26. S. software, Synergy software, Reading, Editon edn., 2002.
27. A. C. Larson and R. B. V. Dreele, Los Alamos National Laboratory Report LAUR 86-748, Los Alamos, Editon edn., 2004.
28. T. Shodai, Y. Sakurai and T. Suzuki, *Solid State Ionics*, **122**, (1999), 85.
29. S. Suzuki, T. Shodai and J. Yamaki, *J. Phys. Chem. Solids*, **59**, (1998), 331.
30. D.-L. Liu, F. Du, Y.-J. Wei, C.-Z. Wang, Z.-F. Huang, X. Meng, G. Chen, Y. Chen and S.-H. Feng, *Mater. Lett.*, **63**, (2009), 133.
31. M. Nishijima, T. Kagohashi, M. Imanishi, Y. Takeda, Yamamoto and S. Kondo, *Solid State Ionics*, **83**, (1996), 107.
32. T. Shodai, S. Okada, S. Tobishima and J. Yamaki, *J. Power Sources*, **68**, (1997), 515.
33. D. H. Gregory, *J. Mater. Chem.*, **18**, (2008), 2321.
34. Y. M. Kang, S. C. Park, Y. S. Kang, P. S. Lee and J. Y. Lee, *Solid State Ionics*, **156**, (2003), 263.
35. D. Liu, F. Du, W. Pan, G. Chen, C. Wang and Y. Wei, *Mater. Lett.*, **63**, (2009), 504.

36. T. Shodai, S. Okada, S. Tobishima and J. Yamaki, *Solid State Ionics*, **86-8**, (1996), 785.

37. L. P. Ma, P. Wang, H. B. Dai, L. Y. Kong and H. M. Cheng, *J. Alloys Compd.*, **466**, (2008), L1.

# 6. Appendix

## 6.1 Supplementary data for Chapter 3

Material [1], data for all four temperatures of CW PND Rietveld refinement found on accompanying CD titled DKC75N_70K.TBL, DKC75N_RT.TBL, DKC75N_389K.TBL, DKC75N_482K.TBL

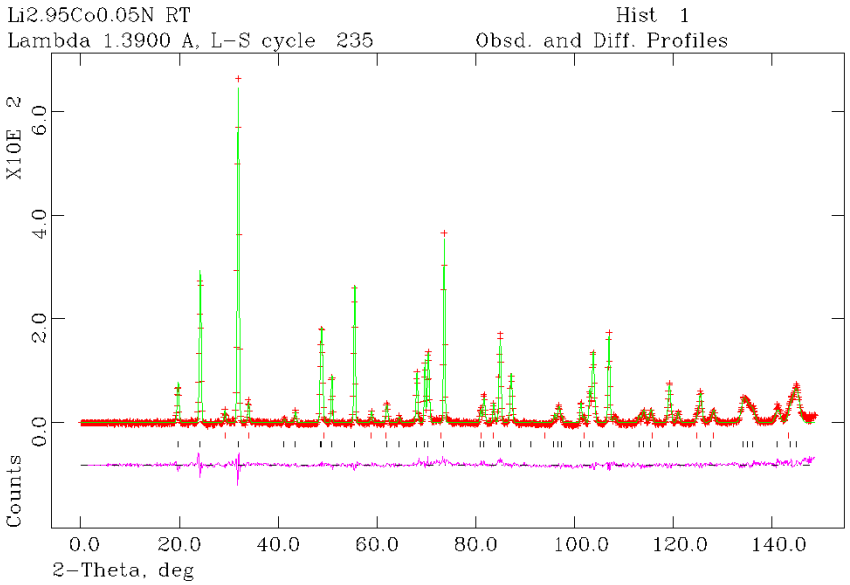


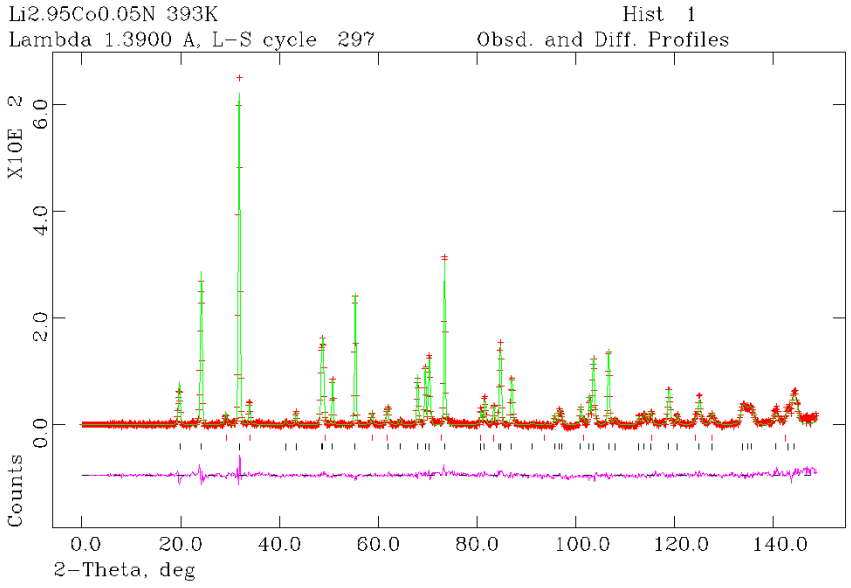

Material **[2]** data for all four temperatures of CW PND Rietveld refinement found on accompanying CD titled DKC76N_70.TBL, DKC76N_RT.TBL, DKC76N_388.TBL, DKC76N_482.TBL

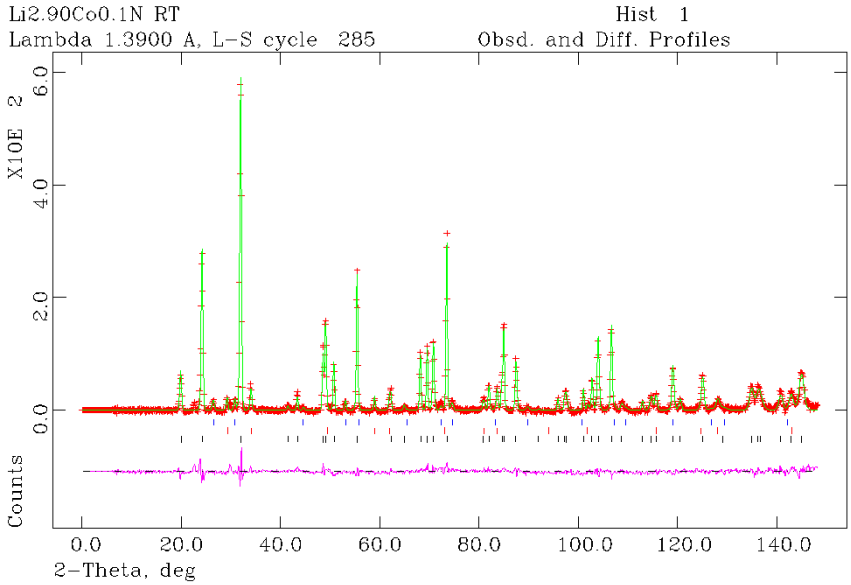


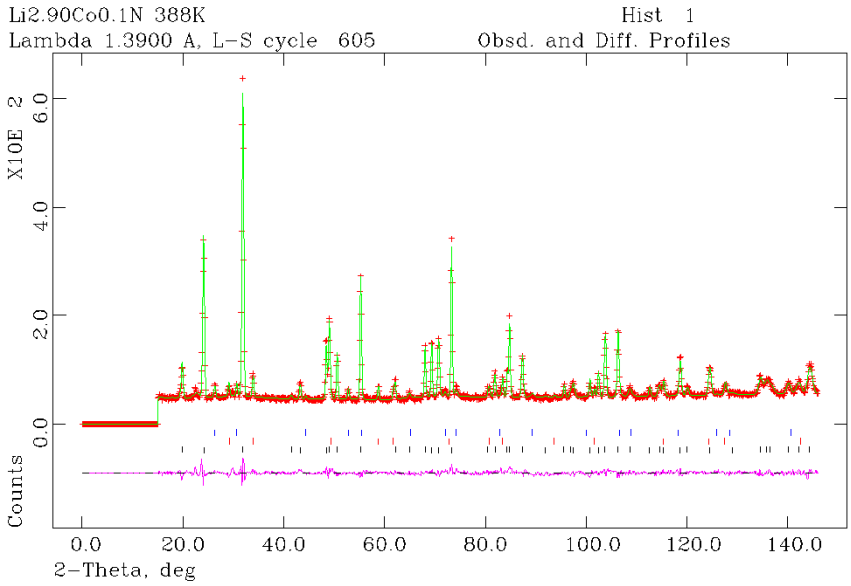


Material **[3]** data for all four temperatures of CW PND Rietveld refinement found on accompanying CD titled DKC82N_70K.TBL, DKC82N_RT.TBL, DKC82N_393K.TBL, DKC82N_493K.TBL

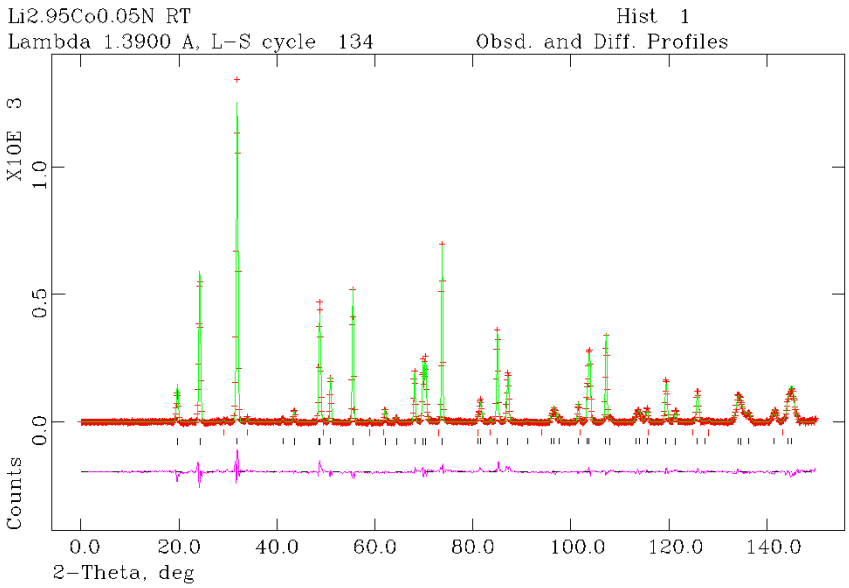


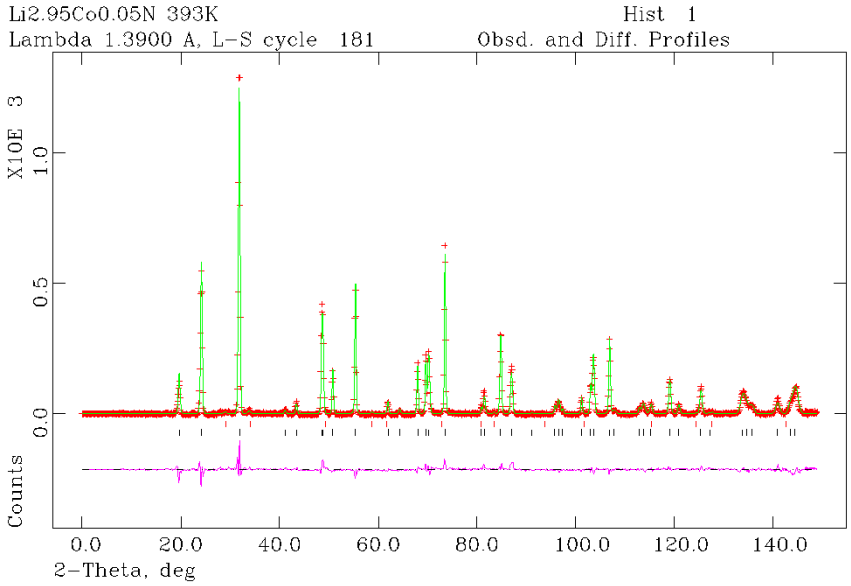


Material **[4]** data for all three histograms from ToF PND Rietveld refinements found on accompanying CD titled DKC-112-GEM.TBL

## 6.2 Supplementary data for Chapter 4

Material **[5]** data for XRD Rietveld refinement found on accompanying CD titled DKC12.TBL

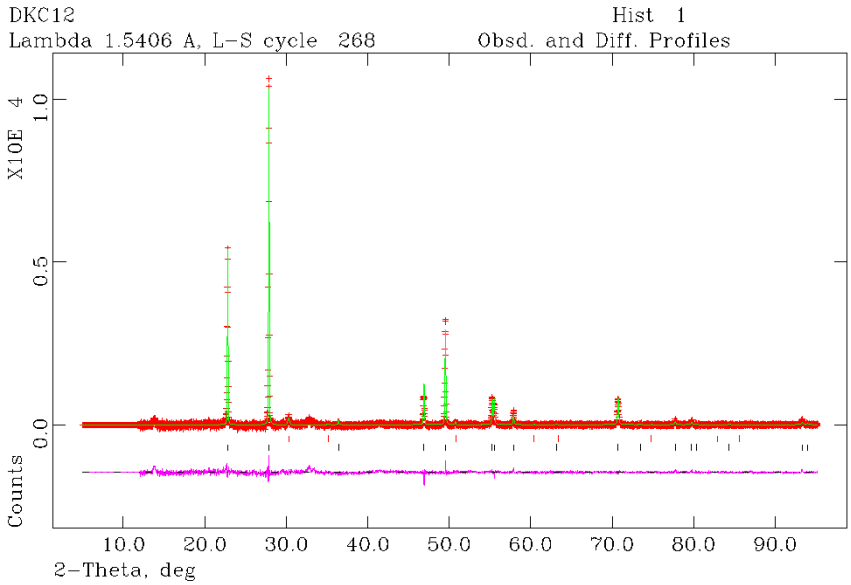


Material **[6]** data for XRD Rietveld refinement found on accompanying CD titled DKC-79TBL

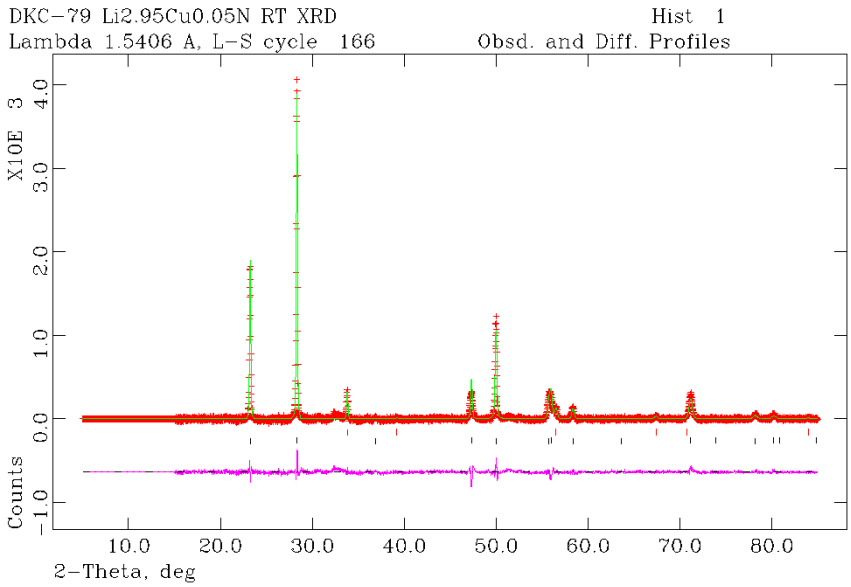


Material **[6]** data for CW PND Rietveld refinement found on accompanying CD titled DKC79N_70K.TBL, DKC79N_RT.TBL, DKC79N_389K.TBL, DKC79N_482K.TBL

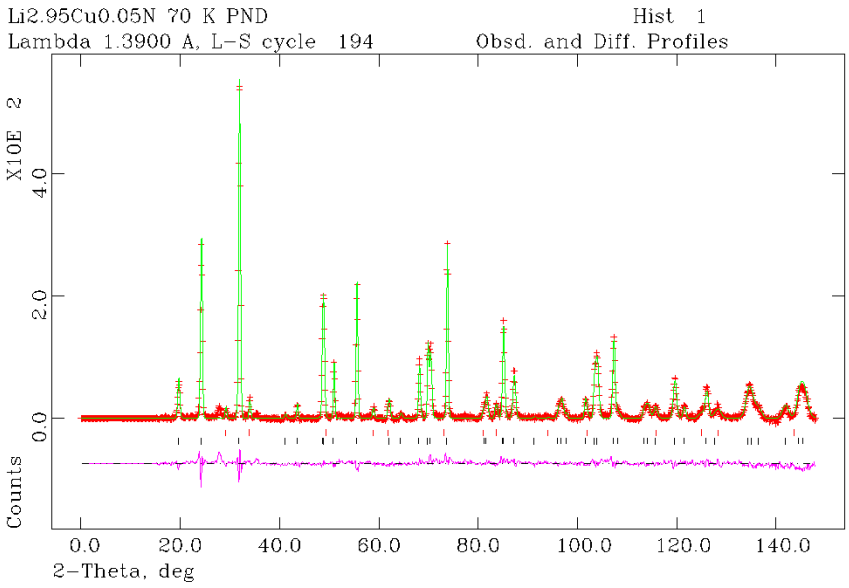
Li2.95Cu0.05N 70 K PND
Hist 1
Lambda 1.3900 A, L-S cycle 194
Obsd. and Diff. Profiles
X10E 2
4.0
2.0
0.0
Counts
0.0
20.0
40.0
60.0
80.0
100.0
120.0
140.0
2-Theta, deg

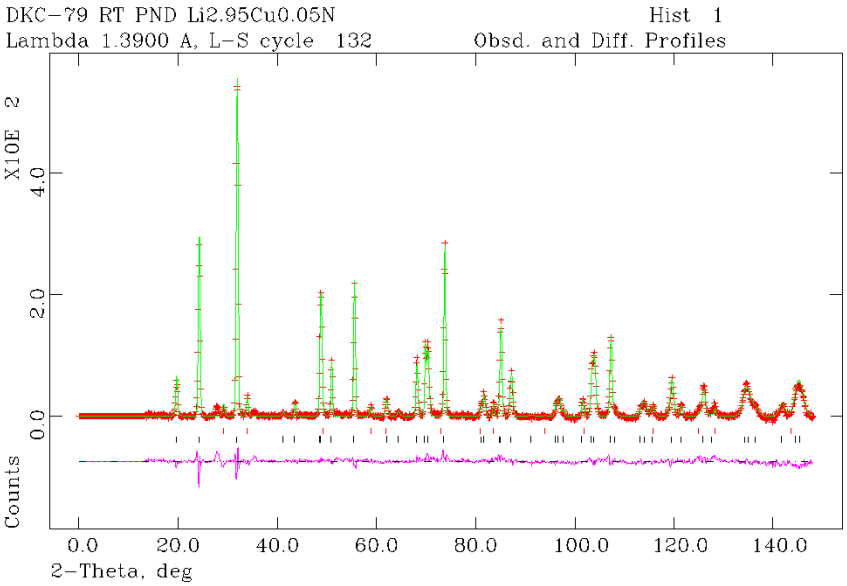
DKC-79 RT PND Li2.95Cu0.05N
Hist 1
Lambda 1.3900 A, L-S cycle 132
Obsd. and Diff. Profiles
X10E 2
4.0
2.0
0.0
Counts
0.0
20.0
40.0
60.0
80.0
100.0
120.0
140.0
2-Theta, deg

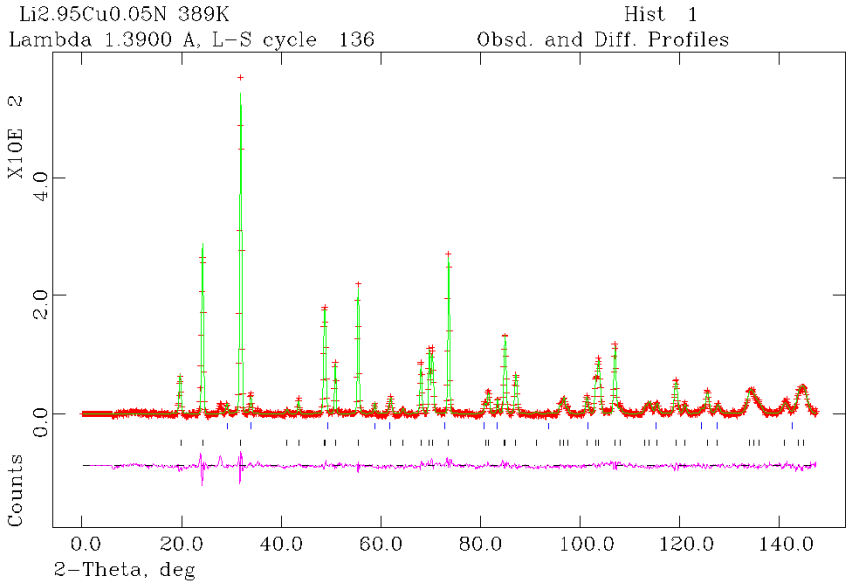


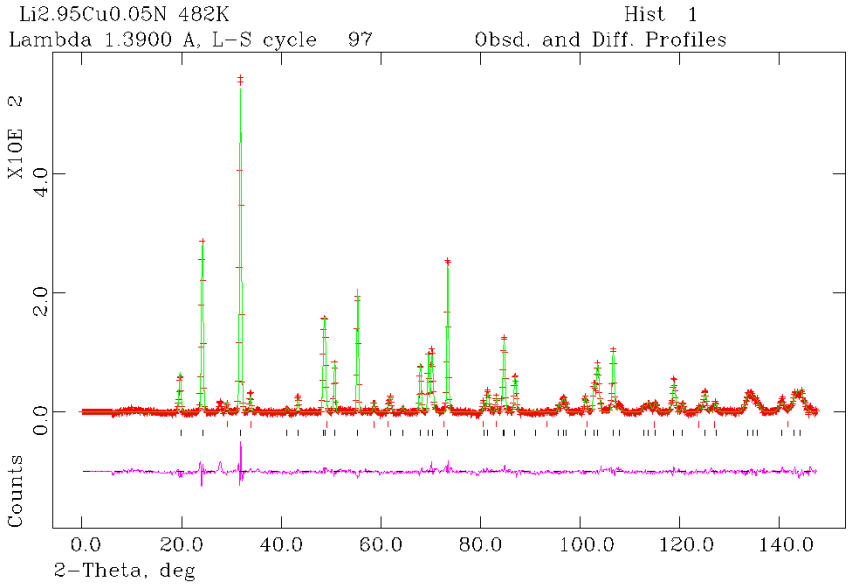


Material **[7]** data for XRD Rietveld refinement found on accompanying CD titled DKC13.TBL

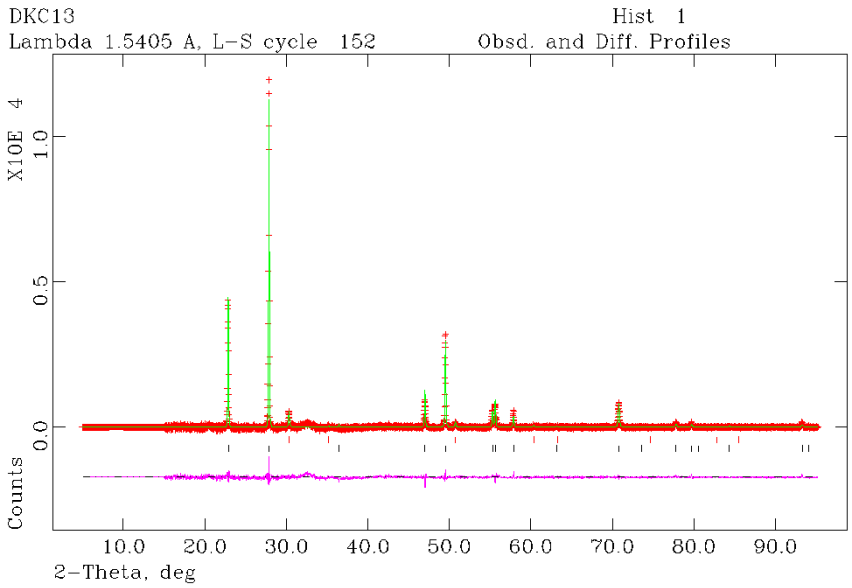


Material **[8]** data for XRD Rietveld refinement found on accompanying CD titled DKC-80.TBL

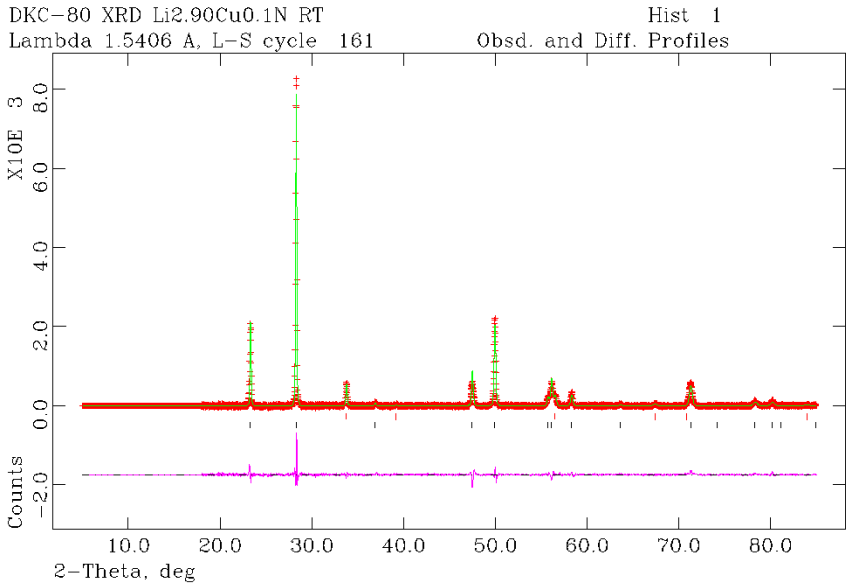


Material **[8]** data for CW PND Rietveld refinement found on accompanying CD titled DKC80N-70K.TBL, DKC80N-RT.TBL, DKC80N-393K.TBL, DKC80N-493K.TBL

Material **[9]** data for XRD Rietveld refinement found on accompanying CD titled DKC-10.TBL

Material **[10]** data for XRD Rietveld refinement found on accompanying CD titled DKC-30.TBL

Material **[11]** data for XRD Rietveld refinement found on accompanying CD titled DKC-11.TBL

Material **[12]** data for XRD Rietveld refinement found on accompanying CD titled DKC-31.TBL

Material **[13]** data for XRD Rietveld refinement found on accompanying CD titled DKC-94.TBL

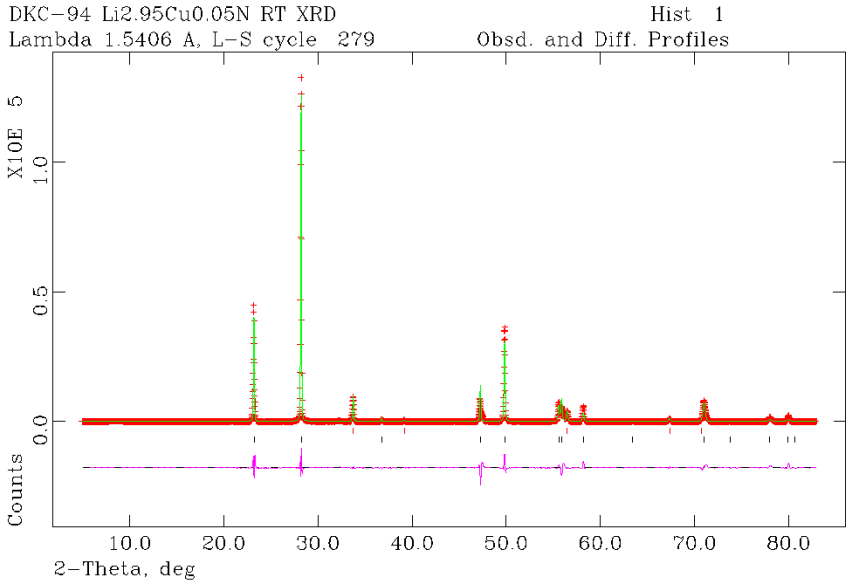


Material **[13]** data for ToF PND Rietveld refinement found on accompanying CD titled DKC-94-GEM(1).TBL

Material **[14]** data for XRD Rietveld refinement found on accompanying CD titled DKC15.TBL

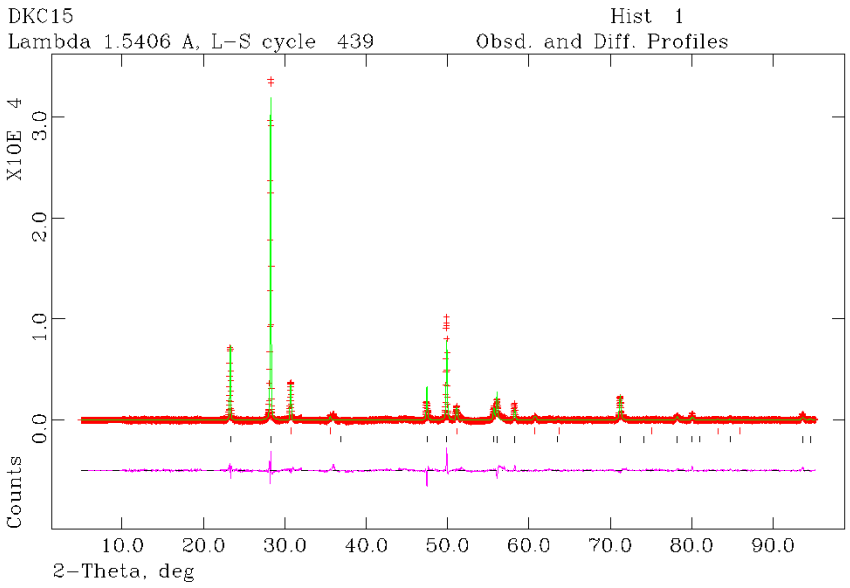


## 6.3 Supplementary data for Chapter 5

Material **[15]** data for XRD Rietveld refinement found on accompanying CD titled DKC-34GOOD.TBL

Material **[17]** data for XRD Rietveld refinement found on accompanying CD titled DKC-73BOB.TBL

Material **[17]** data for CW PND Rietveld refinement found on accompanying CD titled DKC73N_70.TBL, DKC73N_293.TBL, DKC73N_389.TBL, DKC73N_482.TBL

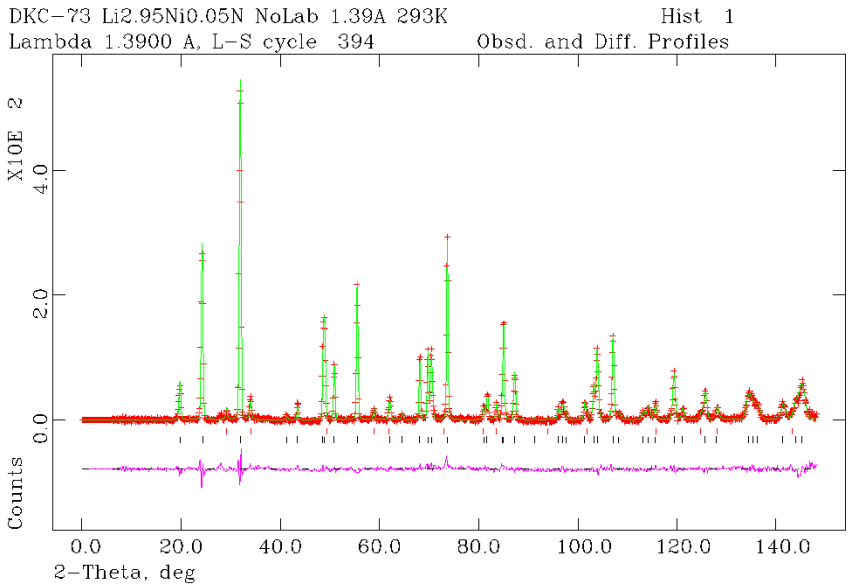

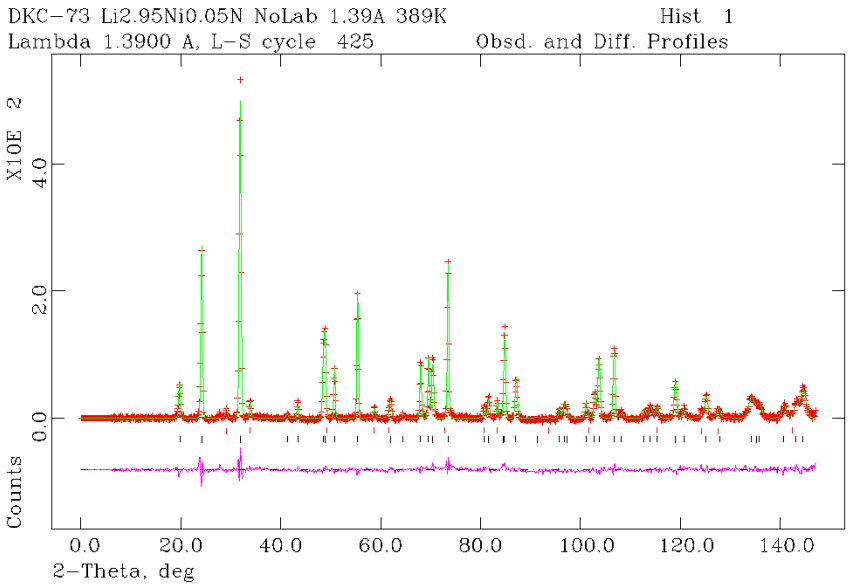


Material **[18]** data for XRD Rietveld refinement found on accompanying CD titled DKC-74.TBL

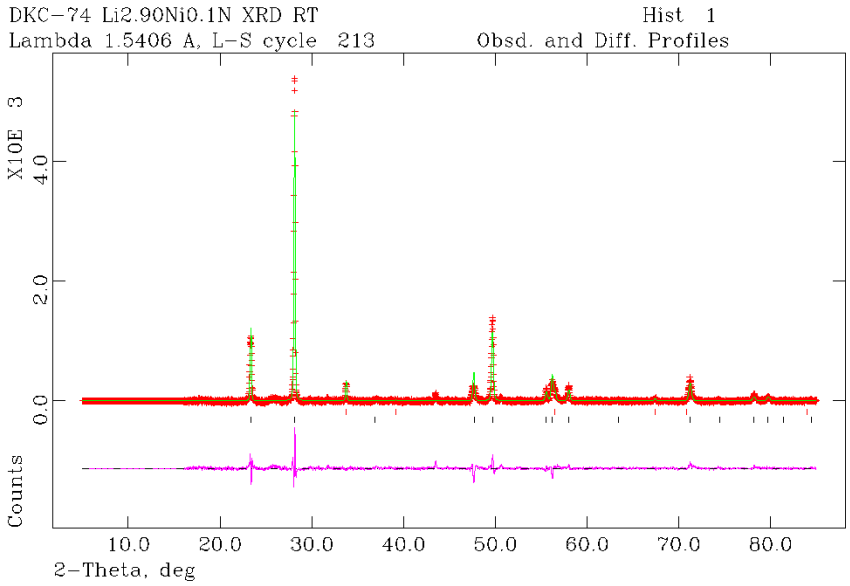


Material **[18]** data for CW PND Rietveld refinement found on accompanying CD titled DKC74N_70K.TBL, DKC74N_RT.TBL, DKC74N_389K.TBL, DKC74N_482K.TBL

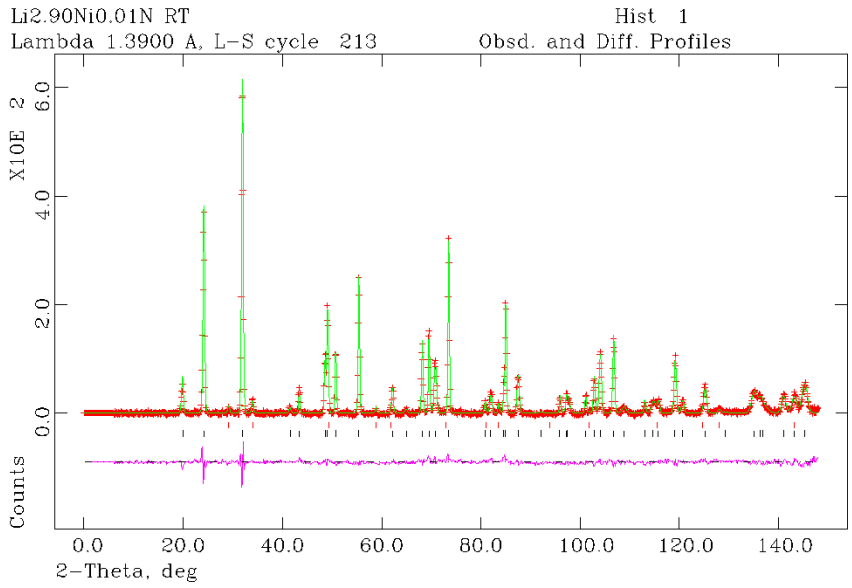


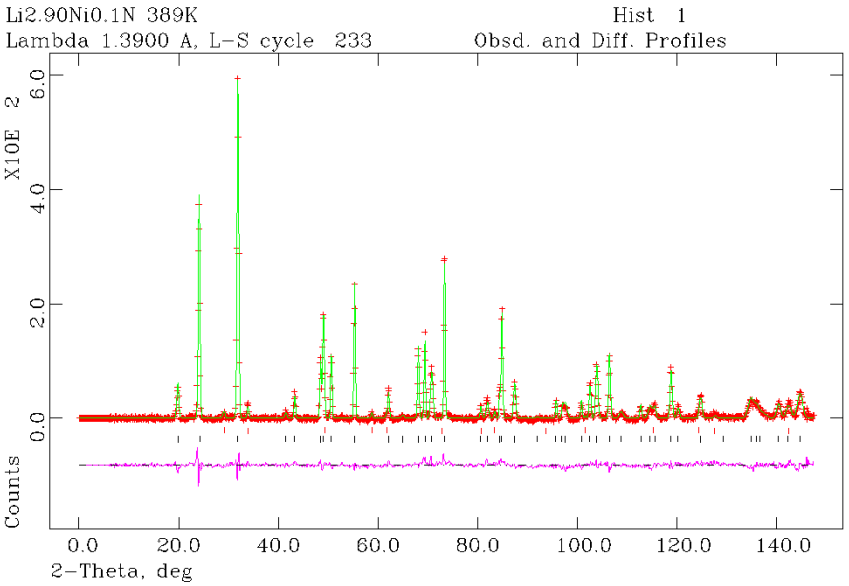


Material **[19]** data for XRD Rietveld refinement found on accompanying CD titled DKC-78BOB.TBL

Material **[18]** data for CW PND Rietveld refinement found on accompanying CD titled DKC78N_70LAB.TBL, DKC78N_RTLAB.TBL, DKC78N_388LAB.TBL, DKC78N_483LAB.TBL

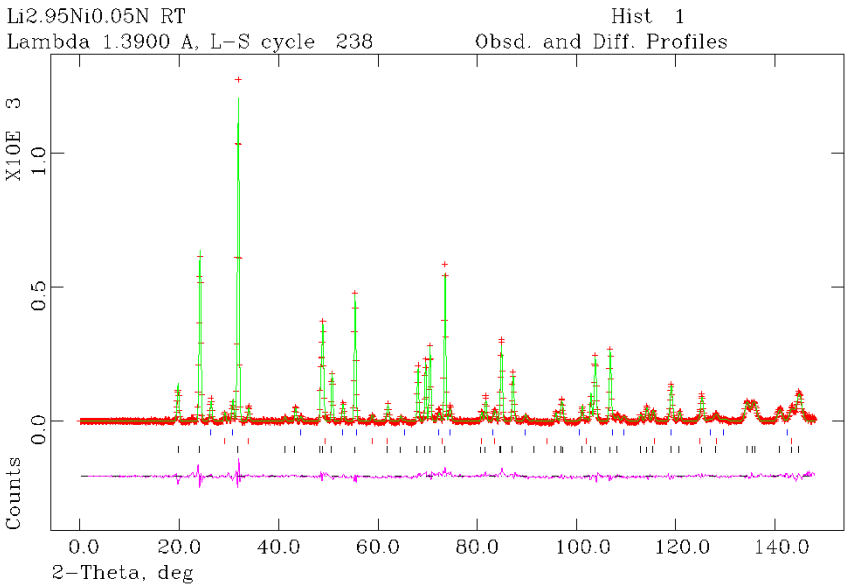


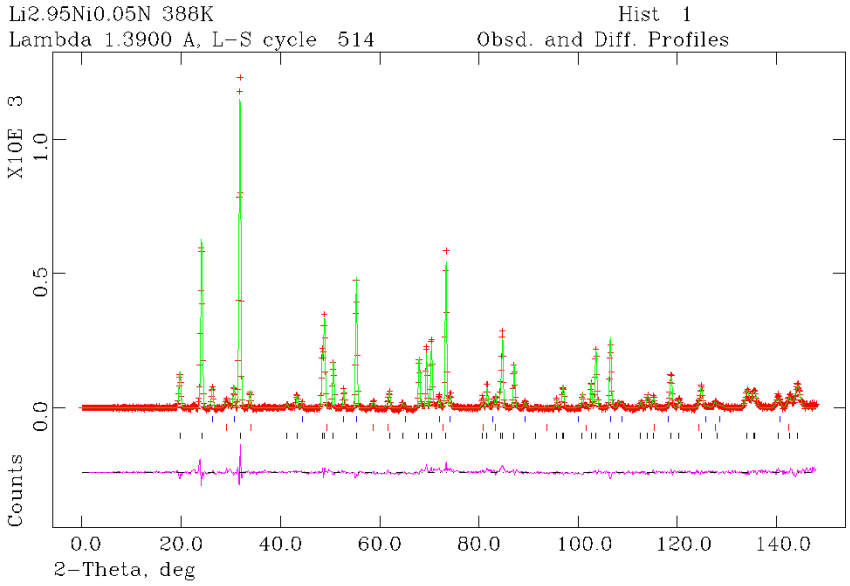


Material **[20]** data for XRD Rietveld refinement found on accompanying CD titled DKC-113BOB.TBL

Material **[20]** data for ToF PND Rietveld refinement found on accompanying CD titled DKC-113-GEM.TBL